XVIIth Symposium on Atomic, Cluster and Surface Physics 2010 (SASP 2010)

January 24 - 29, 2010
Universitätszentrum Obergurgl, Austria

International Scientific Committee:

Davide Bassi, Universitá degli Studi di Trento
Tom Rizzo, Ecole Polytechnique Fédérale Lausanne
Tilmann D. Märk, Universität Innsbruck
Martin Quack, Eidgenössische Technische Hochschule Zürich
Paul Scheier, Universität Innsbruck

Local Organizing Committee:

Paul Scheier
Arntraud Bacher
Alexander Kendl
Tilmann Märk
Irene Milewski
Renate Rödiger

Universität Innsbruck

Preface

In 1978 SASP was founded as a biennial winter conference by members of the Institute for Atom Physics (afterwards named Institute for Ion Physics, and since 2006 the Institute for Ion Physics and Applied Physics) of the Leopold-Franzens University of Innsbruck, Austria.

Since the beginning the format of SASP has been similar to that of a Gordon Conference, with invited lectures, poster presentations with ample time for discussion and indoor and outdoor activities. The attendance of the symposium has been kept to about 100 participants.

This international symposium seeks to promote the growth of scientific knowledge and effective exchange of information among scientists in the field of atomic, molecular, and surface physics. A special emphasis of this conference will be to focus on nano particles, biomolecules and astrochemistry. The symposium deals in particular with collisional interactions involving different types of collision partners, i.e. electrons, photons, molecules, nano particles, and surfaces.

SASP usually takes place in Austria, but every second time it may be held in another alpine country.

So far the SASP conferences were held at the following locations:

1978	Zirog, Italy
1980	Maria Alm
1982	Maria Alm
1984	Maria Alm
1986	Obertraun
1988	La Plagne, France
1990	Obertraun
1992	Pampeago, Italy
1994	Maria Alm
1996	Engelberg, Switzerland
1998	Going
2000	Folgaria, Italy
2002	Going
2004	LaThuile, Italy
2006	Obergurgl
2008	Les Diablerets, Switzerland
2010	Obergurgl

SASP Erwin Schrödinger Gold Medal 2010

In 1992 the ‚SASP Award for Outstanding Scientific Achievements' was initiated by the SASP International Scientific Committee. This award is granted during the biennial SASP meeting to one or two scientists, chosen amongst those who have strong connections to the activities of SASP.

So far the award was granted to

1992	David Smith, Birmingham
1994	Zdenek Herman, Praha
1996	Werner Lindinger and Tilmann Märk, Innsbruck
1998	Eldon Ferguson, Boulder, and Chava Lifshitz, Jerusalem
2000	Jean H. Futrell, Richland
2002	Eugen Illenberger, Berlin
2004	Anna Giardini-Guidoni, Roma
2006	Davide Bassi, Trento, and Martin Quack, Zürich
2008	Helmut Schwarz, Berlin

Recipient of the SASP Award 2010 – in the form of the 'Erwin Schrödinger Gold Medal' designed by Zdenek Herman – will be

Kurt Becker, Polytechnic Institute of New York University

Kurt Becker from Polytechnic Institute of New York University, USA, will receive the award for his outstanding contributions to molecular physics (interaction of electrons with molecules and clusters) and plasma physics (properties and applications) .

Program

Sunday	**Monday**	**Tuesday**	**Wednesday**	**Thursday**
	9:00 (invited) R.I. Kaiser	9:00 (invited) M. Arndt	9:00 (invited) A. Solov'yov	9:00 (plenary) F. Aumayr
	9:30 (invited) O. Dutuit	9:30 (invited) D. Stranges	9:30 (invited) R. Beck	09:40 (invited) F. Gianturco
	10:00 (invited) N.J. Mason	10:00 (invited) D. Schooß	10:00 (invited) R. Marquardt	10:10 (invited) T. Takayanagi
	10:30 Coffee break	10:30 Coffee break	10:30 Coffee break	10:40 Coffee break
	11:00 (invited) G. Ganteför	11:00 (invited) J. Bredehöft	11:00 (invited) P. Defrance	11:10 (invited) M. Quack
	11:30 (invited) W. Christen	11:20 (invited) K. Hermansson	11:20 (invited) C. Mayhew	11:40 (hot topic) A. Stace
	12:00 *ski &coffee*	11:50 *ski &coffee*	11:50 *ski &coffee*	12:00 *ski &coffee*
	16:30 (invited) O. Echt	16:30 (invited) B. Huber	16:30 (hot topic) S. Ptasinska	16:30 (invited) K. Becker
	17:00 (invited) A.M. Ellis	17:00 (invited) K. V. Haeften	16:50 (hot topic) M. Mudrich	17:00 (invited) O. Ingolfsson
	17:30 (invited) W.E. Ernst	17:30 (invited) S. Feil	17:10 (invited) S. Matejcik	17:20 (invited) F. Ferreira da Silva
	18:00 (invited) E. Campbell	17:50 (hot topic) M. Farnik	17:30 (hot topic) V. Kresin	17:40 (invited) T. Field
		18:10 (hot topic) M. Beyer	17:50 (hot topic) L. Feketeova	
			18:10 (hot topic) S. Price	
	18:30 *Dinner*	18:30 *Dinner*	18:30 *Dinner*	18:30 *Conference Dinner*
20:30 (plenary) J. Ullrich	**Poster**	20:30 (hot topic) J. Seebacher	**Poster**	
21:10 (invited) M. Lezius		20:50 (hot topic) R. Fantoni		

Contents

Invited Papers

Hot Topic Papers

Contributed Papers (Poster)

Invited Papers

The Chemical Evolution of Titan´s Atmosphere: From Homogeneous to Heterogeneous Chemistry

Brant Jones, Fangtong Zhang, Pavlo Maksyutenko, Ralf I. Kaiser
Department of Chemistry, University of Hawaii at Manoa, Honolulu, HI 96822, USA
NASA Astrobiology Institute, University of Hawaii at Manoa, Honolulu, HI 96822, USA

ralfk@hawaii.edu

The arrival of the Cassini-Huygens probe at Saturn's moon Titan - the only Solar System body besides Earth and Venus with a solid surface and thick atmosphere – in 2004 opened up a new chapter in the history of Solar System exploration. Titan's most prominent optically visible features are the aerosol-based haze layers, which give Titan its orange-brownish color. However, the underlying chemical processes, which initiate the haze formation, have been the least understood to date. Based on limited laboratory studies related to the formation of soot, planetary chemists proposed that polyacetylenes such as diacetylene (HCCCCH) and triacetylene (HCCCCCCH) play a crucial role. It is remarkable that, based on reasonable alternative choices for the unknown reaction dynamics, photochemistry, and reaction rates, the models show completely inconsistent mechanisms for the principal routes to polyynes in Titan's atmosphere. The reaction products are either guessed or often analyzed off-line and ex situ. Hence, the detailed chemical dynamics of the reactions such as the role of radicals and unstable, transient species cannot always be obtained, and reaction mechanisms can at best be inferred qualitatively. However, recent data from the Cassini-Huygens mission have revealed that the transformation of simple molecules such as acetylene (HCCH) and diacetylene (HCCCCH) to complex polyacetylenes such as triacetylene (HCCCCCCH) likely present one of the most fundamental steps in the context of the evolution of planetary atmospheres. Therefore, an experimental investigation of these elementary reactions under single collision conditions is desirable.

Here, we report data on recent laboratory and modeling studies on the role of polyacetylenes (polyynes) in the formation of Titan's organic haze layers utilizing crossed molecular beam experiments. These studies focus on the photodissociation of the diacetylene monomomer and its dimer and on the synthesis of diacetylene and triacetylene under single collision conditions. Those investigations provide key concepts on the formation mechanisms of unsaturated hydrocarbon molecules – in particular polyynes and their related compounds - together with their hydrogen deficicient precursors from the 'bottom up' in the atmosphere of Saturn's moon Titan.

Brilliant FEL Light: New Frontiers in AMO Research

J. Ullrich
Max-Planck-Institut für Kernphysik, Heidelberg

Upcoming 4th generation lights sources, Free Electron Lasers (FEL), will provide, for the first time, intensities, coherence properties, short-time and pump-probe options in the VUV to X-ray regimes comparable to those presently realized by intense, ultra-short laser pulses in the visible. At least three completely new fields of research are expected to open up in atomic and molecular physics. First, the huge integrated radiation flux enables to investigate in unprecedented detail dilute samples, as for example positive ions up to the highest charge states, negative atomic ions, negative or positive state-prepared molecular and size-selected cluster ions. Second, the tremendous peak intensities allow investigating, for the first time, fundamental non-linear processes where few photons interact with few electrons in atoms, molecules, clusters or ions. Third, the short-time properties will enable unique time dependent experiments with any of these targets and first femtosecond VUV-VUV pump-probe measurements have been demonstrated recently. In the talk, these novel fields will be highlighted and first results of pioneer experiments at the **F**ree Electron **Las**er at **H**amburg (FLASH) [1-6] as well as at the **S**pring8 **C**ompact **S**ASE **S**ource (SCSS) in Japan will be discussed. Future possibilities opened e.g. by the integration of large area imaging photon CCD detectors into reaction microscopes (REMI) [7] or by providing ultra-cold targets via a magneto-optical trap (MOT) in a REMI, the streaking of electrons and ions by overlapping phase stabilized THz radiation etc. will be envisioned.

References

[1] R. Moshammer et al., Phys. Rev. Lett. **98** (2007) 203001
[2] S.W. Epp et al., Phys. Rev. Lett. **98** (2007) 183001
[3] H.B. Pedersen et al., Phys. Rev. Lett. **98** (2007) 223202
[4] A. Rudenko et al., Phys. Rev. Lett. **101** (2008) 073003
[5] Y. H. Jiang et al., Phys. Rev. Lett. **102** (2009) 123002
[6] M. Kurka et al., J. Phys. B (submitted)
[7] J. Ullrich et al., Prog. Rep. Phys. **66** (2003) 1463

Structures of Gold Cluster Ions by Trapped Ion Electron Diffraction

D. Schooss[1], A. Lechtken[1], C.Neiss[1], and M.M. Kappes[2]

[1] *Institut für Nanotechnologie, Forschungszentrum Karlsruhe, Postfach 3640, 76021 Karlsruhe, Germany*

[2] *Institut für Physikalische Chemie, Universität Karlsruhe, Kaiserstr. 12, 76128 Karlsruhe, Germany*

detlef.schooss@int.fzk.de

Physical and chemical properties of clusters are directly related to their structure, the identification of gas phase structures is therefore a central point in cluster science. To experimentally determine gas phase structures of size selected cluster ions we use trapped ion electron diffraction (TIED), a hybrid of the electron diffraction method and the ion trap mass spectrometry technique. Structures are assigned by comparison of experimental and simulated molecular scattering functions, the latter are calculated from candidate structures obtained from a density functional theory.

In particular the structures of small bare gold cluster have attracted much interest recently. After a short introduction into the method, we present our recent work on structures of anionic [1] and cationic [2] gold clusters $Au_n^{+/-}$(n=11-20). For Au_n^- experiment and theory have been at odds with respect to the specific cluster size at which the transition from 2D to 3D structures occurs. Using TIED in combination with state of the art DFT calculation we show that the 2D-3D transition is at 12 gold atoms, in good agreement with former investigations. Au_{13}^- to Au_{15}^- are flat 3D structures. Hollow cage structures were found for Au_{16}^--Au_{18}^-, Au_{19}^- and Au_{20}^- are tetrahedral structures. The same structural families are realized for the cations Au_n^+ (n>14), however, structures for a given size as well as the transition sizes differ significantly. Additionally structures of transition metal doped gold clusters [3] are presented and discussed.

References

[1] M.P. Johansson, A. Lechtken, D. Schooss, M.M. Kappes, F. Furche, *Phys. Rev. A* 2008, *77*, 053202; A. Lechtken, C. Neiss, M.M. Kappes, D. Schooss, *Phys. Chem. Chem. Phys.* 2009.

[2] D. Schooss, P. Weis, O. Hampe, M. M. Kappes, *Phil. Trans.*, in press; A. Lechtken, C. Neiss, P. Weis, M.M. Kappes, D. Schooss, *to be published.*

[3] L.-M. Wang, J. Bai, A. Lechtken, W. Huang, D. Schooss, M.M. Kappes, X. C. Zeng, L.-S. Wang, Phys. Rev. B 2009, 79, 033413.

Nanoparticles on a Surface: Atomistic Approach for Structure, Dynamics and Pattern Formation

Ilia A. Solov'yov, Veronika V. Dick, Andrey V. Solov'yov

Frankfurt Institute for Advanced Studies, Goethe University, Ruth-Moufang-Str. 1, 60438 Frankfurt am Main, Germany

solovyov@fias.uni-frankfurt.de

Nanotechnology is an exploding research domain [1]. This generic word refers to physical and chemical research performed on systems having a characteristic length scale of the order of the nanometer. At that particular length scale, new specific physical and chemical properties emerge. One of the main targets of nanophysics and nanochemistry is the development of controlled, reproducible and industrially transposable, nanostructured materials. An issue of fundamental interest is the precise control of the systems' architecture. All technological developments based on nanostructured materials (potential industrial applications are numerous: micro-electronics, heterogeneous catalysis, magnetic storage, etc) require the understanding of the underlying factors controlling the structuring of the systems.

The implementation of nanofabricated systems with functional properties into various devices with real or potential applications requires a detailed understanding of the mechanisms of self-assembly and growth of nanosystems with desired properties and also of the methods for the control of these mechanisms. Here we focus on the exploration of the growth and self-organization of nanosystems with tailored properties for immediate and potential industrial applications. This includes self-organized 1D systems (nanotubes and nanowires), 2D and 3D systems (aggregates of catalytically active nanoparticles and responsive nanostructured surfaces).

We present an overview of recent advances in a systematic theoretical description of physical properties of free and supported nanoparticles (atomic clusters) such as their stability, atomic and electronic structure, magnetic, thermal and optical properties [2-9].

A special attention is paid to the process of deposition of nanoparticles on a substrate at various energies and to the analysis of dynamics of nanoparticles on a surface. It is demonstrated that the pattern formation on a surface depends crucially on the ratio between the flux of nanoparticles to the surface and their mobility over the surface. We demonstrate that stability of the structures on surface depends strongly on several factors, such as the concentration of impurities and temperature [10].

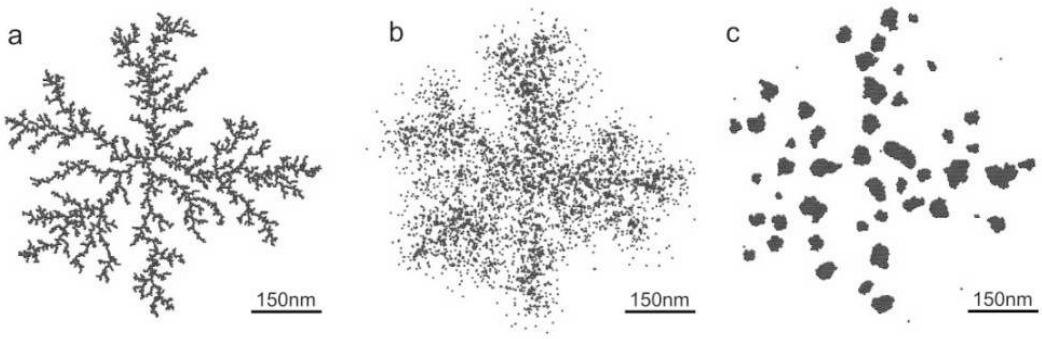

Fig. 1: *Evolution of the fractal structure, calculated with accounting for the internal dynamics of the particles in the fractal. (a) Initial structure of the fractal; (b) rapid fragmentation of the fractal (c) fragmentation of a fractal due to diffusion of the particles along the fractals branches*

We consider the post-growth processes occurring in a nanofractal on surface by accounting for the diffusion and detachment processes in the system. We demonstrate that these kinetic processes control the final shape of the islands on surface after the post-growth relaxation as illustrated in Fig. 1.

An illustrative example of the influence of critical factors on the structure formation in nanosystems is the change in morphology of Ag nanofractals due to their oxidation [10,11] shown in Fig. 2. From a fundamental point of view, the return to equilibrium state for these metastable dendritic structures is the growth reverse process; the same microscopic phenomena govern the formation and the relaxation. A recent systematic study by Bréchignac and co-workers of the influence of the fragmentation dynamics and subsequent relaxation to the equilibrium shapes, have shown that these latter are controlled by the deposition conditions and cluster composition. In particular, incorporating impurities into the incident clusters prior to their deposition induce a post-fractal island fragmentation due to a drastic change of the diffusion parameters.

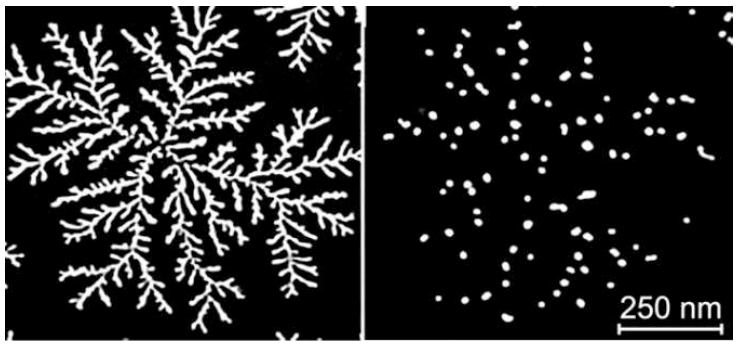

Fig. 2: *Experimental observation of the silver fractal perturbation by adding of oxygen impurities to the silver clusters [11,12].*

Another example is the formation of unusually long fullerene-based nanowires with the length to width aspect ratio exceeding 3000 [13]. Recently it was demonstrated that the growth of these nanowires is strongly solvent-dependant [13]. Thus, they tend to grow from the 1,2,4-trimethylbenzene solution of C_{60}, while only flake-like small particles nucleate if for example toluene is used as a solvent [14], see Fig. 3.

The influence of activators on the catalytic activity of nanoparticles is also studied. A recent systematic study has found that the introduction of B into Ni nanoparticles would significantly alter the ultrafine nanostructure of the metal, which in turn dramatically improves the catalytic activity of Ni in a vast number of industrially important hydrogenation and dehydrogenation reactions [15,16]. In addition by inserting activators in metallic nanoparticles for catalyzing the growth of carbon nanotubes, one can achieve the desired structural characteristics or growth rates [17-20]. We report the results of theoretical investigation of the interaction of Ni nano-particles with silica surface and elucidate the molecular mechanisms leading to catalytic role of Ni nano-particles in the nanotube growth process. We suggest a simple model for the description of stability and energetics of a nanotube with arbitrary chirality [4]. The proposed method is based on the liquid drop model.

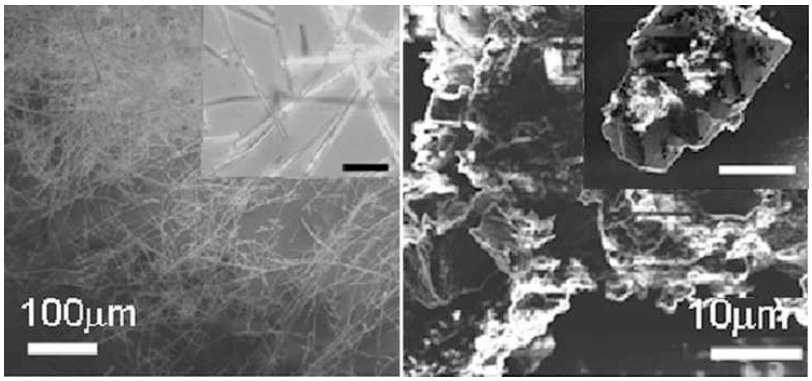

Fig. 3: *Scanning electron microscopic images of the fullerene (C_{60}) crystals (either in the form of wires or particles) grown by using the solvents of 1,2,4-trimethylbenzene (left) and toluene (right). The insets are the corresponding optical microscopic images [21].*

We discuss effects of variation of electric, magnetic, thermal and optical properties of atoms and nano-particles caused by the interaction with a surface [5,6,7]. Special attention is paid to the formation of plasmon resonances and to differences in photo absorption spectra and thermal properties of free and supported or embedded nanostructures [5,6,7]. We elucidate the role of dynamical screening in the photoionization or photoabsorption process of an atom, which is either confined within a fullerene shell or is adsorbed onto its surface [8,9]. This effect has a general nature. It will also appear for impurity atoms or molecules embedded into or attached onto a metallic cluster or a nanotube. A dynamical screening factor is defined, and

is shown to lead to an enhancement of the amplitude of the electromagnetic wave within a specific range of frequencies [8,9].

References

[1] C. Bréchignac, P. Houdy, M. Lahmani editors, "Nanomaterials and Nanochemistry", Cambridge University Press, Springer, (2007)
[2] A. Lyalin, A.V. Solov'yov and W. Greiner, Phys. Rev. A **74**, 043201, (2006).
[3] V.V. Semenikhina, A. Lyalin, A.V. Solov'yov and W.Greiner, JETP **106**, 678, (2008).
[4] I.A. Solov'yov, M. Mathew, A.V. Solov'yov and W. Greiner, Phys. Rev. E **78**, 051601, (2008).
[5] A.V. Solov'yov, Int. J. Mod. Phys. B **19**, 4143, (2005).
[6] A.V.Korol, A.V. Solov'yov, Phys.Rev.Lett. **98**, 17960, (2007).
[7] A.Lyalin, A.Hussein, A.V. Solov'yov, Phys.Rev. E, Phys. Rev. B **79**, 165403, (2009).
[8] J.P. Connerade, A.V. Solov'yov, J. Phys. B: At.Mol.Opt.Phys. **38**, 807, (2005).
[9] S. Lo, A. Korol, A.V. Solov'yov, J.Phys.B: At.Mol.Opt.Phys **40**, 3973, (2007).
[10] V.V. Dick, I.A. Solov'yov, A.V. Solov'yov, Proceedings of 4th International Symposium "Atomic Cluster Collisions: structure and dynamics from the nuclear to the biological scale", ISACC 2009, Ann Arbor, USA, July 14-18, in print, (2009).
[11] A. Lando, N. Kébaïli, Ph. Cahuzac, C. Colliex, M. Couillard, A. Masson, M. Schmidt, C. Bréchignac, Eur. Phys. J. D **43**, 151, (2007).
[12] A. Lando, N. Kébaïli, Ph. Cahuzac, A. Masson, C. Bréchignac, PRL **97**, 133402, (2006).
[13] J. Geng, I.A. Solov'yov, W. Zhou, A.V. Solov'yov, and B.F.G. Johnson, J. Phys. Chem. C, **113**, 6390, (2009).
[14] I.A. Solov'yov, J. Geng, A.V. Solov'yov, B.F.G. Johnson, Chem. Phys. Lett., **472**, 166 (2009).
[15] J. Geng, D.A. Jefferson, B.F.G. Johnson, Chemistry: A European Journal **15**, 1134, (2009).
[16] J. Geng, D.A. Jefferson, B.F.G. Johnson, Chem. Commun., 969, (2007).
[17] V.B. Golovko, H.W. Li, B. Kleinsorge, S. Hofmann, J. Geng, M. Cantoro, Z. Yang, D.A. Jefferson, B.F.G. Johnson, W.T.S. Huck and J. Robertson, Nanotechnology **16**, 1636, (2005).
[18] J. Geng, D.A. Jefferson, B.F.G. Johnson, J. Mater. Chem., **15**, 844, (2005).
[19] J. Geng, I.A. Kinloch, C. Singh, V.B. Golovko, B.F.G. Johnson, M.S. P. Shaffer, Y. Li, and A.H. Windle., J. Phys. Chem. B **109**, 16665, (2005).
[20] J. Geng, H. Li, V.B. Golovko, D.S. Shephard, D.A. Jefferson, B.F.G. Johnson, S. Hofmann, B. Kleinsorge, J. Robertson, C. Ducati, J. Phys. Chem. B **108**, 18446, (2004).
[21] J. Geng, W. Zhou, P. Skelton, W. Yue, I.A. Kinloch, A.H. Windle, B.F.G. Johnson, J. Am. Chem. Soc. **130**, 2527, (2008).

Photodesorption from Metal Clusters

Kiichirou Koyasu, Marco Niemietz, and Gerd Ganteför

Department of Physics, University of Konstanz, 78457 Konstanz, Germany,
Email: gerd.gantefoer@uni-konstanz.de

There is a simple scheme explaining photodesorption from bulk surfaces: the so-called Menzel-Gomer-Redhead mechanism (Fig. 1). The photon excites the molecule-surface complex into a repulsive state and the molecule desorbs. However, on metal surfaces the mechanism does not work because of short live time of the excited state, which is quenched by the interaction with the metal conduction electrons. For clusters, the situation is different due to much lower density of states in the conduction band. We studied O_2 photodesorption from size-selected metal clusters using time-resolved photoelectron spectroscopy. The lifetime of the repulsive excited state is sufficiently long to allow for desorption. As a consequence, desorption yield is high approaching 100 %, which makes metal clusters interesting candidates for photochemistry.

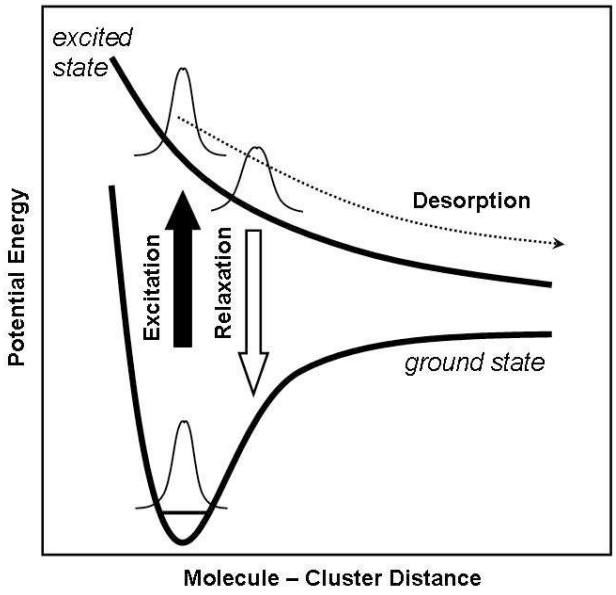

Fig.1. *Scheme of photodesorption of a molecule adsorbed to a bulk surface or a cluster. The photon excites the molecule-surface complex into an antibonding state resulting in desorption. On metal surfaces, relaxation competes with desorption resulting in low desorption yields. For metal clusters, relaxation can be slow.*

References:

[1] M. Niemietz, et al., Chem. Phys. Lett. **438**, 263 (2007).
[2] K. Koyasu et al., Chem. Phys. Lett. **450** , 96 (2007).
[3] K. Koyasu et al., Appl. Phys. A **96**, 679 (2009).

Probing Supersonic Beams from Supercritical Fluids — An Experimental and Theoretical Study

Wolfgang Christen
Institut für Chemie, Humboldt-Universität zu Berlin, Brook-Taylor-Str. 2, 12489 Berlin, Germany, christen@wolfgang-christen.net

Supersonic molecular beams continue to constitute an extremely versatile and rather popular tool in modern chemical physics. They are of prime importance in basic as well as applied research fields such as analytical chemistry, cluster science, optical spectroscopy, surface science, and thin film growth. Supercritical fluids have received considerable attention in materials science and engineering. In particular, jet expansions from the supercritical state are used to grow nanoparticles or to transfer molecules of pharmaceutical interest into the gas phase.

Focusing on the numerous applications, more fundamental topics of supersonic jet expansions such as the real gas behaviour have not been investigated in great detail. Until now, in most studies the characteristics of supersonic jets are treated in the approximation of ideal gas expansions. Here, particle associations are completely ignored, although they are responsible for the formation of clusters, both in the stagnation reservoir at elevated pressures and during the jet expansion.

In continuation of our earlier work on supersonic beams of supercritical fluids[1-6] we investigate the influence of thermodynamic quantities on the resulting beam velocity, beam temperature, and cluster size. The assumptions of an ideal gas treatment and its shortcomings are reviewed. A straightforward thermodynamic approach is presented that is capable to overcome most of those difficulties. It is shown that the experimental beam velocities are well described by considering the initial and final fluid enthalpies. These are computed using high accuracy equations of state explicit in the Helmholtz energy. The model calculations are complemented by a comprehensive set of experimental data covering a wide range of stagnation conditions. Particularly we focus on the gas-liquid phase transition of fluid systems and report surprising observations in the close vicinity of the critical point.

[1] W. Christen, K. Rademann, U. Even, submitted.
[2] W. Christen, K. Rademann. *Phys. Scr.* **80**, (2009), in press.
[3] W. Christen, T. Krause, K. Rademann, *Int. J. Mass. Spectrom.* **277**, 305 (2008).
[4] W. Christen, K. Rademann, *Phys. Rev. A* **77**, 012702 (2008).
[5] W. Christen, K. Rademann, U. Even, *J. Chem. Phys.* **125**, 174307 (2006).
[6] W. Christen, S. Geggier, S. Grigorenko, K. Rademann, *Rev. Sci. Instrum.* **75**, 5048 (2004).

Clusters in Clusters - Synthesis and Characterization of Clusters Embedded in Helium Nanodroplets

O. Echt,[1,2] A. Aleem,[1] P. Bartl,[1] F. Ferreira da Silva,[1] S. Jaksch,[1] I. Mähr,[1] H. Schöbel,[1] P. Waldburger,[1] A. Bacher,[1] D. K. Bohme,[3] S. Denifl,[1] P. Mach,[4] A. Mauracher,[1] M. Probst,[1] J. Urban,[4] F. Zappa,[5] T.D. Märk,[1] and P. Scheier[1]

[1] *Institut für Ionenphysik und Angewandte Physik, Leopold Franzens Universität, Technikerstr. 25, Innsbruck, Austria*

[2] *Dept. Physics, University of New Hampshire, Durham, NH 03824, USA, olof.echt@unh.edu*

[3] *Dept. Chemistry, York University, Toronto, Ontario M3J 1P3, Canada*

[4] *Dept. Nuclear Physics and Biophysics, Comenius University Bratislava, 84248 Bratislava, Slovakia.*

Clusters of helium atoms were among the very first atomic clusters deliberately synthesized in the gas phase in order to investigate their properties, including the possible occurrence of superfluidity in finite systems [1]. However, interest in these very weakly bound systems faded when methods were designed to prepare and investigate more strongly bound clusters that showed a range of intriguing features, including electronic shell structure in alkali metals, size-dependent chemical reactivity of transition metals, and the unique geometric structures of carbon clusters.

Renewed interest in helium awakened in the early nineties with the realization that helium droplets offer a new avenue for synthesis of novel complexes and their interrogation at ultralow temperatures [2]. As aptly noted by Toennies and coworkers [3], helium droplets may serve as *flying nano-cryo-reactors*. In this article we will highlight recent work in our laboratory in which helium droplets are used to synthesize weakly bound clusters of argon, hydrogen, water, ammonia, and complexes of C_{60} with water and ammonia clusters. The response of these systems to electron impact ionization and low-energy electron attachment reveals various intriguing features, including the formation of even-numbered hydrogen cluster cations due to reduction of intramolecular fragmentation, enhanced stability (magic numbers) of argon clusters containing nitrogen or water impurities, and novel ion-molecule reactions between C_{60} and small water or ammonia clusters. Other intriguing observations involve a hydrogen-helium $H_2He_2^+$ complex that had been predicted to occur in a linear, centrosymmetric He-H-H-He$^+$ structure [4], and anomalies in the size distribution of He_nX^+ and He_nX^- (X = atomic or molecular impurity) that make it possible to determine the size of ions solvated in helium.

What's so special about helium droplets?

Several features make helium droplets unique:

- The ease with which they can be synthesized with sizes ranging from 10^3 to 10^8 atoms, equivalent to droplet radii of 2.2 to 100 nm.
- The ultralow temperature of 0.37 K that droplets achieve shortly after their formation or after any kind of excitation, as a result of efficient evaporative cooling via emission of weakly bound helium atoms. Previously, researchers had cooled clusters by expanding them in a beam of helium, but the method was effective only for very small clusters, and the temperature attained remained unknown.
- The fact that they are superfluid at $T = 0.37$ K. Thus, almost any atom or molecule that collides with a droplet is swallowed and quickly moves to the center where it will coagulate with previously swallowed molecules. One consequence is that helium droplets offer a novel way to grow clusters of other species. Another is the possibility to grow complexes in metastable configurations.

Case studies

Argon clusters in helium droplets

Argon enjoys favorite status among experimentalists because it is inexpensive and essentially monisotopic; spectral congestion that plagues mass spectra of neon, krypton and xenon clusters is thus avoided. For theorists, neutral argon clusters come closest to a classical system characterized by simple pairwise additive interactions. However, argon cluster ions present a major, as yet unexplained puzzle. Size distributions of Ar_n^+ with $n \leq 79$ atoms are strikingly different when ions are produced by different methods. Distributions obtained by electron impact ionization of free pre-formed neutral clusters are smooth, with the exception of a deep minimum at $n = 20$, and a less prominent ledge at $n = 23$ [5]. In contrast, when Ar_n^+ is formed by expanding weakly ionized pure argon, a rich pattern of abundance maxima at $n = 19$, 23, 26, 29, 32, 34, 43, 49, 55 and beyond is found [6]. The numbers below 55 can be assigned to closure of icosahedral subshells around a rigid icosahedral Ar_{13}^+ core, essentially

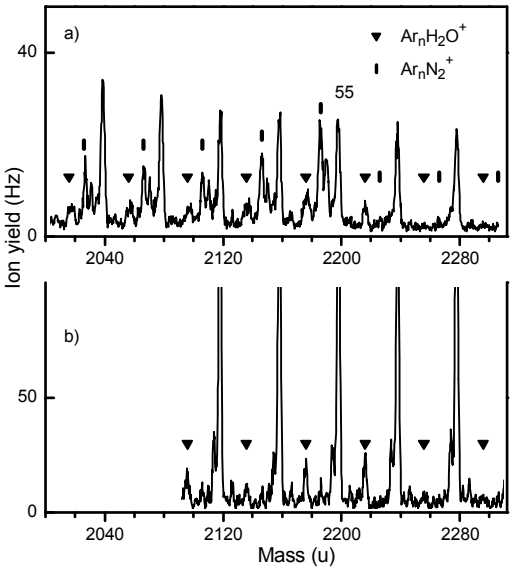

following the Aufbau principle explored by Hoare and others for arrangement of atoms that interact via a Lennard Jones potential.

When argon clusters embedded in helium droplets are ionized by electron impact one observes anomalies in the size distributions that closely resemble those observed after ionization of bare argon clusters; this demonstrates that caging and cooling effects provided by the helium matrix do not suffice to quench fragmentation of the nascent argon cluster ion [7]. However, striking abundance anomalies are observed in distributions of argon cluster ions that contain one H_2O, N_2 or O_2 molecule, see Figure 1. Two ion series are marked in the upper panel, $Ar_nN_2^+$ (vertical lines) and $Ar_{55}H_2O^+$ (triangles). The strong abundance of $Ar_{54}N_2^+$ and $Ar_{55}H_2O^+$ contrasts with the near-absence of slightly larger cluster ions containing the corresponding impurity. Close inspection also shows an abrupt drop in the ion abundance of $Ar_nO_2^+$ beyond $n = 54$. The features are most likely related to enhanced stability upon closure of the second icosahedral shell, but the difference in magic numbers (54 versus 55) and the well-known reactivity of charged argon-nitrogen complexes suggest structural differences that remain to be explained.

Water and ammonia clusters complexed with C_{60}

We have probed ion-molecule reactions between C_{60} and water or ammonia clusters in helium droplets; experimental results are augmented by ab-initio Hartree-Fock calculations [8]. C_{60} is hydrophobic; it does not dissolve in water nor ammonia although stable dispersions of C_{60} have been prepared by transferring organic solutions into an aqueous phase. The water solubility of fullerenes strongly changes upon chemical derivatization but so does its toxicity.

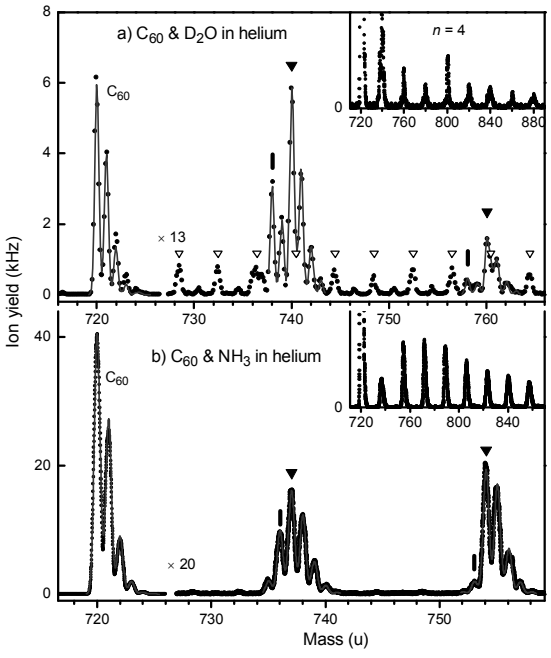

In the present experiments, helium droplets doped with C_{60} are co-doped with water or ammonia, and then ionized by electron impact. Among the various observations, two stand out. First, the weak interaction between neutral C_{60} and water extends to the cationic system. Ab-initio calculations show that the positive charge is localized on the fullerene and the water cluster remains weakly attached. In agreement with the theoretical results we observe that for water clusters $(H_2O)_n$ of size $n = 3$, 4, and 6 a

favored fragmentation channel is desorption of the complete cluster from C_{60}^+ rather than the common mechanism, evaporation of individual molecules.

When pure water or ammonia clusters are ionized by electron impact the main products are *protonated* cluster ions. This also holds for pure clusters embedded in helium. However, when helium droplets are co-doped with C_{60}, mass spectra as shown in Figure 2 result. One observes stoichiometric and dehydrogenated complexes (marked by triangles and vertical lines, respectively); the abundance of dehydrogenated ions is particularly strong for $n = 1$, i.e. $C_{60}OH^+$ and $C_{60}NH_2^+$. This strong signal of dehydrogenated cluster ions would seem to be a counterexample to the notion that fragmentation of clusters embedded in helium is suppressed compared to the same free clusters. We attribute the appearance of dehydrogenated ions to a novel mechanism that involves charge transfer from the primary He^+ to C_{60}, resulting in C_{60}^{2+}. This ion may then undergo ion-molecule reactions with other molecules, as previously observed in gas-phase experiments [9]. Reaction with water clusters would result in $C_{60}OH^+ + (H_2O)_{x-2}H_3O^+$; reaction with ammonia to $C_{60}NH_2^+ + (NH_3)_{x-2}NH_4^+$. The formation of doubly charged intermediates in doped helium droplets also offers a compelling explanation for previous observations of facile hydrogen loss from clusters of organic molecules and biomolecules.

On the size of ions in helium

Solvation is a unifying concept in chemistry. Gas-phase studies of ions in which physical properties are measured as a function of the number of solvent molecules have helped unraveling microscopic details of solvation shells. Closure of the first solvation shell in a complex XY_n (where the solute X is either neutral or charged) can be inferred from data that reflect evaporation energies of cluster ions in a qualitative way. In the present work 10] we apply mass spectrometry to determine the size of the first solvation shell for several ions embedded in helium droplets. Cations X^+He_n with $X^+ = F^+$, Cl^+, Br^+, I^+, I_2^+, or CH_3I^+ are formed by electron impact ionization of helium droplets doped with SF_6, C_4F_8, CCl_4, C_6H_5Br, CH_3I, or I_2; anions X^-He_n with $X^- = F^-$, Cl^- and Br^- are formed by electron attachment to helium droplets doped with SF_6, CCl_4 or C_6H_5Br.

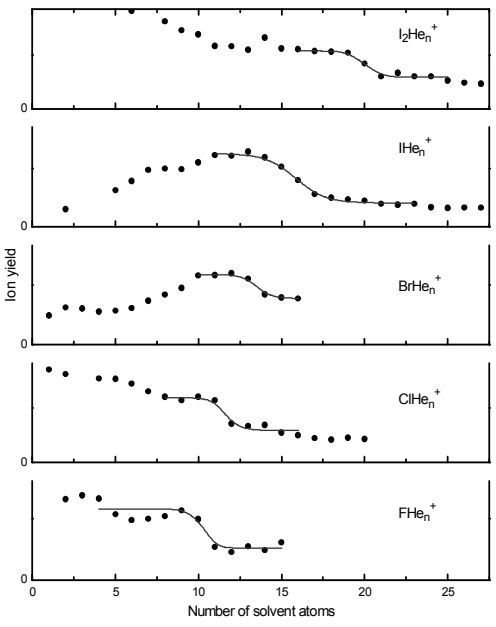

Our observations may be summarized as follows:

- Each ion series $X^{\pm}He_n$ exhibits a stepwise drop in the yield at some characteristic value n_s, see Figure 3.
- Anions of F, Cl and Br are much larger than their cations; the average ratio n_s(anion)/n_s(cation) is 1.70.
- For a given charge state, n_s values of halogen ions increase with increasing atomic number.

The stepwise drops provide a measure of the number of solvent atoms in the first solvation shell. A simple classical model is used to derive ionic radii from n_s. Assuming a helium density equal to the bulk value we find that halide anions in helium are nearly twice as large as in alkali halide crystals. The radii agree, within 10 %, with values derived from ion mobilities in superfluid bulk helium [11] and with values derived from radial density profiles computed by quantum Molecular Carlo methods [12].

References

[1] E.W. Becker, R. Klingerhöfer, and P. Lohse, Z. Naturforsch. A **16**, 1259 (1961); J. Gspann and H. Vollmar, J. Chem. Phys. **73**, 1657 (1980).
[2] S. Goyal, D. L. Schutt, and G. Scoles, Phys. Rev. Lett. **69**, 933 (1992).
[3] M. Farnik and J. Toennies, J. Chem. Phys. **122**, 014307 (2005).
[4] A. Krapp, G. Frenking, and E. Uggerud, Chem. Eur. J. **14**, 4028 (2008).
[5] P. Scheier and T.D. Märk, Int. J. Mass Spectrom. Ion Proc. **102**, 19 (1990); W. Miehle, O. Kandler, T. Leisner, and O. Echt, J. Chem. Phys. **91**, 5940 (1989).
[6] I.A. Harris, R.S. Kidwell, and J.A. Northby, Phys. Rev. Lett. **53**, 2390 (1984).
[7] F. Ferreira da Silva, P. Bartl, S. Denifl, O. Echt, T. . Märk, and P. Scheier, Phys. Chem. Chem. Phys. in print.
[8] S. Denifl, F. Zappa, I. Mähr, F. Ferreira da Silva, A. Aleem, A. Mauracher, M. Probst, J. Urban, P. Mach, A. Bacher, O. Echt, T.D. Märk, P. Scheier, Angew. Chemie (Int. Ed.), in print.
[9] G. Javahery, S. Petrie, A. Ketvirtis, J. Wang, and D.K. Bohme, Int. J. Mass Spectrom. Ion Proc. **116**, R7 (1992); J. J. Stry, M.T. Coolbaugh, E. Turos, and J.F. Garvey, J. Am. Chem. Soc. **114**, 7914 (1992).
[10] F. Ferreira da Silva, P. Waldburger, S. Jaksch, A. Mauracher, S. Denifl, O. Echt, T.D. Märk and P. Scheier, Chem. Eur. J. **15**, 7101 (2009).
[11] A.G. Khrapak, JETP Lett. **86**, 252 (2007); A.G. Khrapak and W.F. Schmidt, Int. J. Mass Spectrom. **277**, 236 (2008).
[12] E. Coccia, F. Marinetti, E. Bodo, and F. A. Gianturco, ChemPhysChem **9**, 1323 (2008).

Spectroscopy of Metal-Solvent Clusters: a Gas Phase Journey to Solvated Electrons

L. Varriale, N. Bhalla, N. Tonge, T. E. Salter, V. E. Mikhailov, and Andrew M. Ellis
Department of Chemistry, University of Leicester, Leicester LE1 7RH, UK
Email address: andrew.ellis@le.ac.uk

Many molecules dissolve in solution by forming ions. Spectroscopic studies of neutral solute-solvent clusters of the type $XY \cdot S_n$, where XY is the solute and S is the solvent, offers the opportunity to explore how the heterolytic dissociation into ions X^+ and Y^- evolves as the number of solvent molecules, *n*, is altered. Here we address a special case, where the solute is a metal atom and the solvent is ammonia. Certain metals, such as the alkalis, dissolve in liquid ammonia and among the potential products are M^+ and e^-. This heterolytic dissociation process can lead to an electron embedded in the solvent and has a major effect on solution properties, such as the electrical conductivity.

In order to explore some of the factors that lead to solvated electron formation, we have investigated a series of metal-solvent clusters as a function of size, with particular emphasis on the alkalis, but also for other metals too. The questions we wish to answer include: are discrete solvent shells formed and what are their structures? What evidence do we see for solvated electron formation in very small clusters? What happens if the solvent is changed, e.g. from ammonia to methyalamine?

An overview of our spectroscopic work on metal-solvent clusters will be given and some of the latest results will be presented. This will include not only mid-infrared studies aimed at exploring solvation structures in small clusters using vibrational spectroscopy, but also some recent near-infrared work exploring electronic transitions.

Experimental

The experiment seeks to obtain infrared spectra as a function of cluster size for *neutral* species. This is challenging as mass selection *prior* to spectroscopic probing is not possible. We use mainly IR-induced predissociation spectroscopy, which requires the absorbed IR photon to cause the ejection of one or more solvent molecules. This is registered by a dip in the ion signal in a given mass channel in a subsequent photoionization mass spectrum. The apparatus employed is illustrated in the figure, which shows cluster formation by a standard laser ablation/supersonic expansion arrangement. The output from an optical parametric oscillator is used for IR excitation and a dye laser for subsequent photoionization. Mass spectra are recorded using a time-of-flight mass spectrometer.

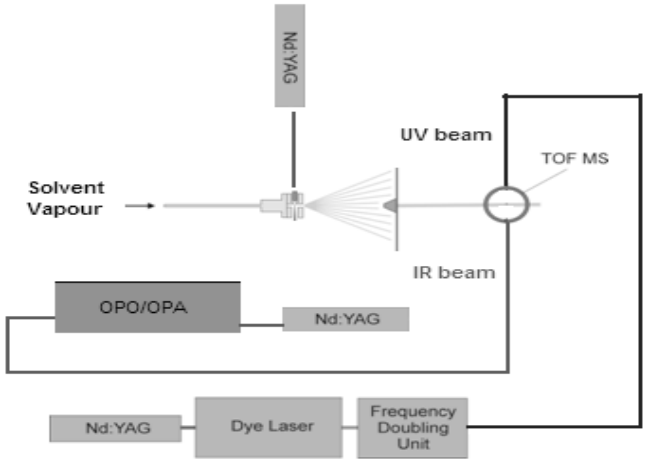

Results and Discussion

To illustrate some of the findings, one specific cluster is highlighted here, $Li(NH_3)_4$, but several others will be covered in the oral contribution.

$Li(NH_3)_4$ – vibrational spectroscopy

We have used IR spectroscopy to determine the structure of the solvent around the metal atom in $M(NH_3)_n$ clusters. For example, the IR spectrum of $Li(NH_3)_4$ in the N-H stretching fundamental region shows three bands in close proximity which have been attributed to the antisymmetric N-H stretching mode in the ammonia sub-units along with a perturbation by a bending mode overtone ($2\nu_4$). [1] There are several possible structures for $Li(NH_3)_4$. Supporting *ab initio* calculations suggest a global minimum in which all four NH_3 molecules occupy a single solvent shell, while the next lowest structure (approx. 0.25 eV above the global minimum) has three NH_3 molecules in the inner solvent shell and the fourth in the second solvent shell. These two structures are referred to as 4+0 and 3+1 according to the number of solvent molecules in the first and second shells, respectively. The IR spectrum is consistent only with a 4+0 structure. By way of contrast the vibrational spectra of larger clusters cannot be explained on the basis of single solvent shell occupancy, showing that the first solvent shell around Li can hold a maximum of four NH_3 molecules.

$Li(NH_3)_4$ – electronic spectroscopy

Using a similar photodepletion technique, we have recently recorded the first electronic spectrum of $Li(NH_3)_4$. This is postulated to be an important moiety in lithium/liquid ammonia solutions and very recent theoretical studies have suggested that the electronic

spectrum of $Li(NH_3)_4$ will strong overlap with that of the solvated electron, casting doubt on the utility of simple absorption spectroscopy for probing solvated electrons. Our work provides experimental confirmation of this suggestion, with a strong and broad electronic spectrum being recorded in the near-infrared which would overlap strongly with the well-known solvated electron spectrum. Part of the electronic spectrum is shown below, where it is recorded in two channels: (i) as depletion in $Li(NH_3)_4^+$ or enhancement in $Li(NH_3)_3^+$. An assignment of this spectrum will be presented and discussed in the oral presentation.

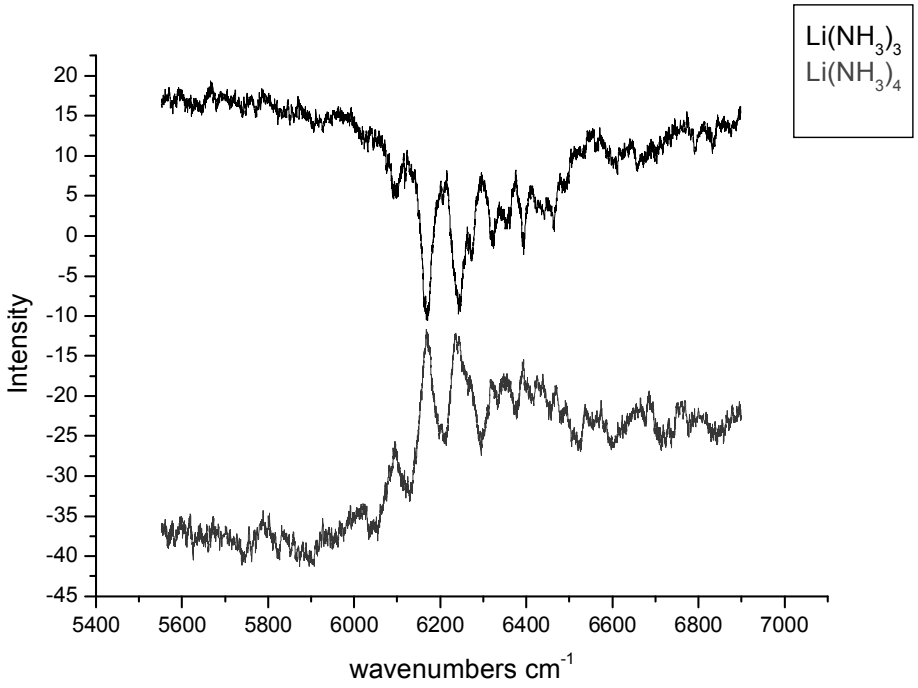

Other clusters

In addition to $Li(NH_3)_n$, a selection of findings for other clusters will be presented, including $Na(NH_3)_n$ and our preliminary work on clusters of metals in other groups such as $Ca(NH_3)_n$ and $Yb(NH_3)_n$.

Reference

[1] T. E. Salter, V. A. Mikhailov, C. J. Evans, A. M. Ellis, J. Chem. Phys. **125**, 034302 (2006).

Alkali Aggregates on Cold Helium Droplets: Formation of High-Spin States and Electron Spin Resonance

Wolfgang E. Ernst
Institute of Experimental Physics, Graz University of Technology,
Petersgasse 16, A-8010 Graz, Austria, wolfgang.ernst@tugraz.at

High-spin states of alkali dimers and trimers

Droplets of about 10^4 helium atoms generated in a supersonic expansion, represent a nanometer-sized superfluid medium of 0.4 K temperature and can be doped with one or several atoms or molecules that may form complexes in this cold environment. In principle, all spectroscopic techniques can be applied that are common in molecular beam spectroscopy. Using two-laser excitation schemes, we were able to identify the alkali dimers K_2, Rb_2 and KRb and the trimers K_3, Rb_3, K_2Rb and KRb_2 in their lowest quartet states formed on droplets loaded with potassium and rubidium atoms [1] . Electronic excitations of the trimers yielded insight into several states that underlie both Jahn-Teller and spin-orbit coupling [1,2].

Zeeman effect and magnetic circular dichroism

Although helium provides a gentle and only weakly perturbing matrix, line widths in optical spectra amount to about 1 cm^{-1} or more. Higher resolution has been obtained in vibration-rotation spectra, which made it attractive to look for ways to measure fine and hyperfine structure directly in the microwave or radiofrequency regime. In preparation for experiments involving optical detection of electron spin transitions in cold molecules, we studied the electronic spin relaxation in alkali atoms and molecules that reside on the surface of a droplet. Measurements of the circular dichroism in the presence of a magnetic field showed that the populations of Zeeman sublevels in alkali atoms are not thermalized [4], while for dimers and trimers a temperature of 0.4 K was found, implicitly providing a first determination of the droplet's surface temperature [5].

Electron spin resonance and Rabi oscillations

Optical detection of spin resonance is achieved in an optical pump-probe experiment with the electron spin transition induced in a microwave cavity in a magnetic field between the pump and probe regions (Fig. 1). While in traditional pump-probe schemes state selection is provided by narrow optical linewidths, droplet-induced line broadening prevents the resolution of Zeeman substates in the optical regime. A magnetic dichroism scheme is used

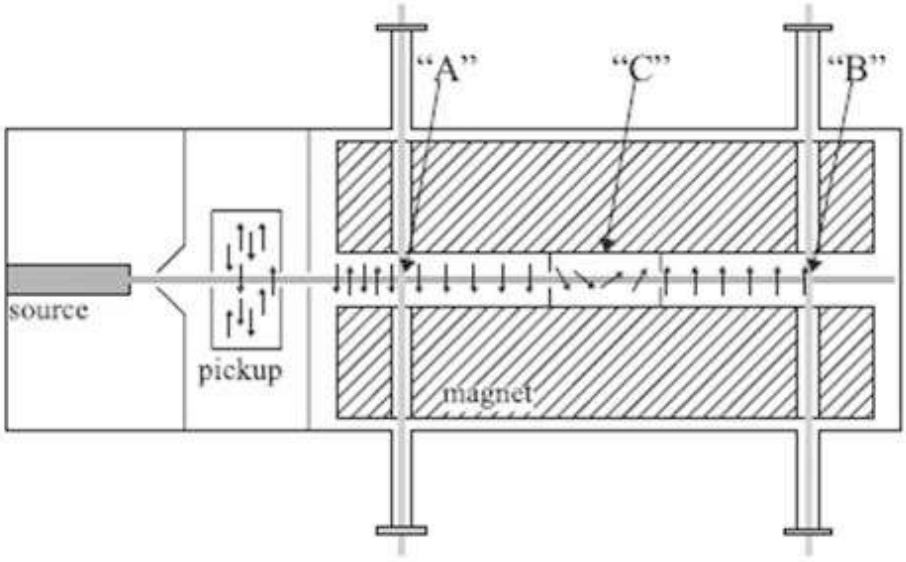

FIG. 1. Schematic diagram of ODMR on doped He nanodroplets. The pump laser beam (A field) exciting an unpolarized ensemble creates a net spin polarization, which is coherently manipulated with a resonant microwave C field. Because the probe beam (B field) only excites spin-up atoms, a correlated change of fluorescence is observed [7].

instead, exploiting the favourable selection rules for the absorption of circularly polarized light. A circularly polarized laser beam can either deplete a particular spin state by desorption of the respective atoms or molecules from the helium droplet beam or by truly optical pumping [6]. In both cases, the probe laser detects the successful spin flip induced by the microwave field. Examples will be presented showing up to 50 Rabi cycles of an electron spin transition on an alkali doped helium droplet during the flight time of 57 μs through the cavity [7]. In our measurements of sharp, hyperfine-resolved ESR spectra of single K and Rb atoms isolated on helium nanodroplets, the shift of the ESR lines with respect to free atoms directly reflects the distortion of the valence-electron wavefunction due to the helium nanodroplet and denotes in an increase of the hyperfine constant consistent with an increase of the Fermi contact interaction. We are able to follow this change as a function of droplet size attesting the sensitivity of the method for many foreseeable applications [8].

References

[1] Johann Nagl, Gerald Auböck, Andreas W. Hauser, Olivier Allard, Carlo Callegari, and Wolfgang E. Ernst, Phys. Rev. Lett. 100, 063001 (2008)
[2] Gerald Auböck, Johann Nagl, Carlo Callegari, and Wolfgang E. Ernst, J. Chem. Phys. 129, 114501 (2008)
[3] Andreas W. Hauser, Gerald Auböck, Carlo Callegari, and Wolfgang E. Ernst, submitted to J. Chem. Phys.
[4] Johann Nagl, Gerald Auböck, Carlo Callegari, and Wolfgang E. Ernst, Phys. Rev. Lett. 98, 075301 (2007)
[5] Gerald Auböck, Johann Nagl, Carlo Callegari, and Wolfgang E. Ernst, J. Phys. Chem. A 111, 7404 (2007)
[6] Gerald Auböck, Johann Nagl, Carlo Callegari, and Wolfgang E. Ernst, Phys. Rev. Lett. 101, 035301 (2008)
[7] Markus Koch, Gerald Auböck, Carlo Callegari, and Wolfgang E. Ernst, Phys. Rev. Lett. 103, 035302-1-4 (2009)
[8] Markus Koch, Carlo Callegari, and Wolfgang E. Ernst, submitted to Mol. Phys.

Angle-resolved Photoelectron Spectroscopy of Fullerenes with fs and ps Laser Excitation

O. Johansson[1], M. Kjellberg[2], G.G. Henderson[1], K. Hansen[2], E.E.B. Campbell[1]

[1] School of Chemistry, Edinburgh University, Edinburgh EH9 3JJ, U.K.
[2] Dept. of Physics, Gothenburg University, 41296 Gothenburg, Sweden,
Email: Eleanor.campbell@ed.ac.uk

The photoelectron spectra from fullerenes excited with femtosecond and picosecond laser pulses have been recorded using velocity map imaging. As observed previously, using a time-of-flight electron spectrometer, the photoelectron spectra are composed of two components: a largely structureless component that can be well described as a Boltzmann distribution [1,2] and a structured signal for electron energies below the photon energy, corresponding to excitation and subsequent single photon ionisation of excited Rydberg states [3]. The structureless component has been interpreted as being due to a thermal electron emission from the hot, equilibrated electron gas prior to coupling to the vibrational degrees of freedom [2]. Velocity map imaging provides a powerful technique to study the origin of these two sets of electrons in more detail. In contrast to time-of-flight electron spectroscopy, the technique is sensitive to low energy electrons and also allows the simultaneous determination of the photoelectron angular distributions. With this technique, we are therefore interested in determining whether a thermal ionisation mechanism is actually responsible for the structureless „Boltzmann-like“ component and also in determining the mechanism for the excitation of the relatively long-lived Rydberg states as well as identifying the nature of these excited states. The results provide strong support for the thermal nature of the emission leading to the structureless contribution. Studies on related complex organic molecules suggest that this can be regarded as a rather general ionisation mechanism and the very efficient thermalisation that takes place provides a limitation to the degree of coherent control that can be expected in such large molecular systems. The highly excited Rydberg states show remarkably simple angular distributions and may be related to the „superatom“ states observed recently by STM for fullerene molecules on a Cu surface [4].

Experimental Setup

Experiments whose results are reported here were carried out at both Gothenburg University and Edinburgh University. Both sets of apparatus are similar. A sketch of the Edinburgh apparatus is shown in Fig. 1. The gas phase fullerenes are produced in a resistively heated effusive sublimation source situated in a small differentially pumped chamber. The fullerene

beam is intersected with the laser pulses in the main chamber and either the electrons are extracted using VMI extraction conditions to obtain the energy- and angular-resolved photoelectron distributions or the positive ions are extracted in the opposite direction with a Wiley-MacLaren extraction configuration to give a linear time-of-flight ion mass spectrum. The VMI spectrometer design is closely based on that of the Bordas group [5]. The entire spectrometer is surrounded by a mu-metal shield. The electron detector consists of dual, chevron style microchannel plates followed by a phosphor screen. A CCD camera rcords the images and transfers the data to a computer where they are accumulated and further analysed using LabView routines. The optimum focus conditions and calibration of the spectrometer are achieved by optimising the images obtained from Xe, this also serves to calibrate the laser intensity. The Gothenburg apparatus differs from the Edinburgh one by having the fullerene source in the same chamber as the VMI detector and in using a reflectron to determine the ion mass spectra. The lasers are commercial Ti:Sapphire amplified laser systems with repetition rates of 1 kHz and pulse duration in the range 120-150 fs. Both systems can be used to pump fs OPAs (optical parametric amplifiers) and the Edinburgh system also has the option of producing bandwidth limited ps pulses combined with a ps OPA.

Fig. 1. *Schematic picture of the VMI spectrometer setup*

Results

If electrons are being ejected due to a thermal ionisation mechanism, then one could expect that the emission is homogeneous in space. This is the situation for ionisation of fullerenes with ns laser pulses which is well known to occur predominantly via thermionic (delayed) ionisation, implying that the excitation energy is equilibrated among electronic and

vibrational degrees of freedom. The VMI inverted image and the corresponding electron angular distribution that result from nanosecond laser (3.68 eV photon energy) ionisation of C_{60} is shown in Fig. 2(a,b) and clearly agrees with a homogeneous emission. A typical VMI inverted image for ionisation of C_{60} with 120 fs, 800 nm laser pulses and a laser intensity of is shown in Fig. 2(c), using a logarithimic intensity scale, with the corresponding photoelectron distributions for angular ranges of 10-20^o and 80-90^o 2(d). The VMI inverted image of the Boltzmann-like contribution is not completely symmetric. This could perhaps be considered as an argument against a thermal emission mechanism, however, it is important to consider the timescales involved. The „thermal“ emission from the hot electrons, prior to equilibration with vibrational degrees of freedom is expected to happen very quickly on the fs timescale, based on a statistical Weisskopf model treatment [2]. This implies that the thermal electrons can be emitted while the laser field is still present. Preliminary studies indicate that the interaction of the electrons with the field can lead to the observed asymmetry. Further work is needed to investigate this further and attempt to more clearly distinguish between a thermal and any possible field-enhanced emission processes. Strong evidence for the thermal mechanism is provided by a comparison between the apparent temperature (determined from the slope of the photoelectron spectra) and the laser fluence / laser intensity. If the laser field strength was the important parameter (in e.g. a field-enhanced process) then the apparent temperature would scale with the laser intensity. If the mechanism is predominantly thermal then the apparent temperature would be expected to scale with the laser fluence. Recent results from our laboratory provide evidence that the latter dependence is the relevant one [6].

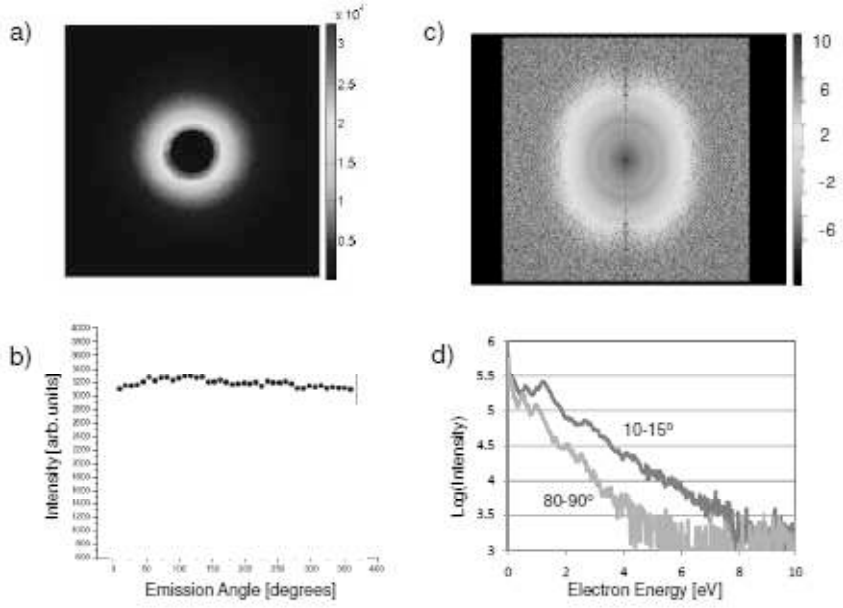

Fig. 2 *(a) Inverted VMI image from ns (N_2 laser) ionisaton of C_{60} (b) Angular distribution of ns data (c) Inverted VMI image (logarithmic intensity, 130 fs, 800 nm, 7 x 10^{12} W/cm^2) of C_{60}. The vertical line in the centre of the image is an artefact of the inversion procedure.*
(d) Photoelectron spectra extracted from the data of 2(c).

A closer look at the angular distribution of the structured „Rydberg peak“ part of the photoelectron spectrum is shown in Fig. 3 for low laser intensity excitation (800 nm, 3 x 10^{12} W/cm^2), leading to the presence of only C_{60}^+ ions in the mas spectrum and a negligible contribution of the structureless, thermal ionisation component.

(a) (b)

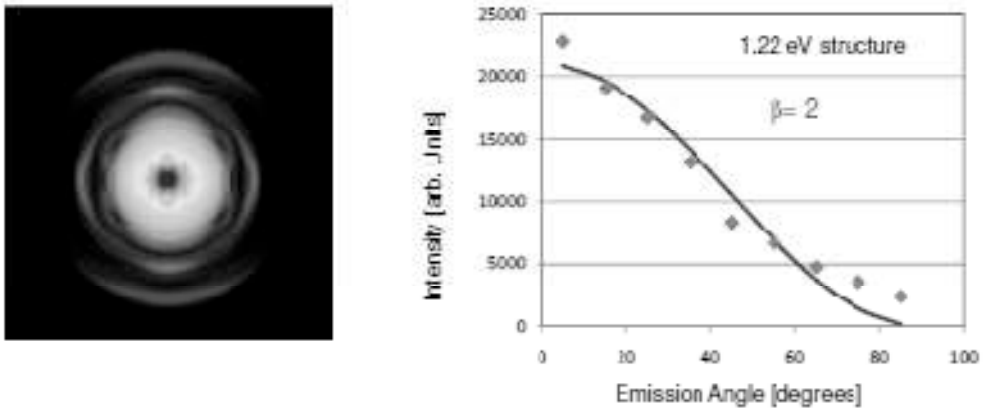

Fig. 3. *(a) Inverted VMI image of the low energy part of the photoelectron spectrum for 3x10^{12} W/cm^2, 800 nm, 130 fs ionisaion. The plot covers the region from ca. 0-2 eV (b) Angular distribution of the outermost intense structure, corresponding to an electron enegy of 1.22 eV. The full line corresponds to an asymmetry parameter, $\beta = 2$.*

The angular distributions of the more highly lying Rydberg states are remarkably simple, with the most prominent signal around 1.22 eV yielding an asymmetry parameter of 2. The asymmetry is retained for higher laser intensities. These initial data indicate that the excited state orbitals of the molecule have a rather simple form and may be considered similar to the „superatom“ states detected recently in STM studies [4]. Further work is underway using ps laser ionisation that provides a higher energy resolution and thus better resolved molecular structure.

References

[1] E.E.B. Campbell et.al., Phys. Rev. Lett. **84** (2000) 2128
[2] K. Hansen, K. Hoffmann, E.E.B. Campbell, J. Chem. Phys. **119** (2003) 2513
[3] M. Boyle et al., Phys. Rev. Lett. **87** (2001) 273401
[4] M. Feng, J. Zhao, H. Petek, Science **320** (2009) 359
[5] B. Baguenard et al., Rev. Sci. Instrum. **75** (2004) 324
[6] M. Kjellberg et al., to be submitted.

On the Influence of the Internal Properties on Quantum Interference with Clusters and Molecules

Markus Arndt
University of Vienna, Faculty of Physics, Boltzmanngasse 5, 1090 Vienna, Austria

Matter wave interference is a ubiquitous phenomenon and a pillar in the fundament of quantum mechanics. When we talk about de Broglie physics we usually refer in particular to the center-of-mass motion of particles that may travel along at least two indistinguishable paths from the source to a certain point in the detection plane. In the past, various different interferometer arrangements have been successfully used to demonstrate the wave-particle duality of large molecules. In all these experiments, enormous efforts have been undertaken to isolate the traveling quantum object from its environment, in order to shield it from decoherence and dephasing.

The present talk shifts the viewpoint by investigating what we can learn from the high sensitivity of quantum interference experiments to external perturbations. We shall discuss the relevance of Earth's gravity and rotation, the influence of molecular polarizabilities, permanent and thermodynamically induced dipole moments, scattered light and particles as well as the molecular absorption of light.

We will show how the interaction with static and time-varying external fields may lead to position information about the quantum particle, which is accompanied by an effective reduction of the quantum interference visibility, and to fringe shifts that can be accurately measured. From both, the degree of decoherence and the fringe shifts, we can extract valuable information about molecular properties.

References:

[1] Klaus Hornberger et al. New J. Phys. 11 043032 (2009).
[2] Stefan Nimmrichter et al., Phys. Rev. A 78, 063607 (2008).
[3] Stefan Gerlich et al., Angew. Chem. Int. Ed. 47, 6195 – 6198 (2008).
[4] Lucia Hackermüller et al., Appl. Phys. B 89, 469 – 473 (2007).
[5] Martin et al., Phys. Rev. A. 76, 013607 (2007)

Ultraviolet Photodissociation Dynamics of the Allyl and Isopropyl Radicals

Domenico Stranges, Giorgio Scotti, and Enrico Ripani
Dipartimento di Chimica, Università di Roma La Sapienza,P.le Aldo Moro, 5, I-00185 Roma, Italy
domenico.stranges@uniroma1.it

Photodissociation dynamics of the allyl, CH_2CHCH_2, and isopropyl, $(CH_3)_2CH$, radicals have been studied using the method of molecular beam Photofragment Translational Spectroscopy (PTS) following excitation by 248 nm photons. Hydrocarbon radicals have received substantial recent attention due to their importance in combustion and atmospheric chemistry. The spectroscopy of allyl radical has been detailed by several studies, and its photodissociation has been examined both by sophisticated laser techniques [1] and by molecular beam methods [2,3]. Following excitation to the $C(^2B_1)$ electronic state, fast internal conversion takes place and is followed by dissociation on the ground electronic surface to give principally hydrogen atom loss. A second channel, observed in earlier molecular beam measurements [2], leads to methyl radicals plus acetylene. We have studied the photodissociation of 2-*d*-allyl radical in order to elucidate the mechanisms involved for the latter channel. The results demonstrate that there are two different mechanisms leading to the formation of methyl radicals plus acetylene.

Very recently we have undertaken a study on the photodissociation of the isopropyl radical at 248 nm. Preliminary results show the presence of at least two primary dissociation channels: $H + CH_3\text{-}CH{=}CH_2$ and $H_2 + C_3H_5$. The analysis of the experimental data has been complicated by the absorption of a second photon from propene, which cannot be avoided.

References

[1] I. Fischer, P. J. Chen, *Phys. Chem. A* **2002**, 106, 4291.
[2] D. Stranges, M. Stemmler, X. Yang, J. D. Chesko, A. G. Suits, Y. T. Lee, *J. Chem. Phys.* **1998**, 109, 5372.
[3] D. E. Szpunar, Y. Liu, M. J. McCullagh, L. J. Butler, *J. Chem. Phys.* **2003,** 119**,** 5078.

Parity and Nuclear Spin Symmetry: Their Conservation and Violation in Intramolecular Dynamics

Martin Quack
ETH Zurich, Laboratory of Physical Chemistry, Wolfgang-Pauli-Str. 10, CH-8093 Zürich, Switzerland, Martin@Quack.ch

Abstract

We summarize the current status of the role of parity and nuclear spin symmetries and their violations in molecular primary processes and molecular spectroscopy.

(1) Introduction

The greatest inspiration is a challenge to attempt the impossible. Albert A. Michelson

When we introduced the principles of approximate parity and nuclear spin symmetry conservation for the theory of detailed state-to-state symmetry selection rules in chemical reactions such as

$$\mathrm{H}_2^+(n_1) + \mathrm{H}_2(n_2) \rightarrow \mathrm{H}_3^+(n_3) + \mathrm{H}(n_4) \qquad (1)$$

where the n_k are labels defining the complete internal quantum state of the reactant or product atoms or molecules, the experimental study of such selection rules still seemed difficult [1]. In the meantime some experimental confirmations have become available (see for example [2, 3]). Even more remote, if not impossible seemed the study of molecular parity violation resulting in a parity violating energy difference $\Delta_{pv}E$ between the ground state energies of enantiomers (R and S) of chiral molecules, corresponding to a non zero reaction enthalpy $\Delta_{pv}\mathrm{H}_0^0$ for the stereomutation reaction [4]

$$R = S \quad \Delta_{pv}\mathrm{H}_0^0 = N_A \Delta_{pv}E \qquad (2)$$

Although this latter phenomenon has not yet been confirmed experimentally, there has been substantial theoretical and experimental progress following our theoretical discovery in 1995 that $\Delta_{pv}E$ is one to two orders of magnitude larger [5-7] than anticipated on the basis of earlier theoretical calculations (for a recent review see [8]). For the prototype example of CHFClBr, $\Delta_{pv}E$ is now predicted to be about 100 aeV or $\Delta_{pv}\mathrm{H}_0^0 \approx 10^{-11}$ Jmol^{-1} [9, 10].

In our 2010 SASP Paper we shall first summarize some fundamental concepts illustrating the importance of the study of fundamental symmetries and symmetry violations and then provide a summary of current results from our group and further work of importance in a variety of applications ranging from astrophysics to the standard model of high energy physics and biomolecular evolution.

(2) Fundamental aspects of symmetries, symmetry breakings and time scales for intramolecular processes.

There are thus two types of Cartesian coordinate systems, which are called "right-handed" and "left-handed" systems. The difference between the two is familiar to every physicist and engineer. It is interesting that an absolute geometric definition of the right or left handedness is impossible, only the relationship of opposition between the two can be defined." [1]

Albert Einstein [11]

We shall address here the fundamental symmetries of physics and how they can be investigated by molecular physics, in particular molecular spectroscopy [12, 13]. The following symmetry operations leave a molecular hamiltonian invariant within the framework of traditional quantum chemical dynamics including only the electromagnetic interaction and considering the isolated system (see [1, 14-16], for example).

(1) Translation in space
(2) Translation in time
(3) Rotation in space
(4) Inversion of all particle coordinates at the origin (parity operation P or E^*)
(5) "Time reversal" or the reversal of all particle momenta and spins (operation T for time reversal)
(6) Permutation of indices of identical particles (for instance nuclei and electrons).
(7) The replacement of all particles by their corresponding antiparticles (operation C for "charge conjugation", for instance replacing electrons by positrons and protons by antiprotons etc.).

1 The original is in German: „Es gibt also zweierlei kartesische Koordinatensysteme, welche man als „Rechtssysteme" und „Linkssysteme" bezeichnet. Der Unterschied zwischen beiden ist jedem Physiker und Ingenieur geläufig. Interessant ist, dass man Rechtssysteme bzw. Linkssysteme an sich nicht geometrisch definieren kann, wohl aber die Gegensätzlichkeit beider Systeme."

These symmetry operations form the symmetry group of the molecular hamiltonian. They are our “seven pillars of wisdom”. It is well known following the early work of Emmy Noether [17] and even earlier work by C. G. J. Jacobi [18] that in connection to an exact symmetry we have a corresponding exact conservation law. For instance (1) leads to momentum conservation, (2) leads to energy conservation, (3) to angular momentum conservation [19] and (4) to parity conservation, that is conservation of the quantum number parity which describes the symmetry (even or odd, positive or negative) of the wavefunction under reflection at the origin [20]. Another interesting observation is that an exact symmetry and conservation law leads to a fundamentally non-observable property of nature (see the discussion in [16, 21-23]). For example P corresponds to the fundamentally non observable property of the left-handedness or right-handedness of space. That implies that it would be fundamentally impossible to say what is a left handed or right handed coordinate system or an R or S enantiomeric molecular structure, only the opposition of left and right would have a meaning.

While the relationship between symmetries and conservation laws is a common textbook subject, the resulting “non observability” is less widely appreciated. This consequence of an exact symmetry and conservation law is mentioned in the early citation from Einstein [11] at the top of this chapter. At that time it was believed that the space inversion symmetry was an exact (and unquestioned) property of nature, similar to the other symmetries. It implies that, in the presence of such a symmetry, there is a fundamental property of nature, which we cannot know for fundamental reasons: It is hidden from our eyes by a veil due to the conservation law. This results then in a great importance of finding an experimental violation of that exact symmetry: The veil is removed and we find an experimental window to observe this property of nature, which was completely hidden to us before we observed the symmetry violation. In this sense, observation of symmetry violations and violations of conservation laws are among the most fundamental observations in the natural sciences. The basic concept has a long history (see [24])

The example of intramolecular parity violation can be considered to be one special example in a hierarchy of symmetry breakings in molecules. This hierarchy of symmetry breakings can be related to the size of contributions to the molecular hamiltonian and to time scales for intramolecular primary processes ranging from about 10 fs for fast intramolecular vibrational redistribution to about 1 s for intramolecular parity violation (see Table 1 for a survey). We shall discuss new results from our current work, which will illustrate some of the primary processes mentioned in the table.

Table 1: Time scales for intramolecular primary processes as successive symmetry breakings (after [8], see also [12, 13, 15], where references to the original literature can be found).

Symmetric state	**Coupling and symmetry breaking**	**Time scale**
Uncoupled oscillators, conservation of separable vibrational quantum numbers	Selective vibrational CH-stretch-bend-Fermi-Resonance in R_3CH Coupling across bonds Ordinary nonselective anharmonic couplings in CF_3R, Δl coupling in asymmetric $R_1R_2R_3CH$	10 – 200 fs 500 fs – 10 ps
Uncoupled oscillators (nearly adiabatically separable)	Adiabatically decoupled dynamics $R-C\equiv C-H$ $(HF)_2$ Δl coupling in C_{3v}-symmetric R_3CH	10 ps – 1 ns
Separable rotation – vibration –nuclear spin states (conservation of nuclear spin symmetry)	Violation of nuclear spin symmetry (nuclear spin-rotation –vibration coupling)	1 ns – 1 ms
Space inversion symmetry, Parity conservation P	Parity violation	1 ms – 1 ks
Time reversal symmetry T	T-violation in chiral and achiral molecules	molecular time scale not known
CPT symmetry	hypothetical CPT violation	∞ (?)

References:

[1] M. Quack, *Mol. Phys.* **34**, 477-504 (1977).
[2] D. Uy, M. Cordonnier, T. Oka, *Phys. Rev. Lett.* **78**, 3844-3847 (1997).
[3] M. Cordonnier, D. Uy, R. M. Dickson, K. E. Kerr, Y. Zhang, T. Oka, *J. Chem. Phys.* **113**, 3181-3193 (2000).

[4] M. Quack, *Chem. Phys. Lett.* **132**, 147-153 (1986).
[5] A. Bakasov, T. K. Ha, M. Quack, in *Chemical Evolution, Physics of the Origin and Evolution of Life, Proc. of the 4th Trieste Conference (1995)* (Eds.: J. Chela-Flores, F. Raulin), Kluwer Academic Publishers, Dordrecht (1996), 287-296, .
[6] A. Bakasov, T. K. Ha, M. Quack, *J. Chem. Phys.* **109**, 7263-7285 (1998).
[7] R. Berger, M. Quack, *J. Chem. Phys.* **112**, 3148-3158 (2000).
[8] M. Quack, J. Stohner, M. Willeke, *Annu. Rev. Phys. Chem.* **59**, 741-769 (2008).
[9] M. Quack, J. Stohner, *Phys. Rev. Lett.* **84**, 3807-3810 (2000).
[10] M. Quack, J. Stohner, *J. Chem. Phys.* **119**, 11228-11240 (2003).
[11] A. Einstein, *Grundzüge der Relativitätstheorie*, Vieweg, Wiesbaden, (1922).
[12] M. Quack, *Chimia* **55**, 753-758 (2001).
[13] M. Quack, *Chimia* **57**, 147-160 (2003).
[14] M. Quack, in *Symmetries and properties of non-rigid molecules: A comprehensive survey., Vol. 23* (Eds.: J. Maruani, J. Serre), Elsevier Publishing Co., Amsterdam (1983), 355-378.
[15] M. Quack, in *Femtosecond Chemistry, Proc. Berlin Conf. Femtosecond Chemistry, Berlin (March 1993)* (Eds.: J. Manz, L. Woeste), Verlag Chemie, Weinheim (1995), Chapt. 27, 781-818.
[16] M. Quack, *Nova Acta Leopoldina* **81**, 137-173 (1999).
[17] E. Noether, *Nachr. Akad. Wiss. Göttingen, Math. Phys. Kl.*, 235-257 (1918).
[18] C. G. J. Jacobi, *Vorlesungen über Dynamik*, Reimer, Berlin, (1866).
[19] R. N. Zare, *Angular Momentum*, Wiley, New York, (1988).
[20] E. P. Wigner, *Group theory and its application to the quantum mechanics of atomic spectra*, Expanded and improved ed., Academic Press, New York, (1959).
[21] T. D. Lee, *Symmetries, Asymmetries and the World of Particles*, University of Washington Press, Seattle, (1988).
[22] M. Quack, *Angew. Chem. Int. Ed. (Engl.)* **28**, 571-586 (1989).
[23] M. Quack, *Angew. Chem. Int. Ed. (Engl.)* **114**, 4618-4630 (2002).
[24] M. Quack, in *Handbook of High Resolution Spectroscopy* (Eds.: M. Quack, F. Merkt), Wiley, Chichester, New York (2010), (in preparation).

Low Energy Electron Induced Reactions in Astrochemistry

Jan Hendrik Bredehöft[1], Thorben Hamann, Petra Swiderek

Universität Bremen, Fachbereich 02 - Chemie/Biologie, Institut für Angewandte und Physikalische Chemie, Leobener Str. D-28359 Bremen, [1] thoralf@uni-bremen.de

Astrochemistry is a field in chemistry that deals with the formation and reactions of molecules outside our planet Earth. One of the major topics in Astrochemistry is the formation of molecules that are necessary for life. It is closely related to studies on the origin of life itself, but also to the fields of Astrophysics that deal with the formation of dustclouds, stars, planets, and all the other "furniture" found in the Universe. On one end of the scale of molecular complexity, the formation of the simplest molecule H_2 from H atoms is if not understood than at least thoroughly investigated [1]. On the other side of said spectrum the precursors to biopolymers, like amino acids [2,3], sugars [4], lipids, cofactors [5], etc, and the kerogen-like organic polymer material in carbonaceous meteorites called "black stuff" can be found [6]. These have also received broad attention in the last decades. Sitting in the middle between these two extremes are simple molecules that are observed by radio astronomy throughout the Universe. These are molecules like methane (CH_4), methanol (CH_3OH), formaldehyde (CH_2O), hydrogen cyanide (HCN), and many many others. So far more than 40 such species have been identified [7]. These are often used in laboratory experiments to create larger complex molecules on the surface of simulated interstellar dust grains [2,8]. The formation of these observed starting materials for prebiotic chemistry is however largely unclear.

Astrochemical conditions

In order to induce chemical reactions one or more molecules as reaction partners and a source of energy to overcome activation barriers are needed. The regions in which interstellar chemistry occurs are characterized by an extreme sparseness of both of these. The particle density even in the darkest, densest interstellar clouds is something like 10^5 to 10^6 particles per cubic cm, which in a gas would correspond to a pressure of less than 10^{-11} mbar. It is probably safe to say that at such pressure gas phase reactions can be neglected. Also the temperature is mostly somewhere between 10 and 20 K, which rules out chemistry's most favourite form of supplying energy to reactions, namely heat. It is difficult to see how under such conditions any kind of chemical reaction can occur and yet we can observe an abundance of molecules throughout the Universe. So obviously we need to have a closer look at how and where interstellar chemistry occurs.

Dust

Those interstellar clouds in which chemistry takes place might be called molecular clouds, but they are in fact dust clouds. Dust is ubiquitous; not only on bookshelves and all over Earth but all over the Universe. The dust grains that make up interstellar dust clouds are tiny silicate grains [9]. These are absolutely vital to even the simplest chemical reactions in space in that they provide a surface to host those chemical reactions. At 10 K any molecule that hits a dust grain will stick to it, frozen in place. The dust grains in interstellar clouds are in fact covered by icy mantles that are thicker than the actual grain at its core. These mantles act as concentrating sponges for molecules that would otherwise probably never even meet. In these solid mantles all kinds of chemical reactions can take place if their activation barriers are overcome in some way.

While heat might be a very common way of providing energy to chemical reactions it is not by a long way the only one. Its biggest benefit is that it is easily created, spread across a medium and thus stored, so that it is readily available whenever two reaction partners meet. In the case of our dust grains this process is reversed. The reaction partners are held in place and are ready to react whenever there is enough energy, even if it is available only for a very short period and in a very small space.

In space there is a lot of radiation of different sorts. There is electromagnetic radiation (UV light, X-Rays, γ rays, etc.) and there is particulate radiation as well in the form of high energy ions. This radiation will provide energy for the chemical reactions in the ice mantles of interstellar dust grains. And while the multitude of different kinds of radiation might be a little confusing, they all have one thing in common: Upon hitting anything solid, they will create secondary electrons. These electrons are in fact the energy source needed to run interstellar chemistry.

Low energy electron induced chemistry

Electrons can be created in the laboratory quite easily which makes them a nice tool in research. The conditions found in interstellar clouds (very low pressure, very low temperature) can also be re-created in a laboratory setting. A liquid He cryostat in an UHV chamber with an electron source is an ideal setup to study not only interstellar chemical processes but all kinds of elementary chemical reactions in solids and on surfaces. The study of heterogeneous catalysis has established a number of experimental techniques that are very widely used by now. Usually this kind of research is performed in very thin layers (monolayers mostly) on well defined crystal surfaces (Ag(111), Pt(111), Au(111), Si(111), etc.) Our experimental approach is slightly different. We use a polycrystalline metal as substrate and the layers that we study are so thick (10 to 20 molecular layers usually) that chemistry is dominated by interactions within the film and not by the boundary layer on the metal surface. The electrons are created thermally and then accelerated towards the surface by

means of an electrostatic field. The energy of the electrons can be tuned to allow for the study of different processes within the same system.

Creating ions

Slow electrons can in principle trigger three different primary processes in a molecule. The best known of those is ionisation by electron impact (EI), which is used to create ions in mass spectrometry. In this process an electron e^- hits a molecule M and knocks an outer shell electron from it to create a cation M^+. This occurs whenever the electron energy is above the ionisation threshold of the target molecule. Another possibility is the attachment of a slow electron e^- to a molecule M to create an anion M^-. This can occur at sharply defined resonance energies specific to the molecule M. A third possibility is to excite the molecule M to a neutral state M* by means on an electron [11].

$M + e^- \rightarrow M^+ + 2\ e^-$ (Electron impact ionisation)
$M + e^- \rightarrow M^-$ (Electron attachment)
$M + e^- \rightarrow M^* + e^-$ (Neutral excitation)

The created states M^+, M^- and M* are usually not stable states so they very often dissociate into ions and radicals, which can then further react with neighbouring molecules to form new chemical species. In these chemical reactions some products can be formed even at very low temperatures that would otherwise require a lot of thermal energy and/or special catalysts. The formation of ethylamine from ethylene and ammonia by hydroamination is one such example. The reaction is characterized by a high activation barrier caused by the electronic repulsion between the electron density rich C=C double bound and the lone pair electrons of ammonia. The reaction also has a highly negative entropy, so it becomes less favourable at higher temperatures, ruling out heat as a means to facilitate reaction. In classical chemistry this is overcome by the use of catalysts. Unfortunately there still is no general catalyst for this kind of reaction. Recently it was shown that the reaction can efficiently be induced by low energy electron radiation [12]. One of the reaction partners is ionized and the reaction barrier is so drastically lowered that instant reaction between ethylene and ammonia occurs.

Astrochemical reactions

This hydroamination reaction by means of low energy electrons or an analogous reaction mechanism could also help in clarifying the formation of the intermediate molecules observed in interstellar dust clouds. The formation for example of formamide from CO and NH_3 could be facilitated by a very similar process. Formamide is a very interesting molecule in Astrochemistry as well as Astrobiology, since it is the smallest molecule with a peptide bond, the kind of bond that forms proteins from amino acids.

Such ionisation-driven reactions leading to the formation of larger molecules appear to be more generally relevant than previously thought as will be discussed in this contribution.

References

[1] Cazaux S., Caselli P., Tielens A.G.G.M., Le Bourlot J., Walmsley M: Molecular Hydrogen formation on grain surfaces. *J of Phys. Conf. Series* **6** (2005), 155–160

[2] Muñoz Caro G.M., Meierhenrich U.J., Schutte U.W., Barbier B., Arcones Segovia A., Rosenbauer H., Thiemann W.H.-P., Brack A. and Greenberg J.M.: Amino acids from ultraviolet irradiation of interstellar ice analogues. *Nature* **416** (2002), 403-406

[3] Bredehöft, J.H., Meierhenrich U.: Amino acid structures from UV irradiation of simulated interstellar ices. in Takenaka N. (ed): Recent Developments of Chemistry and Photochemistry in Ice. Transworld Research Network, Kerala, India (2008)

[4] Cooper G., Kimmich N., Belisle W., Sarinana J., Brabham K. and Garrel L.: Carbonaceous meteorites as a source of sugar-related organic compounds for the early Earth. *Nature* **414** (2001), 879-883

[5] Meierhenrich U.J., Muñoz Caro G.M., Schutte W.A., Thiemann W.H.-P. Barbier B., Brack A.: Precursors of biological cofactors from ultraviolet irradiation of circumstellar / interstellar ice analogs. *Chemistry - A European Journal* **11** (2005), 4895-4900

[6] Matthews C.N. and Minard R.D.: Hydrogen cyanide polymers, comets and the origin of life. *Faraday Discuss.*, **133** (2006), 393–401

[7] Snow T.P. and Bierbaum V.M.: Ion chemistry in the interstellar medium. *Ann. Rev. Analyt. Chem.* **1** (2008), 229–259.

[8] Nuevo M., Meierhenrich U.J., Muñoz Caro G.M., Dartois E., d'Hendecourt L., Deboffle D., Auger G., Blanot D., Bredehöft J.H. and Nahon L.: The effects of circularly polarized light on amino acid enantiomers produced by the UV irradiation of interstellar ice analogs. *A&A* **457** (2006), 741–751

[9] Savage B.D. and Mathis J.S.: Observed Properties of Interstellar Dust. *Ann. Rev. of Astron. and Astrophys.* **17** (1979), 73-111

[10] Li A. and Greenberg J.M.: A unified model of interstellar dust. *A&A* **323** (1997), 566-584

[11] Shimamura I and Takayanagi K. (eds): Electron-Molecule Collisions. Plenum Press, New York, USA (1984)

[12] Hamann T., Böhler E., Swiderek P.: Low-energy-electron-induced hydroamination of an alkene. *Angew Chem Int Ed Engl.* **48(25)** (2009), 4643-4645.

Fragmentation and Fusion of Molecular Systems Induced by Ion Impact

A. Lawicki[1], M. Capron[1], A. Mery[1], L. Adoui[1], JY Chesnel[1], J. Rangama[1], P. Rousseau[1], B. Manil[2], S. Bari[3], J. Postma[3], T. Schlathölter[3], S. Brønstedt Nielsen[4], P. Hvelplund[4], C. Stöchkel[4], H. Cederquist[5] A. Holm[5], F. H.T. Schmidt[5], F. Seitz[5], H. Zettergren[5], and B.A. Huber[1]

[1] *Centre de Recherche sur les Ions, les Matériaux et la Photonique (CIMAP), Bd Henri Becquerel, F-14070 Caen Cedex 05, France*

[2] *Université Paris 13, Villetaneuse, France*

[3] *KVI Atomic Physics, University of Groningen, Zernikelaan 25, 9747AA Groningen, The Netherlands*

[4] *Department of Physics and Astronomy, Aarhus University, Ny Munkegade, DK-8000 Aarhus C, Denmark*

[5] *Department of Physics, Stockholm University, S-10691, Stockholm Sweden*

In recent years, fragmentation studies of molecules have become an intense field of research, in particular concerning biomolecular species, with the aim to better understand radiation damage processes on a molecular level. These studies involve isolated molecules in the gas phase as well as systems in a more realistic environment, namely in form of clusters containing the same species or water molecules.

When regarding slow collisions of multiply charged ions with molecules, it is very likely that multi-electron capture processes lead to the multi-ionisation of the target. The degree of ionisation or the charge state distribution of the intermediate molecular ion depends on several parameters, in particular on the projectile charge and its velocity. In addition to charge transfer also energy will be transferred which may reach large amounts when collisions occur at small impact parameters. On the one hand, multi electron capture will lead to more weakly bound molecular systems, which, when their internal energy stays low, may reach the limit of charge stability and reveal the so-called appearance sizes of multiply charged molecules. On the other hand, an increased internal energy, larger than the barrier height of the weakest dissociation channel will lead on a long time scale to the fragmentation of the system. Depending on the number of degrees of freedom, the time scales may vary from ps to ms, or even longer. However, under certain conditions the excess energy may be used also to rearrange the molecules, to create covalent bonds between neighboured molecules in a cluster or to initiate fusion of molecules.

In the present contribution, we will discuss the fragmentation of isolated polycyclic aromatic hydrocarbon molecules (PAHs) as well as the changes occurring when the corresponding clusters are used as a target. Furthermore, we will show that in the case of β-alanine clusters peptide bond formation can be induced by ion impact. Finally, in a third example, we will demonstrate that van der Waals clusters of C_{60} molecules can be fused to larger fullerenes when the transferred energy is sufficiently high and when the initial clusters size is large enough to hold the disintegrating system together for times necessary to fuse a part of the system.

Fluorescence of Silicon Nanoparticles Suspended in Water

Klaus von Haeften[1], Mark Lowe[2], Anthony Brewer[1]

[1] *University of Leicester, Department of Physics & Astronomy, Leicester, UK, kvh6@le.ac.uk*

[2] *University of Leicester, Department of Chemistry, Leicester, UK*

Following the discovery of intense fluorescence of porous silicon [1] there is recent interest from the semiconductor industry to implement silicon light emitters in integrated electronic circuits. This interest stems from the ongoing miniaturisation of integrated circuits which has reached a size regime where serious performance losses due to signal transmission delay are expected. These delays are caused by the increasingly longer interconnects in high-density integrated electronic circuits and it has therefore been suggested to replace electric signal transmission by optical transduction [2]. A second, similarly important, field for application of fluorescent silicon nanoparticles are thin film solar cells. These types of cells use only a limited fraction of the solar light spectrum and to improve their conversion efficiency it has been suggested to employ fluorescent nanoparticles to down-convert ultraviolet light into a wavelength to which the solar cell responds to [3].

The present paper is motivated by these needs. Our method to achieve luminescent silicon is to generate quantum confinement using cluster beams because the degree of confinement can be controlled by changing the average cluster size. Free silicon clusters are known to exhibit dangling bonds that quench fluorescence and therefore we passivate the cluster surface in a second step. In first experiments silicon clusters have been co-deposited with water onto a cold target. Melting of the ice yielded a suspension that fluoresces in the deep-blue when excited with UV light. The silicon nanoparticles produced in this way show a number of remarkable properties, for instance, their fluorescence remains stable in intensity for more than a year [4]. In this paper, we report on the spectroscopic characterisation of the nanoparticles. We observed water Raman emission and we found that the intensity of the Raman lines were enhanced by the presence of nanoparticles.

Experiment

Here, we give only a brief description of the experiment. Silicon clusters are produced in a gas-aggregation source in a He/Ar atmosphere using DC sputtering of a doped silicon target. The silicon clusters fly through a three-stage aerodynamic lens system and a differential pumping stage into a UHV chamber where they are co-deposited with water vapour onto a liquid nitrogen cooled target. Typical deposition times are 30 minutes. Thereafter the target is heated up to room temperature whereupon the ice layer melts and drops into a dish. The liquid suspension is then bottled and investigated by photo-fluorescence spectroscopy. More details and a schematic of the experiment are given in ref. [4] and ref. [5].

Results and Discussion

Figure 1 shows fluorescence spectra of the liquid samples recorded at different excitation wavelengths. The most prominent band is located at 420 nm. The intensity maximum varies slightly in wavelength within 20 nm between different samples as well as with age of the samples. Fresh samples show the band maximum shifted to somewhat shorter wavelengths and also a rugged structure on the short wavelength side from the maximum. We also recorded photo luminescence excitation (PLE) spectra for the 420 nm emission (shown elsewhere [4]). The PLE spectrum shows that the 420 nm emission is most efficiently excited at a wavelength of 307.5 nm. When excited with shorter wavelengths additional bands emerge between 320 and 380 nm. We note, that further to these bands, sharp lines are observed at 480 and 540 nm in two of the spectra in figure 1. These lines are the second order of the Rayleigh line of the excitation light that becomes scattered by the nanoparticles and the silica cell. Other sharp features are observed at 345, 300 and 260 nm, respectively. At longer wavelengths the second order of these lines are also visible. These lines are due to Raman emission of water and will be discussed later.

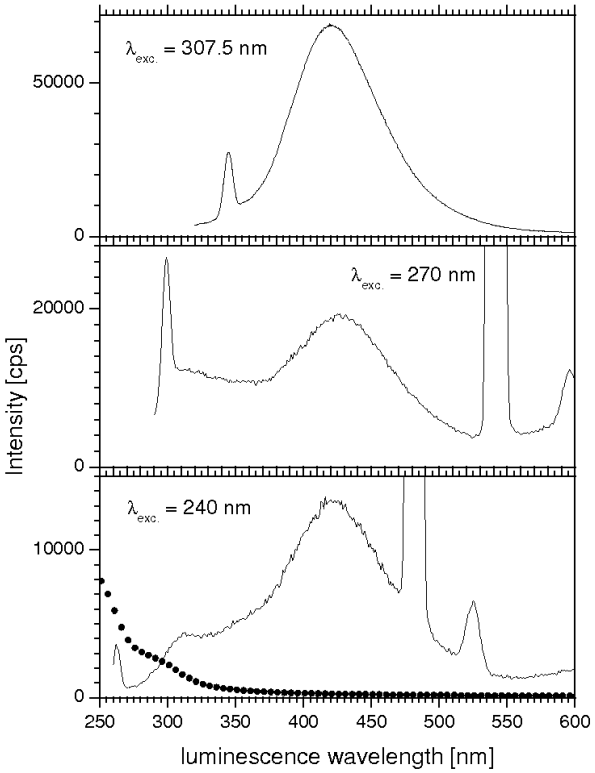

Fig. 1: *Fluorescence and UV/VIS (dots) spectra*

We assigned the fluorescence at 420 nm to the T_1 -> S_0 defect fluorescence of twofold coordinated silicon in (O-Si-O) in a SiO_2 layer at the surface. This assignment is based on the similarity with the peak wavelengths of the well-known defect luminescence of bulk SiO_2 reported in the literature and also on the fact that the rugged features of the fresh samples change into a smooth band with time, which is indicative for a defect-healing process. No fluorescence is observed below 275 nm. This cut-off at short wavelengths coincides well with the onset of UV/VIS absorption which is shown in figure 1 as filled circles (note that the intensity scale does not apply to this spectrum). This behaviour would be expected for particles with a band gap energy corresponding to 275 nm. Bulk SiO_2 has a much larger band gap energy than 4.5 eV and thus we interpret our observation as showing the presence of a silicon core. Quantum confinement is well known to increase the effective band gap energy and according to theoretical work the diameter of the core should be approximately 1.5 nm [6,7].

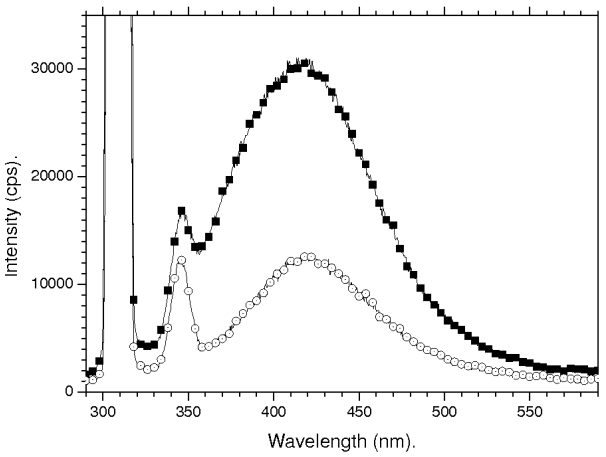

Fig. 2: *spectrum of diluted sample*

In the following we will discuss the sharp lines on the short wavelength side of the prominent fluorescent band. In contrast to the 420 nm fluorescence these lines shift with the excitation energy and have been assigned to Raman Stokes emission of water. The energetic difference between the wavelength of excitation at 307.5 nm and the Stokes line at 345 nm is 3535 cm^{-1} and this value is close to the ν_1 symmetric stretch vibration of water in the gas phase (3657 cm^{-1}, [8]) and in the liquid phase (3280 cm^{-1}, [9]). The difference between liquid and gas-phase frequencies results from the additional coupling of the O-H stretch vibration to hydrogen bonds in the liquid and the fact that the frequency of the Stokes line of the nanoparticle suspension lies between those two values can be explained by a reduced water-coordination of those water molecules that are adsorbed at the surface of the nanoparticles.

A remarkable observation is that the intensity of the Raman line is correlated with the concentration of the silicon nanoparticles. Figure 2 shows the emission spectrum for 307.5 nm excitation (solid squares) together with the spectrum of the same sample, but diluted with water by a factor of 10 (open circles). It can be seen that with increasing nanoparticle concentration the Raman intensity rises. Enhancement of Raman emission is a well-known effect for molecules adsorbed onto rough metal surfaces. Recently, SERS from non-metallic surfaces was reported [10] and explained by charge transfer from filled adsorbate levels to empty InAs/GaAs quantum dot levels. Here, we observe an enhancement effect due to the presence of nanostructured semiconductors as well, however, the effect is caused by the oscillators involved in the fluorescence process. In a previous publication we pointed out that the fluorescence evolves in different steps, notably by excitation of excitons located at the Si/SiO_2 interface followed by an energy transfer to the defected fluorescent SiO_2 sites [4].

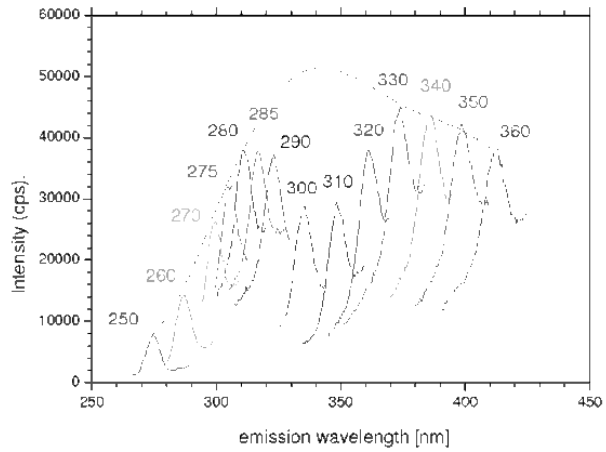

Fig. 3: *Raman spectra*

Figure 3 shows a series of Raman spectra recorded for the same sample but with different excitation energies. The line intensity increases

with decreasing excitation energy, passes through a maximum with a dip for excitation energy of 307.5 nm, and decreases at longer excitation wavelengths. To better visualise the intensities the envelope of these curves has been marked by a dotted line. This envelope shows that the Raman intensity becomes enhanced when the excitation energy approaches values where the fluorescence is maximum.

The dip around the maximum fluorescence excitation is probably a consequence of the coupling between the two relaxation channels. Within the electronically excited nanoparticles the two relaxation channels compete and ultimately the fluorescence is more efficient. The fact that the envelope of the Stokes line intensities in figure 3 follows the PLE spectrum [4] shows that the origin of the enhanced Raman emission is very likely linked to the field of the oscillators that are involved in the fluorescence process, presumably the state that is excited by the absorption of 307.5 nm photons in the first step. This effect may have more general implications for the assessment of radiative and non-radiative relaxation processes.

Acknowledgements: KvH acknowledges funding by the Royal Society through a Research Grant. We also gratefully acknowledge discussions with A. Pucci and A. Otto at the early phase of this project.

References:

[1] L. T. Canham, "Silicon quantum wire array fabrication by electrochemical and chemical dissolution of wafers", Appl. Phys. Lett. 57 (1990).

[2] L. Pavesi, "TOPICAL REVIEW: Will silicon be the photonic material of the third millenium?" J. Phys. C 15 (2003)

[3] V. Svrcek, A. Slaoui and J.C. Muller, "Silicon nanocrystals as light converter for solar cells", Thin Solid Films 451 (2004).

[4] A. Brewer and K. von Haeften, "In-situ passivation and blue luminescence of silicon clusters using a cluster beam/H_2O co-deposition production method", Appl. Phys. Lett. 94 (2009).

[5] K. von Haeften et al., "A novel approach towards the production of luminescent silicon nanoparticles: sputtering, gas aggregation and co-deposition with H_2O," Eur. J. Phys. D: At., Mol. Clusters 52/1-3 (2009)

[6] N.A. Hill and K.B. Whaley, "Size Dependence of Excitons in Silicon Nanocrystals", Phys. Rev. Lett. 75/6 (1995).

[7] Z. Zhou, R.A. Friesner and L. Brus, "Electronic Structure of 1 to 2 nm Diameter Silicon Core/Shell Nanocrystals: Surface Chemistry, Optical Spectra, Charge Transfer, and Doping," J. Am. Chem. Soc. 125/50 (2003).

[8] P.F. Bernath, "The spectroscopy of water vapour: Experiment, theory and applications", Physical Chemistry Chemical Physics 4/9 (2002).

[9] D. Eisenberg and W. Kauzmann, "The Structure and Properties of Water", Clarendon, 1969.

[10] L.G. Quagliano, "Observation of Molecules Adsorbed on III-V Semiconductor Quantum Dots by Surface-Enhanced Raman Scattering," J. Am. Chem. Soc. 126 (2004).

Protonated Molecular Clusters for Studies of Radiation Mechanisms

G. Bruny[1], C. Montano[1], S. Feil[1], S. Eden[2], H. Abdoul-Carime[1], B. Farizon[1], M. Farizon[1], S. Ouaskit[3], T. D. Märk[4]

[1] *Université de Lyon, F-69003 Lyon, France ; Université Lyon, Villeurbanne ; CNRS/IN2P3, UMR5822 Institut de Physique Nucléaire de Lyon, F-69622 Villeurbanne*

[2] *Department of Physics and Astronomy, The Open University, Walton Hall, Milton Keynes MK76AA, UK.*

[3] *Université Hassan II-Mohammedia, Faculté des Sciences Ben M'Sik (LPMC), B.P. 7955 Ben M'Sik, Casablanca Morocco*

[4] *Institut für Ionenphysik und Angewandte Physik, Leopold Franzens Universitaet, Technikerstr. 25, A-6020 Innsbruck, Austria*

While the use of ionizing radiation is well established, notably in therapies and analytical techniques, each new development opens a field of investigation around the possible dangers to our health and the environment. Concurrently, besides applications and risk evaluations, the effect of ionizing radiation in biomolecular nanosystems (biomolecule solvated by water molecules) is emerging as a major area of research, both on a fundamental level and as a source for experimental and technical innovations.
The present experimental challenge is to observe interactions between molecules (and water clusters) after proton impact induced ionization. For that reason a new experimental set-up is being developed at the Institut de Physique Nucléaire de Lyon.

The presentation will focus on the production of protonated molecular (mixed) clusters (e.g. $H^+(H_2O)_n$, $PyrH^+(H_2O)_n$) and the characterisation of mass selected cluster ions by collision induced dissociation experiments. First results with a newly developed detection system will be presented.

This work is supported by the French national agency of research (ANR-06-BLAN-0319-02)-MIRRAMO project.

Titan Ionospheric Chemistry

Odile Dutuit

Laboratoire de Planétologie de Grenoble - Bât.D de Physique, BP 53 - 38041 Grenoble Cedex 9 (France), Odile.dutuit@obs.ujf-grenoble.fr

Introduction

The recent space missions bring a large amount of new and precise data concerning the chemistry in planetary atmospheres. It is particularly the case for the Cassini-Huygens space mission, which reached Saturn at the end of 2004 and reveals the very complex chemistry occurring on Titan, its biggest satellite. An interdisciplinary approach involving planetary scientists and chemists has become essential for the understanding of the processes leading to the molecular synthesis in the atmospheres, still unknown for a large extent.

Titan is a laboratory for pre-biotic chemistry that can be compared with the chemistry at the early Earth, as well as at the Jovian satellites that, hypothetically, could sustain life (Europa, Ganymede). Orbiting the Saturn system since 2004, the Cassini-Huygens mission will perform measurements for at least 2 more years. On one end, through its descent in January 2005, The Huygens Probe unveiled the deep and dense atmosphere of the satellite as well as surface features. On the other hand, the Cassini orbiter keeps visiting the satellite, performing specific measurements at each flyby. An important instrument on-board Cassini is the INMS mass spectrometer, which measures the composition and density in the upper part of the atmosphere, where solar and magnetospheric inputs ionise species, i.e. the ionosphere. The ionosphere is sufficiently diffuse for an orbiter to perform in-situ repetitive measurements of its composition. By modelling this region, and confront with measurements, it is possible to evaluate the neutral atmosphere, the ionising processes, and their variation with time and the conditions of the flyby (day, night, latitude). Moreover, hydrocarbon and nitrile ions are particularly reactive, and in the case of Titan, the ionosphere is a region of intense chemistry, leading to an increase of molecular size. Therefore Titan ionosphere was recently proposed to be the location of the primordial molecular building [1], which ends in the production of the complex aerosols observed at lower altitudes [2]. For all this, it is therefore very important to describe in great details the ionosphere of Titan.

Our objective is to improve the modelling of the ionospheric chemistry of Titan by application for the first time of a strategy involving a new experimental method, based on very high resolution mass spectrometry, in order to obtain high quality data for determination of reaction rate constants and description of the ionospheric chemistry. The close coupling between the fields and methods provides with very innovative results, which help not only in the interpretation of the data from the Cassini-Huygens mission, but also provide with predictive information concerning the future models and missions that will be designed.

Beyond this, our aim is to obtain a very large quantity of well-defined laboratory data, in order to extract general rules on the way that the chemistry of Titan builds up. This will help developing new models with a so-called simplified Titan Chemistry, which is mandatory in order to reach the goal of global modelling of the planet.

Modelling and Space results

The Voyagers observations, as well as the design of the Cassini mission, triggered a modelling effort, aimed at predicting the chemistry that is taking place in the atmosphere, in order to design the on-board instruments [3,4,5]. Models of planetary atmospheres are built by considering an equilibrium resulting from production and destruction reactions, of an initial mixture of species. The models can be restricted to specific regions of the atmosphere and specific dimensionality (from 0 to 3 dimensions) with increasing complexity when describing either microphysical state or the whole atmosphere of the planet. Depending on the objectives, the number of reactions has to be adjusted for calculation feasibility. What is particular with Titan, is the necessity to handle very complex chemistry networks, and a very large number of reactions and species.

The Cassini INMS mass spectrometer is a quadrupolar mass filter [6]. It measures mass spectra between 1-100 amu with a resolving power of 1 mass unit in the whole range. The INMS instrument has performed 6 series of measurements during flybys of the ionosphere. The recorded spectra confirm the general trend predicted by models: of an operative and complex chemistry, resulting in the major ion $HCNH^+$, and seven "families" of ion species, separated by 12 amu. The mass spectra reveal a fast increase of ions' size when getting deeper in the atmosphere, resulting in detectable ionic species containing more than 7 heavy atoms at the lowest probed altitude of 1025km, very close to ionospheric peak density. The ions constituting the INMS spectrum can be described in terms of $C_xH_yN_z^+$, but with the mass resolution of the instrument, there is an inherent ambiguity as both N or CH_2 correspond to mass 14.

A new laboratory approach

Clear discrepancies are already pointed out between models and observations [7,8,9]. Important species such as ammonia ions are detected but are missed by two orders of magnitude in models. These results call for ongoing laboratory collection of reaction rates. But when dealing with Titan ionosphere, a new instrument is necessary.

To this end, we use methods of characterization of ions routinely used in modern mass spectrometry and apply them to the Titan case. We built a set-up based on a commercial, high-resolution mass spectrometer, which will was modified in order to add the possibility to measure ion molecule reaction rate constants relevant for the microphysical conditions of

Titan ionosphere. The instrument is also used for the analysis of laboratory analogues of Titan aerosols.

Early steps of the molecular growth

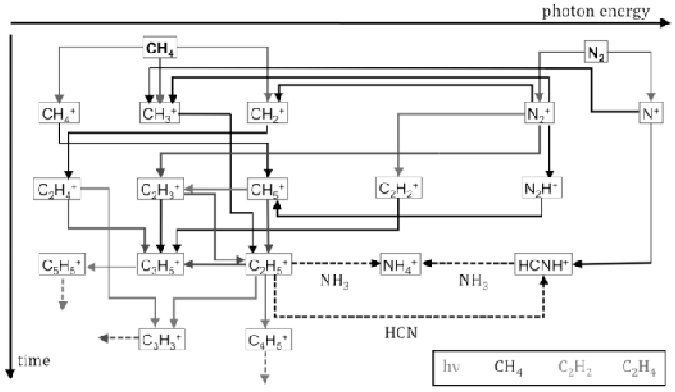

Experimental simulations of the initial steps of the ion-molecule reactions occurring in the ionosphere of Titan were performed at the synchrotron source ELETTRA in Italy. The measurements consisted in irradiating gas mixtures with a monochromatic beam, from the methane ionization threshold at 12.6 eV, up to beyond the molecular nitrogen dissociative ionization threshold at 24.3 eV. Three gas mixtures of increasing complexity were used: N_2/CH_4 (0.96/0.04), $N_2/CH_4/C_2H_2$ (0.96/0.04/0.001) and $N_2/CH_4/C_2H_2/C_2H_4$ (0.96/0.04/0.001/0.001). The resulting ionic chemistry was recorded with a high-resolution (1T) FT-ICR mass spectrometer as a function of time and VUV photon energy. In order to interpret the experimental results, a Titan ionospheric model was adapted to the laboratory conditions. This model had previously allowed the identification of the ions detected in the Titan upper atmosphere by the Ion Neutral Mass Spectrometer (INMS) onboard the Cassini spacecraft. Comparison between observed and modeled ion densities validates the kinetic model (reactions, rate constants, product branching ratios) for the primary steps of molecular growth. It also reveals differences that we attribute to an intense surface chemistry. This result implies that heterogeneous chemistry on aerosols might efficiently produce HCN and NH_3 in the Titan upper atmosphere [10].

Analogue material analysis

The red to dark matter observed on many bodies of the outer solar system including asteroids, comets, planets and moons is explained by the presence of heterogeneous nitrogen-bearing organic solids on the surface or in the atmosphere of these objects. A number of analogs have been prepared in the laboratory and their optical (spectral) properties satisfactory match the observations [11] However, these complex organic compounds have proven difficult to analyze fully from a chemical point of view. Recently, Somogyi et al. demonstrated that high resolution mass spectrometry is a suitable method to determine the chemical composition of the soluble fraction of the samples [12]

We built on these previous studies in order to analyze two kinds of nitrogen-bearing organic solids: (i) tholins, obtained by exposing a mixture of nitrogen-methane to a cold plasma discharge[13], (ii) polyHCN, resulting from the polymerization of liquid HCN catalyzed by ammonia. Tholins are considered as good analogs of the aerosols that give rise to the orange

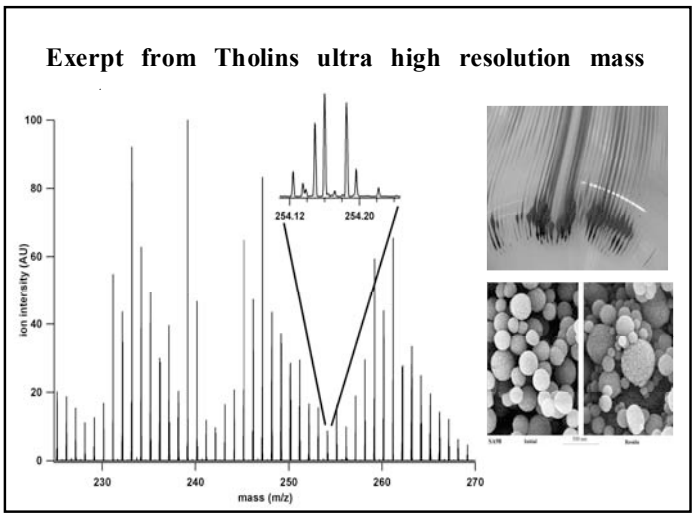

haze in the atmosphere of Titan, Saturn's largest moon [14]. PolyHCN has also been suggested as a component of Titan's haze and is thought to be present in cometary ices [15]. Both are at the origin of complex molecules of potential prebiotic character.

Tholins and polyHCN have been dissolved in CH_3OH and injected in a LTQ-Orbitrap mass spectrometer by ElectroSpray Ionization (ESI), producing protonated (positive mode) or deprotonated (negative mode) ions. Thanks to the high resolution in mass of the instrument, the atomic content of each ion present in the mass spectrum was retrieved. In addition, fragmentation analysis (MS/MS methods) provided complementary information on the chemical functionalities present in the molecules. We show that although both samples are composed of molecules of general formula $C_xH_yN_z$, tholins are a complex mixture of extremely diverse molecules while polyHCN exhibits a much more simple composition.

References

[1] J. H. Waite et al. 2007, Science **316,** 870-875
[2] A. J. Coates et al. 2007, Geophysical Research Letters **34** L22103
[3] Wilson & Atreya 2004, J. Geophys. Res. 109**,** E06002;
[4] Yung et al. 1984, Astrophys. J. Suppl. Ser. 55**,** 465-506
[5] Lavvas et al. Planet. Space Sci. 56**,** 27-66 & Planet. Space Sci. 56**,** 67-994]
[6] Waite et al. 2007, Science. 316**,** 870-875
[7] Vuitton et al. 2006, Icarus. 185**,** 287-300;
[8] Vuitton et al. 2009, Phil. Trans. R. Soc. A. 367**,** 729-741
[9] Vuitton et al. 2007, Icarus. 191**,** 722-742
[10] Thissen et al. 2009, J. Phys Chem. A, in press.
[11] D.P. Cruikshank et al.. *Adv. Space Res.* **2005**, *36*, 178.
[12] N. Sarker et al. *Astrobiology* **2003**, *3*, 719.
[13] C. Szopa et al. P. *Planet. Space Sci.* **2006**, *54*, 394.
[14] C.P. McKay et al. P. *Planet. Space Sci.* **2001**, *49*, 79.
[15] C.N. Matthews and R.D. Minard. *Faraday Discuss.* **2006**, *133*, 393.

Quantum-State Resolved Studies of Gas / Surface Reaction Dynamics

Bruce Yoder, Régis Bisson, and Rainer D. Beck
Laboratoire de Chimie Physique Moléculaire
Ecole Polytechnique Fédérale de Lausanne
CH1015 Lausanne, Switzerland
rainer.beck@epfl.ch

We study chemical reactions at the gas/solid interface through quantum state resolved gas/surface reactivity measurements. Our method uses a molecular beam to direct reagent molecules with well-defined incidence energy towards a single crystal target surface in an ultrahigh vacuum surface science apparatus. Before the reagent species collide with the target surface, they are prepared via rapid adiabatic passage in a specific ro-vibrationally excited eigenstate by a single-mode tunable infrared laser. Auger electron spectroscopy is used to quantify the surface bound products of the dissociative chemisorption yielding quantum state-resolved reaction probabilities under highly specified reaction conditions.

This presentation will discuss recent progress in our state resolved reactivity measurements for methane on platinum and nickel surfaces, where we study steric effects in the dissociative chemisorption of methane.

Using one-photon excitation by linearly polarized laser light, we align the angular momentum and the C-H stretch transition dipole moment of methane in a molecular beam incident on a Ni(100) surface and observe how the state-resolved reactivity of methane depends on the laser polarization direction relative to the plane of the target surface. Depending on the ro-vibrational transition chosen, we observe an increase in methane sticking coefficient of as much as 50%, when the polarization direction is changed from normal to parallel to the surface. The results provide the first detailed information about the dynamical stereochemistry of this benchmark gas/surface reaction.

Multidimensional Molecular Quantum Dynamics in the Gas Phase and on Substrates

Roberto Marquardt
Laboratoire de Chimie Quantique - Institut de Chimie UMR 7177 CNRS/UdS
Université de Strasbourg - F-67000 Strasbourg - roberto.marquardt@unistra.fr

Abstract

Realistic studies of multidimensional molecular quantum dynamics rely on accurate potential energy hypersurfaces (PES). In the first part of this paper, a brief account will be given on strategies to derive analytical potential energy surfaces in multidimensional spaces that satisfy three essential criteria: flexibility, robustness and accuracy. Recent examples will be shown for compact, global PES of XY_n type of molecules and for the adsorption system AB/M, where AB is a diatomic molecule and M represents a (metallic) substrate. In the second part, the quantum dynamics underlying the prototype reaction NH_3(R) to NH_3(L) will be elucidated in full dimensional vibrational space.

Introduction

Molecular quantum dynamics are related with the motion of the heavy molecular components (nuclei, atoms or atomic groups). When electronic motion is concentrated in well defined, adiabatically well separated electronic states, the concept of a potential energy surface (PES) for the motion of the nuclei is a good working hypothesis. Potential energy surfaces may be obtained directly from *ab initio* calculations of the electronic structure in the adiabatic approximation as a collection of discrete points in the multidimensional configuration space. They may also be obtained, on one hand, from *ab initio* data by the intermediate of analytical representations. On the other hand, potential energy surfaces may be obtained from experiment via intermediate analytical (model) potentials, an idea used already by Bjerrum [1]. Analytical PES representations allow to concentrate the huge amount of information needed to characterize a complex structured potential energy hypersurface in a few set of mathematical expressions. Particularly important are functional forms that allow furthermore to obtain, with a very limited set of adjustable parameters, a *global* PES representation, specially in those regions of configuration space that become important for reaction dynamics. Adequate model potential have to fulfill a number of criteria: accuracy, flexibility and robustness; for the purpose of using them in reaction dynamics, analytical PES representations should also fulfill the globality criterion.

A useful concept to access time dependent molecular quantum dynamics is based on the generation of non-stationary molecular structures with coherent irradiation. Conceptually important is the model stereomutation reaction

$$NHXY(R) + h\nu = NHXY(L) \quad (1)$$

at pyramidal nitrogen centers, which may be considered to be a prototype photoinduced stereomutation reaction with a low barrier (E_b = 2000 hccm^{-1} for ammonia and its isotopologues). Excitation in the infrared region, i.e. between 2500 to 3500 cm^{-1}, allows to deposit sufficient energy into the molecule after absorption of a single photon to overcome this barrier. This reaction has been investigated in a previous paper [2], where intense field infrared multiphoton excitation of the NH stretching vibration in NHD_2 has been used to generate semi-classical vibrational wave packet motion and to analyze the subsequent flow of vibrational energy into the reaction coordinate. While the investigation in [2] was performed in a four dimensional space, we discuss here full six-dimensional results obtained from the MCTDH program package [3].

Methods

The method used for the determination of highly accurate PES representation of the electronic ground states of ammonia follows a merging strategy that includes 10000 geometries at the CCSD(T) level and 500 geometries at the MR-CI level [5]. The PES representation of the CO/Cu(100) system is based on a slab type DFT calculation of the electronic structure [5,6]. The dipole moment hypersurface used for the excitation quantum dynamics of is from [7]. The general method used to calculate the quantum dynamics is described in [3]. For the particular implementation of the calculations leading to the six-dimensional excitation quantum dynamics of NHD_2 using the MCTDH program package [8], the reader is referred to [9].

Results

Figure 1 shows the electronic (lower line) and first adiabatic potential energy surface for the lateral diffusion of CO along the <110> direction on Cu(100), as obtained from the new analytical representation of the PES from slab type DFT data. The adiabatic barrier height agrees well with the experimental value of 240 hccm^{-1} [10].

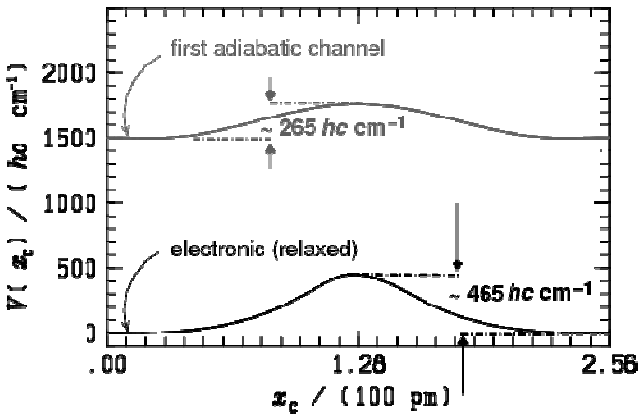

Fig. 1: *Lateral diffusion barriers of CO/Cu(100).*

The lateral diffusion potential leads to a very dense vibrational energy spectrum; the fundamental of the frustrated translational mode is roughly 30 cm^{-1}, overtones are clustered following a pattern similar to that of the Mathieu potential.

For the excitation dynamics in NHD_2 we considered a fast deposition of vibrational energy in the NH stretching mode (Figure 2, left hand side). Within less than 500 fs, the deposited energy exceeds 3000 hccm^{-1}. The wave packet performs semi-classical vibrational motion along the excitation mode. Although this energy is yet insufficient for a classical over-the-barrier motion, if other modes are not relaxed accordingly, such a motion should be possible, in principle, after relaxation of the HNH angles (Figure 3, right hand side). We show that, despite the energetically favorable situation, the quantum dynamics is governed by a non-classical (five-dimensional) tunneling motion.

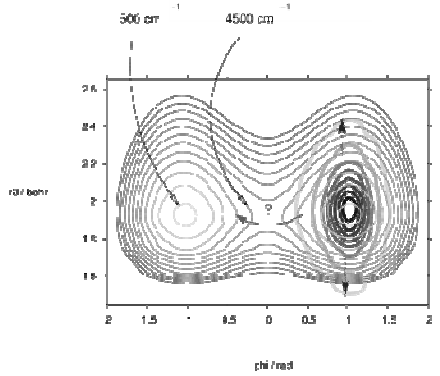

Fig. 2: *2D sections, PES NH_3, along the inversion mode (abscissa), the NH stretching mode (ordinate, left hand side). the HNH bending mode (ordinate, right hand side).*

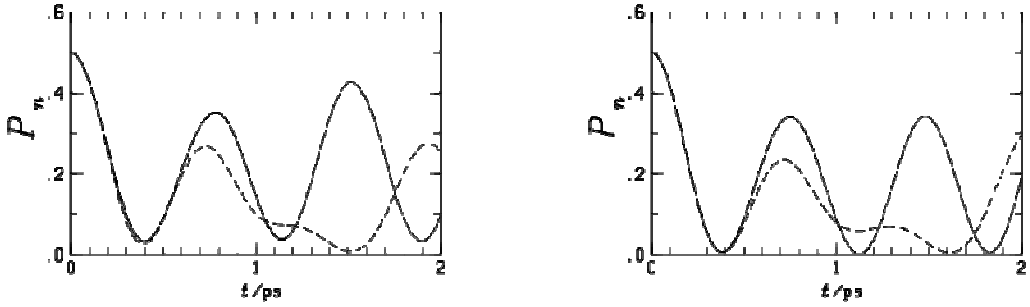

Fig. *3: Our results include an unprecedented comparison between two rather different quantum dynamical codes: MCTDH and URIMIR [11]: Population evolution of spectroscopic states*

Conclusions

Analytical representation of PES are powerful tools for the calculation of multi-dimensional quantum dynamics. Accurate, robust and flexible representations are needed, though, in order to obtain realistic simulations. Reliable predictions are based on the quality with which the PES reproduces available data from thermochemical, spectroscopic and scattering experiments.

While the quantum dynamics of adsorbed species seems to be promising because of the rich and dense structure of vibrationally stationary states, the dynamics underlying the prototype infrared photoinduced stereomutation reaction at the pyramidal nitrogen atom in the ammonia isotopologue NHD_2 is highly non-classical. The reliability of the predictions receives further support from the excellent comparison between different program packages for the calculation of the multi-dimensional quantum dynamics.

Acknowledgment

The author thanks E. J. Baerends, R. Olsen, J. C. Tremblay, P. Saalfrank, F. Gatti, M. Sanrey and F. Le Quére for valuable contributions to this paper.

References

[1] N. Bjerrum, Verh. d. Deut. Phys. Ges., 16, 737–753 (1914).
[2] R. Marquardt, M. Quack, I. Thanopulos, and D. Luckhaus, J. Chem. Phys., 118, 643–658 (2003).
[3] M.H. Beck, A. Jäckle, G. A. Worth, and H.-D. Meyer, Phys.Rep., 324, 1 (2000).
[4] R. Marquardt, K. Sagui, J. Zheng, W. Thiel, S.Yurchenko, D. Luckhaus, F. Mariotti, and M. Quack. To be published.
[5] P. Fouquet, R.A. Olsen, and E.J. Baerends, J.Chem. Phys., 119, 509–514 (2003).
[6] R. Marquardt, F. Cuvelier, R.Olsen, J.E. Baerends, J.C. Tremblay, and P. Saalfrank. Submitted.
[7] R. Marquardt, M .Quack, I. Thanopulos, and D. Luckhaus, J. Chem. Phys., 119, 10724–10732 (2003)
[8] R. Marquardt, F. Le Quéré, F. Gatti, and M. Sanrey. To be published.
[9] F. Richter, F. Gatti, C. Léonard, F. Le Quéré, and H.-D. Meyer, J. Chem. Phys., 127, 164315 (2007).
[10] A.P. Graham and J.P. Toennies, J. Chem. Phys., 114, 1051–1052 (2001).
[11] M. Quack and E. Sutcliffe, QCPE Bulletin, 6, 98 (1986).

Electron-Impact Ionization and Dissociation of Molecular Ions: The CD_n^+ (n=1-4) Series

P. Defrance[1], J. Jureta[1], J. Lecointre[2] and R.K. Janev[3,4]

[1]*Université Catholique de Louvain, Département de Physique, unité PAMO, Chemin du Cyclotron 2, B-1348 Louvain-la-Neuve, Belgium*

[2]*Durham University, Department of Chemistry, South Road, Durham DH1 3LE, United-Kingdom.*

[3]*Institut für Plasmaphysik, Forschungszentrum Jülich Gmbh, EURATOM Association, Trilateral Euregio Cluster, D-52425 Jülich, Germany*

[4]*Macedonian Academy of Sciences and Arts, 1000 Skopje, Macedonia*

A comprehensive modelling of the hydrocarbon transport in tokamak divertors requires a complete set of cross-sections for all collision processes affecting the hydrocarbon fragmentation and chemistry. Among these molecular ions, the deuterated methane family (CD_n^+, n= 1–4) evidently plays a particular role. To get some more insight into the complexity of multispecies hydrocarbon plasmas, experimental electron-impact collisions with the deuterated methane family members CD_n^+ have been systematically investigated in our laboratory by means of a crossed electron-ion beam set-up. Each possible singly-charged ionic fragment has been detected separately and cross-sections for its production have been determined from their respective thresholds up to 2.5 keV. The absolute cross-sections and kinetic-energy-release distributions have recently been published [1-4] for the CD_n^+ (n= 1–4) series.

Usually, for these experiments the deuterated target is chosen rather than the hydrogenated one, since the light D^+ fragment energy spread is lower in that case and consequently its collection is much easier than that of the H^+ fragments. Within the Born-Oppenheimer approximation and disregarding vibrational excitation, the energies as well as the lifetimes of the electronic states of the deuterated target are identical to those of the hydrogenated one.

The present paper reports on the available results regarding the production of the singly-charged ionic fragments from the (CD_n^+, n= 1–4) molecular ion:

$$CD_n^+ + e^- \rightarrow CD_n^{+*} \rightarrow F_p^+ + \ldots \qquad \sigma_{np} \qquad (1)$$

with p= 1-6 for fragments $F_p^+ = D^+$, D_2^+/H_2^+, C^+, CD^+, CD_2^+, CD_3^+, CD_n^{2+}, respectively.

These singly-charged ions are produced both by dissociative excitation (DE) and by dissociative ionization (DI) processes, so that, in the experiment, the ion production measurements correspond to the sum of the DE and the DI signals:

$$\sigma_{np} = \sigma_{np}^{DE} + \sigma_{np}^{DI} \qquad (2)$$

where σ_{np}^{DE} and σ_{np}^{DI} stand for the excitation and ionization contributions, respectively.

A specific procedure has been developed to separate the DE and DI contributions to the total cross section for each particular fragment [1] so that absolute cross sections are reported separately for DE and for DI from the threshold up to 2.5 keV. Dissociative excitation can occur via direct (DDE) and via indirect (IDE) channels. Indirect dissociative excitation channels can be predissociative DE (PDE) or resonant DE (RDE) ones.

Doubly-charged molecular ions CD_n^{2+} result from single ionization (SI) of the molecular target. They have been observed only for n = 2 and n = 4, the corresponding reactions are labelled as σ_2^{SI} and σ_4^{SI}. Otherwise, CD_n^{2+} ions are formed in excited states, which preferentially dissociate to the singly-charged ion pair above the ionization threshold. A specific method for analysis of fragment velocity distributions is used to determine the kinetic energy released to dissociation products so that kinetic-energy-release distributions (KERDs) are determined for each ionic fragment, at selected electron energies.

The potential energy curves or surfaces relevant for the present discussion are well known for CH^+ and for CH_4^+ only, while for CH_2^+ and for CH_3^+, detailed information is not available. The reader may refer to the above-mentioned papers and reference therein for the description of ion structures. It is worth mentioning that metastable excited bound state may be formed in the ion source. Some of these states (electronically or vibrationally excited) have lifetimes which allow them to survive until ions reach the collision region, so that they may affect the experiment, in particular in the threshold energy region. This is the case for CD^+ and for CH_4^+.

Janev and Reiter (JR) [5] have developed a semi-empirical model to evaluate cross-sections for electron-impact ionization and dissociation of hydrocarbon anions. Cross-sections for one electron ejection from all the orbitals of molecular ions are calculated both by the Deutsch-Märk (DM) [1, 6] theoretical model. Results are found in overall good agreement with the experimental ones.

The present work provides a database which includes cross-sections, thresholds and kinetic energies presented in a convenient form for their application in plasma physics.

References

[1] Lecointre J, Cherkani-Hassani S, Belic DS, Jureta JJ, Becker K, Deutsch H, Märk TD, Probst M, Janev RK and Defrance P 2007 J. Phys. B: At. Mol. Opt. Phys. **40**, 2201

[2] Lecointre J, Belic DS, Jureta JJ, Janev RK and Defrance P 2008 Eur. Phys. J. D **50**, 265

[3] Lecointre J, Belic DS, Jureta JJ, Janev RK and Defrance P 2009 Eur. Phys. J. D/**e2009-00241-3**

[4] Lecointre J, Belic DS, Jureta JJ, Janev RK and Defrance P 2009 Eur. Phys. J. D/**e2009-00242-2**

[5] Janev R K and Reiter D 2002 Phys. Plasmas **9**, 4071; see also: *Berichte des Forschungszentrum Jülich* **3966** (2002) ISSN 0944-2952

[6] Becker K, Deutsch H, Probst M and Märk TD 2009 private communication, to be published

The Development and Applications of a Novel Ion Mobility Spectrometer - Ion Trap Mass Spectrometer (IMS-ITMS) for the Detection of Threat Agents*

S Price[1], D Howse[1], L Rycroft[1], P Watts[1], A Clark[2], AMcNeish[2] and C A Mayhew[1]

[1]Molecular Physics Group, School of Physics and Astronomy, University of Birmingham, Birmingham, B15 2TT, UK

[2]Smiths Detection Ltd, Watford, WD23 2BW, UK

Abstract

A military IMS (GID-M) (Smiths Detection Ltd - the world's leading manufacturers and suppliers of IMS systems) has been adapted and attached to an ITMS. The IMS system is found to have a good resolution (approx. $t/\Delta t$ 50), but the signal-to-noise is compromised by the vibrations from the ITMS. With the ITMS we have the capability of trapping ions and then fragment them to perform MS/MS investigations. To illustrate the applications of this instrument a series of studies involving G-type nerve agent simulants are presented.

1. Introduction

Fears of terrorism and the requirement to detect dangerous chemicals in low concentrations are leading to an ever-increasing need, within homeland security, for reliable, real-time and sensitive detection of a wide range of substances that are a threat to the safety of our society. The chemicals that need to be detected range from explosives, through to narcotics and chemical and biological agents

Commonly used trace gas detection systems for this type of security are often based on Ion Mobility Spectrometry (IMS). IMS is the base technology used in a wide range of chemical warfare agent (CWA), drug and explosive detectors, and environmental monitors [1,2].

IMS systems can be extremely sensitive, but they are not very selective and can produce false positives and negatives. This is due mainly to two factors. Firstly, the gas-phase ion chemistry is complex and needs to be better understood. Secondly, the resolution is often not sufficient to distinguish between ionic species of similar mobilities.

The chemistry occurring in atmospheric pressure IMS systems has previously been studied directly by using various mass spectrometers[3] including Time-of-Flight (TOF) [4,5] and quadrupole [6-13]. However, whilst the information obtained from such instruments can be detailed and of considerable value, quadrupole and TOF mass spectrometry are limited particularly by the fact that no tandem mass spectrometry is possible. In these machines only

* Dedicated to the late Dr R.B. Turner OBE Smiths Detection Ltd without whom this project would not have been possible.

the *m/z* value of the ions can be determined and no information concerning the structure can be obtained. These difficulties can be overcome by the use of an Ion Trap Mass Spectrometer (ITMS). An ITMS offers one more dimension of analysis than most mass spectrometers. Not only does it provide the conventional mass spectra, but ions can be trapped and then isolated and fragmented in order to obtain information about their structure.

2. Experimental

A schematic representation of the instrument is provided in figure 1. In the GID-M-IMS, ions are generated at atmospheric pressure by a ^{63}Ni source. Ions of a particular polarity migrate under the influence of an electric field, *E*, towards an electronic gate. A pulse of ions is introduced into the drift tube via the first gate. This swarm of ions has a mean drift velocity given by $v_d=KE$, where *K* is the ion mobility coefficient, which is characteristic of a particular ion, and is dependant on the mass and shape of the ion, the drift gas, and the temperature and pressure in the drift tube [5]. The ions are detected via a Faraday plate which is at a distance of approximately 8 cm from the first gate. The first gate can also be operated in DC mode, which maximises the transmission of ions through the IMS, and therefore increases the signal intensity in the ITMS. In order select specific ion mobility peaks for mass analysis, a second gate has been installed near to the Faraday plate. Similar to the first gate, the second gate could either be operated in pulse or DC mode. To select a mobility peak of interest for mass analysis, the second gate pulse is delayed from the first gate pulse by the required amount so that it opens when the mobility peak to be selected has reached it.

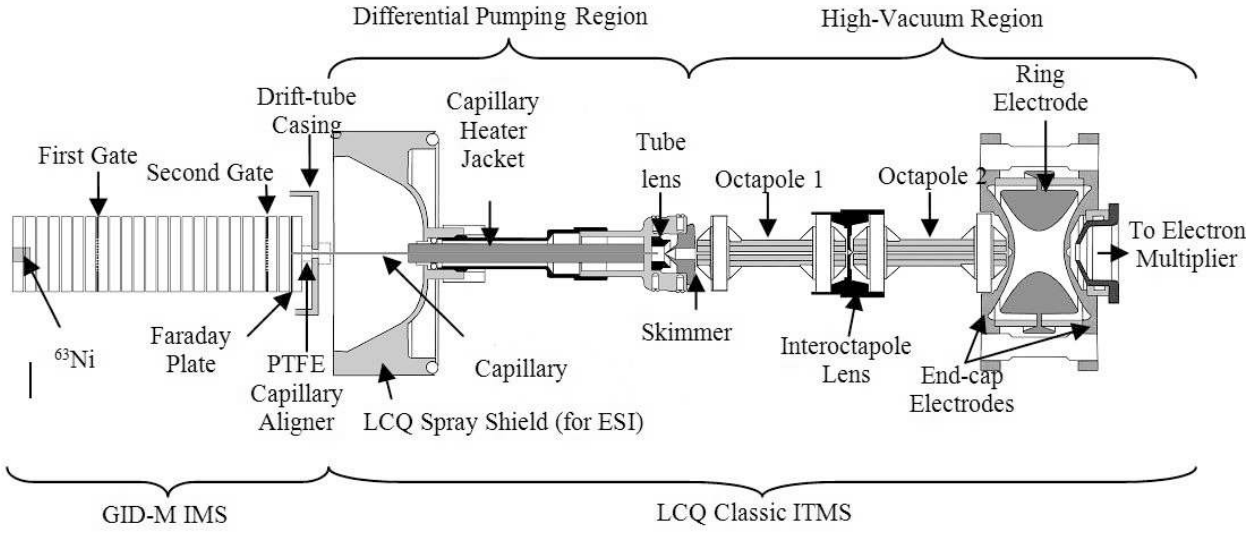

Fig. 1. *A schematic cross section of the IMS-ITMS system (ITMS adapted from a LCQ Classic Manual)*

3. Preliminary Results

A mobility spectrum is shown in figure 2, where the Reactant Ion Peak (RIP) and two further peaks due to dimethyl methylphosphonate (DMMP) are evident. The second peak is due to the DMMP monomer ion and the third due to the DMMP dimer ion.

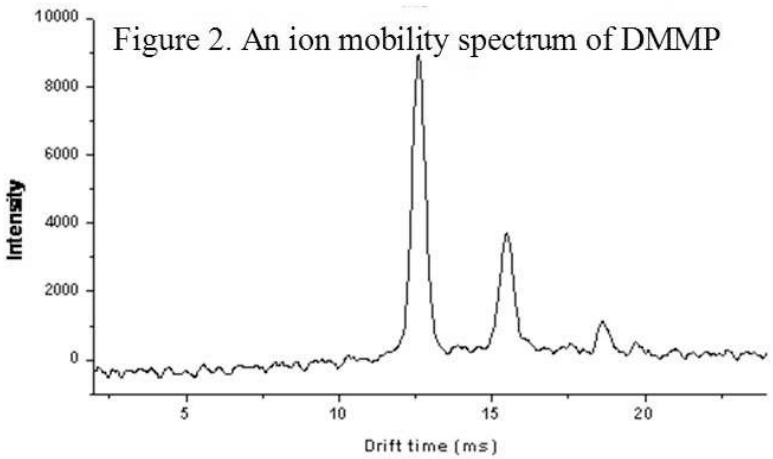

Figure 2. An ion mobility spectrum of DMMP

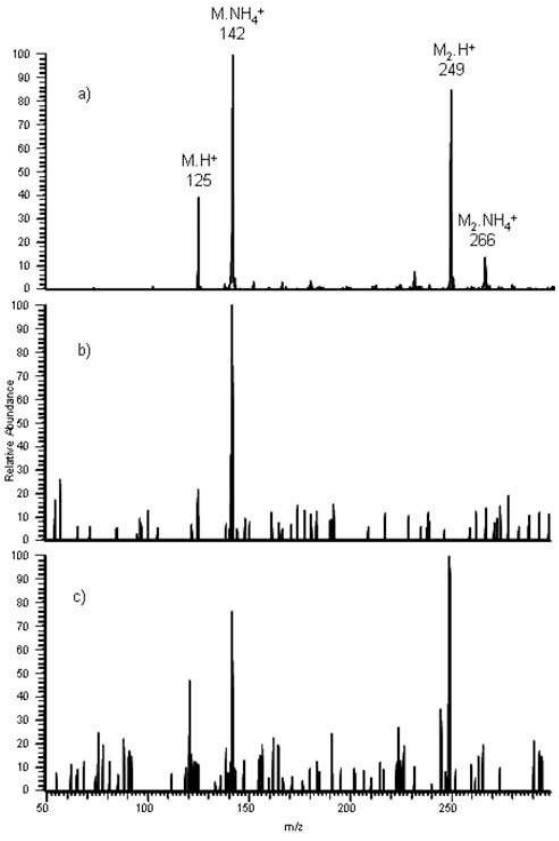

Fig. 3 *a) is the mass spectrum of DMMP taken in DC mode and b) and c) are the second gate mobility peak selection of the second and third mobility peaks shown in the mobility spectrum in figure 2*

A mass spectrum of DMMP taken in DC mode is shown in figure 3 a). The second gate was used to individually select the monomer and dimer mobility peaks as shown in figure 3 b) and c). The data were taken with a first gate width of 500 μs and the second gate width of approximately twice that. It is evident that both the protonated monomer and dimer are present at 125 *m/z* and 249 *m/z*, respectively, as are the ammoniated monomer and dimer at 142 *m/z* and 266 *m/z* as can be seen in the mass spectrum obtained with the IMS in DC mode. Only the monomers are present upon selection of the first mobility peak. Upon selection of the second mobility peak both the monomers and dimers are present. This is due to two factors. Firstly there are a series of voltage gradients in the lens system of the ITMS that, in the higher pressure region, could fragment the bound dimers via collision induced dissociation. Secondly in the low pressure region of the ITMS, there is no DMMP in the ITMS to reform the dimer once dissociated (it is irreversible), so the monomer can also be seen on the mass spectra.

References

[1] Li, F.; Xie, Z.; Schmidt, H.; Sielemann, S.; Baumbach, J. I. *Spectrochimica Acta Part B-*Atomic Spectroscopy **2002**, 57, 1563.

[2] Smiths Detection Ltd., *http://www.smithsdetection.com/eng/GID-M.php,* The GID-M chemical agent detector, 2007.

[3] Kanu, A. B.; Dwivedi, P.; Tam, M.; Matz, L.; Hill, H. H. *Journal of Mass Spectrometry* **2008**, *43*, 1.

[4] Steiner, W. E.; Klopsch, S. J.; English, W. A.; Clowers, B. H.; Hill, H. H. *Anal. Chem.* **2005**, *77*, 4792.

[5] Steiner, W. E.; Clowers, B. H.; Fuhrer, K.; Gonin, M.; Matz, L. M.; Siems, W. F.; Schultz, A. J.; Hill, H. H. *Rapid Communications in Mass Spectrometry* **2001**, *15*, 2221.

[6] Proctor, C. J.; Todd, J. F. J. *Analytical Chemistry* **1984**, *56*, 1794.

[7] Munro, W. A.; Thomas, C. L. P.; Langford, M. L. *Analytica Chimica Acta* **1998**, *374*, 253.

[8] Hill, C. A.; Thomas, C. L. P. *The Analyst* **2003**, *128*, 55.

[9] Giles, K.; Grimsrud, E. P. *Journal of Physical Chemistry* **1992**, *96*, 6680.

[10] Lee E. P. F.; Dyke J. M.; Wilders A. E.; Watts P. *Mol. Physics* **1990**, *71*, 207.

[11] Hayhurst C. J.; Watts P.; Wilders A. *Int. J. Mass Spec. Ion Proc*. **1992**, *121*, 127.

[12] Bell A.; Hayhurst C. J.; Mayhew C. A.; Watts P.; *Int. J. Mass Spec. Ion Proc*. **1994**, *140*, 133

[13] Bell A. J.; Giles K.; Moody S.; Watts P.; Int. J. Mass Spec. Ion Proc.**1998**, *173*,65.

Surface Nanostructures Created by Irradiation with Slow Highly Charged Ions

F. Aumayr, G. Kowarik, R. Ritter, C. A. Vasko, C. Gösselsberger, W. Meissl, and A. S. El-Said
Institute for Applied Physics, Vienna University of Technology, 1040 Wien; Austria; EU

Irradiation of solid targets with swift or fast heavy ions can lead to severe structural modifications at the surface and in the bulk (see e.g. [1-4] and refs. therein). These modifications include the formation of latent tracks in the solid, the creation of hillock- (or crater-) type nanostructures on the surface, and the occurrence of phase transitions, e.g. from crystalline to amorphous or from superconducting to insulating. The formation of tracks or hillocks is usually linked to a critical energy loss (dE/dx) of the projectiles and occurs particularly in insulators (e.g., polymers, oxides, ionic crystals). While there is no question that the intense electronic excitation of a confined volume around the ion trajectory due to the electronic stopping of the swift ions is the major cause for these modifications [5], the exact mechanism how this energy is transferred to the lattice is still under discussion and probably strongly depends on the type of material [6-12].

Highly charged ions (HCI) carry a large amount of potential energy [13]. For slow HCI this potential energy (equal to the total ionisation energy which had to be spent for producing the HCI from its neutral atomic ground state) can become comparable to or even considerably exceed the ions kinetic energy, resulting in additional electron emission or sputtering (potential electron emission [14-16], potential sputtering [13, 17-20]), phenomena which are usually dominated by kinetic effects (kinetic electron emission [21-23], kinetic sputtering [5, 24]). In the case of Xe^{44+}, for example, this potential energy amounts to about 51 keV. Upon interaction with solid surfaces the HCI deposit their potential energy within a very short time (a few femto-seconds) within a nanometer size volume close to the surface [13, 16, 25, 26]. It is therefore not astonishing that similar to the case of swift heavy ions surface modifications with nanometer dimensions have also been demonstrated for the impact of slow highly charged ions on various surfaces [27,28].

Figure 1 shows, as an example, irradiation induced defects on CaF_2 [27-29]. The image is a topographic contact mode AFM image taken in air, showing hillocks, which appear to be caused by impact of single Xe^{44+} (Ekin 2.2 keV/amu) ions. Recently the mechanism of the hillock formation on CaF_2 could be related to a local solid-liquid phase transition (melting) of the crystal around the impact site of a single highly charged ion [29-31]. The dependence of the hillock diameter on the projectiles' potential energy, as shown in the figure (right), reveals two sharp thresholds occurring at around 14 keV and 50 keV. The first is related to local melting, similar as in the case of swift heavy ions, where such a scenario has been observed before [7]. The latter threshold could be related to another phase transition (sublimation) [28].

As another example of investigated materials, figure 2 shows an image of defects on highly oriented pyrolytic graphite (HOPG) caused by irradiation with Xe^{23+} ions. On this material, one can observe defects in STM even for singly charged, ultra-slow (150 eV) singly charged Argon ions [32]. A summary of the reported defect sizes in the literature is given in fig. 2 [32-38]. Similar to the case of CaF_2, the slope of the defect-diameter's energy dependence changes significantly at some keV. This indicates a possible difference of the underlying mechanism. With an ambient AFM used in contact mode, we observed structures correlated with ion irradiation in the lateral force images, but not in the topography. This means, the impact site is an area of enhanced friction, rather than a topographic defect. These observed structures can be removed by the scanning tip of a contact mode AFM even at low normal forces applied to the tip. Further investigations are still planned to clarify the nature of the observed defects.

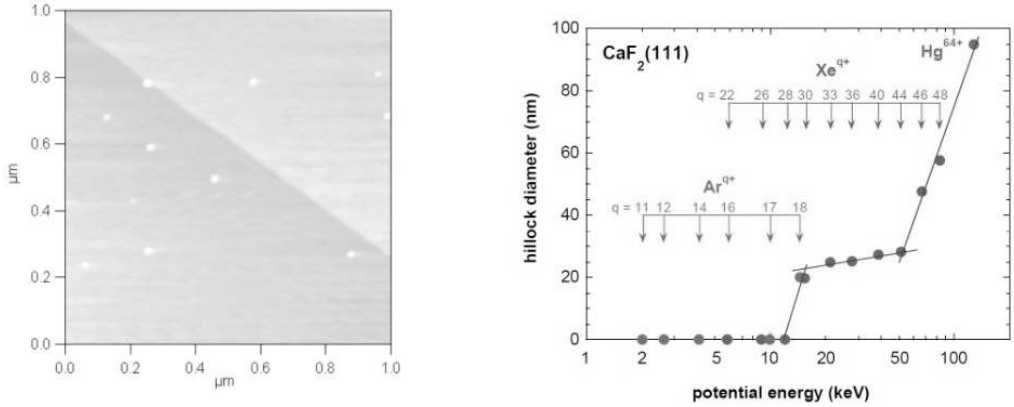

Fig. 1: Ambient c-AFM image of ion induced hillocks on a CaF2 (111) surface (left) [27]. The diameter varies strongly as a function of the projectiles' potential energy (right) [28]. For details see text.

In the semiconductor industry, Polymethyl methacrylate (PMMA) is a common photoresist, used for patterning Silicon wafer surfaces. It is applied onto a Si surface as thin film of a few 10 nm thickness. The irradiations are usually done using a high fluence of singly charged Argon ions (~10^{13} cm^{-2}) at moderate kinetic energies in the 10 keV regime, followed by developing the resist with e.g. isopropanol. First investigations of HCI induced defects on PMMA have been done in the late 1990s by Gillaspy et al. [39] using Xe^{44+} projectiles, showing single impact pit-style defects after developing the sample in isopropanol. They could not find any direct modifications on the undeveloped surface. At that time, no further systematic studies have been performed. Very recently Papaleo et al. [40] showed how the charge state of swift ions (3 MeV/amu Au^{q+}) influences the size of craters formed on the PMMA surface and found a strong increase of crater volume with the deposited energy density along the central track.

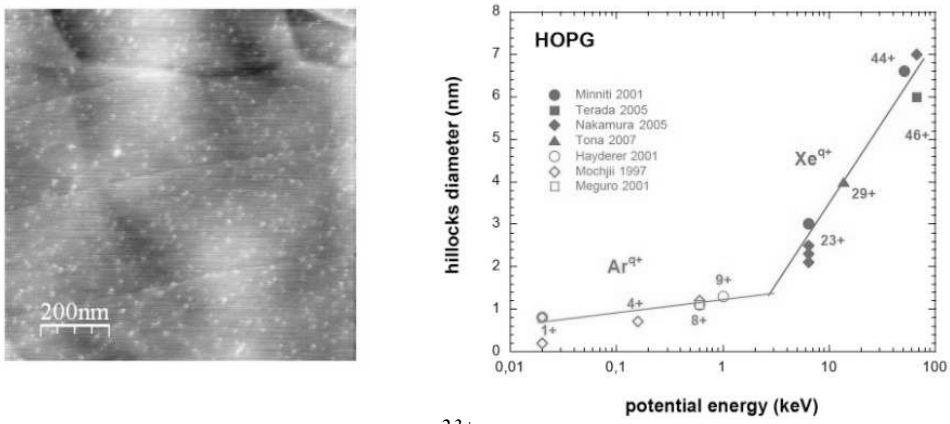

Fig. 2: *Lateral force AFM image of Xe^{23+} irradiated HOPG (left). The applied fluence is about 10^3 ions/µm^2. In the corresponding topography image, no structures appeared. The observed hillock diameters (measured by STM) from the literature are summarised in the right part [32-38].*

We are currently performing a systematic investigation of the defects on PMMA produced by slow Argon and Xenon ions, ranging from singly- up to highly-charged. The irradiations so far have been performed at the Heidelberg EBIT, the Dresden EBIT, as well as at the ECR Ion source Aribe in Caen, France, covering a potential energy range from about 5 keV to 92 keV and kinetic energies around 0.25 to 4 keV/amu. The samples from two different suppliers consist of a 40-60 nm layer PMMA on top of a Si substrate. The films were applied using a spin coating technique and temperature treated. Typical applied ion fluences range from 20 µm^{-2} to 1000 µm^{-2}, depending on the ion source.

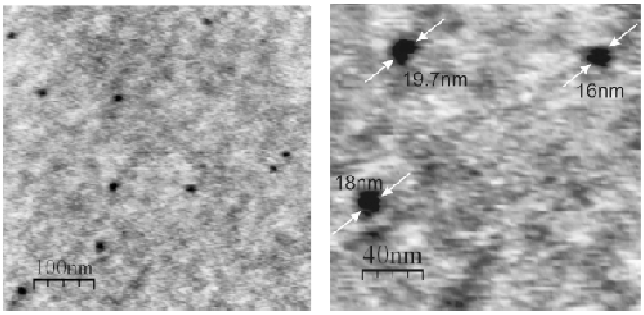

Fig. 3: *Topographic AFM image (contact mode) of PMMA irradiated with Xe^{47+}. The pits are roughly 1 nm deep, the diameter is of the order of 20 nm. The applied fluence was about 25 ions/µm^2, which correlates nicely with the number of observed pits.*

After irradiation the samples were investigated using ambient AFM in contact and non-contact mode (fig.3). In contrast to the earlier mentioned investigations [39] we find pits even for non-developed surfaces at least for projectiles with charge-states above 32. For lower potential energies we found structures after development. So far, our investigations do not allow a conclusive interpretation but further irradiation experiments are already scheduled.

Acknowledgement

This experiment has been performed at the distributed LEIF-Infrastructures at ARIBE and MPIK, supported by Transnational Access granted by the European Project HPRI-CT-2005-026015. Transnational access to the Rossendorf ion-beam facilities was provided through AIM (EU Contract No. 025646).

References

[1] R. L. Fleischer, P. B. Price, and R. M. Walker, J. Appl. Phys. 36, 3645 (1965).
[2] H. Dammak, et al., Phys. Rev. Lett. 74 1135 (1995).
[3] G. Schiewietz, et al., Nucl. Instrum. Meth. Phys. Res. B 175, 1 (2001).
[4] L. T. Chadderton, Radiation Measurements 36, 13 (2003).
[5] H. Gnaser, Low-Energy Ion Irradiation of Solid Surfaces (Springer Berlin, 1999), Vol. 146.
[6] D. Lesueur, and A. Dunlop, Rad. Eff. Def. Sol. 126, 163 (1993).
[7] M. Toulemonde, C. Dufour, and E. Paumier, Phys. Rev. B 46, 14362 (1992).
[8] C. Müller, et al. Nucl. Instrum. Meth. Phys. Res. B 209, 175 (2003).
[9] C. Müller, et al., Nucl. Instrum. Meth. Phys. Res. B 191, 246 (2002).
[10] N. Khalfaoui, et al., Nucl. Instrum. Meth. Phys. Res. B 240, 819 (2005).
[11] A. S. El-Said, et al., Nucl. Instrum. Meth. Phys. Res. B 218, 492 (2004).
[12] A. S. El-Said, et al., Rad. Eff. Def. Sol. 157, 649 (2002).
[13] F. Aumayr, and HP. Winter, Phil. Trans. Roy. Soc. (London) 362, 77 (2004).
[14] H. D. Hagstrum, Phys.Rev. 96, 325 (1954).
[15] H. D. Hagstrum, Phys.Rev. 96, 336 (1954).
[16] A. Arnau, et al., Surf. Sci. Reports 27, 113 (1997).
[17] T. Neidhart, et al., Phys.Rev.Lett. 74, 5280 (1995).
[18] M. Sporn, et al., Phys.Rev.Lett. 79, 945 (1997).
[19] K. Kuroki, et al., Appl. Phys. Lett 81, 3561 (2002).
[20] N. Okabayashi, et al., Nucl. Instrum. Meth. Phys. Res. B 232, 244 (2005).
[21] D. Hasselkamp, in Particle Induced Electron Emission II, (Springer, Heidelberg, 1992),
[22] J. Schou, Scanning Microsc. 2, 607 (1988).
[23] M. Rösler, W. Brauer, in Particle Induced Electron Emission I, (Springer, Berlin, 1991).
[24] P. Sigmund, Mat.Fys.Medd. 43, 2 (1993).
[25] HP. Winter, and F. Aumayr, J. Phys. B: At. Mol. Opt. Phys. 32, R39 (1999).
[26] HP. Winter, and F. Aumayr, Euro. Phys. News 33, 215 (2002)
[27] A. S. El-Said, et al., Nucl. Instrum. and Meth. Phys. Res. B 256, 346 (2007).
[28] A. S. El-Said, et al., Nucl. Instrum. Meth. Phys. Res. B 258, 167 (2007).
[29] A. S. El-Said, et al., Phys.Rev.Lett. 100, 237601 (2008).
[30] C. Lemell, et al., Solid State Electr. 51, 1398 (2007).
[31] F. Aumayr, et al., Nucl. Instrum. and Meth. Phys. Res. B 266, 2729 (2008).
[32] G. Hayderer, et al., Physica Scripta T92, 156 (2000).
[33] K. Mochiji, et al., J.Appl.Phys. 82, 6037 (1997).
[34] T. Meguro, et al., Nucl. Instrum. Meth. Phys. Res. B 209, 170 (2003).
[35] R. Minniti, L. P. Ratliff, and J. D. Gillaspy, Phys. Scripta T92, 22 (2001).
[36] N. Nakamura, et al., Nucl. Instrum. Meth. Phys. Res. B 232, 261 (2005).
[37] M. Terada, , et al., Nucl. Instrum. Meth. Phys. Res. B 235, 452 (2005).
[38] M. Tona, , et al., J. Phys. Conf. Ser. 58, 331 (2007).
[39] J. D. Gillaspy, D. C. Parks, and L. P. Ratliff, J. Vac. Sci. Technol. B 16, 3294 (1998).
[40] R. M. Papaléo, et al., Phys.Rev.Lett. 101, 167601 (2008).

Structural Microtransitions in ^{4}He Droplets: Stochastic Calculations for Anionic and Cationic Dopants

F.A. Gianturco, E. Coccia. , F. Marinetti
Department of Chemistry, The University of Rome "La Sapienza",
Piazzale A. Moro 5, 00185 Rome, Italy

The helium isotopes ^{4}He and ^{3}He are unusual among the elements of the periodic table in that they do not exhibit a triple point and consequently remain in the liquid state at atmospheric pressures down to the lowest temperature of T=0. They are also the only liquids exhibiting superfludity below $T_c = 2.18$ K (^{4}He) and $T_c = 2.4 \cdot 10^{-3}$ K (^{3}He). The many properties related to superfluidity have puzzled scientists for many years and it is now realized that superfluidity and superconductivity are closely related phenomena which are in fact rather ubiquitous and can occur in many different environments [1-3]and can be detected by a variety of spectroscopic tools.

About ten years ago it was found that finite sized droplets of helium could pick up atoms and molecules singly and that even specified mixtures of different species can be prepared inside helium droplets where, in order to remain inside, have to be cooled down to expected temperatures of 0.2-0.5 K [4-8], where spectra become drastically simplified.

It has therefore become clear from the intense experimental work following the earlier discovery that such containers provide the ideal study environments for probing the solvation process and several other chemical processes like reactions, excitations, clustering and fragmentations, at unusually low temperatures. The above phenomena can thus be analysed at the nanoscopic level and under special low-temperature conditions which can complement what we know about traditional solvation processes in classical solvents.

Theoretical analysis of such events can therefore provide a molecular picture for the quantum behaviour of heliophobic and heliophilic species and can also allows us to follow in detail the structural and dynamical evolution of the observed chemical events as a function of the changing sizes of these nanocryostats [9-11]. The effects of this special quantum solvent on anionic dopants are still to be fully explored experimentally and only now begin to get analysed theoretically, providing additional fascinating information on the solvation process at the molecular level.

References

[1] F. London, Superfluids, Vol. II, J. Wiley, New York (1954)
[2] J.F. Allen and A.D. Misener, natures, **141**, 75 (1938)
[3] A.B. Migdal, Soviet. Phys. JETP 37, **176** (1960)
[4] J.P. Toennies and A.F. Vilesov, Am. Rev. Phys. Chem. **49**, 1 (1998)
[5] J.P. Toennies, K.B. Whaley and A.F. Vilesov, Physics Today. Feb. 2001
[6] A.Scherdemann, J.P. Toennies and J.A. Natby, Phys. Rev. Lett. **64**, 1899 (1990)
[7] M. Hartmann, R.E. Miller, J.P. Toennies and A.F. Vilesov, Science **272**, 1631 (1996)
[8] S. Grebenev, J.P. Toennies and A.F. Vilesov, Science **279**, 2083 (1998)
[9] E. Marinetti, E. Bodo, F.A. Gianturco, Chem. Phys. Chem. **8**, 93 (2007)
[10] E. Yurtsever, E. Yildrim, M. Yurtsever, E. Bodo, F.A. Gianturco, Eur. Phys. J. D **43**, 105 (2007)
[11] E. Marinetti, E. Coccia, E. Bodo, F.A. Gianturco,E. Yurtsever, M. Yurtsever, E. Yildrim, J. Chem. Phys. **126**, 124319 (2007)

Quantum Dynamics Studies of Molecules and Clusters

Toshiyuki Takayanagi
Department of Chemistry, Saitama University, Saitama City, Japan

Introduction

It is quite well-known that quantum effects, including vibrational quantization (zero-point vibrational energy), tunneling of light particles, scattering resonance, and electronically nonadiabatic transitions, are playing a very important role in various chemical dynamics phenomena. Therefore, from the theoretical side, quantum effects should be properly described in theoretical calculations in order to interpret various experimental results at a quantitative level. In this meeting, I present results of our recent theoretical calculations on the HeBeO molecule embedded in a helium cluster and low-energy electron collisions with DNA/RNA molecules.

Quantum dynamics calculations of molecules in low-temperature helium clusters

Impurity-doped helium clusters at very low temperatures have attracted widespread attention from both experimental and theoretical viewpoints due to their unique quantum properties. Recent experimental studies using the HENDI (helium nanodroplet isolation) technique show that the large low-temperature helium clusters are able to trap interesting molecules and van der Waals clusters which cannot easily be produced under usual gas-phase and condensed-phase conditions.

Recently, we have theoretically studied the experimental possibility that HeBeO can be formed in such helium clusters [1,2]. HeBeO is a very unique molecule for which a He atom is bound to BeO through a very strong attractive force ~ 5 kcal/mol. This value is comparable to the water-water hydrogen-bonding strength. Notice that this binding energy is much larger than usual van der Waals interaction between He and other atoms or molecules. The large stability of this HeBeO molecule comes partly from the same symmetric nature of an occupied 1*s*-orbital of He and an empty σ-orbital of BeO and was firstly predicted by Frenking and his coworkers [3-5] almost 20 years ago. Unfortunately, the HeBeO molecule has not yet been detected in previous experimental studies.

At first, our research group has developed a global three-dimensional potential energy surface for HeBeO using highly-accurate *ab initio* electronic structure calculations at the CASPT2 level with a large flexible basis set. Using the developed potential energy surface, we have

carried out wave packet quantum dynamics calculations in order to obtain vibrational quantum states (both bound and predissociative resonance states). Next, we have then estimated interaction energies between He and HeBeO. Finally, we have carried out quantum path-integral molecular dynamics simulations using the obtained potential energy interaction information in order to understand the BeO solvation mechanism in helium clusters. It was found that the first He atom is bound to BeO to form the stable HeBeO complex and that the other helium atoms form solvation shell structures around HeBeO. The helium exchange effect between HeBeO and the outer solvation shells can safely be ignored.

Quantum effects in low-energy electron collisions with DNA/RNA molecules

Since the observation that low-energy electrons can cause significant DNA/RNA damage including strand breaks, many studies have been carried out for electron collisions with isolated nucleic acid base molecules in the gas phase. In recent electron-scattering studies with a high collision energy resolution, several narrow resonance peaks have been observed in dissociative electron attachment cross sections of the $(M-H)^-$ + H production channel at low collision energies below 2 eV for uracil (U). Motivated by this experimental finding, we have recently carried out quantum wave packet dynamics calculations for this dissociation process [6,7].

We have developed reduced-dimensionality potential energy surface for the U + e^- collision system, where two degrees of freedom including the uracil out-of-plane vibrational mode and N_1-H dissociation coordinate were taken into account. The BHLYP hybrid density-functional exchange-correlation method with a large basis set including highly diffuse orbitals was used to develop the potential surface since we found that this functional can reasonably describe both the dipole-bound and valence-bound anion states of uracil at a fairly good level. We have then performed two-dimensional wave packet calculations in order to obtain resonance states. Although our two-dimensional model is too simple for quantitative assignments of the experimental results, we were able to obtain a qualitative picture of the resonance phenomenon observed in the previous experiments.

Acknowledgements

This work was financially supported by the Grant-in-Aid for Scientific Research of the Ministry of Education, Culture, Sports, Science, and Technology of Japan (Grant No. 20038011, 21550005).

References

[1] "Accurate ab initio electronic structure calculations of the stable helium complex: HeBeO," T. Takayanagi, H. Motegi, Y. Taketsugu, and T. Taketsugu, *Chem. Phys. Lett.*, **454**, 1-6 (2008).

[2] "Path-integral molecular dynamics simulations of BeO embedded in helium clusters: Formation of the stable HeBeO complex," H. Motegi, A. Kakizaki, T. Takayanagi, Y. Taketsugu, T. Taketsugu, and M. Shiga, *Chem. Phys.*, **354**, 38-43 (2008).

[3] W. Koch, J.R. Collins, G. Frenking, Chem. Phys. Lett. 132 (1986) 330.

[4] W. Koch, G. Frenking, J. Gauss, D. Cremer, J.R. Collins, J. Am. Chem. Soc. 109 (1987) 5917.

[5] G. Frenking, W. Koch, J. Gauss, D. Cremer, J. Am. Chem. Soc. 110 (1988) 8007.

[6] "Theoretical study on the mechanism of low-energy dissociative electron attachment for uracil," T. Takayanagi, T. Asakura, and H. Motegi, *J. Phys. Chem. A*, **113**, 4795-4801 (2009).

[7] "Theoretical study on the transformation mechanism between dipole-bound and valence-bound anion states of small uracil-water clusters and their photoelectron spectra," H. Motegi and T. Takayanagi, *J. Mol. Struct.* (*THEOCHEM*), **907**, 85-92 (2009).

The Deutsch-Märk (DM) Formalism: A Versatile Approach for Calculating Electron Ionization Cross Sections of Atoms, Molecules, Ions, and Clusters

Deutsch H[1], Becker K[2], Probst M[3], Märk T D[3,4]

[1] *Institut für Physik, Universität Greifswald, GERMAN;* deutsch@physik.uni-greifswald.de

[2] *Dept. of Physics, Polytechnic Institute of New York University, Brooklyn, NY, USA;* kbecker@poly.edu

[3] *Institut für Ionenphysik und Angewandte Physik, Universität Innsbruck, AUSTRIA;* michael.probst@uibk.ac.at, tilmann.maerk@uibk.ac.at

[4] *Also: Dept. of Plasma Physics, Univerzita Komenskeho, Bratislava, SLOVAK REPUBLIC*

Abstract

Collisions of electrons with matter causing ionization are among the most fundamental processes in collision physics. The knowledge of cross sections for electron-impact ionization is of basic importance to our understanding of collision physics and critical to many applications such as processing plasmas, fusion edge plasmas, gas discharges, planetary, stellar, and cometary atmospheres, radiation chemistry, mass spectrometry, and chemical analysis. While much progress has been made in the experimental determination of cross sections for atomic and molecular targets, rigorous quantum mechanical calculations of ionization cross sections are scarce and exist only for some simple atoms in their electronic ground state. The need to incorporate ionization cross sections in modeling codes in many applications has stimulated a renewed interest in the use of less rigorous approaches to the calculation of ionization cross section ranging from simplistic additivity rules to semi-rigorous methods that incorporate aspects of established collision theories and some quantum mechanically calculated target properties. Here we present calculations of absolute electron ionization cross sections using the Deutsch-Märk (DM) formalism for a variety of targets ranging from ground-state and excited-state atoms to atoms to molecules, free radicals and clusters, and to positive and negative ions. Comparisons will be made with available experimental data and, where possible, with results from other cross section calculations.

Introduction

The production (and interaction) of charged particles, in particular collisions of electrons with matter causing ionization, i.e. producing ions and secondary (ejected) electrons is among the most fundamental processes in collision physics. Cross sections for electron-impact ionization have been measured and calculated since the early days of collision physics (see e.g., [1,2]), because of their basic importance to our understanding of collision physics as well as their relevance in many applications. Electron-impact ionization cross sections of molecules are important quantities in a variety of applications and technologies as diverse as low-temperature processing plasmas, fusion edge plasmas, gas discharges, planetary, stellar, and cometary atmospheres, radiation chemistry, mass spectrometry, and chemical analysis [2].

Much progress has been made in the experimental determination of cross sections for atomic and molecular targets in the past two decades. Rigorous quantum mechanical calculations of ionization cross sections have only appeared in the literature recently and only for some simple atoms in their electronic ground state (see e.g. [3]). The rigorous theoretical treatment of ionization cross sections for complex atoms, atoms in excited states, molecular targets, ions, and clusters is beyond the capability of current quantum-mechanical electron collision theory. The need to incorporate ionization cross sections for these targets in modeling codes for various applications (e.g. in fusion edge plasmas, in plasma processing, in the modeling of atmospheric processes, and more recently, in the connection of modeling biological and biomedical processes) has stimulated a renewed interest in the use of less rigorous approaches to the calculation of ionization cross sections.

The first semi-rigorous ionization cross section calculation approaches appeared in the literature in the late 1980s by Khare and co-workers [4] and by Deutsch and Märk [5]. The late 1990s marked the emergence of the the binary– encounter dipole (BED) and binary-encounter Bethe (BEB) theories of Kim, Rudd, and co-workers [6]. More recently, Joshipura and co-workers [7] introduced a method to determine total ionization cross sections of molecules from the total elastic cross section and the total inelastic cross section. The sum of these two cross sections yields the total cross section and the total inelastic cross section is used to calculate the total ionization cross section.

Here we present calculations of absolute electron-impact ionization cross sections using the DM formalism for a variety of targets ranging from ground-state atoms to atoms in excited states to molecules, free radicals and clusters, and to positive and negative ions. The main emphasis is on demonstrating the versatility of the DM formalism as its range of applicability has been extended over the years, both in terms of range of impact energies covered and range of target species studied. Extensive comparisons will be made with available experimental data and, to the extent possible, with results from other calculations in order to demonstrate accuracy, reliability, and predictive potential of the DM formalism.

The DM Formalism

The DM formalism was originally developed in 1987 as a semi-empirical approach for the calculation of electron-impact ionization cross sections for atoms in the energy region from threshold to about 100 eV [5]. Subsequently, the DM formalism was modified and extended, both in terms of range of targets to which it was applied and range of impact energies covered. The formalism was quickly extended to targets such as molecules, clusters, and ions and the energy range was expanded to thousands of electronvolts with the proper, quantum mechanically correct high-energy behavior.

In its most recent version [8], the DM formula expresses the single ionization cross section of an atom as a function of the reduced energy u, $\sigma(u)$, as:

$$\sigma(u) = \sum_{n,l} g_{nl}\, \pi\, r_{nl}^2\, \xi_{nl}\, b_{nl}^{(q)}(u)\, [\ln(c_{nl}\, u)/u] \qquad (1)$$

where r_{nl} is the radius of maximum radial density of the atomic sub-shell characterized by quantum numbers n and l (column 1 in the tables of Desclaux [9]), ξ_{nl} is the number of

electrons in that sub-shell, and the reduced energy u is given by $u = E/E_{n\ell}$. Here E refers to the incident energy of the electrons and $E_{n\ell}$ is the ionization energy in the (n,ℓ) subshell. The sum in (1) extends over all atomic sub-shells labelled by n and ℓ. The factors $g_{n\ell}$ are weighting factors which were originally determined from a fitting procedure. The energy-dependent function $b_{n\ell}^{(q)}(u)$ in equation (1) has the explicit form

$$b_{n\ell}^{(q)}(u) = \frac{A_1 - A_2}{1 + (u/A_3)^p} + A_2 \qquad (2)$$

and the 4 quantities A_1, A_2, A_3, and p are constants that had to be determined (in conjunction with the constant $c_{n\ell}$) from reliable measured cross sections for the various values of n and ℓ. The superscript "q" refers to the number of electrons in the (n,ℓ) subshell and allows the possibility to use slightly different functions $b_{n\ell}^{(q)}(u)$ depending on the number of electrons in a given (n,ℓ) sub-shell. The constant $c_{n\ell}$ in (1) was found to be close to one except for d-electrons. All quantities needed for the application of the DM formalism have been summarized in a recent review [10] to which we refer the reader for further details.

Discussion and Outlook

To date, the DM formalism has been successfully used to calculate electron-impact cross sections for the single and multiple ionization of ground-state atoms as well as excited state atoms, for selectively removing electrons from designated atomic shells (e.g. K-shell ionization), for the ionization of a wide range of molecules from diatomics and simple polyatomics to complex molecules of technological and/or biological importance to free radicals to clusters of various sizes, to the ionization of positively and negatively charged atomic as well as molecular ions. The energy range, for which the DM formalism is now valid, goes from the ionization threshold (below 10 eV) to many thousands of electronvolts. A summary of the application of the DM formalism to the wide range of targets (atoms, molecules, ions, and clsutes) can be found in the recent review by Deutsch et al. [10].

In addition,, the DM formalism has proved to be an invaluable tool in predicting electron-impact ionization cross sections for a variety of targets, for which no experimental data have been reported in the literature, primarily neutral targets. Based on the level of agreement between DM calculations and existing experimental data, the level of confidence into the predictive capabilities of the DM formula ranges from about 20% for atoms and simple molecules to about 50% for complex molecules and clusters. In the case of positively and negatively charged atomic and molecular ions, there are simply not enough critically assessed experimental data to ascertain the predictive capability of the DM formula in these cases. Excellent agreement in some cases is contrasted by poor agreement in other cases, most notably in the case of electron detachment from negatively charged molecular ions.

Going forward, the main challenge to semi-rigorous electron-impact ionization cross section calculation approaches such as the DM formalism (and others) is at least 4-fold,

(1) to scrutinize the areas where calculations and critically assessed reliable
(2) experimental data disagree in an effort to further expand the range of applicability of the method and enhance the level of confidence in its predictive capabilities,

(3) to serve as a guide to the evaluation of experimental data in cases where available data for a given target disagree (e.g. by margins that significantly exceed their combined total margin of error),
(4) to further expand their range of applicability to final-state specific ionization processes such as dissociative ionization of molecules, and
(5) to stimulate new experiments with targets that have traditionally received little attention by providing calculated data against which measured data can be benchmarked.

Rigorous and fully quantum mechanical ionization cross section calculations, while in their infancy, have the potential to become formidable theoretical tools in the future. This will require the confluence of ever more powerful and versatile computational resources with new ideas that address the inherent challenges of the quantum mechanical treatment of the ionization process and, in case of targets other than atoms, also the more complicated structure of the target. However, there will always be a need for semi-rigorous calculation schemes such as the DM formalism (or the BEB method and others) when it comes to providing cross sections for a large number of diverse target species for practitioners and modelers quickly, accurately, and reliably.

Acknowledgements

This work was partially supported by the FWF, Wien, Austria. One of us (KB) would like to acknowledge the partial support of the Chemical Sciences, Geosciences, and Biosciences Division, Office of Basic Energy Sciences, U.S. Department of Energy.

References

[1] L.J. Kieffer, G.H. Dunn, Rev. Mod. Phys. 38 (1966) 1, and references therein
[2] "Electron Impact Ionization", T.D. Märk, G.H. Dunn (Eds.), Springer Verlag, Vienna (1985)
[3] I. Bray and A.T. Stelbovics, Adv. At. Mol. Phys. 35 (1995) 209; see also P.R.Bartlett and A.T. Stelbovics, Phys. Rev. A 66 (2002) 012707
[4] S.P. Khare, W.J. Meath, J. Phys. B 20 (1987) 2101; see also S.P. Khare, "Introduction to the Theory of Collisions of Electrons with Atoms and Molecules", Springer Verlag, Heidelberg (2002)
[5] H. Deutsch, T.D. Märk, Int. J. Mass Spectrom. Ion Proc. 79 (1987) R1
[6] Y.-K. Kim, M.E. Rudd, Phys. Rev. A 50 (1994) 3954
[7] K.N. Joshipura and C.G. Limbachiya, Int. J. Mass Spectrum. 216 (2002) 239
[8] H. Deutsch, P. Scheier, K. Becker, and T.D. Märk, Int. J. Mass Spectrom. 233 (2004) 13
[9] J.P. Desclaux, Atom. Data Nucl. Data Tables 12 (1973) 325
[10] H. Deutsch, K. Becker, M. Probst, and T.D. Märk, Adv. AMO Physics, editors: E. Arimondo, P. Berman, C. Lin, Vol. 57, 87-154 (2009), Elsevier Publ.

Electron Induced Fluorescence Study of the Second Positive System of N_2

Kočíšek J[1], Kubala D[1], Matejčík Š[1]

[1] *Department of Experimental Physics, Comenius University Bratislava, Slovakia, matejcik@fmph.uniba.sk*

The electron impact excitation of the second positive system of N_2 (2nd PS N_2) have been studied in a new crossed electron/molecular beams apparatus. The excited statets $C\ ^3\Pi_u(v')$ (v'=0..3) were excited using high resolution electron beam. The electron induced optical spectra in UV/VIS range (290 – 440 nm), the excitation thresholds of particular vibrational states $C\ ^3\Pi_u(v')$, the emission cross sections of the 2nd PS and the excitation cross sections of the $C\ ^3\Pi_u(v')$ states were measured with high resolution and sensitivity.

Introduction

Electron excitation of the nitrogen molecule plays an important role in atmospheric phenomena and laser physics. The second positive system $C\ ^3\Pi_u(v') \rightarrow B^3\Pi_g(v'')$ belongs to the most intensive bands in the emission spectrum of the nitrogen. Thus the electron impact excitation of the $C\ ^3\Pi_u(v')$ draws much attention due its importance for atnospheric processes and the electric discharges in nitrogen. The electron-impact cross sections for the various vibrational bands of the second positive systems have been already measured by researchers in several laboratories [1-4] still exist considerable discrepancies in the published data. Therefore an accurate knowledge of the excitation cross sections of the $C\ ^3\Pi_u(v')$ state is of primaly interest for the understanding of several important phenomena in nitrogen. In the present work the total cross sections for excitation of the v'=0,1, 2 and 3 vibrational levels of the $C\ ^3\Pi_u(v')$ state have been measured by the detection of the photonsfrom the second positive system in the 290-440 nm spectral range. Excitation functions of several optical lines have been measured and normalized to obtain absolute values of the cross sections. The present measurements have been carried out with higher electron energy resolution and more accurate incident energy calibration than the previous studies of the emission cross sections. This has allowed the energy dependence of the cross sections to be established with higher accuracy and the excitation cross sections to be determined in the near-threshold region.

Experimental setup

The new apparatus for electron impact excitation, used to study the optical excitation of N_2 is shown schematically in the Figure 1. It consists of an electron monochromator to produce a collimated beam of electrons, a collision chamber filled with a target gas and a system to detect spectrally analysed photons. The incident beam with an energy spread of

approximately 100 meV and a typical electron current of 20 nA is produced by a trochoidal electron monochromator (TEM). Photons emitted from the collision region are collected by a lens and transmitted via vacuum window outside of the vacuum chamber and refocused by second lens onto the entrance slit of an 0.25 m optical monochromator equipped with a cooled Hamamatsu H8259 photomultiplier at its exit slit. The magnetic field (5×10^{-3} T) is produced by a pair of coils which allow for accurate alignment of the direction of the field with respect to the electron spectrometer symmetry axis. The measurements were carried out for a pressure range in the collision region which gave linear dependence between detected photons intensity and target pressure. It was also ensured that the detected photon intensity increased linearly with the electron beam current.

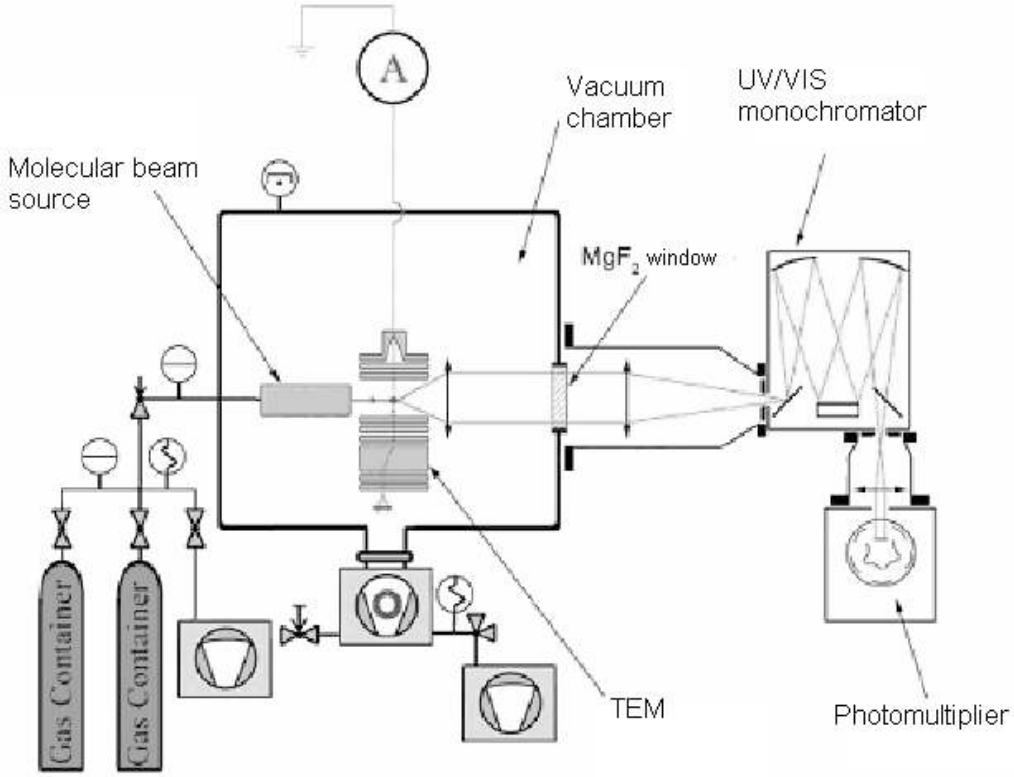

Fig. 1. *Schematic vie of the experimental setup*

Results and discussion

The fluorescence spectrum of the 2nd PS N_2 induced by the electrons with kinetic energy of 14.2 eV is shown shown in the Figure 2. The (v',v'') transitions of the second positive system have been identified and are idicated in the spectrum. The intensities of the observed transitions enable to estimate the relative emission cross sections.

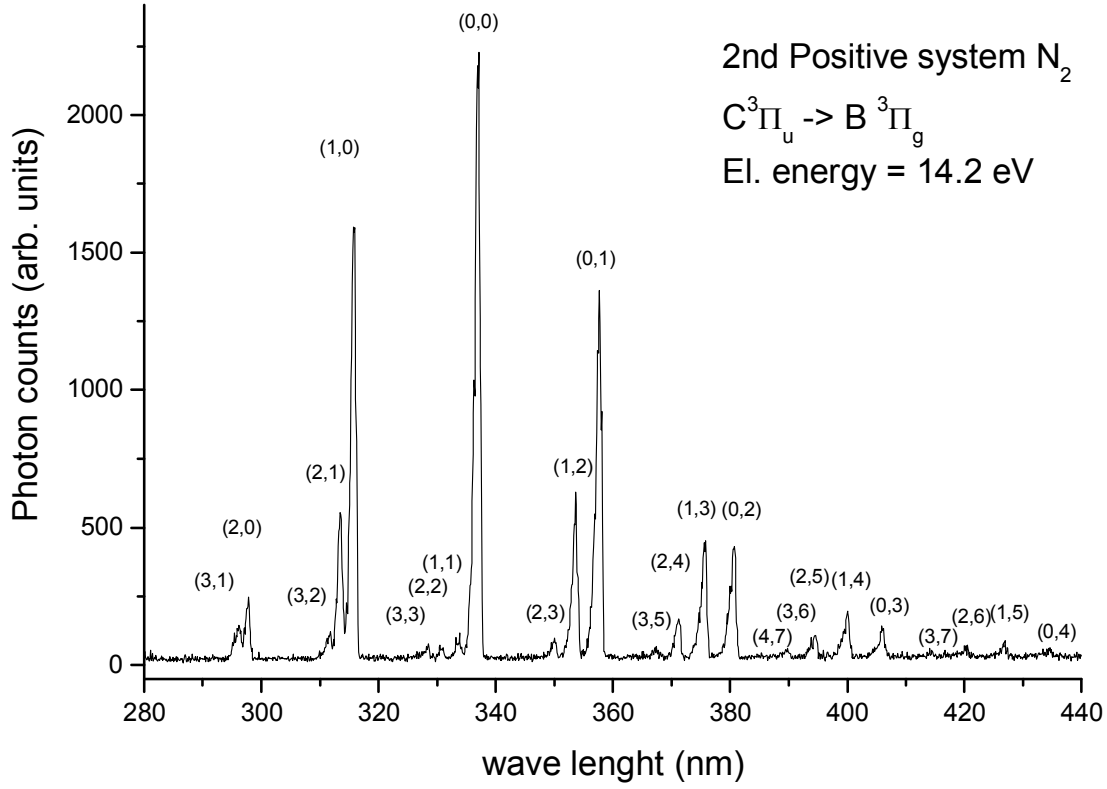

Fig. 2 Emission spectrum of the 2nd PS in N_2 induced by the electrons with kinetic energy of 14.2 eV.

The excitation cross section of the strongest emission band of the 2nd PS $C\,^3\Pi_u(v'=0)$ to $B\,^3\Pi_g(v''=0)$ (337 nm) is presented in the Figure 3. The excitation cross section has been measured in the energy region from threshold to 80 eV and it has been norinelized to the absolute emission cross section at its maximum at 14.1 eV. The electron energy range and the absolute value of the cross section has been calibrated to cross section measured by Zubek[1]. Excitation cross sections of additional transition lines of the 2nd PS of the N_2 have been measured. The excitation cross sections σ_v of the particular vibrational states of the $C\,^3\Pi_u$ can be obtained from the measured emission cross sections σ_v^{em} using following relation:

$$\sigma_{v'} = \sigma_{v''}^{em} A_{v',v''} \tau_{v'} \qquad (1)$$

where $A_{v',v''}$ is the transition probability and $\tau_{v'}$ is the mean lifetime of level v'.

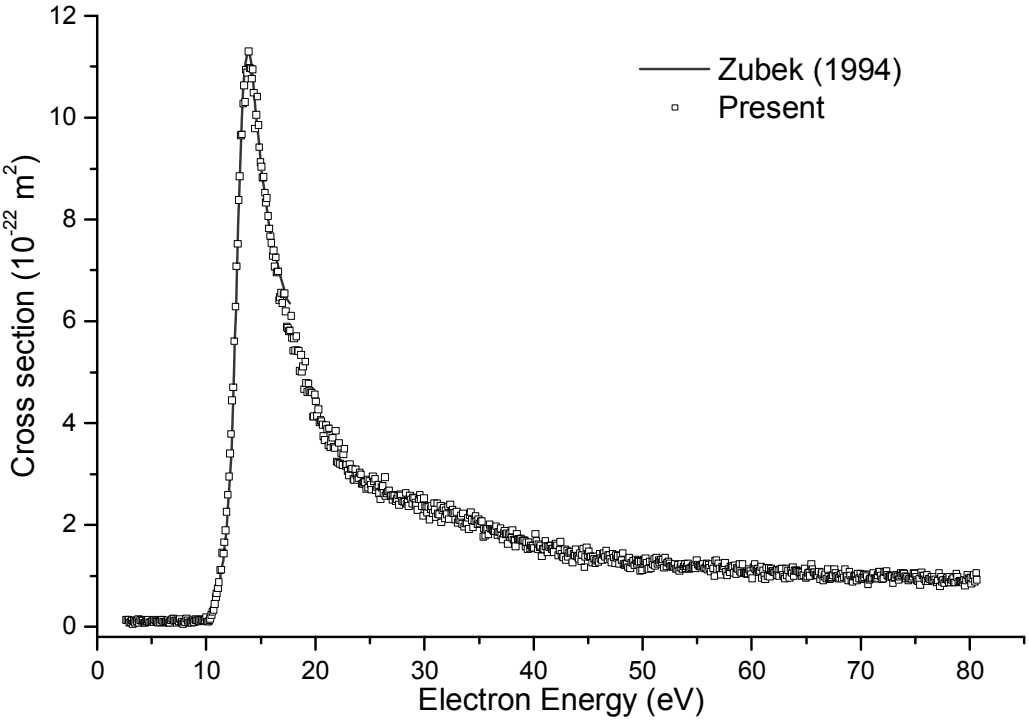

Fig. 3 *Emission cross section of the C $3\Pi_u(v'=0)$ to B $3\Pi_g(v''=0)$ (337 nm) transition of 2nd Positive system in N_2.*

The high energy resolution of the electron beam has been used to estimate with high precision the thresholds of the excitation functions for particular vibrational states v' of the $C\,^3\Pi_u$ electronic state of N_2.

Acknowledgment

This work was supported by Slovak Science and Technology Assistance Agency under the contracts No. APVV-07-0365 and LPP-0143-06.

References

[1] M. Shaw and J. Campos, J. Quont. Speetrosc. Radiat. Transfer 30 (1983) 73
[2] M. Zubek, J. Phys. B: At, Mol. Opt. Phys., 27 (1994) 573
[3] J.T. Fons, Phys. Rev. A, 53 (1996) 2239
[4] D.E. Shemansky, J.M. Ajello, I. Kanik, Astrophys. J., 452(1995) 472

Combined Experimental and Theoretical Study on the Nature and the Metastable Decay Pathways of the Thymine Ion Fragment $[M-H]^-$

Oddur Ingólfsson[1], Helga Dögg Flosadóttir[1], Hannes Jónsson[1], Stephan Denifl[2] and Paul Scheier[2].
[1] *Department of Chemistry, Science Institute, University of Iceland, Dunhaga 3, 107 Reykjavik, Iceland*
[2] *Institut für Ionenphysik und Angewandte Physik and Center for Molecular Biosciences Innsbruck, Leopold-Franzens-Universität Innsbruck Technikerstr. 25, 6020 Innsbruck, Austria*

Here we present a collaborative study which combines three different experimental approaches as well as *ab initio* molecular dynamics calculations to reveal the nature of the dehydrogenated thymine $[T-H]^-$ and the pathways of its decay. The study is conducted on the ion when formed up on low energy electron attachment in the energy range from about 0 eV to about 12 eV and on the ion when it is formed through deprotonation of the neutral thymine in the expanding plume in a matrix assisted laser desorption ionization (MALDI) mass spectrometer. The metastable decay pathways are compared and by using both 1N- and 3N-methyl thymine the role of the different dehydrogenation (deprotonation) sites is reviled.

Introduction

Electron induced fragmentation of molecules in the gas phase, clusters and condensed phase have been the subject of numerous studies in the last decades [1,2]. The earlier studies dealt mainly with halogenated compounds and were aimed at their dielectric properties, their use as gas phase insulators, their role in plasma etching and their role as pollutants in the Earth's atmosphere. More recently the interest in electron induced fragmentation of molecules has turned in the direction of biologically relevant molecules such as amino acids and the building blocks of the DNA. This interest was mainly triggered by a study by B. Boudaiffa et al. that showed that low energy electrons can cause both single strand breaks (SSB) and double strand brakes (DSB) in plasmid DNA [3,4]. Moreover, it was shown that the SSBs and DSBs induced by these electrons (which kinetic energy is below the ionization threshold) is a resonant process with energy dependent efficiency. These findings were of considerable significance as they indicated that low energy electrons may play a significant role in the damage high energy radiation causes in living organisms. This is a complex and not well understood process, and though the direct damage through radiation of sufficient energy may be lethal to the cell, the production of secondary reactive species along its track is believed to play the dominant role in damaging the relevant molecules [5]. One of the most abundant of these secondary species are electrons with kinetic energies below 20 eV [6], hence low energy electrons that may cause both SSBs and DSB in the DNA.

In general the fragmentation process induced by low energy electrons is preceded by the resonant formation of a transient negative ion. This is a process that proceeds through a vertical transition from the neutral ground state of the molecule to the corresponding anionic state. In most cases the TNI formed is thus energetically above its ground state and hence instable. In the gas phase such an ion can relax through autodetachment i.e. by ejecting the electron again or by bond cleavage, i.e., by dissociation. The dissociative process which is termed dissociative electron attachment (DEA) may in the simplest case proceed directly along a repulsive state. However, it may also proceed through considerable redistribution of the excess energy or even through rearrangement within the molecular anion. However, though a considerable number of complex dissociation processes have been observed, little attention has been given to secondary processes, i.e., the further (metastable) fragmentation of anionic fragments formed upon DEA. In a recent study on the fragment formation upon DEA to valine it was shown that the most abundant product is the dehydrogenated molecular ion; $[Val\text{-}H]^-$ [7]. These studies did however not reveal the nature of the anions, i.e., from where within the molecule the hydrogen loss takes place, nor did they reveal any information on the stability of these anions with respect to further dissociation. In a combined experimental and theoretical study of the metastable decay of $[Val\text{-}H]^-$ ions formed through DEA, after collisional activation and when they are formed through deprotonation of the neutral precursor in MALDI we could unambiguously identify the precursor ions and reveal their dissociation pathways [8].

Similar to valine, the most dominating DEA process observed for the nucleobase thymine is the hydrogen abstraction. This is a process that proceeds through a number of overlapping resonances in the energy range from 1 to 3 eV and it was shown that the low energy contribution around 1 eV was exclusively due to the dehydrogenation at the 1N position [9]. Here we present a collaborative study which combines three different experimental approaches as well as *ab initio* molecular dynamics calculations to look at the further metastable decay pathways of this ion and the role of the different deprotonation sites.

Experiments and Calculations

The metastable decay up on DEA and the CID studies were conducted in Innsbruck on a double focusing sector field mass spectrometer [10]. A molecular beam was crossed with an electron beam of about 1 eV resolution from a Nier-type ion source. Metastable dissociation in the field free region between the magnetic and electric sector, and the resulting kinetic energy release distribution (KERD) was investigated by mass analyzed ion kinetic energy scans (MIKE) [11]. The dehydrogenated parent anion passes this region 13-26μs after its formation. CID experiments are performed with this instrument by collision of the mass selected ions with stagnant N_2 target gas. The kinetic energy in the center of mass is about 500 eV and thus sufficiently high to induce any relevant fragmentation reaction. Metastable

decay of the deprotonated ions is measured at the University of Iceland with a commercial reflectron-type UV-MALDI-TOF instrument RFLEX IV (Bruker ,Germany). All experiments were carried out in post source decay mode (PSD) as described in detail elsewhere [12]. The ions are formed by MALDI of thymine embedded in a Bisbenzimide matrix. After a linear flight of about 13 μs the ions were reaccelerated with an ion mirror to acquire mass spectra of their fragmentation products. Samples were prepared by pre-spotting 0.5 μL of matrix solution (1 mg/mL) on a stainless steel sample plate, drying at air and then spotting 0.5 μL of 10 mg/mL thymine in methanol.

To identify possible fragmentation channels for the different precursor anions formed we conducted molecular dynamics (MD) simulations of the dissociation process assuming the ion is stable enough to reach the thermally equilibrated ground electronic state before fragmentation. The calculations where carried out using density functional theory with the PW91 functional and the VASP code [13,14]. First, a geometric energy minimization of the two different thymine anions (deprotonation sites) was carried out. The lowest energy structures were then heated to 400 K to account for the sublimation temperature in the DEA experiments. Ten geometric snapshots were then taken for each ion and to account for the initial electron energy an internal energy of 8 eV was added to the system by scaling the atomic velocities. Constant energy trajectories were then calculated for up to one pico second.

Results and discussion

DEA to thymine leads to formation of the dehydrogenated molecular anion in the energy range from about 1 eV to about 3.5 eV. Metastable decay of these anions is however only observed in the higher energy region of the spectra, hence above 2 eV. This is the energy region in which the hydrogen abstraction proceeds from the 3-N position of the thymine in the DEA experiments [8]. In this energy range the only metastable fragment observed from the native dehydrogenated thymine formed in the DEA experiments is NCO^-. This fragment is also the only one observed in the metastable decay process in MALDI.

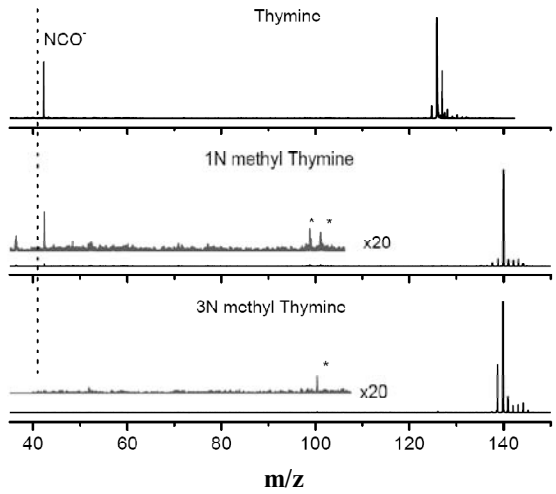

Fig. 1. *MALDI PSD spectra of thymine, 1N- and 3N-methyl thymidine.*

Figure 1 compares the MALDI metastable decay spectra of thymine with that of 1-N-methyl thymine and 3-N-methyl thymine. In these experiments the only observable metastable decay fragment is NCO^-. This fragment is only observed from the native thymine and from 3-N-methyl thymine. Hence, metastable decay of the

deprotonated thymine to form NCO^- proceeds only if the deprotonation takes place from the 3-N position. This is in good agreement with our preliminary DEA experiments where metastable NCO^- formation is only observed at higher energies, i.e., in the energy range where it has been shown that hydrogen abstraction from the 3-N position dominates. To verify that the reason for this energy selectivity is indeed due to the dehydrogenation site and not simply governed by the energetic threshold for the process we are also conducting CID experiments and MIKE scans of the 1-N and 3-N-methyl thymine. Furthermore, simulations have been performed on the native thymine deprotonated at 1-N and the 3-N side respectively as well as the respective methyl thymines. From the 10 trajectories simulated for native thymine deprotonated at 1-N no fragmentation occurs, however when the thymine is deprotonated at the 3-N position NCO^- formation is observed in 6 out of 10 simulations. Figure 2 shows selected snapshots from the simulations for native thymine deprotonated at th3 3-N position.

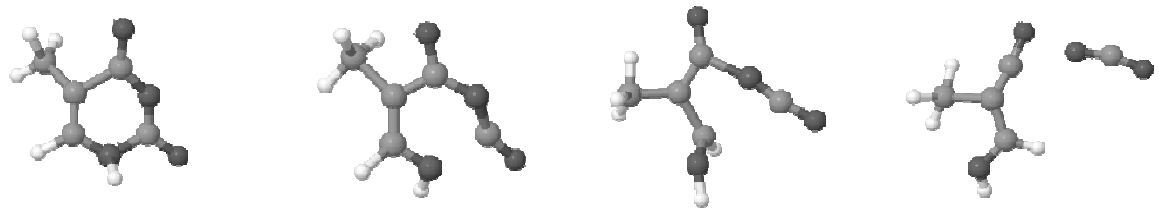

Fig. 2. *Selected snapshots from the simulations for native thymine deprotonated at th3 3-N position.*

Acknowledgements

This work has been supported by The Icelandic Centre for Research (RANNIS) and the FWF, Wien. HDF acknowledges support for a visit to Innsbruck from the COST Action P9 (Radiation Damage in Biomolecular Systems; RADAM)

References

[1] O. Ingolfsson et al. Int. J. Mass Spectrom. Ion. Process. 1996, 155, 1.
[2] I. Bald et al. Int. J. Mass Spectrom. Ion. Process. 2008, 277, 4.
[3] B. Boudaiffa et al.. Sanche, Science 287 (2000) 1658-60.
[4] L. Sanche, Eur. J. Phys. D 2005, 35, 367.
[5] L. Sanche, Mass Spectrometry Reviews 2002, 21, 349.
[6] V. Cobut et al. Radiat. Phys. Chem. 1998, 51, 229.
[7] P. Papp et al. J. Chem. Phys. 2006, 125.
[8] S. Ptasinska et al. Angew. Chem. Int. Ed. 2005, 44, 6941.
[9] HD. Flosadóttir et al. Angew. Chem. Int. Ed. 2008, 46, 8057.
[10] D. Huber et al. J. Chem. Phys. 2006, 125.
[11] J. H. B. R. G. Cooks et al. Metastable Ions, Elsevier, Amsterdam., 1973.
[12] M. Stano et al. Rapid Commun. Mass Spectrom. 2006, 20, 3498.
[13] G. Kresse, J. Furthmuller, Physical Review B 1996, 54, 11169.
[14] G. Kresse, J. Hafner, Physical Review B 1994, 49, 14251.

K^+ CD_3NO_2 Collision Experiments

F. Ferreira da Silva[1], Y. Nunes[1], G. Garcia[2] and P. Limão-Vieira[1]

[1] *Laboratório de Colisões Atómicas e Moleculares, CEFITEC, Departamento de Física,Universidade Nova de Lisboa, 2829-516 Caparica, Portugal*

[2] *Instituto de Matemáticas y Física Fundamental, Consejo Superior de Investigaciones Científicas (CSIC), Serrano 113-bis, 28006 Madrid, Spain*

Nitromethane, CH_3NO_2, have been extensively studied [1–4] because it may play a particular role in the chemistry of the earth's atmosphere (up to the stratosphere), is a simple organic-nitro compound with typical characteristics of explosives and propellants and forms dipole-bound as well as valence anions upon binding an extra electron [5–6]. Electron transfer (harpooning) in low energy atom-molecule collision is usually mediated by the crossing of the covalent and ionic potential energy surfaces. Despite the fact that the ionic surface lies above the covalent at large atom-molecule distances, due to the Coulomb potential there is a crossing point at which both potential energy surfaces have the same value [7]. This crossing processes leads to the formation of both K^+ and a molecular anion and allows access to states which are not accessible in free EA experiments [8, 9]. In particular, states with a positive electron affinity can be formed, and the role of vibrational excitation of the parent neutral molecule can be studied [7]. In the present experiments we have studied the formation of negative ions in a crossed molecular beam configuration, where a neutral hyperthermal beam of potassium atoms, formed in a charge exchange source, crosses with a CH_3NO_2 and CD_3NO_2 effusive molecular target. Negative ions formed in the collision region are extracted into a TOF mass spectrometer. Recent complementary studies on dissociative electron attachment experiments (DEA) [9] to nitromethane have revealed a wide range of anionic species and the present harpooning experiments are compared on the light of the intramolecular energy redistribution and resonances for those DEA processes [10].

[1] A. Di Domenico and J.L. Franklin, Int. J. Mass Spectrom. Ion Phys., 9 (1972) 171.
[2] A. Modelli and M. Venuti, Int. J. Mass Spectrom., 205 (2001) 7.
[3] I.C. Walker, M.A.D. Fluendy, Int. J. Mass Spectrom., 205 (2001) 171.
[4] W. Sailer, A. Pelc, S. Matejcik, E. Illenberger, P. Scheier and T.D. Märk, J. Chem. Phys., 117 (2002) 7989.
[5] R.N. Compton, H.S. Carman Jr, C. Desfrancois, H. Abdoul-Carime, J.P. Schermann, J.H. Hendricks, S.A. Lyapustina and K.H. Bowen, J. Chem. Phys., 105 (1996) 3472.
[6] T. Sommerfeld, Phys. Chem. Chem. Phys., 4 (2002) 2511.
[7] P. Limão-Vieira, A.M.C. Moutinho and J. Los, J. Chem. Phys., 124 (2006) 054306-1.
[8] L.G. Christophorou, D.L. Mc Corkle, A.A. Christodoulides, in: Electron-molecule interactions and their applications, Vol.2, ed. L.G. Christophorou, Acad. Press, NY, 1984.
[9] E. Alizadeh, F. Ferreira da Silva, F. Zappa, A. Mauracher, M. Probst, S. Denifl, A. Bacher, T.D. Märk, P. Limão-Vieira, P. Scheier, Int. J. Mass Spectrom., 271 (2008) 15.
[10] P. Limão-Vieira et al., in preparation.

Radiative Electron Attachment and Formation of Negative Molecular Ions in the Interstellar Medium

Thomas A Field[1], Karola Graupner[1], Graham C. Saunders[2]

[1] Centre for Plasma Physics, School of Mathematics and Physics, Queen's University Belfast, University Road, Belfast, BT7 1NN, N. Ireland, U.K., t.field@qub.ac.uk

[2] School of Chemistry and Chemical Engineering, Queen's University Belfast, BT9 5AG, N. Ireland, U.K. (present address Department of Chemistry, Science & Engineering, University of Waikato, Private Bag 3105, Hamilton, New Zealand)

Introduction

Over the past few years the first astronomical observations of molecular anions such as C_4H^- (Sakai et al. 2008), C_6H^- (Mccarthy et al. 2006), C_8H^- (Brunken et al. 2007) and C_3N^- (Thaddeus et al. 2008) have been reported. The formation of anions in astrophysical environments was predicted by radiative attachment in chemical models of astrophysical environments some time ago (Herbst 1981; Millar et al. 2000, 2007).

In radiative electron attachment the excess energy of the transient negative ion is lost by the emission of a photon to a stable negatively charged molecule. This is a key mechanism in astrophysical environments where the rate of collisional stabilization is very slow due to the very low pressure. Furthermore, dissociative electron attachment may not play a major role if it is not active at zero energy because of the low temperatures in molecular clouds, for example.

Experimental Results

Here investigations of electron attachment to astrophysically relevant molecules are reported with a combined trochoidal electron monochromator (TEM) time-of-flight (TOF) mass spectrometer (Field et al. 2005). The anions observed in the interstellar medium so far are all linear molecules with carbon chains based on the acetylene molecule. Investigations of electron attachment to HCCCN found no evidence for radiative attachment (Graupner et al. 2006). In the case of electron attachment to NCCCCN (Graupner et al. 2008), however, the formation of a negatively charged parent ion that is stable for microseconds or longer has been observed. This molecule is a good candidate an overall radiative electron attachment process, like SF_6, though this would require the molecule to be stable on millisecond timescales, which are the timescales for infrared photon emission.

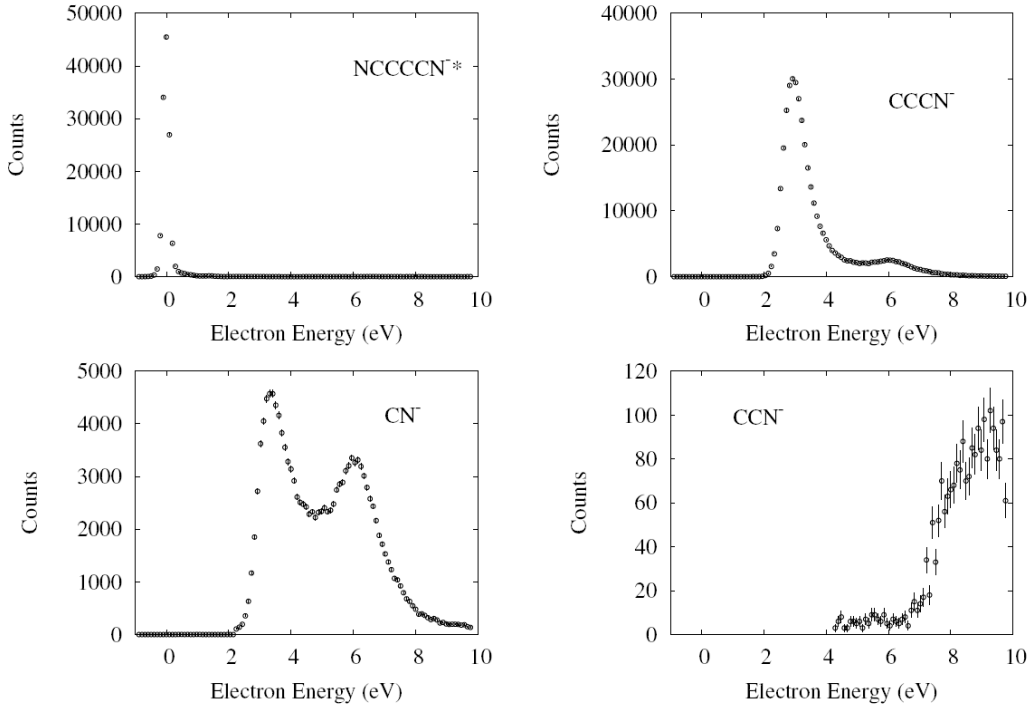

The Figure shows anion intensities observed follow electron attachment to NCCCCN.

Acknowlegdement: Thanks to the EPSRC for financial support (EP/F031025/1).

References

[1] Brunken S., Gupta H., Gottlieb C. A., McCarthy M. C. & Thaddeus P. 2007, ApJ, 664,L43
[2] Field T. A., Slattery A. E. , Adams D. J. & Morrison D. D. 2005, J. Phys. B, 38, 255
[3] Graupner K., Merrigan T. L., Field T. A., Youngs T. G. A. & Marr P. C. 2006, New J. Phys., 8, 117
[4] Graupner K., Field T. A., & Saunders G. C., 2008 ApJ, 685, L95
[5] Herbst E., 1981, Nature, 289, 656
[6] McCarthy M. C., Gottlieb C. A., Gupta H. & Thaddeus P. 2006, ApJ, 652, L141
[7] Millar T. J. , Herbst E. , & Bettens R. P. A. 2000, MNRAS, 316, 195
[8] Millar T. J. , Walsh C., Cordiner M. A., Chuimín R. Ní & Herbst E. 2007, ApJ, 662, L87
[9] Sakai N., Sakai T., & Yamamoto S. 2008, ApJ, 673, L71
[10] Thaddeus P., Gottlieb C. A. , Gupta H., Brunken S. , Mc-Carthy M. C., Agúndez M., Guélin M. & Cernicharo J. 2008, ApJ, 677, 1132

Hot Topic Papers

Photochemistry in Clusters and Nanoparticles of Atmospheric Relevance

Fárník M.[1], Poterya V.[1], Ončák M.[1,2], Slavíček P.[1,2], Buck U.[3]

[1] *J.Heyrovský Institute of Physical Chemistry AS CR, Dolejškova 3,18223 Prague 8, Czech Republic, michal.farnik@jh-inst.cas.cz*

[2] *Institute of Chemical Technology, Technická 5, Prague 6, Czech Republic*

[3] *Max-Planck-Institut für Dynamik und Selbstorganisation, Bunsenstr. 10, Göttingen, Germany*

Ice nanoparticles and water clusters play a key role in many processes in our atmosphere and also in astrochemistry. By the way of example, the ice particles in the polar stratospheric clouds (PSC) catalyze the reactions which lead to the ozone depletion process in the stratosphere above Antarctica [1]. Reservoir species such as hydrogen halides HX (X=Cl, Br) undergo chemical reactions on the ice particles in the PSC converting them to the active species such as Cl_2 molecules, which are then photolyzed by the UV sun radiation to the ozone destroying Cl radicals. Some models also suggest a direct photochemistry of Freon molecules (CFC) on PSC particles leading to the generation of Cl· radicals. Therefore studies of the photochemistry of ice clusters with embedded pollutant molecules such as hydrogen halides or CFC is of primary importance for the atmospheric chemistry. Such studies have recently been performed also in our laboratory [2]: large water clusters $(H_2O)_n$, n=10^2-10^3 were doped with foreign molecules such as hydrogen halides and subsequently excited with UV laser radiation (193~nm) and kinetic energy spectra of dissociating H-atom were recorded. Also pure $(H_2O)_n$ clusters were studied [3]. In addition, new experiments with HI and CFC doped water clusters are currently under way and the new results will be presented at the conference too.

The water cluster beam is produced by a supersonic expansion of neat water vapor through a conical nozzle. The clusters can be doped with HX molecules in a pick-up cell. Then the clusters are photolysed with a 193 nm or 243 nm lasers and the H-fragments are subsequently ionized by (2+1) REMPI process at 243 nm. The time-of-flight (TOF) spectra of the H-fragments are measured and converted into the kinetic energy distributions (KED). Strong H-atom signals were obtained from the photodissociation of $HX(H_2O)_n$ systems. The experiments with deuterated species DX and D_2O revealed that the H-fragment signal originates from the presence of the hydrogen halide molecule on the cluster, however, it is not simply due to the direct photolysis of the HX molecule nor H_2O molecule. This indicated an exchange of hydrogen atoms between the hydrogen halide and the water cluster via generation of the radical hydronium H_3O molecule.

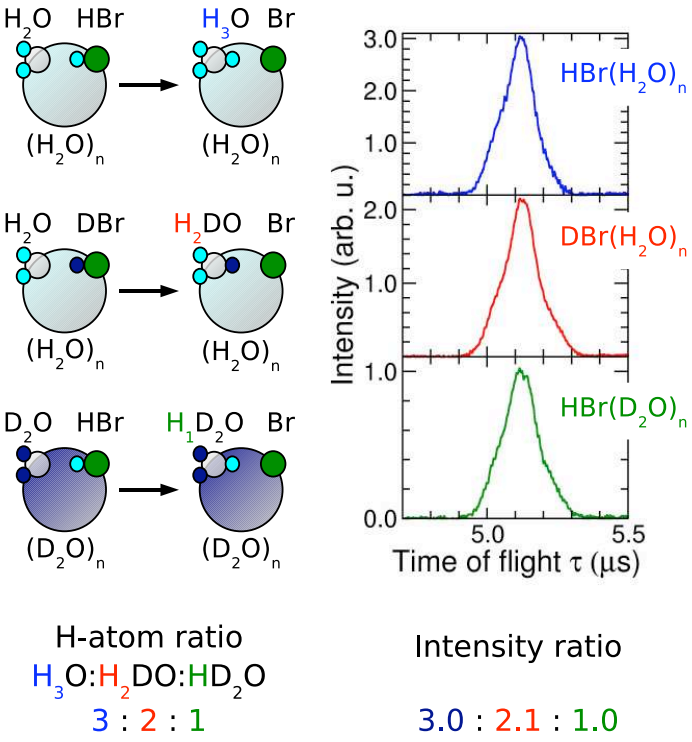

Figure: *Photodissociation of HBr on water clusters. Deuteration experiments pointing to the generation and dissociation of the H_3O radical.*

This photochemical pathway has been previously proposed theoretically by Sobolewski and Domcke [4]. The HX molecule undergoes acidic dissociation on water cluster generating the zwitterionic structure with hydronium cation and halide anion $H_3O^+(H_2O)_{n-1}X^-$. This species are then excited with the 193 nm laser radiation into a charge-transfer-to-solvent (CTTS) state. Subsequently, this state relaxes to a biradical state $H_3O(H_2O)_{n-1}X$, generating the neutral hydronium radical H_3O. Finally, the hydronium dissociates $H_3O \rightarrow H_2O+H$ releasing the H-atom which is emitted from the cluster and detected.

The proposed scenario is supported by further experimental and theoretical findings:

(1) The shapes of the H-fragment KED for HBr and HCl on water are almost identical, suggesting that they originate from the same species, H_3O, in both cases. On the contrary, the shapes of KED from HBr and HCl on Ar_n clusters are different due to the different energetics of the HBr and HCl molecules.

(2) The present model was also supported by measurements of relative photodissociation cross sections for HBr vs. HCl molecules on the $(H_2O)_n$ clusters, and by their comparison to the theoretical calculations also performed in our group. In addition, these theoretical calculations of $HX(H_2O)_n$ absorption spectra, which agree with our experimental findings, suggest that the ice particles in PSC might catalyze the HCl photolysis in a way, that can

potentially play a non-negligible role in the stratospheric Cl budget. These findings might have large consequences for the model calculations of the ozone depletion in the atmosphere.
In the pure water clusters, we observed two-photon photodissociation at 243 nm, where the H_3O radical played again the central role in the photolysis of an H_2O molecule from the cluster interior, while a direct photodissociation is observed for the cluster surface molecules. In addition, we study the competition between the multiphoton photodissociation and ionization at 243 and 193 nm.
Our experiments provide evidence that the hydronium radical H_3O play a central role in the photochemistry of aqueous systems. It was proposed in the literature[4] that these species can be interpreted as the solvated electron-hydronium cation pair. Thus the hydronium radical can serve as the cluster model of the solvated electron. The solvated electrons can be produced by radiation in the aqueous systems:

$$2H_2O(liq) + h\nu \rightarrow H_3O^+ + OH + e^-(aq).$$

The interaction of the solvated electron with CFC molecules on the PSC particles has been suggested to yield the Cl radicals directly. This hypothesis will be also investigated in our cluster experiment.

Acknowledgement:

The present work has been supported by the program "Nanotechnology for society" of the Czech Academy of Sciences KAN400400461, and by the grants Nr. KJB400400902 and 203/09/0422 of the Grant Agency of the Czech Republic.

References

[1] S. Solomon, R.R. Garcia, F.S. Rowland, D.J. Wuebbles, Nature 321, **1986**, 755; M.J. Molina, T.L. Tso, L.T. Molina, F.C.Y. Wang, Science 238, **1987**, 1253.
[2] V. Poterya, M. Fárník, P. Slavíček, U. Buck and V. Kresin J. Chem. Phys. 126, **2007,** 071101; M. Ončák, P. Slavíček, V. Poterya, M. Fárník and U. Buck, J. Phys. Chem. A 122, **2008,** 5344
[3] V. Poterya, M. Fárník, M. Ončák and P. Slavíček, Phys. Chem. Chem. Phys. 10, **2008**, 4835.
[4] A.L. Sobolewski, W. Domcke, Phys. Chem. Chem. Phys. 9, **2007**, 3818.

A New Nanocalorimetric Method to Measure Reaction Enthalpies

Robert F. Höckendorf,[1] Christian van der Linde,[1] O. Petru Balaj,[1] Martin K. Beyer[1]

[1] Institut für Physikalische Chemie, Christian-Albrechts-Universität zu Kiel, Olshausenstraße 40, 24098 Kiel, Germany, beyer@phc.uni-kiel.de

Nanocalorimetry is a powerful tool to determine solution phase electrochemical data from gas phase experiments [1]. The established procedure requires a low-temperature cooled cell and works with mass selected ions in an FT-ICR mass spectrometer. Here we present a new method to extract accurate thermochemical data by counting the number of water molecules which evaporate in a gas-phase reaction of a hydrated ion with a neutral reactant, which works in a room temperature environment without mass selection. This makes the method more generally applicable.

Experimental

Hydrated ions $X^{+/-}(H_2O)_n$, n = 50-80, are reacted with neutral molecules at a constant backing pressure in the 10^{-9} mbar regime in an FT-ICR mass spectrometer at room temperature. Mass spectra are taken for typically 20 reaction delays over 4 s of the reaction. For each mass spectrum, the average number of water molecules in the reactant and product ion distributions is calculated. Parallel to the reaction, black body radiation leads to a shrinking of the cluster size by evaporative cooling. We have developed differential equations which describe the average number of water molecules in the reactant and product ion distributions as a function of time.

Results and Discussion

We have chosen the previously studied reactions [2] of hydrated electrons $(H_2O)_n^-$ with O_2 and CO_2 as a test case of the new method. The number of evaporating water molecules is a parameter in the differential equations which is fitted to experimental data. Reproducible results are obtained for the number of water molecules evaporating. Nanocalorimetric analysis reveals that the CO2 released in the core exchange reaction is vibrationally excited, carrying 52 ± 5 kJ/mol excess energy. Extrapolation to solution phase values suggests hydration enthalpies of ΔH_{hyd} = -375 ± 33 kJ/mol for O_2^- and ΔH_{hyd} = -268 ± 31 kJ/mol for CO_2^-.

[1] W. A. Donald, R. D. Leib, J. T. O'Brien, M. F. Bush, E. R. Williams, *J. Am. Chem. Soc.* **130**, 3371 (2008).

[2] O. P. Balaj, C.-K. Siu, I. Balteanu, M. K. Beyer, V. E. Bondybey, *Chem. Eur. J.* 10, 4822 (2004).

Cross Sections and Reaction Rates for small Hydrocarbons in Fusion Plasma Physics

J. Seebacher[1] , S. Huber[1] , A. Kendl[1] , D. Reiter[2]

[1] *Institute for Ion Physics and Applied Physics, University of Innsbruck, Association EURATOM-ÖAW, A-6020 Innsbruck, Austria*

[2] *Institute for Energy Research – Plasma Physics, Forschungszentrum Jülich Gmbh, Association EURATOM, Trilateral Euregio Cluster, D-54245 Jülich, Germany*

Cross Sections in Fusion Plasma Physics

For understanding fundamental properties of nuclear fusion plasmas atomic and molecular data are required. In particular the transport and chemistry of smaller hydrocarbons is a current topic of interest, because plasma facing components are made from carbon and carbon fibre composite materials. Hydrocarbons are likely to be produced on these surfaces and penetrate into the plasma where they dissociate and stimulate radiation. For a proper description of the break up of these molecules a good knowledge of the reaction rates and cross sections is required. Cross sections may be obtained experimentally, as for example in Ref. [1], where kinetic energy distributions and cross sections of ethylene and its fragments have been measured. For applications in fusion plasma simulations, data for relevant atoms and molecules has been collected. Particular data for hydrocarbons applicable for fusion applications is described in Refs. [2,3]. This data is e.g. used by the EIRENE code, which is a state of the art Monte Carlo transport code for fusion plasma modelling [4]. Its main purpose is to simulate neutral gas and radiation transport processes in the boundary plasma of a tokamak device. Recently a new module has been added to this code allowing also for kinetic ion transport [5]. The break up of hydrocarbon molecules, e.g. CH_4, and the related migration of the fragments, e.g. CH^+,C^+,C^{++}..., in the SOL plasma is the topic of this paper.

Monte Carlo Methods

Monte Carlo methods allow straight-forward approach to study plasma transport and chemistry, because atomic and molecular processes can be directly incorporated. In short, one has to calculate the length s of a free flight of a particle between two collisions by solving

$$\int_0^s ds' \Sigma_t(s') = \ln \xi$$

where Σ_t is the "total macroscopic cross section" (dimension: 1/length) and ξ is a uniformly distributed random number between 0 and 1. The total macroscopic cross section is the sum of all individual macroscopic cross sections for all processes considered in the simulation. At the point of collision s the kind of collision is sampled from a discrete distribution of

probabilities p_k for collisions of type k. For example if the kind of collision is chosen to be electron impact ionization of a CH particle it is transformed into CH^+. The trajectory of CH is then stopped and a new trajectory for CH^+ is started. From a large amount of such particle trajectories macroscopic quantities, e.g. density, temperature..., can be derived. The total macroscopic cross section is the inverse of the total mean free path and can be calculated if all rate coefficients, defined as $\langle\sigma v\rangle$, of the reactions under consideration are known. For each process the macroscopic cross section can be calculated as $\Sigma = n_p \langle\sigma v\rangle / |v|$, where n_p is the density (electrons or ions), σ is the cross section and the brackets denote averaging over relative collision velocities. Cross sections and reaction rate coefficients for various processes are stored in various databases. The database which is used by the EIRENE code for methane is summarized in [2] and for propane and ethane in [3]. These databases store cross sections and reaction rate coefficients for electron impact ionization and dissociation of C_xH_y, dissociative excitation and ionization and recombination of $C_xH_y^+$ with electrons, as well as for heavy particle collisions. The data are being continuously updated.

Outline of this contribution

With this contribution we want to show an application of cross sections and reaction rate coefficients in fusion plasma physics. A methane gas puff test case for the TEXTOR tokamak, located at FZ Jülich, Germany, will be presented. The dissociation of methane is simulated in EIRENE by making use of the data bases of Refs. [2,3]. We will show results of the migration of the methane and its fragments in the scrape-off layer plasma of TEXTOR.

Acknowledgements:

This work was funded by FWF project P21061. This work, supported by the European Communities under the Contract of Association between EURATOM and the Austrian Academy of Sciences, was carried out within the framework of the European Fusion Development Agreement. The views and opinions expressed herein do not necessarily reflect those of the European Commission.

References

[1] N. Endstrasser, F. Zappa, A. Mauracher, A. Bacher, S. Feil, D. K. Böhme, P. Scheier, M. Probst, T.D. Märk, Int. J. Mass. Spectrom. 1-3/**280**, 65 (2009)

[2] R.K Janev, D. Reiter, Phys. Plasmas **9**, 4071 (2002)

[3] R.K Janev, D. Reiter, Phys. Plasmas **11**, 780 (2004)

[4] D. Reiter, M. Baelsmans, P. Börner, Fusion Science and Technology, **47**, 172 (2005). See also www.eirene.de

[5] J. Seebacher, „Consistent kinetic trace-impurity transport and chemistry modelling in fusion plasmas“, PhD Thesis, Innsbruck University of Innsbruck, 2009

LIBS Characterization of Inner Tile Superficial Layers Inside Fusion Reactors

R. Fantoni[1] , S. Almaviva[2,3], L. Caneve[1], F. Colao[1], G. Maddaluno[2]
[1]ENEA, fantoni@frascati.enea.it, FIM FISLAS, CR Frascati, Via Enrico Fermi 45, 00044 Frascati Italy
[2]ENEA, FPN FUSTEC, CR Frascati, Via Enrico Fermi 45, 00044 Frascati (RM)
[3]ENEA FPN FUSTEC research fellow

Introduction

It is well known that the operation of a fusion reactor can be severely affected by the impurities found inside the vacuum chamber and the fuel. During operation polluting particles containing different elements are continuously deposited on the surfaces of the reaction chamber inner walls, their presence significantly altering the on-going process. To assure continuous and fault free operation it is then necessary to monitor the quality grade of inner walls surface layers. This requirement can only be fulfilled developing diagnostic techniques able to monitor the presence and the release of undesired elements acting as pollutants with qualitative and quantitative measurements. Due to the constraints commonly found in fusion reactors, the measuring apparatus must be non invasive, remote and sensitive to light elements. These requirements make LIBS (Laser Induced Breakdown Spectroscopy) [1] an ideal candidate for on-line monitoring elemental impurities on the walls of current fusion reactor and ITER.
In this work we analyze the results of a feasibility study aimed to assess the diagnostic potentialities of the LIBS technique used for the determination of surface contaminants deposited and/or adsorbed on the coating of tiles in a fusion reactor. The surface concentration impurities of carbon, boron, lithium, oxygen and hydrogen were measured on a tile used in the poloidal limiter of the ENEA FTU tokamak. LIBS measurements were used to determine the contaminants depth profile and to hypothesize the stoichiometry of superficial compounds examined under vacuum in conditions similar to those matched in the reactor between successive series of firing.

Experimental

1. LIBS set-up

The LIBS set-up for laboratory measurements has been utilized as developed for different applications, on samples examined either ad atmospheric or at low pressure, the latter for planetary exploration. It consists of a Nd:YAG laser emitting up to 200 mJ and 8 ns pulses at 1064 nm with a 10 Hz repetition rate, which is focused on the sample surface. Optical signal

there generated is collected by a small telescope at the entrance of a fibre optics bundle connected to the spectrograph (TRIAX 550 ISA JOBIN-YVON) equipped with different gratings for operation at medium and high resolution, best resolution achieved at 500 nm with the used entrance slit (100μm) is about 0.1Å. An intensified CCD (ANDOR InstaSpec V) is utilized for time resolved data acquisition. Each sample (tile) was examined inside a stainless steel chamber equipped with three optical windows kept in vacuum (residual pressure about $2 \cdot 10^{-4}$ mbar) [2].
Inner walls of last Frascati Tokamak FTU are covered by tiles made of TMZ, a 99% Molybdenum alloy. New tiles (reference) and tiles exposed to the plasma radiation formed in the reactor were examined as samples in order to obtain information on surface contamination occurred during the former tokamak operation.

2. LIBS methodology

The Laser Induced Breakdown Spectroscopy is nowadays a well established tool for qualitative, semi-quantitative and quantitative analysis of surfaces, with micro-destructive characteristics and some capabilities for stratigraphy.
In LIBS a laser induced plasma is generated upon a surface, causing there both sample vaporization and ionization; the radiation emitted during the successive plasma cooling contains information about the initial surface elemental composition. LIBS analytical performances rely upon the choice of a proper time window for detection of the emitted radiation, since the assumption of LTE (Local Thermodynamic Equilibrium) is mandatory for data reduction [3]. Within this assumption, a single temperature is associated to all species present in the plasma plume (atoms, ions, electrons) which obey to Boltzmann distribution, and a single electron density is ruling the ion/atom ratio (Saha equation).
LIBS quantitative information were retrieved by using the calibration free (CF) procedure [4], which relies on the contemporary determination of all species present at the surface and on the knowledge of the spectroscopic properties for the relevant lines examined. Partition functions for the different elements detected were derived from Irwin work [5].
LIBS stratigraphy is based on the micro-ablation performed at the sample surface by successive laser shots, once the sample is examined firing a sequence of pulses on the same interaction point. Our former experiences on different alloys indicate an average value of ablation rate about 10 μm per shot at the metal surface [6].

Results and discussion

Experiments performed on the new tile allowed to select the experimental conditions in which the LTE conditions where satisfied in vacuum as follows: 200ns gate delay and 10μs width. The corresponding temperature, measured on several atomic and ionic molybdenum lines by

means of an extended Boltzmann plot was 15000 K at the highest laser energy, and varied between 12000 K and 15000 K in all the investigated range of laser parameters. By measuring the Stark broadening of the H_α/D_α line, the electron density value $N_e \approx 3.5 \cdot 10^{14}$ cm^{-3} has been determined with about 50% uncertainty.

High resolution LIBS spectra were collected on three selected spectral ranges (248 nm, 663 nm and 840 nm) in order to quantify the presence and the depth of detected impurities (carbon and boron in the first range, hydrogen unresolved isotopes and lithium on the second, oxygen in the third, respectively), nearby atomic molybdenum lines were utilized for internal standardization. Analytical lines and respective spectroscopic parameters are listed in Table 1.

Element	wavelength [nm]	Partition function at T=15000 K	Upper level energy [eV]	Upper level degeneracy	Transition lifetime [s^{-1}]
B	249.772	7.51	4.96	2	$2.40 \cdot 10^{-8}$
C	247.856	11.5	7.68	3	$0.34 \cdot 10^{-8}$
Li	670.776	24.9	1.85	6	$0.37 \cdot 10^{-8}$
H	656.291	2.04	12.09	2	$0.80 \cdot 10^{-8}$
O	844.636	10.2	10.99	9	$0.28 \cdot 10^{-8}$

Table 1 – Analytical lines and respective spectroscopic parameters

Once identified the surface contaminants, the exposed tile was examined in two different locations, either on the face directly exposed to the plasma (S) or on a side face (L). Significantly different results were obtained for hydrogen and lithium whose concentration on the front face S resulted up to an order of magnitude larger than on the side L, while comparable results were obtained for carbon and boron.

The time evolution of each line was studied in detail in order to obtain information on the stratigraphy. Each element concentration was expressed as ratio to Mo, after extrapolating the intensity on the former to the first laser shot, where its line are missing due to the coverage of the other elements.

Results obtained are reported in table 2, as retrieved for the measured temperature (15000 K). Note that molybdenum (not listed since it is used as reference for relative concentration) starts to appear on the spectra after 4-5 laser shots. The results obtained for the inner layers are to be considered only semi-quantitative due to the large uncertainty in the determination of time constants.

In any case it comes out clearly that carbon contamination occurs only in the outermost surface layer, while boron penetrates more deeply and lithium reaches inner molybdenum layers. Hydrogen and oxygen contamination is also strongly localized on the outer surface layers. Current results support the hypothesis of the formation of the following compounds in the outer surface layers (up to 10 μm depth): carbon dioxide and bicarbonate ion, water/heavy

water, molecular oxygen and lithium carbonates (Li_2CO_3/$LiHCO_3$) with respective ratio 5:60:20:1. At increasing depth carbon concentration drops, so lithium carbonates are replaced by molybdates (Li_2MoO_4). At intermediate depths (10 to 100 μm) lithium is probably bound with boron and at larger depths gives rise to Li/Mo alloys where it lays in interstitial locations.

Laser shot	Depth [μm]	H	Li	B	C	O
1	10	600	5	1	25	500
10	100	40	2.5	~ 0.1	~ 0	7
100	> 100	~ 0.01	0.25	~ 0.01	~ 0	~ 0

Table 2 – Statiphication of impurities on the exposed tile.
Relative concentration are given in arbitrary units.

Preliminary analysis of new ITER tiles will be also presented, as performed on the coated material selected (W-Mo-Ti) prior to plasma exposition and after suitably simulating the process by laser ablation inside the measurement chamber in order to deposit most likely impurities from additional solid or gas targets.

This study is a preliminary part of an activity aimed to design a LIBS system for in-line monitoring the wall surfaces inside next generation of fusion reactors.

References

[1] Miziolek, A.W.; Schechter, I.; Palleschi V. (Eds) "Laser-Induced Breakdown Spectroscopy (LIBS): Fundamentals and Applications" Cambridge University Press, 2006
[2] Colao, F.; Fantoni, R.; Lazic, V.; Paolini A. Appl. Phys. A 79 (2004) 143-152
[3] Liu, H.C.; Mao, X.L.; Yoo, J.H.; Russo R.E. Spectrochim Acta B 54 (1999) 1607-1624
[4] Corsi, M.; Cristoforetti, G.; Palleschi, V.; Salvetti, A.; Tognoni E. Eur. Phys. J. D 13 (2001) 373-377
[5] Irwin, A.W. Astrophys J., 45 (1981) 621-633
[6] Colao, F.; Fantoni, R.; Lazic, V.; Caneve, L.; Giardini, A.; Spizzichino, V. J. Anal. At. Spectrom., 19 (2004) 502-504

DNA Damage Induced by Non-Thermal Atmospheric Pressure Plasma Jet

S. Ptasinska, B. Bahnev, A. Stypczynska, M.D. Bowden, N. St. J. Braithwaite, N.J. Mason
Department of Physics and Astronomy, The Open University, Walton Hall, Milton Keynes, MK7 6AA, United Kingdom
s.ptasinska@open.ac.uk

In this study, we have investigated the effect of a 'cold' Atmospheric Pressure Plasma Jet (APPJ) with dehydrated plasmid DNA. For purpose of these studies a home-built plasma source was constructed and a brief description of used source is given here. The DNA molecule is observed to be very sensitive to short-term exposures to low energy electrons, ions and excited neutral species as well as to UV light, which are all components of an APPJ fed by helium. In order to determine the possible pathways that lead to strand breaks in the DNA, the APPJ exposure was carried out over a range of operating conditions.

Introduction

Since the invention of Atmospheric Pressure Plasma Jet (APPJ) in 1998 [1], a number of devices with different configurations have been developed and their application in industry and medicine is steadily growing [2,3].

A recent extended review provides an update on research related to applications of non-thermal plasmas in medicine and a discussion of the possible mechanisms of interactions between plasma and living matter [4]. In this review the authors presented a very broad overview of the use of "cold" plasmas in the clinic including: tissue sterilization, wound healing, tissue regeneration, treatment of melanoma skin cancer and dental cavities. However these applications are still in the earliest stage of their development and their introduction into general medical practice may be some years away. The main reason for this is a lack of a deeper understanding of the physical, chemical and biological mechanisms underlying the interaction of a non-thermal atmospheric pressure plasma and living cells, tissues and organs.

In the present work we have investigated the formation of single- and double- strand breaks in DNA molecules induced by an atmospheric pressure plasma jet (APPJ). The complexity of plasma-generated species. i.e. excited atoms, charged particles, electrons and UV light gives a variety of possible pathways by which DNA can be damaged. Therefore our aim is to understand the interaction of particular components of the plasma with DNA.

Experimental set-up

The home-built experimental set-up is shown in Figure 1. The plasma jet is produced using a dielectric barrier discharge with the plasma being ignited in a quartz tube (a length of 25 cm and an inner diameter of 4 mm) placed between two external tubular electrodes made of brass. The length of both electrodes is 5 cm and the distance between them can be adjusted. The front electrode is connected to a high voltage power supply and the rear one grounded; The discharge is fed by helium, the flow rate was set at 10 m/s to ensure laminar mode. At this velocity a visible plasma plume is launched into the surrounding air, with its length being up to 5.5 cm long with a diameter of 4 mm. The plasma is powered by a radio frequency supply unit which consists of a pulse generator. Here, the sinusoidal shaped pulses were generated with voltage of 8 kV and 20 mA peak-to-peak and repetition rate of 3.2 kHz.

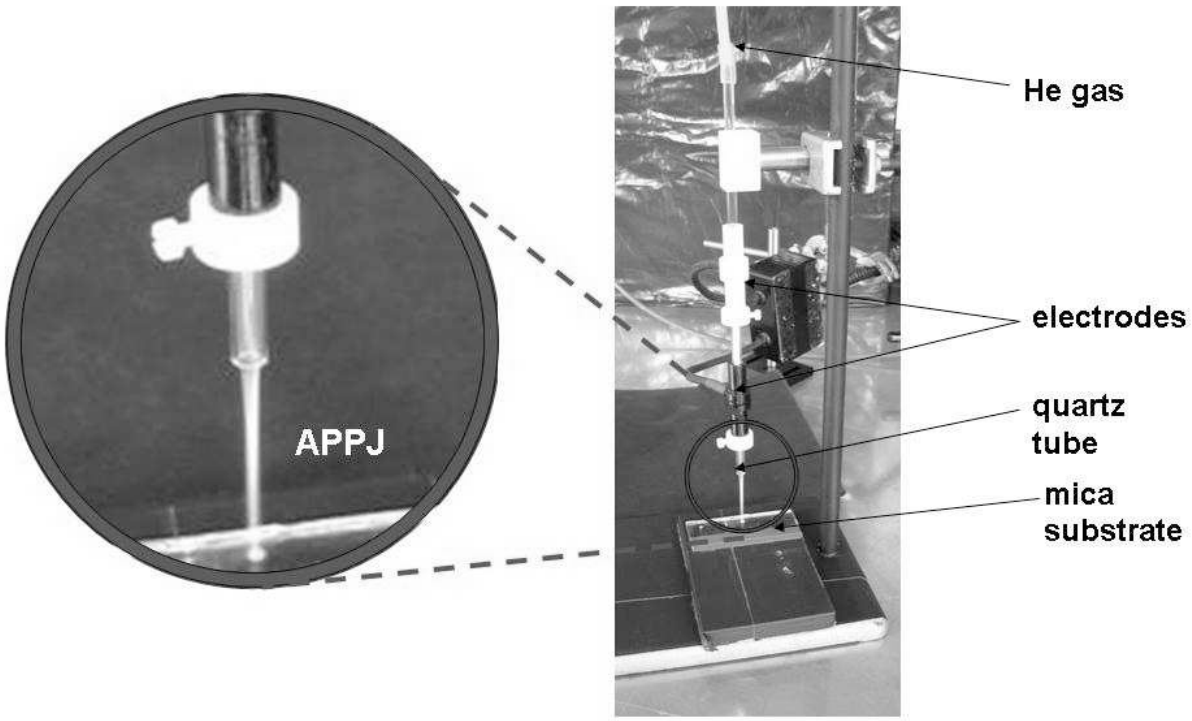

Fig. 1. Experimental set-up for the formation of the atmospheric pressure plasma jet.

Results

In this experiment we used extra-chromosomal (plasmid) DNA extracted from E. coli bacteria and purified to ensure only a relatively small amount of residual proteins. The plasmid purity was assessed using both the gel electrophoresis technique and by measuring the ratio of absorbance at 260 nm to that at 280 nm [A(260/280)]. The ratio of A(260/280) for DNA samples was between 1.85 and 1.9, indicating a high purity of samples and gel electrophoresis Revealed that ninety five per cent of the plasmid was in supercoiled form. Plasmid DNA (pBR322, 4361 base pair) was dissolved in autoclaved ultra-pure water and 2 μL of such an aqueous DNA (200 ng μL^{-1}) solution was deposited onto mica slides that were then dried at room temperature. The DNA covered mica slides were then placed perpendicularly to the 'cold' plasma jet formed in helium. After exposure the DNA samples were recovered with water and analysed by 0.8 % agarose gel electrophoresis, pre-stained with SYBR green dye. All samples were loaded into wells in the agarose gel and 'run' for 3 hours prior to imaging. The gels were imaged by means of the fluorescent scanner and analysed by using the ImageJ software.

Plasmid DNA is a good indicator molecule to use for recognition of single- and double strand breaks in helix DNA owing to its different topological states: supercoiled represents the undamaged molecule; open circle and linear conformers are formed due to the disruption of a backbone on one and both strands, respectively. The mobility in the gel electrophoresis of these three forms is different, thus three particular forms can be separated. The intensity of bands indicates the relative concentration of different types of DNA conformers.

Samples located at the tip of the jet were exposed for different time durations, i.e. 0, 1 and 5 min (Fig. 2). Control experiments were also performed by leaving a few samples at room temperature while the other samples were treated. In this control measurement, 85-75% of intact DNA was recovered from the mica slides, that is shown as) min irradiation in Fig. 2. Additionally, experiments were also performed where the dry DNA samples were exposed to a helium stream with the same flow rate, but without applying the electrical excitation necessary to create the plasma jet. No detectable damage of DNA due to its exposure to a stream of flowing helium was observed. Results from at least three different samples with the same irradiation conditions were summed. A mean was calculated for each form and an error bar calculated as one standard deviation from the mean.

Rapid degradation of supercoiled DNA is observed, up to 60% within one minute of He plasma treatment, followed by a period when there was a slower accumulation of damage. Upon exposure, the amount of linear DNA was initially observed to increase by 10%, and remained constant. Most remarkable is the production of open circle forms due to single strand breaks in DNA, yielding a 70% rise after five minutes of He plasma treatment.

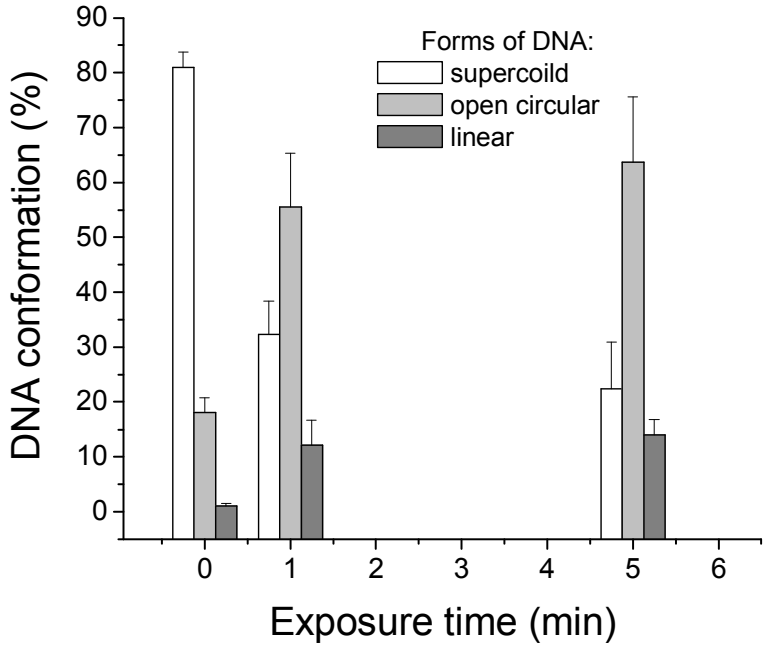

Fig. 2. The effect of plasma exposure time upon the change in percentage abundance of each of the plasmid forms.

Future work

Recently we have started studies on effect of water and amino acids on DNA damage using plasma exposure. We expect that the presence of water will increase the damage to DNA due to the formation of highly reactive radicals during the APPJ interaction. In contrast the presence of amino acids around DNA molecules may shield them from the plasma-generate species and so reduce the amount of damage. Results will be reported at the conference.

Acknowledgment

This work was financially supported by Engineering and Physical Sciences Research Council EPSRC, UK (EP/D067138/1).

[1] A. Schütze, J.Y. Jeong, S.E. Babayan, J. Park, G.S. Selwyn, R.F. Hicks, *IEEE Transactions on Plasma Science* 1998, 26, 1685
[2] J.F. Kolb, A.A.H. Mohamed, R.O. Price, R.J. Swanson, A. Bowman, R.L. Chiavarini, M. Stacey, K.H. Schoenbach, *Appl. Phys. Lett.* 2008, 92, 241501
[3] Z. Cao, J.L. Walsh, M.G. Kong, *Appl. Phys. Lett.* 2009, 94, 021501
[4] G. Fridman, G. Friedman, A. Gustol, A.B. Shekhter, V.N. Vasilets, A. Fridman, *Plasma Process. Polim.* 2008, 5, 503-533

Femtosecond Spectroscopy of Alkali Molecules Attached to Helium Nanodroplets

M. Mudrich, Ch. Giese, B. Grüner, L. Fechner and F. Stienkemeier
Physikalisches Institut, Universität Freiburg, 79104 Freiburg, Germany
M. Schlesinger and W. Strunz
Institut für Theoretische Physik, Technische Universität Dresden, 01062 Dresden, Germany

Helium nanodroplets doped with alkali atoms and molecules are intriguing systems at the border between gas-phase molecules and large heterogeneous clusters. Upon femtosecond laser excitation, alkali molecules exhibit vibrational wave packet oscillations which are only weakly affected by the helium environment due to the fast desorption of the molecule from the droplet. This allows for high-resolution Fourier spectra of vibrational levels in the electronic ground and excited states, as demonstrated e.g. for Rb_2 [1] and Rb_3 (Fig. 1). In contrast to the vibration, the rotational and spin dynamics appear to be strongly perturbed by the interaction with the helium.

The absence of vibrational damping in the triplet ground state of K_2 in contrast to damped wave packet motion in electronically excited states is discussed in the context of Landau's critical velocity and frictionless motion in superfluid helium on the nano-scale [2].

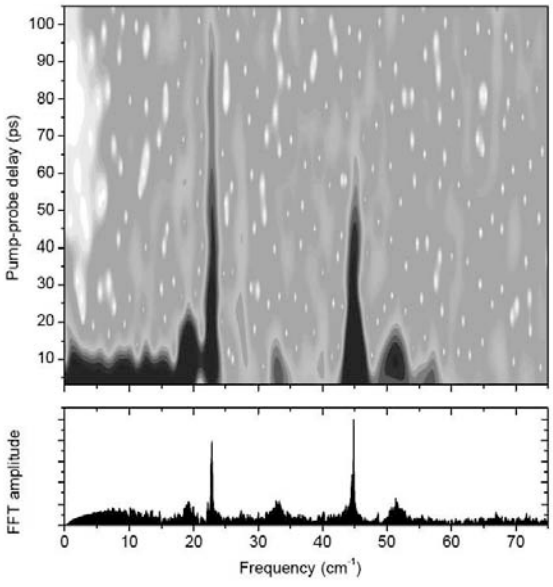

Fig. 1. *Time-resolved Fourier spectrum of the pump-probe photoionization transient (λ=850nm) of Rb_3-molecules attached to helium nanodroplets*

References

[1] M. Mudrich, Ph. Heister, Th. Hippler, Ch. Giese, O. Dulieu, and F. Stienkemeier, *accepted by PRA (*arXiv:0907.2774*)*
[2] M. Schlesinger, M. Mudrich, F. Stienkemeier, W. Strunz, *submitted (arXiv:0909.4691)*

Three-Dimensional Momentum Imaging of Electron Wave Packet Interference in Few-Cycle Laser Pulses

M. Lezius[1] , O. Herrwerth[1] , Th. Uphues[1] , M. Schultze[1] , E. Goulielmakis[1] , M. Uiberacker[1] , M. F. Kling[1] , A. Rudenko[2], R. Gopal[3], K. Simeonidis[3], R. Moshammer[3], Th. Ergler[3], M. Dürr[3], M. Kurka[3], K.-U. Kühnel[3], S. Tschuch[3], C.-D. Schröter[3], D. Bauer[3], and J. Ullrich[3]

[1] Max-Planck-Institut für Quantenoptik, Hans-Kopfermann-Strasse 1, D-85748 Garching, Germany

[2] Max-Planck Advanced Study Group at CFEL, D-22607 Hamburg, Germany

[3] Max-Planck-Institut für Kernphysik, Saupfercheckweg 1, D-69117 Heidelberg, Germany

Using a reaction microscope, three-dimensional electron (and ion) momentum spectra have been recorded for carrier-envelope-phase (CEP) stabilized few-cycle (5 fs), intense ($4x10^{14}$ W/cm^2) laser pulses (740 nm) impinging on He. Preferential emission of low-energy electrons (E_e < 15 eV) to either hemisphere is observed as a function of the CEP. Clear interference patterns emerge in P space at CEPs with maximum asymmetry, interpreted as attosecond interferences of rescattered and directly emitted electron wave packets. For a few-cycle sine-like waveform, two tunneling phases, symmetrically spaced around the zero crossing of the field lead to the same momentum of the ejected electron, and the corresponding trajectories can interfere. The first wave packet that was launched at t_1 recollides with the ionic core after ~3/4 of the laser cycle and is thereby being modified in phase and wavefront direction. It overlaps with an unaffected second ‘‘reference’’ wave packet (of the same electron) launched at t_2. A 3D momentum image of these electron wave-packet (EWP) interferences therefore represents a time-dependent hologram of the modulations imposed onto the first wave packet. Attosecond dynamics of the electron cloud bound to the ion might be imprinted and can potentially be reconstructed for atomic, molecular, and cluster targets.

Experimental Results

For the experiment, linearly polarized CEP-stabilized 5 fs pulses at 740 nm with a repetition rate of 3 kHz have been used.. The laser beam, with intensities up to 0.4 PW/cm^2 at the focus of a 125 mm spherical mirror was crossed with a supersonic, cold He jet (~10^{11} atoms/cm^2) in the ultrahigh vacuum chamber (~10^{-10} mbar) of a reaction microscope. The created ions and electrons were guided to two position sensitive channel plate detectors by weak electric (~2 V/cm) and magnetic (~0.8 mT) fields, applied along the laser polarization axis. Superior momentum resolution along the polarization axis (the spectrometer axis) was achieved reaching $\Delta p_{\parallel}$ < 0.02 a.u. for both ions and electrons. Along the transverse directions (i.e., in the plane perpendicular to the laser polarization), the ion momentum resolution varied from

~0.5 a.u. along the gas jet direction to <0.1 a.u. in the direction perpendicular to the jet. The transverse momentum resolution for electrons was on the level of 0.05 a.u. The CEP of the laser field was varied in steps over a range of 2π radians. For each of the phases, the two-dimensional position and time-of-flight spectra for the ions and electrons were recorded in coincidence. Fig. 1(a) shows some electron momentum distributions windowed parallel to the light wave electric field. Clearly visible are peaks, which mostly disappear for $p_{\parallel} < 0$. After changing the CEP by π in Fig. 1(b), these peaks are almost exactly mirrored about $p_{\parallel} = 0$ (black line) as illustrated by the thin blue curve, an exact mirror image of Fig. 1(a). For intermediate phases (not shown here) the visibility of the peaks becomes progressively less pronounced and symmetric about $p_{\parallel} = 0$ for CEP = 0, while maintaining their positions. The momenta ($p_{\parallel}$), where interference peaks occur in Fig. 1, are plotted in Fig. 2 (red full circles) and compared to the results of previous measurements for 25 fs, non-CEP-stabilized pulses (blue open circles) at 790 nm. Obviously the slope of the progressive peaks in this experiment differs from the 25 fs data, which are in excellent agreement with a square root above-threshold-ionization(ATI)-like behavior (black curve), where the spacing between peaks corresponds to the photon energy, i.e., to 0.057 a.u. (790 nm). The spacing between the here observed peaks, however, is much smaller, pointing to the fact that in ultrashort pulses interferences emerging from wave-packet emission at the maxima of the oscillating electric field, i.e., at the carrier frequency corresponding to the photon energy, is widely suppressed. Instead a new, quite regular spacing emerges which turns out to be linear as a function of $p_{\parallel}$.

Theory and Interpretation

We have developed a simple one-dimensional model based on strong-field approximation (SFA). The ionization in this model is confined to the most intense cycle of a sine-like pulse, and the electron motion is confined to the laser polarization axis only. The interference term arising from the superposition of the two quantum paths leading to the same momentum p (Fig. 1), referenced by their classical birth times (t_s, s= 1,2), can be expressed by the p-dependent transition amplitude $T(p)=\Sigma_{s=1,2}C_s\cdot\exp[i(\frac{1}{2}p^2t_s+\varphi_{IR}(t_s))]$ with the phase $\varphi_{IR}(t_s)=\frac{1}{2}\cdot\int^{ts}[2A(t')p+A2(t')]dt'$. A(t) is the vector potential of the laser field and C_s are the amplitudes for wave packets created at t_s. Ignoring the contribution due to Coulomb effects, the final momentum distribution is interpreted as arising from a superposition of these two wave packets, shifted in time, and with additional phases, $\varphi_{IR}(t_s)$, accounting for the Volkov action for a free electron in a strong laser field. It is evident that modulation in the momentum distributions strongly depends on the intensity and, hence, any comparison with the experiment requires us to use intensity averaged distributions. This was done by evaluating the above expressions for a pulse with a $\cos^2$ intensity envelope with FWHM of 5 fs, 0.4

PW/cm^2 at 740 nm, and averaged over intensities in a range of ±6%. In Fig. 2 the respective positions of the interference maxima, at a phase of maximum fringe asymmetry, are indicated as triangles with uncertainty bars. The agreement with the experimental data appears well within the accuracy of our simple model. Our results provide strong evidence that we have realized for the first time a true double-slit arrangement in time, where the slits are experimentally determined. Analyzing the FWHM, i.e., the visibility of the most prominent peaks (~0.05 a.u) and relating it to the uncertainty of the birth time of the electron, we find an effective slit width of $t_{slit} < 20$ attoseconds. *Further information is available in the related publication*: R. Gopal, *et al.*, Phys. Rev. Letters **103**, 053001 (2009)

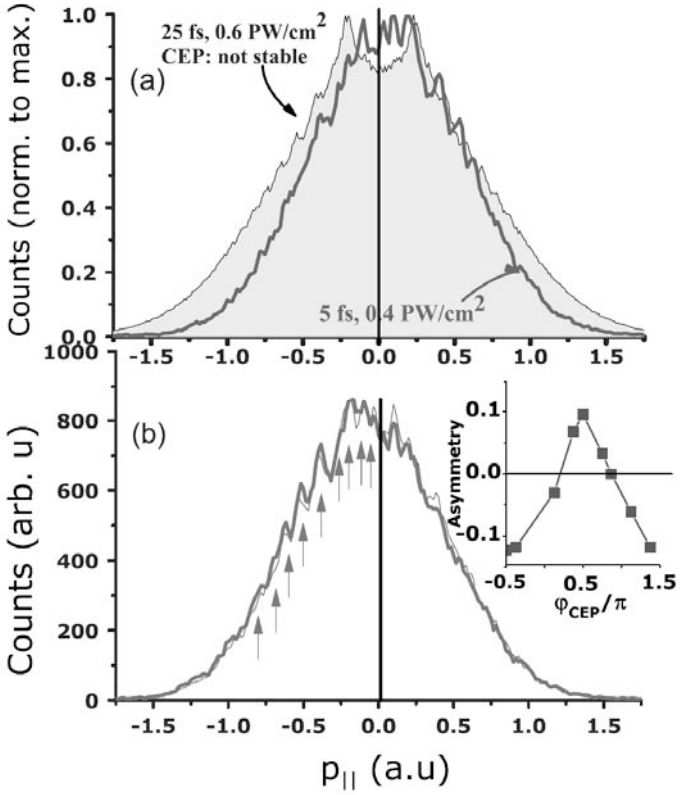

Figure 1: *(a) Recoil-ion (He^+) momentum distributions along the laser polarization axis for CEP with maximum asymmetry towards positive momenta and (b) neative momenta. Shaded curve: ion momentum distribution at a similar intensity but for longer, 25 fs pulses normalized to the integral under the blue line. The thin (blue) curve in (b) is a mirror image of the curve in (a). Inset: Momentum asymmetry as a function of the relative CE phase.*

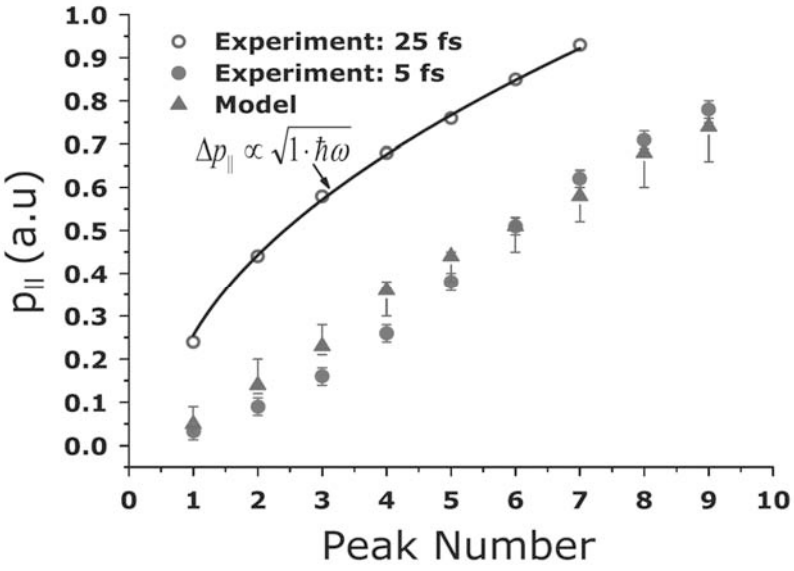

***Figure 2**: Positions of peaks in the parallel momentum $p_{\parallel}$ for 5 fs, 0.4 PW/cm^2 pulses at a phase of maximum asymmetry as extracted from Fig. 1 (red full circles). Blue open circles are from previous results for 25 fs, 0.6 PW/cm^2. The black curve simulates a square-root ATI-like behavior. Triangles represent the SFA model calculation.*

Acknowledgement:

We gratefully acknowledge numerous discussions with A. Voitkiv decisively helping in the interpretation of the data. We thank Ferenc Krausz and Karl-Ludwig Kompa for fruitful discussions and some specialized equipment. We are also grateful for support by the Max-Planck society and the DFG through the Emmy-Noether program and the Cluster of Excellence: Munich Center for Advanced Photonics.

Electrostatic Deflection of Polar Cluster Beams: Behavior of Deflection Profiles; HNO_3 Dissociation in Water Clusters

J. Bulthuis,[1], R. Moro[2], V. Kresin[3]

[1] *Vrije Universiteit, Amsterdam, <jaap.bulthuis@ext.vu.nl>*

[2] *Cameron University, Lawton, OK, <rmoro@cameron.edu>*

[3] *University of Southern California, Los Angeles, CA, <kresin@usc.edu>*

Deflection of free clusters and molecules by an inhomogeneous electric field is a tool that can provide important insight into their structural and electronic properties, often yielding information that cannot be easily accessed by other, e.g. spectroscopic, means. For this reason, the amount of experimental data has been growing in parallel with the theoretical effort to understand the correlation between deflection profile shapes and the inherent (susceptibility, structure, temperature) properties of the system in question (see, e.g., the review [1]).

The correlation in question is, however, nontrivial, because the field-induced orientation, alignment, and deflection of the beam are convoluted and frequently smeared out by rotational and vibrational motion of the particle. At the same time, the polarized ensemble usually passes the field region adiabatically, rather than becoming thermalized in it. This detail, which differs from the standard assumption in textbook treatments of electric susceptibilities, can lead to significant deviations from thermodynamic theory, to nontrivial dependencies on the symmetry and shape of the polar species. This realization needs to be taken into account for accurate interpretation of experimental data.

This contribution reports (1) on some theoretical aspects of deflection behavior of symmetric rotor systems, and (2) on an experimental study of $HNO_3(H_2O)_n$ cluster deflections with an eye towards evidence for molecular dissociation at a critical water cluster size.

1. Deflection and beam broadening of polar symmetric tops

Field-induced motion of rigid polar rotors possessing a symmetry axis is integrable, hence is amenable to the formulation of closed-form expressions for the trajectories (at least, in perturbation theory). As is known, polarization of a thermalized ensemble of dipoles in an external field leads to the Langevin-Debye formula which has a universal shape-independent form. For adiabatically deflected beams, though, one obtains expressions displaying a strong dependence on the asymmetry parameter (i.e., on the ratio of the rotational constants), both for the average deflection of the beam and for its broadening [2,3]. These analytical

expressions are found to be in good agreement with exact numerical calculations based on diagonalization of the rotational Hamiltonian with Stark-induced shifts and mixing.

A corollary to the demonstrated strong dependence of beam deflection parameters on the shape of the system is that if the latter factor is not taken into account, deductions from beam deflection experiments on polar systems may end up being quantitative erroneous.

2. Electric dipole moments of $HNO_3(H_2O)_{n=1-10}$ complexes studied by beam deflection

The electrostatic deflection method is applied to an experimental study of water clusters embedding a nitric acid molecule, $HNO_3(H_2O)_{n=1-10}$ [4]. The measured susceptibilities greatly exceed the electronic polarizability, revealing the contribution of permanent dipole moments (i.e., those of the host water molecules and of the acid impurity). Because of the fluxional nature of this system, it is possible to deduce the dipole moment values from the Langevin response equation.

The moments derived from the data are significantly higher than those of pure water clusters, see the figure. (However, they are considerably smaller than theoretically calculated dipole moments,, implying the need for theory to address the physical properties of this type of clusters at realistic finite temperatures, rather than near the lowest-energy configurations.)

There has been considerable interest in determining the minimal cluster size required for the dissociation solvated acid molecules. The enhancement in the dipole moment of $HNO_3(H_2O)_n$ for n=5,6 and a rise in cluster abundances setting in at n=6 suggest that the dissociation takes place in this size range.

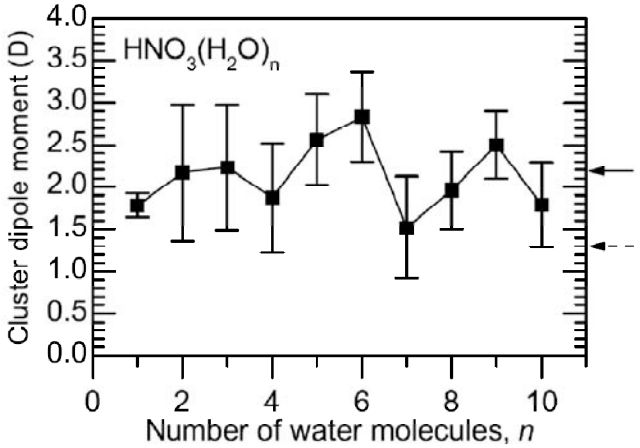

Electric dipole moments of mixed clusters derived from the deflection measurement. The dipole moment of the gas-phase nitric acid molecule is shown as the solid arrow and the dipole moment of pure water clusters is shown as the dashed arrow.

This work has been supported by the U.S. National Science Foundation.

References

[1] W. A. de Heer and V. V. Kresin, to appear in *Handbook of Nanophysics*, ed. by K. D. Sattler (CRC Press, 2010) [arXiv:0901.4810].
[2] J. Bulthuis, J. A. Becker, R. Moro, and V. V. Kresin, J. Chem. Phys. **129**, 024101 (2008).
[3] J. Bulthuis and V. V. Kresin, to be published.
[4] R. Moro, J. Heinrich, and V. V. Kresin, to be published.

Radical Propagation from Nucleobase to Sugar Moiety as a Model of Damage in DNA

L. Feketeová,[1,2,3] B. Chan,[1,4] L. Radom,[1,4] R. A. J. O'Hair[1,2,3]

[1] *ARC Centre of Excellence for Free Radical Chemistry and Biotechnology, Australia*

[2] *School of Chemistry, University of Melbourne, Victoria 3010, Australia, lfe@unimelb.edu.au*

[3] *Bio21 Institute of Molecular Science and Biotechnology, the University of Melbourne, Victoria 3010, Australia*

[4] *School of Chemistry, University of Sydney, NSW 2006, Australia*

Radicals play key roles in a wide range of reactions involving biomolecules such as proteins and DNA. Radicals are involved in DNA damage, e.g., via the direct effect of radiation such as ionization, and the indirect effect resulting in $H^{\bullet}$ and $OH^{\bullet}$ and carbon radicals derived from drugs. These may attack the nucleobases or the sugar moieties leading to DNA strand breaks. A number of mass spectrometry based methods have been developed to generate and study the properties of radicals derived from biomolecules. One that has been widely exploited in peptide radical ion formation involves the use of collision-induced dissociation (CID) of complexes of a metal with biomolecules, where the reduction of the metal, i.e. an electron transfer reaction, and subsequent fragmentation, may result in the formation of radical cations of the biomolecules [1,2]. There we show that this method can be extended to the formation of the deoxyguanosine (dG) – deoxycytidine (dC) radical cation ($[dGdC]^{\bullet+}$). This result is important since $(dGdC)^{\bullet+}$ represents a simple model for radical cation formation in the complimentary base pairs found in DNA. The investigation of dissociation of this radical dimer has revealed a radical migration. Thus, it is possible that radical damage to the nucleobase can propagate to the sugar backbone, leading to the cleavage of the DNA strand. Further experimental and theoretical studies have been implemented in order to understand this mechanism.

Experiment and Theory

The experiments have been performed using a Finnigan LTQ-FT mass spectrometer, which consists of an electrospray ionization (ESI) source coupled to a linear ion trap, ion transfer optics and Fourier Transform (FT) ion cyclotron resonance (ICR) cell [3]. Briefly, ESI of solutions of copper (II) nitrate and nucleosides generated a series of doubly charged complexes. Complexes of the form $[Cu(AB)_2]^{2+}$, where A = dG and B = dC or 5-fluoro-deoxycytidine (FdC), were transferred into the linear ion trap and subjected to CID in the He bath gas at room temperature. CID of the complexes yielded the $(dGdC)^{\bullet+}$ and $(dGFdC)^{\bullet+}$ radical cations. Dissociation of these dimers was further investigated in the ion trap using

CID. All ions were transferred to the FT-ICR cell for high-resolution mass analysis. We have also used computational quantum chemistry calculations with the Gaussian 03 package to investigate the dissociation mechanisms of these radical dimers.

Results

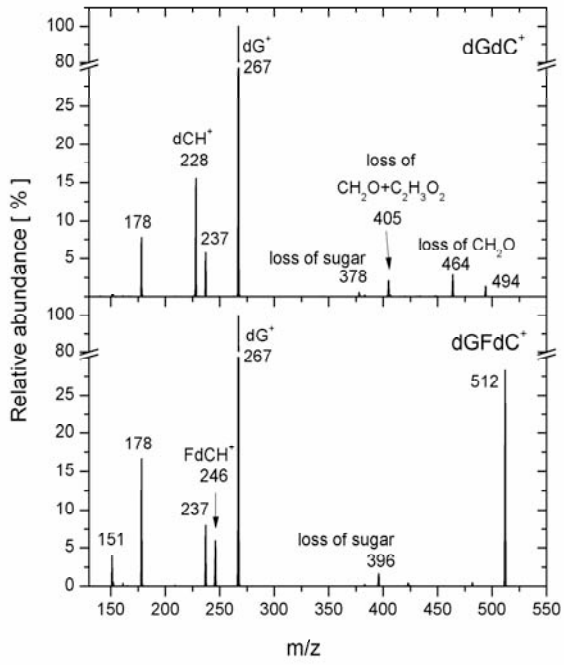

Figure 1: *CID of* $(dGdC)^{\bullet+}$ *m/z=494 and* $(dGFdC)^{\bullet+}$ *m/z=512 radical cations, upper and lower panel, respectively.*

The gas phase chemistry of the base paired dimer $(dGdC)^{\bullet+}$ was examined in detail. The upper panel of Figure 1 shows the CID mass spectrum of this dimer. Three main types of fragmentation reactions were observed: (i) monomer loss to form the radical cation of dG at *m/z*=267; (ii) monomer loss coupled with proton transfer to form protonated dC at *m/z*=228; (iii) radical induced sugar fragmentation from the dG site, i.e. loss of CH_2O (*m/z*=464) and further loss of $C_2H_3O_2$ (*m/z*=405). The breakage of the N-C bond between the nucleobase and sugar was also observed to a small extent.

The formation of the radical cation $dG^{\bullet+}$ was observed directly in the ESI, as well as in the dissociation of the $Cu(dG)_3^{2+}$ complex. Both $dG^{\bullet+}$ radical cations dissociate predominantly into the guanosine (G) radical cation $G^{\bullet+}$, see Figure 2 upper panel. However, if radical cation $dG^{\bullet+}$ is formed from the dissociation of the radical dimer $(dGdC)^{\bullet+}$ or $(dGFdC)^{\bullet+}$ (see Figure 1), its further fragmentation shows damage of the sugar moiety through observation of the loss of CH_2O and $C_2H_3O_2$ as depicted in Figure 2 lower panel. This shows that the radical cation $dG^{\bullet+}$ has a different structure after the dissociation of the radical dimer.

In order to obtain further insight into the fragmentation mechanism, we compared the fragmentation of $(dGdC)^{\bullet+}$ radical dimer with a fluorinated analogue $(dGFdC)^{\bullet+}$, where the reduced basicity of FdC should inhibit the proton transfer [4]. The fragmentation of the $(dGFdC)^{\bullet+}$ is shown in Figure 1, lower panel. One can see that the proton transfer to FdC is

indeed inhibited. The resulting product $FdCH^+$ at *m/z*=246 is less abundant than dCH^+ at *m/z*=228 in the case of $(dGdC)^{\bullet+}$. Thus, the fragmentation of $(dGFdC)^{\bullet+}$ results mainly in the FdC monomer loss to form radical cation $dG^{\bullet+}$ and its complimentary fragments at *m/z*=237, 178 and 151. The breakage of the N-C bond between the nucleobase and sugar is also observed at *m/z*=396 (see Figure 1b). Fragments corresponding to induced damage of the sugar were also detected, though with less than 1.5% relative abundance. This finding suggests that the proton transfer and radical propagation from guanine base to its sugar moiety are connected.

Computational quantum chemistry calculations are under way to investigate the energetics and details of the radical migration. Preliminary results show that the radical dimer ejects CH_2O more easily than the $dG^{\bullet+}$ radical cation on its own. Further results and their implications will be presented.

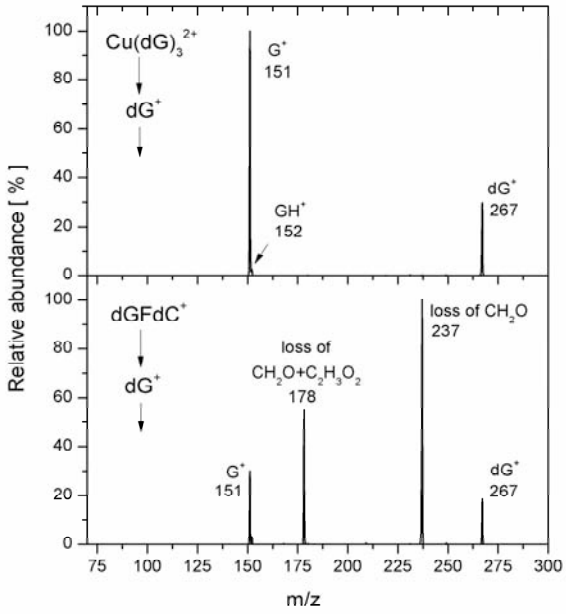

Figure 2: *CID of $dG^{\bullet+}$ (m/z=267) radical cation formed from $Cu(dG)_3^{2+}$ complex and from $(dGFdC)^{\bullet+}$ dimer, upper and lower panel, respectively.*

Conclusion

The gas phase mass spectrometry and computation quantum chemistry data are consistent with current models for damage in DNA, whereby initial ionization at the guanine sites is followed by proton transfer and/or strand breaks.

References

[1] J.Y. Ke, U.H. Verkerk, P.Y.I. Shek, A.C. Hopkinson, K.W.M. Siu, J. Phys. Chem. B 110 (2006) 8517.
[2] P. Cheng, D.K. Bohme, J. Phys. Chem. B 111 (2007) 11075.
[3] L. Feketeová, G. N. Khairallah, R. A. J. O'Hair, Eur. J. Mass Spectrom. 14 (2008) 107.
[4] A. K. Gosh, G. B. Schuster, J. Am. Chem. Soc. 128 (2006) 4172.

"Non-Statistical" Behaviour in the Symmetric Electron Transfer Reactions of Dications Explained: CO_2^{2+} + CO_2 and O_2^{2+} + O_2

Price SD,[1], Lockyear JF[1], Parkes MA[1], Schröder D[2], Roithová J[23] and Herman Z[4]

[1] *University College London, Department of Chemistry, 20 Gordon Street, London, WC1H 0AJ, UK*

[2] *Institute of Organic Chemistry and Biochemistry, Academy of Sciences of the Czech Republic, Flemingovo nám. 2, 166 10 Prague 6, Czech Republic*

[3] *Department of Organic Chemistry, Faculty of Sciences, Charles University in Prague, Hlavova 8, 12083 Prague 2, Czech Republic*

[4] *J. Heyrovsky Institute of Physical Chemistry, V. Cermak Lab., Academy of Sciences of the Czech Republic, Dolejskova 3, 18223 Prague 8, Czech Republic*

Simulations have recently revealed that molecular doubly-charged ions (dications) may be important in the chemistry of a variety of planetary ionospheres, such as those of Mars and Titan [1-3]. These simulations have stimulated an upsurge of interest in the bimolecular chemistry of dications, an upsurge due also in part to the development of new experimental techniques to study these exotic species. These experiments have revealed that dications exhibit a unique and varied bond-forming chemistry in collisions with neutral molecules [4-9]. However, the cross-sections for these bond-forming processes are often small, and the dominant reactive channel in dication-molecule encounters is usually single-electron transfer. Thus, one would expect such single-electron transfer process to be a key pathway through which dications can influence ionospheric composition. In such ionospheric environments the single-electron transfer of a molecular dication of a dominant atmospheric molecule, such as CO_2^{2+} on Mars, with the corresponding neutral (CO_2) will be key processes.

Recent guided ion beam studies of the dissociative single-electron transfer reactions of CO_2^{2+} with CO_2:

$$^{13}CO_2^{2+} + CO_2 \rightarrow {}^{13}CO_2^{+*} + CO_2^{+} \rightarrow {}^{13}CO^{+} + O + CO_2^{+}$$
$$\rightarrow O^{+} + {}^{13}CO + CO_2^{+}$$

revealed that the CO_2^{+} monocation formed form the dication by electron capture (the *capture* monocation) was far more likely to fragment that the CO_2^{+} ion formed by ejection of an electron from the neutral (the *ejection* monocation) [10]. This observation is surprising as the similar geometries of the dication and neutral mean that very similar Franck-Condon factors should govern the capture and ejection processes. Hence, one would expect the same states to be populated in the capture and ejection processes and, hence, one would expect similar behaviour of the ejection and capture monocation. This prediction has, perhaps

inappropriately, been termed *statistical behaviour*; a term meant to imply that the behaviour of the ejection and the capture monocations should be indistinguishable. Our experiments show this is clearly not the case.

To account for the surprising observation of the different behaviour of the capture and ejection monocations two hypotheses have been advanced:
Firstly, that electronic structure considerations favour the capture process, from the triplet ground state of CO_2^{2+}, populating dissociative quartet states of the CO_2^+ ion. Such quartet states are less readily populated in the ejection process as their population involves two-electron transitions.
Secondly, the preferential dissociation of the capture monocation might result from the increased vibrational temperature of this reactant ion, which is formed by electron ionization. In contrast the neutral reactant will have a thermal vibrational distribution, and thus form product monocations which are vibrationally colder and less prone to dissociation.

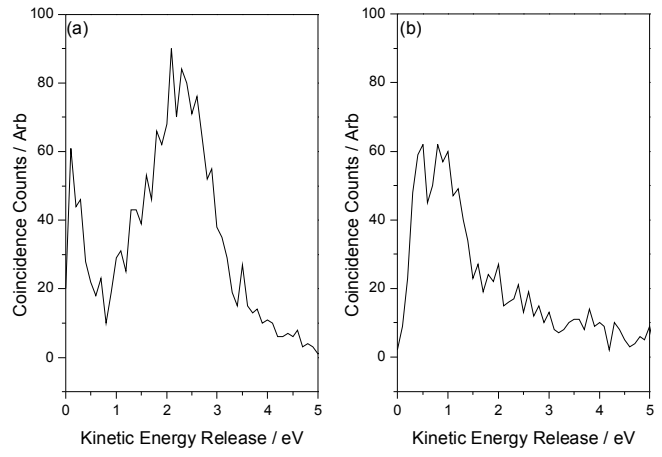

Kinetic energy release distributions for the dissociation of (a) $^{16}O_2^+$ (the ejection ion) and (b) $^{18}O_2^+$ (the capture ion) in the internal frame of reference into O^+

This contribution presents the results of a detailed study of electron transfer in the CO_2^{2+}/CO_2 and O_2^{2+}/O_2 collision systems using the position-sensitive coincidence (PSCO) methodology [4]. This technique involves the detection in coincidence of the pair of monocation products from a dication/neutral reaction. These experiments are a powerful probe of the energetics and dynamics of dication reactions. The O_2^{2+}/O_2 collision system has been carefully selected for study because the two hypotheses, presented above, to account for the preferential dissociation of the capture CO_2^+ in the CO_2^{2+}/CO_2 collision system predict different outcomes for the O_2^{2+} + O_2 reaction. Specifically, the ground state of the O_2^{2+} ion is a singlet state, and electron capture by this species cannot populate the dissociative states of O_2^+ *via* one-electron transitions. However, such dissociative states of O_2^+ can be populated directly by electron

ejection from O_2. Thus, one would predict, if electronic transition probabilities are at the heart of this phenomenon, that in the O_2^{2+}/O_2 system preferential dissociation should occur for the ejection dication.

Our PSCO experiments clearly show that indeed it is the ejection dication that dissociates in the dissociative single electron transfer reactions of O_2^{2+} with O_2 and reveal in detail the electronic states involved in these fundamental processes. For example, we clearly see that the favoured dissociation of the ejection O_2^+ arises from population of the *B* state, whilst the few capture ions that do dissociate are populated in high vibrational levels of the *b* state. For CO_2^{2+} reacting with CO_2 the PSCO experiments allow us to readily account for the preferential dissociation of the capture monocation and also the variation in the branching in the dissociation of the capture and ejection ions between $CO^+ + O$ and $O^+ + CO$. In summary, these experiments resolve a highly topical debate, and reveal a detailed state-resolved picture of these important fundamental reactions, showing that electron transition probabilities are key in determining the fate of the product ions.

The collaboration involved in this study was supported by the Royal Society by the provision of a International Programmes Award.

References

[1] O. Witasse *et al.*, *Geophys. Res. Lett.* (2002) **29** 1263.
[2] J. Lilensten *et al.*, *Geophys. Res. Lett.* (2005) **32** L03203.
[3] G. Gronoff *et al.*, *Astron. Astrophys.* (2007) **465** 641.
[4] S. D. Price, *Int. J. Mass Spectrom.* (2007) **260** 1.
[5] Z. Herman, *Int. Rev. Phys. Chem.* (1996) **15** 299.
[6] J. Roithova *et al.*, *J. Phys. Chem. A* (2003) **107** 7347.
[7] D. Ascenzi *et al.*, *Phys. Chem. Chem. Phys* (2008) **10** 7121.
[8] P. Tosi *et al.*, *Phys. Rev. Lett.* (1999) **82** 450.
[9] W. Y. Lu *et al.*, *J.Chem.Phys.* (2000) **112** 4648.
[10] C. L. Ricketts *et al.*, *Phys.Chem.Chem.Phys.* (2008) **10** 5135.

Delayed Asymmetric Coulomb Fission in Size-selected Molecular Dication Clusters

Xiaojing Chen, Guohua Wu and Anthony J. Stace
School of Chemistry, University of Nottingham, University Park, Nottingham NG7 2RD, UK.

During the past 30 years considerable experimental effort has been devoted to an ongoing search for evidence of spontaneous or metastable Coulomb fission in multiply charged clusters [1-4]. Such experiments have explored a range of systems covering most of the rare gases through to clusters containing molecules as large as SF_6 and benzene [1]. Whilst there has been good evidence of delayed unimolecular dissociation in triply and quadruply charge clusters [1], confirmation of similar behaviour on the part of either atomic or molecular dication clusters has not be forthcoming. The only demonstration of Coulomb fission on the part of molecular dication clusters has come from processes promoted by collisional activation [2,3]. However, very recent experiments on metal dication complexes have shown that electron capture from a collision gas, even at very low pressures, can play a significant role in the fragmentation of these ions [5]. The very high cross section for electron capture at keV kinetic energies, particularly with O_2 and N_2 as collision gases, results in considerable interference and confusion between electron capture-induced dissociation and Coulomb fission. Fragments previously assigned as the products of Coulomb fission have subsequently been shown to correspond to the products of reactions induced by electron capture [6,7].

Evidence of metastable Coulomb fission in metal/molecule dication complexes, such as $[Cu(H_2O)_6]^{2+}$, has been found recently [7]; however, metal dications are a special case because the delay in fragmentation is created by the timescale for charge transfer from the metal to a molecule. When in solution, the charge on Cu^{2+} can be expected to remain localised on the metal, however, there is a minimum to the number of solvent molecules required to stabilise the ion and once below that number there is a high probability that charge transfer will occur. For Cu^{2+} stabilisation is achieved with eight water molecules [6,7]. For pure atomic and molecular cluster ions the circumstances are very different. There is a minimum size below which the ions are unstable, but this time that number is very much larger than is observed for the metal dication complexes. The reason for this is that in molecular dications the charges occupy separate sites and it is the strength of the intermolecular interactions that determines stability. Thus, for Ar_N^{2+} the minimum value observed for N is 91 and for $(H_2O)_NH_2^{2+}$ the value is 35, which reflects the difference in strength between van der Waals interactions and hydrogen bonds [1].

Presented here are new results from a series of experiments in which it has been possible to take molecular dication clusters of a single size and record events arising from their metastable Coulomb fission. A detailed description of the apparatus used for generation,

resolution and detection of the cluster ions has been given elsewhere [3]. Briefly, neutral clusters of ammonia were formed via the adiabatic expansion of an ammonia/argon mixture (1:99) through a 200 μm diameter pulsed supersonic nozzle. After passing through a 1 mm diameter skimmer, the clusters entered the ion source of a high resolution, double focussing mass spectrometer (VG ZAB-E) where they were ionised by electron impact with 70 eV electrons. Ions were extracted from the source with an accelerating potential of 5 kV and passed through a magnetic sector where they were selected according to their m/z value. They then entered a field-free region approximately 1.5 m in length and approximately 10^{-4} s after their formation. The time spent by the cluster ions passing through this region, *ca.* 5×10^{-5} s, was sufficiently long for some of them to undergo a range of metastable (unimolecular) and internal bimolecular chemical reactions. Fragments arising from metastable decay were identified by scanning an electrostatic analyser in the form of a MIKE (Mass-analysed Ion Kinetic Energy) scan. Scans performed on doubly charged ions with an initial kinetic energy of 10 keV made the detection and verification of fragment ions resulting from metastable Coulomb fission very straightforward, since the only fragments seen at laboratory-frame kinetic energies of between 5 and 10 keV are the products of charge reduction. Metastable decay processes were typically recorded with a background pressure in the flight tube of ~ 5 x 10^{-8} mbar therefore, interference from collision-induced processes, such as electron capture, were minimise. As a result, ions arising from charge reduction *via* Coulomb fission could be detected at very high sensitivity against an extremely low background signal.

Previous experiments of this nature have shown that for hydrogen bonded molecular clusters several types of doubly charged ion are observed [8,9], and for ammonia these take the form: $(NH_3)_N^{2+}$, $(NH_3)_N H^{2+}$, and $(NH_3)_N H_2^{2+}$ [9]. With reference to the minimum size of cluster that can support two charges, that value has been reported as $N = 51$ (see below) for each of the ammonia cluster ions given above. Therefore, a search has been undertaken for evidence of metastable fragmentation on the part of each of the above cluster ions at specific values of N that were very close to this critical size. Figure 1 shows examples of metastable fragmentation recorded for $(NH_3)_{52}H_2^{2+}$ and where it can be seen that the decay pattern is very asymmetric. For this particular example fragmentation takes the form:

$$(NH_3)_{52}H_2^{2+} \rightarrow NH_4^+(NH_3)_{52-K-2} + NH_4^+(NH_3)_K$$

where K ranges from 9 – 14. The fragment detected is the heavier $NH_4^+(NH_3)_{52-K-2}$ ion. Probably because of a much higher degree of instrumental discrimination, no evidence of the lighter fragment could be found. As can be seen, each peak has the shape characteristic of a Coulomb explosion process, where ions with high centre of mass kinetic energies that would have contributed to the centres of the profiles have been discriminated against by their failure to pass through the apparatus to the detector. The features that are visible correspond to

fragment ions that have been scattered either forward or backward with respect to trajectories taken by the centres of mass of the cluster ions.

Results similar to those given in figure 1 have been recorded for each of the different types of cluster ion identified above and for $N = 51 - 55$. For $N > 55$ no evidence could be found for Coulomb fission and at $N = 50$, features very similar to those shown in figure 1 have been recorded but no assignment has yet been possible. Across the series $N = 51 - 55$ a general trend is for slightly larger values of K to be favoured as N increases. However, expressed as a fraction K/N the trend is for this ratio to decrease with N. It is quite possible that these effects are as a consequence of the metastable time window open to each ion of a different size.

The number given below each peak is the average kinetic energy release, $<\varepsilon_t>$, calculated from the FWHM for each of the profiles. Although the values fluctuate, a general trend across all the data recorded so far is for $<\varepsilon_t>$ to decrease as K increases. Results similar to those given in figure 1 have also been recorded for $(H_2O)_N^{2+}$, $(H_2O)_N H_2^{2+}$, $(C_6H_6)_N^{2+}$, and $(CH_3CN)_N^{2+}$ cluster ions and where similar evidence of asymmetric fragmentation is seen. A model derived from a classical electrodynamic analysis of separating dielectric spheres is currently being explored as a means of interpreting the results. A similar, but much simpler image charge model has previously been used to interpret Coulomb fission fragmentation patterns in the electrospray process [10].

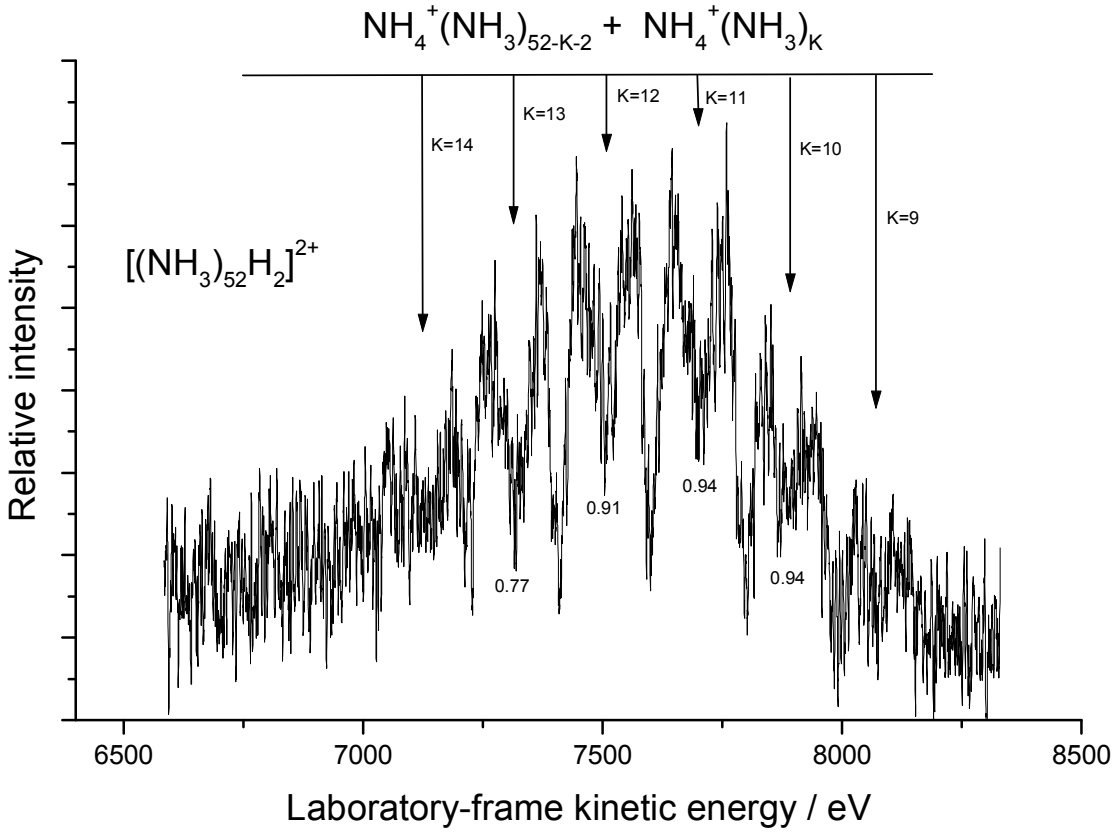

Figure 1. Coulomb fission fragmentation pattern recorded for $(NH_3)_{52}^{2+}$.

References

[1] O. Echt *et al*, Phys. Rev. A **38**, 3236 (1988).
[2] N. G. Gotts and A. J. Stace, Phys. Rev. Lett. **66**, 21 (1991).
[3] N. G. Gotts *et al*, J. Chem. Phys. **96**, 408 (1992).
[4] I Mähr *et al*, Phys. Rev. Lett. **98**, 023401 (2007).
[5] B. Wu *et al*, J. Phys. Chem. A, **110**, 8423 (2006).
[6] A. J. Stace *et al*, J. Am. Chem. Soc., **119**, 10239 (1997).
[7] B. J. Duncombe *et al*, J. Phys. Chem. A **111**, 5158 (2007).
[8] A. J. Stace, Phys. Rev. Lett., **61**,306 (1988).
[9] M. T. Coolbaugh *et al*, Chem. Phys. Lett., **156**, 19 (1989).
[10] M. Labowsky *et al*, Anal. Chim. Acta, **406**, 105 (2000).

Contributed Papers

Poster Session

Synchrotron-Based High Resolution Infrared Spectroscopy of Naphthalene ($C_{10}H_8$): Rovibrational Analysis of the ν_{46} Band

S. Albert[1], K.K. Albert[1], Ph. Lerch[2] and M. Quack[1]

[1] *Physical Chemistry, ETH Zurich, CH-8093 Zurich, Switzerland*

[2] *Swiss Light Source, Paul-Scherrer-Institute, CH-5232 Villigen, Switzerland*

Abstract

We report a rotationally resolved analysis of the high resolution FTIR spectrum of the simplest Polycyclic Aromatic Hydrocarbon (PAH), naphthalene. The spectrum has been measured with a new high resolution FTIR spectrometer connected to the Swiss Light Source (SLS) at the Paul-Scherrer-Institute (PSI). Due to the high brightness of the synchrotron radiation in the spectral region of interest and the high resolution of the new interferometer, it was possible to record the rotationally resolved infrared spectrum of naphthalene and to analyse the ν_{46} band (ν_0 = 782.330753 cm^{-1}). The results are discussed in relation to the Unidentified Infrared Band (UIB) found in interstellar spectra at 11.25 μm.

1. Introduction

Our current high resolution FTIR technology now makes it possible to explore the spectroscopy and dynamics of large carbon ring systems of aromatic and non-aromatic character, in particular in the THz region. The FTIR experiment uses a synchrotron radiation source, which is effectively at least up to 10 times brighter than light emitted by conventional thermal sources in this spectral region, and a highly resolving interferometer with a maximum optical path difference (MOPD) of 11.20 m and an instrumental band width of about 20 MHz [1]. We have started using this set-up to investigate the spectra of aromatic and saturated carbon ring systems, in particular the spectra of PAHs. These PAHs are proposed in the literature [2,3] as the source of the Unidentified Infrared Bands (UIBs). The simplest PAH is naphthalene ($C_{10}H_8$), strictly bicyclic, which has already been analysed at high resolution in the UV region [4,5] and in the IR region [6-8]. We present an analysis of the out-of-plane mode ν_{46} of naphthalene at 12.78 μm which includes more than 3000 absorption lines. Based on the rotational constants, we have simulated the band at resolutions which are used for the interstellar detection of the UIBs. Clearly, this band is not responsible for the UIB at 11.25 μm [7]. However, the shape of the recorded naphthalene band, ν_{46}, provides valuable insights into the shape of bands of out-of-plane modes of PAHs. As a comparison we have also recorded the IR spectrum of the saturated carbon ring compound, cyclohexane, in this region. Cyclohexane has two bands at 11.58 μm and at 11.04 μm, in which the band shapes, in terms of intensity distribution, are completely different from that of the ν_{46} band of naphthalene.

2. Experimental

We have interfaced a new FTIR spectrometer, the Bruker IFS125 prototype 2009, to the infrared port available at the Swiss Light Source (SLS). This spectrometer has a MOPD of 11.20 m and is a further development of our IFS125 prototype 2001 [9,10] (MOPD of 10 m). Due to the high brightness of the synchrotron radiation in the spectral region of interest, we can use apertures as small as 0.8 mm to apply the full resolution of our interferometer, which is on the order of 20 MHz. The FTIR spectrum of naphthalene was recorded at 295 K in the region 600-900 cm^{-1} with a resolution of 25 MHz (0.0008 cm^{-1}), which is less than the Doppler width of the molecule in this spectral region. Sample pressures of 0.05 to 0.2 mbar were used. The room temperature spectra were recorded in a White-type cell with path lengths up to 19.6 m. 250 scans were co-added and the spectrum was calibrated using OCS as the wavenumber standard.

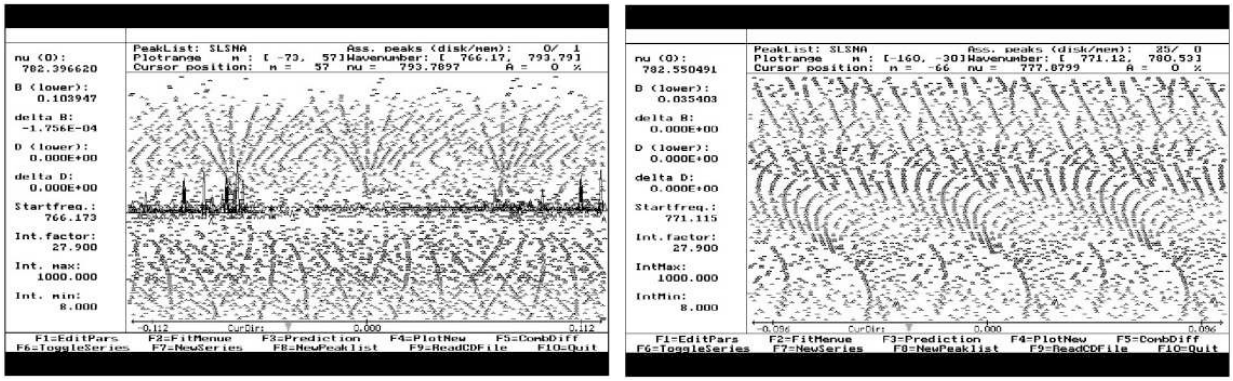

***Figure 1**: LW plot of the c-type transitions in the P and R branches. The different K_c series are visible. The quantum number J is plotted versus A (left) and versus (B+C)/2 (right).*

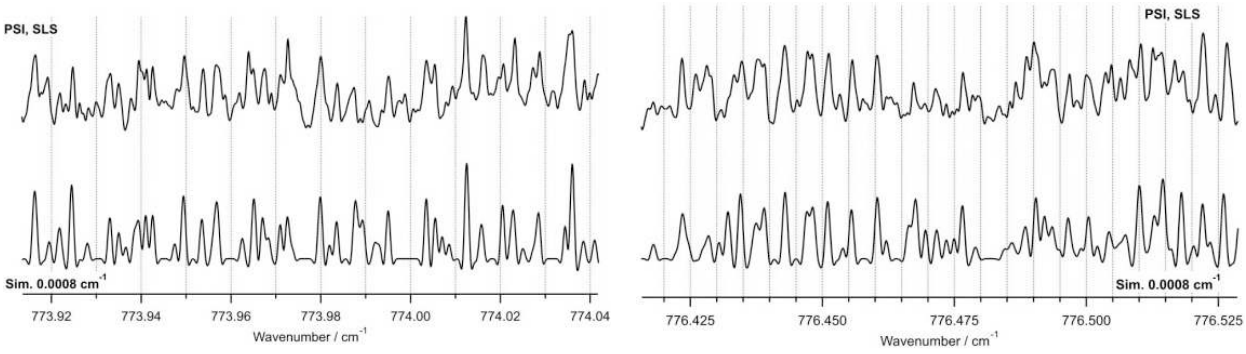

***Figure 2**: A comparison of small parts of the measured P branch c-type lines of the out-of-plane band ν_{46} of naphthalene (top trace: observed spectrum, T = 295 K, path length = 9.6 m) with a simulation of naphthalene (bottom trace: resolution = 0.0008 cm^{-1}).*

3. Analysis and discussion

Naphthalene is of symmetry D_{2h} and has 48 normal modes. Only modes with b_{1u}, b_{2u} and b_{3u} symmetry are infrared active. These generate *a*-type, *b*-type and *c*-type bands, respectively. The ν_{46} band is of b_{3u} symmetry and shows *c*-type transitions in the spectrum. The spin statistical weights for each line (K_a, K_c) are ee:eo:oe:oo = 76:60:60:60. The assignment of the observed rovibrational transitions belonging to a particular subband consisting of P and R branches has been carried out efficiently with an interactive Loomis-Wood assignment program previously designed for linear molecules [11]. The *c*-type bands were identified as P and R branches up to $J < 95$, $K_a < 44$ and $K_c < 66$ as illustrated in Figure 1. The different *c*-type series are clearly visible in the LW plots and are grouped into three groups as shown in Figure 1 (left). The rovibrational analysis was carried out with Watson's *A* reduced effective Hamiltonian in the III^r representation up to sextic centrifugal distortion constants using the WANG program described in [12]. The spectroscopic constants of the ν_{46} band of naphthalene were fitted according to the *A* reduction resulting in a standard deviation of d_{rms} = 0.000327 cm^{-1}. The spectroscopic constants for the ground state were fixed to the values given in [5]. No perturbation was observed despite the large density of states. Comparisons between the experimental spectrum and a simulation of the ν_{46} band are shown in Figure 2. The agreement between simulated and experimental spectra is very good considering the large number of hot bands. The hot band structure is clearly visible in the Q branch region (Figure 3). By means of the simulation, the position of the band center is well determined, as the enlargement in Figure 3 (left) illustrates.

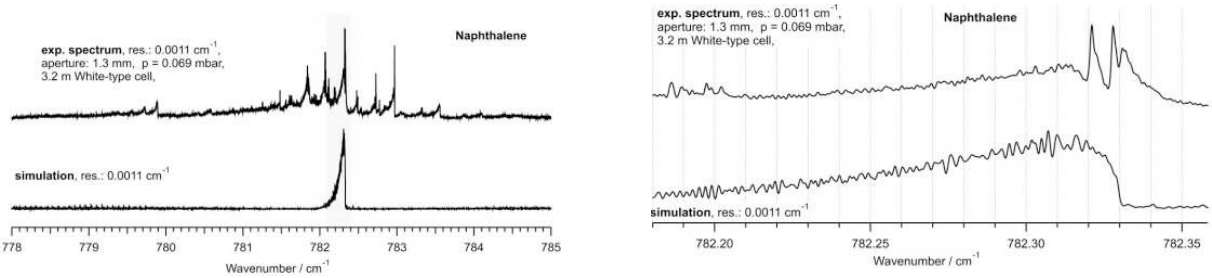

***Figure 3 (left)**: A comparison of the Q branch region of the out-of-plane band ν_{46} of naphthalene. Hot bands are visible. **Right**: Enlargement of the central Q branch region.*

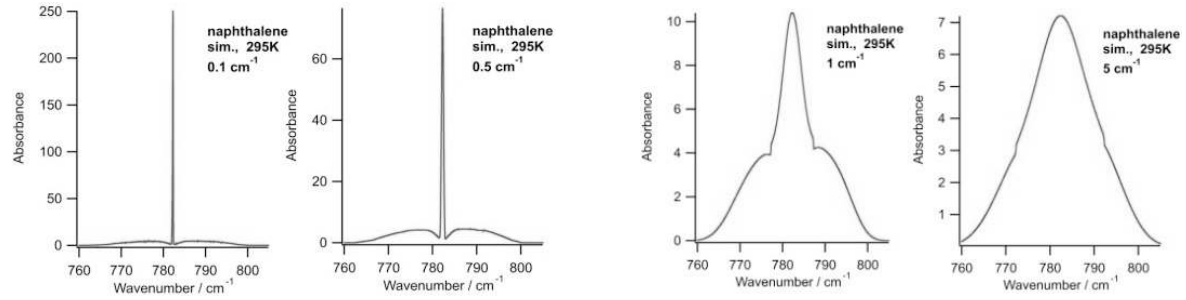

Figure 4: Simulated out-of-plane band ν_{46} of naphthalene at different resolutions (T = 295 K).

The ν_{46} band is the strongest band of naphthalene. If one wants to detect naphthalene in interstellar space, one must search for this band at 782.33 cm^{-1} (12.78 μm). This band has *c*-type character which can be seen in the very strong Q branches dominating the spectrum. These strong Q branches are very characteristic for the out-of-plane modes of aromatic systems. Normally, the UIBs are described as Lorentzian shape bands. If we simulate the ν_{46} band (out-of-plane) of naphthalene with a resolution of 5 cm^{-1} we obtain a similar shape, as shown in Figure 4. In order to make a first assignment of the UIBs we propose recording these bands at slightly higher resolution by astronomical spectroscopy. As shown in Figure 4, a simulation with a resolution of 1 cm^{-1} already illustrates the typical *c*-type character of this band with the prominent Q branch. If the UIB at 11.25 μm is of *a*-type or *b*-type character, which could be tested by obtaining higher resolution spectra as discussed, then an even stronger *c*-type band of an out-of-plane bending mode of a PAH, if any, would be expected at lower energy.

4. Conclusions

We have rovibrationally resolved the infrared spectrum of naphthalene at room temperature using very high resolution FTIR spectroscopy in combination with synchrotron radiation. We were able to analyse the spectrum in the ν_{46} region. We determined the spectroscopic constants of the ν_{46} state for the first time. We have simulated the spectrum at different resolutions based on these constants. If the UIB at 11.25 μm results from a PAH, it is likely to be a *c*-type band because these are the strongest absorption bands of aromatic systems in this spectral region. The *c*-type band is easy to identify through its strong Q branch, which should be visible with a resolution of 1 cm^{-1}. The numerous hot bands do not disturb this general feature. They only make the spectrum in the Q branch region asymmetric.

Acknowledgment

Our work is supported financially by the Schweizerischer Nationalfonds and ETH Zürich.

References:

[1] S. Albert, *21st Colloquium on High Resolution Molecular Spectroscopy, Castellammare di Stabia, Italy, 31.8-4.9.2009*, p. 129, E1.
[2] L.J. Allamandola, A.G.G.M. Tielens and J.R. Baker, *Astrophys. J.* **290**, L25 (1985).
[3] A.G.G.M. Tielens, *Annu. Rev. Astron. Astrophys*. **46**, 289 (2008).
[4] W.Majewski and W.L. Meerts, *J. Mol.Spectrosc*. **104**, 271 (1984).
[5] M.H. Kabir, S. Kasahara, W. Demtroeder, Y. Tatamitani, A. Doi, H. Kato and M. Baba, *J. Chem. Phys*. **119**, 3691 (2003).
[6] O. Pirali, M. Vervloet, G. Mulas, G. Malloci, C. Joblin, *Phys. Chem. Chem. Phys*. **11**, 3443, (2009)
[7] S. Schlemmer, D.J. Cook, J.A. Harrison, B. Wurfel, W. Chapman and R. Saykally, *Science* **265**, 1686 (1994).
[8] K.B. Hewett, M. Shen,C.L Brummel and L.A. Philips, *J. Chem. Phys*. **100**, 4077 (1993).
[9] S. Albert, K. K. Albert, and M. Quack, *Trends in Optics and Photonics* **84,** 177 (2003).
[10] S. Albert and M. Quack. *ChemPhysChem* **8**, 1271 (2007).
[11] S. Albert, M. Winnewisser, B.P. Winnewisser, *Ber. Bunsen-Ges*. **100**, 1876 (1996).
[12] D. Luckhaus and M. Quack, *Mol. Phys*. **68**, 745 (1989).

Synthesis and Concomitant Solvation of Hydrazine Anions upon Low-Energy Electron Attachment to Ammonia Doped Helium Nanodroplets

A. Aleem, T. D. Märk and P. Scheier

Institut für Ionenphysik und Angewandte Physik, Universität Innsbruck, Technikerstraße 25, A-6020, Innsbruck, Austria. E-mail: Muhammad.Aleem@uibk.ac.at

Abstract

The phenomenon of electron attachment and solvation in polar molecule ammonia has inspired the study to further investigate this complex chemical reaction. Ultracold clusters of ammonia are formed via pickup of NH_3 molecules into superfluid He nanodroplets. Electron attachment to ammonia doped helium nanodroplets supports chemical reactions forming complexes of the form $(NH_3)_n{\cdot}N_2H_4^-$. A redshift of the threshold energy for the formation of these complexes is observed and can be assigned to solvation effects of the ammonia molecules surrounding the hydrazine anion core.

Introduction

Ammonia is an important substance for engineering applications such as plasma reactors of the waste treatment or the plasma surface treatment. The outer planets and comets are also consisting of much ammonia. NH_3 is supposed to taking part in the synthesis of larger organic molecules in the interstellar medium, especially molecules relevant for life, i.e., amino acids and DNA bases [1,2]. The formation of the amino acids upon irradiation of ice, containing ammonia and other simple molecules, with UV light and high-energy electrons has been reported [2].

The individual NH_3 molecules can not bind an excess charge but their association does make it possible [3]. A free electron can be trapped by solvent reorientation in polar solvents such as ammonia or water [4]. These solvated electrons form a cavity due to Pauli Exclusion of the excess electron by the valence electrons of the ammonia[5]. Both Haberland and Kondow determined the minimum size of ammonia cluster anions to be n = 35 for $(NH_3)^-_n$ and n =41 for $(ND_3)^-_n$. Photoelectron spectra of $(NH_3)^-_{n\ =41\text{-}1100}$ have been recorded using 2.54eV photons. The vertical detachment energies in this size range are linear with $n^{-1/3}$ and extrapolate to a value for n = ∞ that is very close to the measured photoelectric threshold energy of the condense phase ammoniated electrons [3].

Femto second photoelectron spectra plotted as two-dimensional contour plots of electron kinetic energy versus pump-probe delay time manifests the temporal behavior of the electron and anion solvation [4]. More promised, consistent and coherent experimental studies are

required to fully grasp the understanding and unravel the electron solvation in ammonia. We report in this contribution the novel method of cluster formation by doping ammonia molecules in helium nanodroplets at 0.37K. Ammonia cluster anions maintain this temperature by evaporation of helium. Further the evolution of ammonia cluster anions is recorded as a function of the kinetic energy of the projectile electron.

Experimental

Since the main parts of the experimental set-up have already been described in our previous contributions [6,7], a brief overview is presented here. The helium droplets are formed by supersonic expansion of high-pressure (30 bar), high-purity helium gas (>99.9999%), which flows through a 5μm aperture into vacuum. Before expansion, the gas is also cleaned and pre-cooled by a liquid-nitrogen cold trap and cooled down to 12K by a closed cycle helium cryostat. The pressure in the chamber where expansion takes place is kept below10^{-2} Pa by a 1200 l/s turbo-molecular pump. Under these conditions, the average droplet size is expected to be several 10^4 atoms [8]. The flow of the helium droplets and He gas emerging from the aperture is skimmed 10mm downstream to block most of the He gas while letting through the inner, colder part of the expansion plume. The unperturbed central beam of helium droplets then passes into another vacuum chamber. High purity ammonia gas is introduced via needle valves into the vacuum chamber. Ammonia (purity 99.95%) is introduced into the differentially pumped pickup chamber. Optimum conditions are obtained for a dopant pressure between 10^{-3} and 2×10^{-3} Pa. After the passage through a second skimmer, the helium droplets enter another vacuum chamber where they intersect an electron beam of a Nier-type ion source. The energy resolution of the electron beam is around 1 eV, while the electron current is set to 20 μA for measuring mass spectra and ion efficiency curves to achieve optimum conditions of ion source for anions.

Results and Discussion

The mass spectrum shown in Fig. 1 shows two cluster anions at m/q =117 and 134 that can be assigned to $(NH_3)_5{\cdot}N_2H_4^-$ and $(NH3)_6{\cdot}N_2H_4^-$. SF_6 was introduced in small amounts into the ion source chamber to calibrate the mass scale with help of the anions SF_5^- and SF_6^- that dominate the mass spectrum with their isotopomers due to ^{32}S, ^{33}S and ^{34}S, respectively. In contrast to cluster anions of water or biomolecules no He atoms bind to the hydrazine ammonia cluster anions.

The anion efficiency curves in Fig. 2 indicate that hydrazine ammonia clusters are efficiently formed at two different resonances, i.e., a narrow resonance at very low energies (about 2eV) and a second broad feature between 5 eV and 17 eV. The third peak centered at about 22 eV can be assigned to inelastic scattering of the electron at a He atom prior to the interaction with the ammonia core. With increasing cluster size a clear shift of the first resonance to lower electron energies can be seen. This redshift is a consequence of the solvation of the hydrazine anion in ammonia.

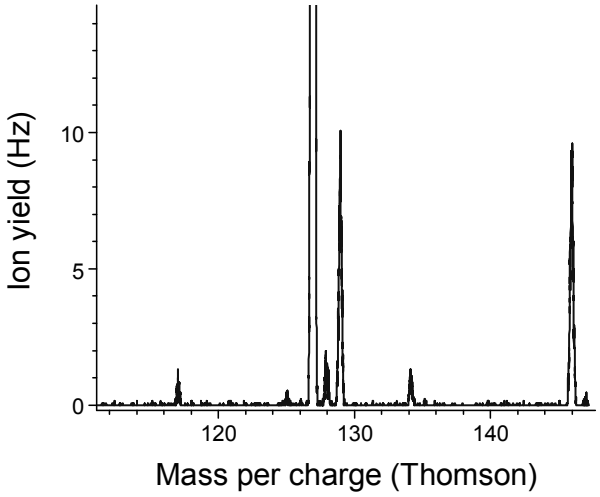

Fig.1 *Mass spectrum of the ammonia cluster anions and SF_6 as calibrant on stagnation conditions of 12K, 30bar and ammonia pressure in the pick up chamber 4.5mPa.*

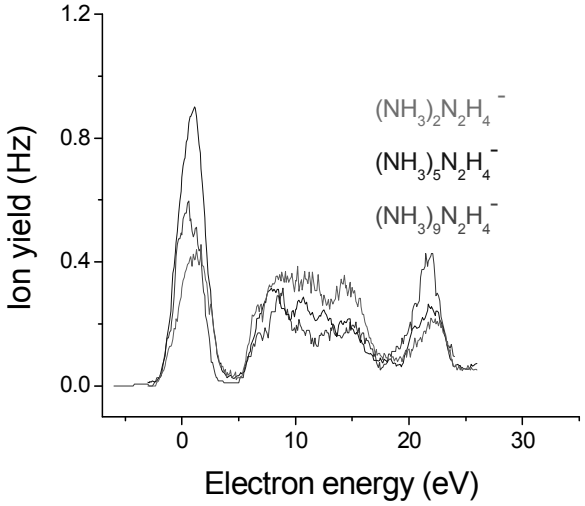

Fig.2 *Anion efficiency curves of $(NH_3)_2{\cdot}N_2H_4^-$, $(NH_3)_5{\cdot}N_2H_4^-$ and $(NH_3)_9{\cdot}N_2H_4^-$. Stagnation conditions are 12K, 30bar and ammonia pressure in the pick up chamber 4.5mPa.*

Acknowledgement

This work was supported by the FWF, Wien and the European Commission, Brussels.

References

[1] J.M. Greenberg, Surf. Sci. 500 (2002) 793.
[2] P. Dholtom, C.J. Bennet, Y.Osamura, N.J. Mason, R.I. Kaiser, Astrophys. J. 626 (2005) 940; M.P. Bernstein et al, Nature 416 (2002) 401.
[3] H.W. Sarkas, S.T Arnold, J.G. Eaton, G.H. Lee, and K.H. Bowen, J. Chem. Phys.116 (2002)
[4] L. Lehr, M.T. Zanni, C. Frischkorn, R. Weinkauf, D.M. Neumark, Science. 284 (1999)
[5] Ilya A. Shkrob, J. Phys. Chem. A. 110 (2006)
[6] S. Denifl, M. Stano, A. Stamatovic, P. Scheier, T.D. Märk, J. Chem. Phys. 124 (2006) 054320.
[7] S. Feil, K. Gluch, S. Denifl, F. Zappa, O. Echt, P. Scheier, T.D. Märk, Int. J. Mass. Spectrom. 252 (2006) 166.
[8] J.P. Toennies, A.F. Vilesov, Angew. Chem. Int. Ed. 43 (2004) 2622.

Influence of a Delay of the Moment of Collision of Ionic Pair with Atom-Acceptor of Energy on Recombination Probability in the System $Cs^+ + Br^- + Xe \rightarrow CsBr + Xe$

V.M. Azriel, L.Yu. Rusin
Institute of Energy Problems of Chemical Physics, the Russia Academy of Sciences,
Leninski prospect 38, Bldg.2, Moscow 119334, Russia
E-Mail address: Azriel_Vladimir@mail.ru

Trajectory simulation of direct three-body recombination of ions in the system $Cs^+ + Br^- + Xe$ has shown that simultaneous collision of three particles is not the unique mechanism of stabilization of a formed molecule [1]. For the purpose of more accurate definition of recombination model we investigated the influence of delay of a stabilizing particle relatively the moment of the closest rapprochement of ionic pair. Figure 1 shows that recombination probability quickly falls with growth of value of delay, decreasing in 2 times for a delay 0,1 and in 4 times for a delay 0,2 in comparison with recombination probability for direct three-body mechanism.

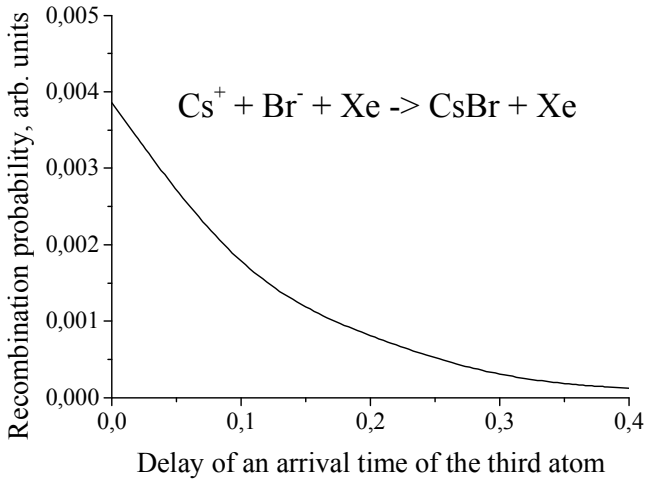

Fig.1. *Dependence of probability of recombination of ions Cs^+ and Br^- from value of a delay of an arrival time of the third atom to the point of a meeting of ionic pair. The arrival time delay is specified in shares from time corresponding to simultaneous collision of three particles.*

Reference

[1] V.M. Azriel, L.Yu. Rusin, Russian J. Phys. Chem. B, 2008, v.2, №4, p.499.

Trajectory Simulation of the Dynamics of Ionic Complexes Formation in the Systems CsBr + Hg and CsBr + CsBr

V.M. Azriel, L.Yu. Rusin
Institute of Energy Problems of Chemical Physics, the Russia Academy of Sciences,
Leninski prospect 38, Bldg.2, Moscow 119334, Russia
E-Mail address: Azriel_Vladimir@mail.ru

Dynamics of formation of ionic complexes RCs^+ and RBr^- in the systems CsBr + R, where R=Hg and R=CsBr, has been investigated by quasiclassical trajectory technique at the range of collision energies from zero to 20,0 eV. Masses of atom Hg and molecule CsBr differ slightly, but potentials of interaction in two systems are essentially various. Calculations show that for both systems the excitation function for complex RCs^+ has almost symmetric narrow bell-like shape with the maximum at 4,0-5,0 eV, and for collision energies above 8,0 eV the cross section falls to zero (figure 1(a)). Excitation functions for complex RBr^- are wider significantly, cross sections reach a maximum at energies 8,0-9,0 eV and further decrease with growth of collision energy (figure 1(b)). It is necessary to note, that cross sections of both ionic complexes formation in the system CsBr + Hg are characterized by the values of one order in a maximum of excitation functions, while for system CsBr + CsBr the maximal value of cross section of formation of complex $CsBrCs^+$ exceeds similar value for complex $BrCsBr^-$ almost in 15 times.

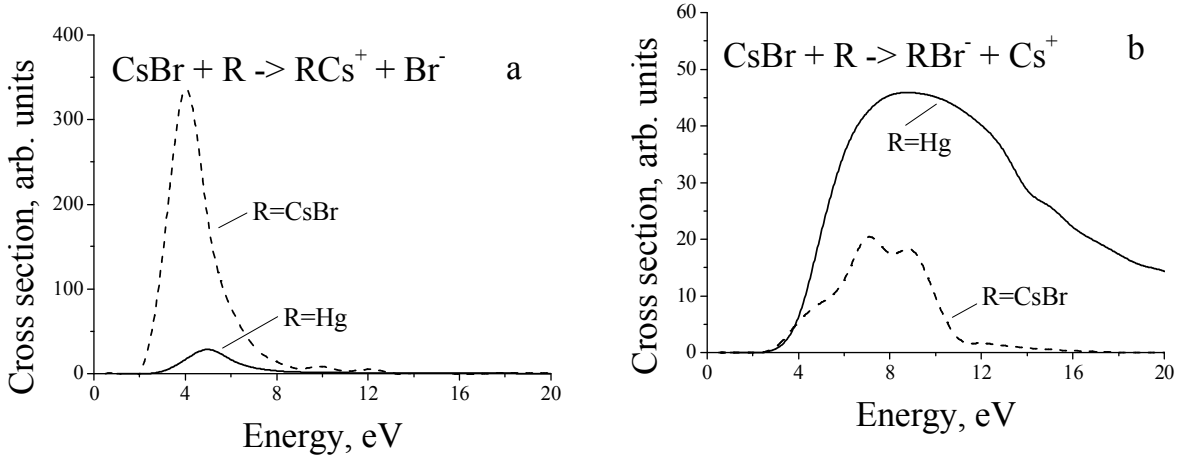

Fig.1. *Excitation functions of formation of ionic complexes RCs+ (a) and RBr- (b) in the systems CsBr + R, where R=Hg and R=CsBr.*

Investigation of Ar-Clusters formed upon Pick-Up in Helium Droplets

P. Bartl[1], F. Ferreira da Silva[1], S. Denifl[1], P. Scheier[1], O. Echt[2], T.D. Märk[1]

Peter.Bartl@uibk.ac.at

[1] *Institute for Ion Physics and Applied Physics, University of Innsbruck,6020 Austria*

[2]*Department of Physics. University of New Hampshire, DeMeritt Hall, Durham, NH 03824-356, USA*

We present results from measurements of argon clusters formed upon pick-up in helium droplets [1]. The experimental setup consists of a He-cluster source (supersonic expansion), a pick-up chamber and a sector field mass spectrometer (reverse BE geometry) with a Nier-type ion source for electron ionization. The cluster source expansion conditions and the partial argon pressure determine the neutral Ar-cluster size distribution. Therefore, within the limitations of the experiment, it is possible to produce clusters mainly in a chosen size regime with a smooth distribution. The investigations include attachment of helium to argon atoms and clusters, size distributions of pristine Ar-cluster ions and a possible icosahedral shell closure at Ar_{55}^+. A previously found abundance for $ArHe_{12}^+$ (Callicoatt et al. [2]) was confirmed and also mixed clusters of argon and helium ($Ar_XHe_Y^+$) have been identified. Our measurements on Ar-cluster size distributions show largely the same features as distributions formed by different techniques where the clusters are considered boiling hot. Surprisingly, even the ultracold helium matrix is unable to quench the fragmentation of Ar-clusters upon ionization. An indication for closure of the second icosahedral shell has been found in the presence of N_2, O_2 and H_2O contaminations in the pick-up chamber. These impurities form ionic cores of Ar-clusters exhibiting a pronounced magic number for $Ar_{54}N_2^+$, $Ar_{54}O_2^+$ and $Ar_{55}H_2O^+$ that can be interpreted as closures of icosahedral shells, while the pristine Ar-clusters show no abundance anomalies.

Acknowledgements:

This work was supported by the FWF and ÖAW, Vienna and the European Commission, Brussels. S.D. gratefully acknowledges an APART fellowship from the Austrian Academy of Sciences.

References:

[1] F. Ferreira da Silva, P. Bartl, S. Denifl, O. Echt, T. D. Märk, P. Scheier, *Phys. Chem. Chem. Phys.*

[2] E. B. Callicoatt, K. Förde, T. Ruchti, L. Jung, K. C. Janda, *J. Chem. Phys.,*1998, **108**, 9371-9382

Effects of Hydrocarbon Contamination in the Feed Gas of Ozone Generators on the Ozone Generation Efficiency: The Role of Surface Effects

Lopez J L[1], Freilich A[1], and Becker K[2]

[1] *Department of Applied Science & Technology, St. Peter's College, Jersey City, NJ, USA;* joselopez@spc.edu

[2] *Dept. of Physics, Polytechnic Institute of New York University, Brooklyn, NY, USA;* kbecker@poly.edu

Abstract

In large-scale ozone generators, low-power consumption, robustness of operation, and minimum maintenance requirements are of the highest importance. Essentially all industrial ozonizers use filamentary dielectric barrier discharges (DBDs) with pure O_2 or air as the feed gas. Hydrocarbons, in particular methane (CH_4), even in concentrations of only 50 ppm in the feed gas, have a deleterious effect on the maximum achievable ozone generation efficiency, particularly in the presence of N_2. This has been attributed to a complex sequence of surface reactions initiated by the plasma chemistry in the O_2 + CH_4 (+ N_2) gas mixture in the DBD microplasma filaments. Here we report results of experiments aimed at elucidating the influence of the HC presence in the ozonizer feed gas on the surface conditions of the DBD electrodes and, in turn, on their effect on the ozone generation efficiency.

Introduction

A variety of factors influence the design of modern ozone (O_3) generators. Low electrical power consumption, ease of operation, reduced down-time, and low maintenance are of the highest importance in ozonizers for large-scale industrial applications. On the other hand, smaller scale applications place a premium on ease of operation and reduced cost per ozonizer unit over power efficiency. The scale of the ozonizer required for a specific application has led to a vast range of different ozonizer designs. The current status of O_3 generator technology and the state of the existing scientific understanding of O_3 generation has recently been reviewed by Kogelschatz [1]. While O_3 can be produced by chemical or photolytic methods, these approaches have been confined to small-scale laboratory applications [2,3]. Small amounts of O_3 can further be created by electrolysis in electrochemical cells, a process almost exclusively used for the preparation of ultrapure water for manufacturing processes in the microelectronics and pharmaceutical industries [4]. Most commonly, O_3 is generated in electrical discharges using a variety of corona discharges [5] or dielectric barrier (or "silent") discharges (DBDs) [6] at ambient temperature and pressure. Essentially, all large-scale industrial ozonizers use DBDs, which create non-equilibrium filamentary discharges [1,6]

either in (dry) air, pure oxygen, or controlled oxygen/nitrogen mixtures. The typical large-scale O_3 generator design has a grounded outer electrode that serves as a gas/water tube heat exchanger and that surrounds a tubular inner electrode covered with a dielectric material, which is connected to a high-voltage power source. The feed gas processing occurs in filamentary DBD microdischarges between these two electrodes. Different engineering realizations generally differ in the diameter, length, and arrangement of the tubular electrodes, along with the type of the dielectric material that covers the inner electrode. The dielectric serves an essential function by limiting the amount of charge transported by a single microdischarge and is an important factor that determines the spatial distribution of the microdischarges across the electrode area [6]. Maintaining the discharge gap and the thickness of the dielectric layer within very tightly controlled tolerances guarantees a homogeneously (i.e., nearly statistically) distributed filamentary DBD pattern and, therefore, facilitates constant and reproducible feed gas processing.

Trace concentrations of hydrocarbons (HCs), especially the presence of methane (CH_4), are known to have a deleterious effect on the O_3 generation efficiency. This is generally attributed to a surface contamination of the powered electrode due to plasma chemically induced gas phase reactions. Here we report the results of a series of experimental studies aimed at elucidating the details of the surface effects resulting from the plasma chemistry in $O_2 + CH_4$ gas mixtures (which often also contain some N_2).

Experimental Details

All experiments were carried out in a standard Ozonia single-tube ozonizer (AT98 configuration), which is used in oxygen-fed, large-scale ozone generation plants. This particular ozonizer has a constant power induction and is therefore a classical representative of a constant feed gas processing ozone generator. The test rig utilized in our studies had the following main components:

- 450 kVA power supply with a kHz regime capable transformer
- Standard tube with 4 electrodes per tube
- Mass flow controller for oxygen, nitrogen and other gases
- Back-pressure control loop with pressure controller
- UV/Visible absorption spectrometer with cuvette for ozone concentration measurement
- IR absorption spectrometer for measurement of NO_x and other side products
- Gas and cooling water temperature sensors at generator inlet and outlet
- Gas pressure sensors at generator inlet and outlet
- HV and current probes connected to a 3-phase power meter
- Chiller with cooling water mass flow controller
- Oscilloscope for peak voltage and breakdown voltage determination
- Various surface analysis tools

Results and Discussion

Under all operating conditions, surface deposits on the powered electrode began to appear in the presence of HCs in the feed gas. In general, the amount of deposits increased from the inlet to the outlet of the ozonizer tube and the time for formation of a specific deposit depended critically on the power induction, the level of HC contamination, and the presence of N_2 in the feed gas (for the same dielectric material !). For moderate power induction and HC concentrations below about 100 ppm and with no discernible N_2 in the feed gas, the deposits were found to build up only very slowly and were limited to the region near the exit of the tube. The effect on the O_3 generation efficiency was only marginal. The absence of the formation of deleterious sticky deposits (see below) under these operating conditions is attibuted to a balance between deposit formation processes and deposit removal by sputtering (vaporization). This is shown symbolically in the diagram below.

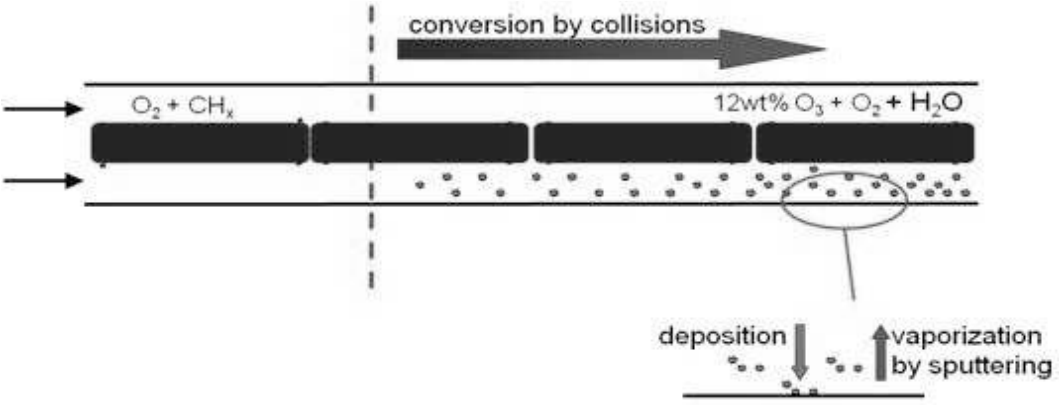

We note that thin deposits formed on the powered electrode could be removed completely by operating the ozonizer in pure (i.e. HC-free) O_2 as long as the initial HC concentration in the feed gas was below about 1000 ppm. We reiterate that the absence of N_2 is critical here.

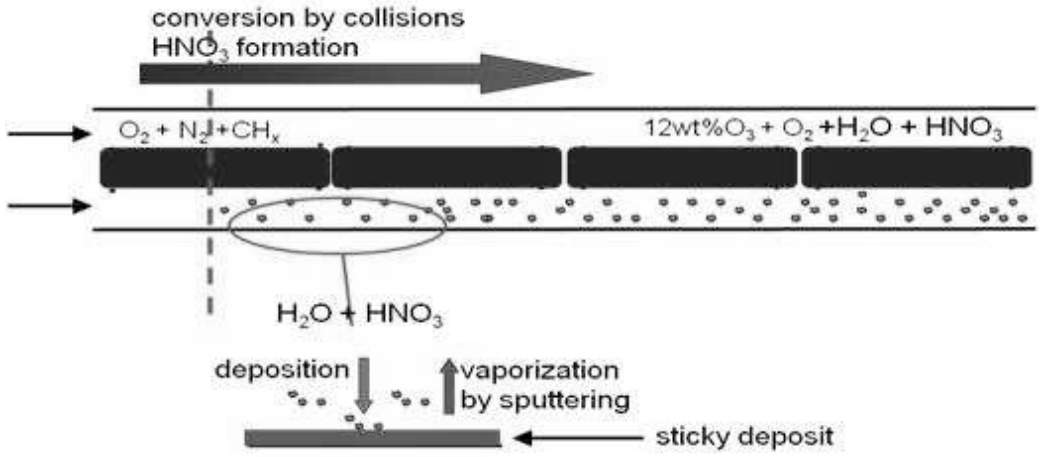

By contrast, the presence of N_2 in the feed gas (even at concentrations as low as 50 ppm) causes sticky deposits to build up within minutes of operation and, before long, the entire tube, with the exception of the area very close to the inlet, is covered with this deposit. The thickness of the deposit increases towards the exit of the ozonizer tube. We attribute this sticky deposit, which can cause a decline in the maximum O_3 generation efficiency of as much as 30%, to the formation of nitric acid in the presence of HCs and N_2 in the O_2 feed gas as shown schematically in the diagram above. Under these operating conditions, it is apparent that the efficiency of the removal of the deposit by sputtering and/or vaporization is most sufficient to counteract the processes that contribute to the formation of the sticky deposits. As a result, deposits form and build up over time.

Further details of the specific experiments that were carried out as part of this study, in particular studies aimed at correlating the presence of surface deposits to the achievable maximum O_3 generation effiicency, will be presented and discussed at the Conference.

Acknowledgements:

This work was supported by Degremont Technologies (Ozonia Ltd, Switzerland.). We acknowledge many helpful discussions with Dr. Guido Vezzu and Dr. Ulrich Kogelschatz.

References

[1] U. Kogelschatz. "Industrial Ozone Generation: Historical Perspective, Current Status and Future Prospects". *Proc. IOA 17th Ozone World Congress, Strasbourg 2005* II.1 1-10, 2005.

[2] U. Kogelschatz. "Advanced ozone generation". *Process Technologies for Water Treatment*, S. Stucki, Ed., New York and London: Plenum. 87-120, 1988; see also M. Salvermoser et al. "Influence of Water Vapor on Photochemical Ozone Generation with efficient 172nm Xe Excimer Lamps", Ozone Sci. Eng. 30, 228-237 (2008).

[3] S. Stucki and H. Baumann. "Applications of electrochemical ozone generators in ultrapure water systems". *Process Technologies for Water Treatment*, S. Stucki, Ed. New York and London: Plenum. 191-203, 1988.

[4] K.H. Becker, U. Kogelschatz, K.H. Schoenbach, R.J. Barker, Eds. "History of Non-Equilibrium Air Discharges – Corona Discharges". *Series in Plasma Physics: Non-Equilibrium Air Plasmas at Atmospheric Pressure*. Bristol and Philadelphia: Institute of Physics Publishing Ltd. 47-68, 2005.

[5] B. Eliasson, M. Hirth, U. Kogelschatz. "Ozone Synthesis from Oxygen in Dielectric Barrier Discharges". *J. Phys. D: Appl. Phys*. 20, 1421–1437 (1987).

[6] H.V. Lang, G. Vezzù, M. Suter, "Science and Experience-based Improvements of Industrial Ozone Generators". *Proceedings IOA 17th Ozone World Congress, Strasbourg 2005* II.3 1-10 (2005).

Tooth-Whitening with H_2O_2 Assisted by a Direct Current, Cold Atmospheric-Pressure Air Plasma Microjet

Peng Sun[1], Jie Pan[2], Ye Tian[1,3], Na Bai[1,3], Haiyan Wu[1], Jue Zhang[1], Weidong Zhu[4], Kurt Becker[5], and Jing Fang[1]

[1] *Academy for Advanced Interdisciplinary Studies, Peking University, Beijing, China*

[2] *School of Stomatology , Peking University, Beijing, China*

[3] *West China College of Stomatology, Sichuan University, Chengdu, China*

[4] *Dept. of Applied Science and Technology, Saint Peter's College, New Jersey, USA;* wzhu@spc.edu

[5] *Dept. of Physics, Polytechnic Institute of New York University, New York, USA;* kbecker@poly.edu

Abstract

A tooth-whitening process with H_2O_2 enhanced by the application of a direct current atmospheric-pressure cold plasma microjet (PMJ) is presented. Compared with the standard clinical method of using H_2O_2 alone, a significant improvement of the tooth-whitening process was observed when the PMJ was applied. The tooth surface temperature was monitored for safety considerations and it did not exceed 37 °C at 1 cm distance between the exit nozzle of the plasma device and the tooth for a treatment time of 20 min. This plasma-enhanced tooth-whitening method could have promising new clinical applications.

Introduction

Tooth-whitening is of great popularity and importance in cosmetic dentistry. The color of teeth is determined by the combined effects of their intrinsic color and the presence of extrinsic stains formed on the tooth surface from e.g. fried food, beverages (tea, coffee, red wine), chemicals, and smoking. Tooth stains are mainly composed of single-bond or double-bond organic compound chromophores. Conventional tooth-whitening treatments are based primarily on bleaching using H_2O_2, however, the exact mechanism is not fully understood [1,2]. Home bleaching uses low levels of whitening agent applied to the teeth via a mouth guard which is worn for about 2-4 weeks. In contrast, in-office bleaching generally uses relatively high doses (25-35% H_2O_2) for a quick effect. Some approaches use light sources to accelerate the bleaching process [3-6]. Non-thermal plasmas have recently attracted much interest in biomedicine due to their potential application in bacteria inactivation, tissue sterilization, blood coagulation, wound healing, and treatment of corneal infections, dental diseases, and possibly cancer [7-16]. Here we report results of the bleaching of extracted teeth induced by H_2O_2 and enhanced by a dc atmospheric-pressure cold plasma microjet (PMJ).

Experimental Details

The PMJ device is comprised of two metal electrodes separated by a dielectric layer ~ 0.5 mm thick. The openings in the two electrodes were ~0.8 mm in diameter. The high-voltage electrode was completely embedded in the device and powered by a DC power supply (negatively biased). The outer electrode was grounded for safety considerations. Compressed

air was used as the working gas at a flow rate of ~ 2 slm. The discharge sustaining voltage was in the range of 400–600 V with an operating current of 20–35 mA. For a detailed device description, please refer to [8]. The generated PMJ was usually between 8-10 mm in length. Fig. 1a shows a picture of the PMJ and fig. 1b shows the schematic experimental setup.

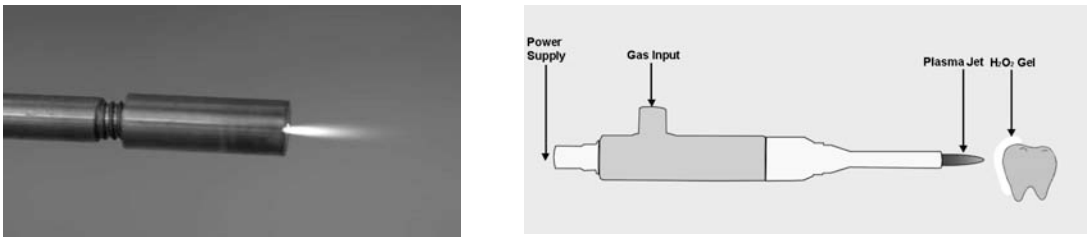

(a) (b)

Fig. 1. *(a) Picture of the atmospheric pressure cold plasma microjet (PMJ); (b) schematic diagram of the PMJ treatment of extracted tooth (clinical H_2O_2 gel was applied to tooth surface every 30 seconds)*

Clinical H_2O_2 gel containing 35% H_2O_2, was used in this study. Sixty intact caries-free human teeth were chosen from among premolars extracted for orthodontic reasons and were divided into three groups. The teeth in group A received H_2O_2 gel only and were kept at room temperature (RT) for 20 minutes; the teeth in group B received H_2O_2 gel and were treated with the PMJ (0.5-0.54 kV, 30 mA, air flow rate: 2 slm) for 20 minutes. In order to eliminate the effect of the increase in temperature due to the PMJ treatment, a third group of teeth (group C) received H_2O_2 gel and were placed into an incubator (38°C) for 20 minutes.

Results and Discussion

Photographs of typical teeth from group A (top) and B (bottom) before (left column) and after (right column) the tooth bleaching treatment are shown in fig. 2. The teeth in group B showed clearly a much more pronounced whitening effect than group A.

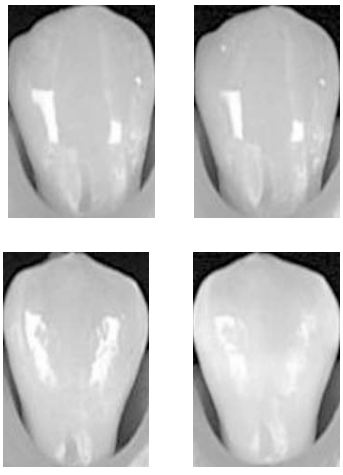

Fig. 2. *Photos of teeth before (left) and after (right) 20min whitening treatment, without (top) and with (bottom) PMJ treatment.*

Since teeth nerves will be severely damaged when the temperature rises above 42 °C, the tooth surface temperatur was evaluated for a plasma treatment with a distance of 1 cm between the tooth and the PMJ exit nozzle. It was found that the tooth surface temperature stabilized at 37 °C after 8 min of PMJ treatment, which is well below the critical temperature. Therefore, the PMJ treatment does not introduce safety issues related to the tooth surface temperature. However, other potential safety issues arising from ultraviolet light irradiation, ozone, nitric oxide due to the PMJ application are not considered here, but will be studied in the very near future.

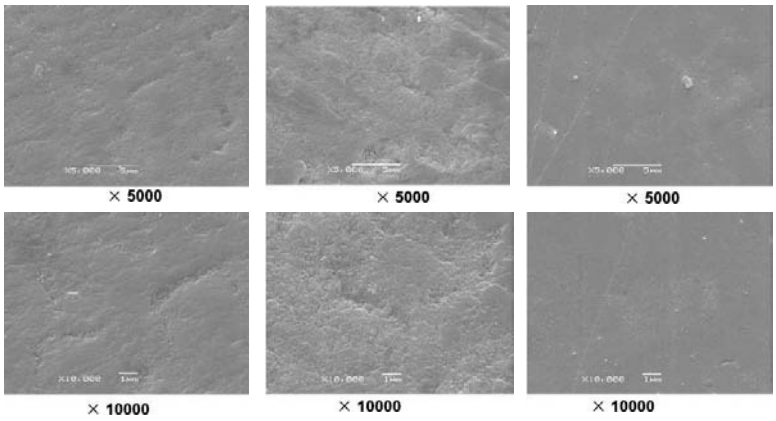

Fig. 3. *SEM photographs of the tooth surface after different bleaching processes.*

Scanning electron microscopy (SEM) was employed to evaluate the tooth surface morphology after different bleaching processes. Fig. 3 shows SEM photographs of a control tooth, a tooth treated with H_2O_2 gel and a tooth treated with H_2O_2 gel and the PMJ. No noticeable changes in the tooth surface morphology were observed at magnifications of 5,000 and 10,000.

In conventional tooth bleaching with H_2O_2 gel, it is not clear which reactive agent is responsible for the key chemical reactions, the hydroxyl radical (OH) or reactive oxygen species generated from the dissociation of H_2O_2. Hydroxyl radicals are strong oxidants with an oxidation potential of 2.8 eV. When H_2O_2 is exposed to the PMJ in our experiments, OH radicals may be generated from (1) UV activation of H_2O_2 or (2) the reaction of H_2O_2 with plasma activated species (including atomic oxygen, ozone, or O_2^-). Furthermore, perhydroxyl (HOO), the direct conjugate of the superoxide radical may also be an important species in the bleaching process.

In one model, it is believed that OH reacts with the chromophores and breaks macromolecular stains into smaller stain molecules [17]. We evaluated OH in a solution consisting of 40 μL H_2O_2 (30%), 40 μL 5,5-dimethyl-1-pyrroline-N-oxide (DMPO, 0.4 mol/L), and 1 mL deoxidized water with ESR spectroscopy spin-trapping with DMPO as the OH trapper. The control group was exposed to an air flow for 1 min and the test group was exposed to the PMJ treatment for 1 min. It was found that the generation of OH nearly doubled as a result of the PMJ exposure. Other bleaching reaction mechanisms have also been proposed.

Lastly, we note that preliminary studies using a PMJ treatment in the absence of H_2O_2 gel seemed to yield whitening results that were comparable, if not superior, to the results obtained with the H_2O_2 gel and the PMJ.

Acknowledgements

This research was sponsored by Bioelectrics Inc. (U.S.A.), the Peking University Biomed-X Foundation and China International Science and Technology Cooperation (2008KR1330). The authors wish to thank Song Yun from the College of Engineering, Peking University, for help with the SEM analysis. We thank Dr. Karl Schoenbach, Dr. Juergen Kolb and Robert Price of the Frank Reidy Research Center for Bioelectrics at Old Dominion University for

their helpful suggestions in designing the initial PMJ device and we are grateful to the Beyond Technology Corp. for providing the tooth whitening gel.

References

[1] A. Joiner, Journal of Dentistry 34 (2006) 412
[2] M. Sulieman, M. Addy, E. Macdonald, J.S. Rees, Journal of Dentistry 33 (2005) 33
[3] N.U. Wetter, M.C. Barroso, J.E.P. Pelino, Lasers in Surgery and Medicine 35 (2004) 254
[4] M. Tavares, J. Stultz, M. Newman, V. Smith, R. Kent, E. Carpino, J.M. Goodson, Journal of the American Dental Association 134 (2003) 167
[5] M. Sulieman, Dental Update 32 (2005) 101
[6] D.K. Hein, B.J. Ploeger, J.K. Hartup, R.S. Wagstaff, T.M. Palmer, L.D. Hansen, Comp. Continuing Education in Dentistry 24 (2003) 340-352
[7] M. Laroussi, IEEE Trans. Plasma Sci. 30 (2002) 1409
[8] H. Feng, P. Sun, Y. Chai, G. Tong, J. Zhang, W. Zhu, and J. Fang, IEEE Trans. Plasma Sci., 37 (2009) 121
[9] A.B. Shekhter, V.A. Serezhenkov, T.G. Rudenko, A.V. Pekshev, A.F. Vanin, Nitric Oxide-Biol. Chem. 12 (2005) 210
[10] G. Fridman, M. Peddinghaus, H. Ayan, A. Fridman, M. Balasubramanian, A. Gutsol, A.D. Brooks, G. Friedman, Plasma Chem. Plasma Process 26 (2006) 425
[11] J. Raiser and M. Zenker, J. Phys. D: Appl. Phys. 39 (2006) 3520
[12] R. Pompl, T. Shimizu, H.-U. Schmidt, W. Bunk, F. Jamitzky, B. Steffes, K. Ramrath, B. Peters, W. Stolz, T. Urayama, R. Ramasamy, S. Fujii, and G.E. Morfill, 6th International Conference on Reactive Plasmas, 2006, Matsushima, Japan
[13] T. Shimizu, B. Stefferd, R. Pompl, F. Jamitzky, W. Bunk, K. Ramrath, B. Peters, W. Stolz, H.-U. Schmidt, T. Urayama, K. Fujioka, R. Ramasamy, S. Fujii, G.E. Morfill, 6th International Conference on Reactive Plasmas, 2006, Matsushima, Japan
[14] X. Lu, Y. Cao, P. Yang, Q. Xiong, Z. Xiong, Y. Xian, and Y. Pan, IEEE Trans. Plasma Sci. 37 (2009) 668
[15] G. Fridman, A. Shereshevsky, M.M. Jost, A.D. Brooks, A. Fridman, A. Gutsol, V. Vasilets, G. Friedman, Plasma Chem. Plasma Process 27 (2007) 163
[16] S. Pesnel, M. Vandamme, S. Lerondel, A. Le Pape, E. Robert, S. Dozias, E. Barbosa, J. Pouvesle, 2. Int. Conference on Plasma Medicine, 2009, San Antonio, TX, USA
[17] M. Kashima-Tanaka, Y. Tsujimoto, K. Kawamoto, N. Senda, K. Ito, M. Yamazaki, J. Endod. 29 (2003)141
[18] F. Liu, P. Sun, N. Bai, Y. Tian, H. Zhou, S. Wei, Y. Zhou, J. Zhang, W. Zhu, K. Becker, and J. Fang, Plasma Processes and Polymers (2009), in press

Investigation of the Reactions of H_3O^+ and $H_3O^+.H_2O$ with a Series of Saturated Alcohols Using a Proton Transfer Reaction Mass Spectrometer

P Brown, P Watts, and C A Mayhew

School of Physics and Astronomy, University of Birmingham, Birmingham, B15 2TT, UK, pab437@bham.ac.uk

Abstract

The use of proton transfer reaction mass spectrometry for trace gas analysis has grown at pace since its development and commercialisation in the mid 1990s [1]. Specific areas of application include atmospheric chemistry, environmental chemistry, plant and tree emissions, food science and medical sciences. Central to using a proton transfer reaction mass spectrometer (PTR-MS) are the reactions occurring within the drift region of the instrument. An operational choice must be made for the optimum ratio between the applied electric field, (E) and the number density, (N). The choice of reduced electric field strength, E/N, affects the profile of the reagent ion signal as well as affecting the energy of the ion collisions. Few studies have analysed the effects that changing this ratio has on the fragmentation ion chemistry of an organic compound family [2].

The aim of this study is to provide valuable information to the PTR-MS community regarding the fragmentation behaviour of alcohols in a PTR-MS drift tube. Product ion branching ratios for a series of saturated alcohols ranging in carbon number from methyl alcohol to hexyl alcohols will be presented. The table shows the proton affinity, molecular weight and chemical formula of the series investigated.

Each compound was analysed using a PTR-MS over a range of drift tube E/N settings from 92 to 138 Td, in approximately 5 Td intervals. Where concentration dependencies were observed the flow rate was extrapolated to zero flow. The concentration of analyte was adjusted using a syringe pump, as shown in the figure. Results will be reported for each alcohol with identification of observed fragments and some explanation of the fragmentation reactions and chemistry.

Chemical Name (proton affinity /kJ mol^{-1})	Chemical Formula (mw)
Methanol (754.3)	CH_3OH (32)
Ethanol (776.4)	C_2H_5OH (46)
1-Propanol (786.5)	C_3H_7OH (60)
2-Propanol (793.0)	C_3H_7OH (60)
1-Butanol (789.2)	C_4H_9OH (74)
Isobutanol (793.7)	C_4H_9OH (74)
tert-Butanol (802.6)	C_4H_9OH (74)
2-Butanol (815.7)	C_4H_9OH (74)
Cyclopentanol	C_5H_9OH (86)
1-Pentanol	$C_5H_{11}OH$ (88)
Cyclohexanol	$C_6H_{11}OH$ (100)
1-Hexanol	$C_6H_{13}OH$ (102)
3,3, Dimethyl-2-butanol	$C_6H_{13}OH$ (102)

Table: Proton affinity, molecular weight and chemical formula for each compound in the investigated series[3]

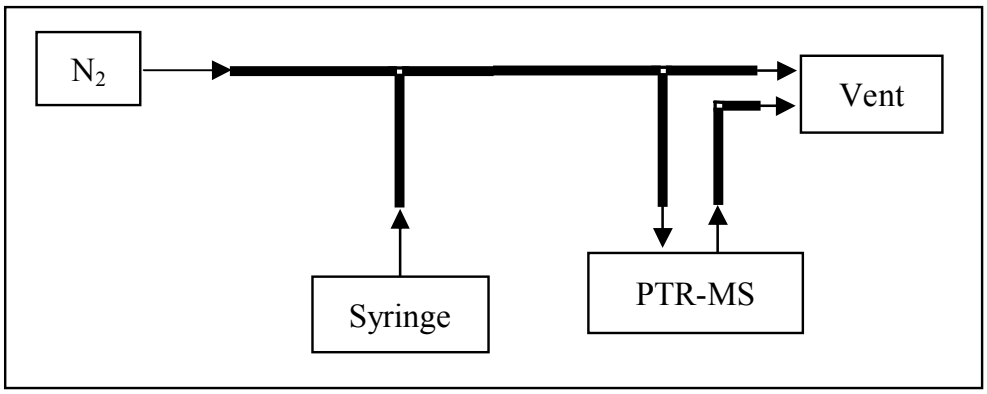

Figure: Block diagram of the experimental set-up used, showing how the alcohol vapour was introduced to the PTR-MS via a flow of oxygen free nitrogen.

References

[1] A. Hansel, A. Jordan, R. Holzinger, P. Prazeller, W. Vogel, and W. Lindinger, International Journal of Mass Spectrometry 149 (1995) 609.

[2] M.M.L. Steeghs, E. Crespo, and F.J.M. Harren, International Journal of Mass Spectrometry 263 (2007) 204.

[3] E. Hunter and S. Lias, NIST Chemistry WebBook, 2009.

Electron-Induced Proton Transfer in Acid-Base Reactions: Anion Photoelectron Spectroscopic Studies

Angela Buonaugurio[1], Jing Chen[1], Soren Eustis[1], Kit Bowen[1], Maciej Gutowski[2], and Alex Whitesides[2]

[1] Dept of Chemistry, Johns Hopkins University, Baltimore, MD 21218, USA[1]

[2] Dept. of Theoretical Chemistry, Heriot-Watt University, Edinburgh, Scotland, UK[2]

When ammonia and hydrogen chloride vapors mix, they form a white cloud due to the formation of ammonium chloride microcrystals. However, when single molecules of ammonia and hydrogen chloride form neutral hetero-dimers, they do not proton transfer (they do not react). We explored the ability of an excess electron to induce proton transfer in these systems by forming the negative dimer anions, $[(NH_3)(HCl)]^-$, and we found that a single electron is sufficient to induce proton transfer and thus salt formation in these systems. The specific mechanism for electron induced, proton transfer involves the formation of dipole bound states and Rydberg molecules. We have enjoyed theoretical support and collaboration in this work with M. Gutowski.

Radical-Radical Reaction Dynamics: a Combined Crossed-Beam and Theoretical Study

Kyoo-Weon Kang, Yong-Pal Park, Se-Hee Jung, and Jong-Ho Choi
Department of Chemistry and Center for Electro- and Photo-Responsive Molecules, Korea University, 1, Anam-dong, Seoul 136-701

Herein, we present *ab initio* calculations of the prototypal radical-radical reactions of ground–state atomic oxygen [$O(^3P)$] with methyl (CH_3) and ethyl (C_2H_5) radicals. The reaction mechanisms and dynamics were investigated using the density functional method and complete basis set model. In both radical reactions, two distinctive pathways were predicted to be in competition: addition and abstraction.

The barrierless addition of $O(^3P)$ to the hydrocarbon radicals led to the formation of energy-rich intermediates that underwent subsequent isomerization and decomposition to yield various products. The products predicted to be found were $H_2CO + H$, $^{1,3}HCOH + H$, and $^{1,3}CH_2 + OH$ for $O(^3P) + CH_3$ and $H_2CO + CH_3$, $CH_3CHO + H$, $c\text{-}CH_2OCH_2 + H$, $^{1,3}CH_3COH + H$, $^{1,3}HCOH + CH_3$, $CH_2CHOH + H$, $C_2H_3 + H_2O$ and $CH_2CH_2 + OH$ for $O(^3P) + C_2H_5$. The minor H-atom abstraction mechanisms producing $^{1,3}CH_2 + OH$ and $CH_2CH_2 + OH$ were calculated to compete with the addition processes in both title reactions.

With the aid of microscopic statistical calculations, the major pathways were predicted to be the formation of $H_2CO + H$ for $O(^3P) + CH_3$ and that of $H_2CO + CH_3$ and $CH_3CHO + H$ for $O(^3P) + C_2H_5$ through the low-barrier, single-step cleavages of the addition intermediates.

The characteristics of the major reaction channels were compared with the experimental results reported in the gas-phase kinetics and crossed-beam investigations.

Reference:

[1] Jong-Ho Choi, Int. Rev. Phys. Chem. **25**, 613 (2006), and references therein.

C_{60} Embedded in Helium Nanodroplets: Novel Ion-Molecule Reactions with Water and Cooling of Nascent Anions

S. Denifl[1], I. Mähr[1], A. Mauracher[1], S. Jaksch[1], M. Probst[1], J. Urban[2], P. Mach[2], A. Bacher[1], O. Echt[3], T.D. Märk[1], P. Scheier[1]

[1] Institut für Ionenphysik und Angewandte Physik, Universität Innsbruck, Technikerstrasse 25, A-6020 Innsbruck, Austria, E-mail: stephan.denifl@uibk.ac.at

[2] Department of Nuclear Physics and Biophysics, Comenius University Bratislava, Mlynska dolina F1, 84248 Bratislava, Slovakia.

[3] Department of Physics, University of New Hampshire, Durham, NH03824, USA.

Introduction

The extensive number of spectroscopy studies with doped helium droplets shows impressively the ability of superfluid helium droplets for preparation of cold targets [1,2]. Any species embedded will be cooled down to 0.37 K which allows the preparation of complex fragile species in the interior of the droplet. In contrast to the vast amount of optical spectroscopy, the inelastic electron scattering with doped helium droplets has been less studied. So far most investigations in this research field covered electron ionization of doped helium droplets (e.g. Refs. [3-5]). In that case an initial helium atom at the surface of the helium droplet is ionized and after subsequent charge transfer via several helium atoms the hole finally localizes at the dopant molecule or cluster inside the helium droplet. This different ionization mechanism compared to molecules in the gas phase can lead to substantial modification of fragmentation pattern upon electron impact ionization. In contrast, electron injection into helium droplets is characterized by the formation of a metastable electron bubble inside the helium droplet. Within a few picoseconds after entering the conduction band the electron will be localized in such cavity of 17 Å radius. Subsequently, the electron undergoes either autodetachment from the droplet or it may attach to a dopand inside the helium droplet to form a temporary negative ion.

Positive and negative ion formation in doped helium droplets are studied in our working-group. In the present experiment we have studied C_{60} in helium droplets. In the course of the present experiments we observed that the strongly hydrophobic C_{60} efficiently forms clusters with residual water molecules inside helium droplets. In order to investigate these remarkable reactions inside helium droplets we have doped helium droplets with C_{60} and H_2O in a controlled manner. The experimental results are interpreted by means of ab-initio Hartree-Fock calculations.

Experimental

Our group has constructed a helium droplet source [6] which was initially used to study the electron ionization of pure helium droplets, as well as the metastable decays of small helium cluster ions. Recently we modified the helium droplet source by adding a pick up chamber with oven, pick up cell and external gas inlet which allows to dope cold superfluid helium droplets with various molecules. Currently the droplet source is mounted at a double focusing two sector field mass spectrometer. Neutral helium nanodroplets are produced by expanding helium from a pressure of 15 bar through a 5 μm nozzle, cooled to 9.6 K by a closed-cycle refrigerator, into vacuum. After passing a 0.8 mm skimmer the droplets enter the pick-up region. C_{60} is vaporized in an oven at temperature of ~460K.

Most helium droplet are doped with up to two molecules before they enter the ion source chamber. The Nier type ion source of the mass spectrometer is capable to produce both positive and negative ions formed upon inelastic interaction of electrons with the doped droplets. Ions formed are accelerated through a potential drop of 3 kV and are then mass analyzed with the two sector field instrument. After passing a first field free region, anions are selected according to their momentum (mass) by a magnetic sector field. Then they pass a second field-free region, until they are finally transmitted through an electric sector field to a detector which is a channeltron type of secondary electron multiplier operated in the single pulse counting regime.

Results

When measuring the electron ionization mass spectrum above the mass of the parent ion C_{60}^+, we obtain a series of $C_{60}(H_2O)_n^+$ cluster ions with a strong local abundance maximum for $C_{60}(H_2O)_4^+$ (see Figure 1). The magic cluster can be ascribed to an enhanced thermodynamic stability of the cluster ion in terms of an increased evaporation energy for loss of a monomer. This explanation is also confirmed by our calculations of evaporation energies by means of Hartree-Fock calculations and the 3-21G double zeta basis set which are to our knowledge the first *ab-initio* studies for $C_{60}(H_2O)_n^+$.

A further remarkable result is the appearance of dehydrogenated water cluster ions with a particular strong abundance for the monomer, $C_{60}OH^+$. We propose a novel mechanism via an ion-molecule reaction of a doubly charged C_{60}^{2+} with water clusters. Formation of C_{60}^{2+} in ionized helium droplets is energetically possible since the ionization energy of helium (24.6 eV) exceeds the double ionization energy of C60 (19 eV). Details of possible reaction pathways will be presented.

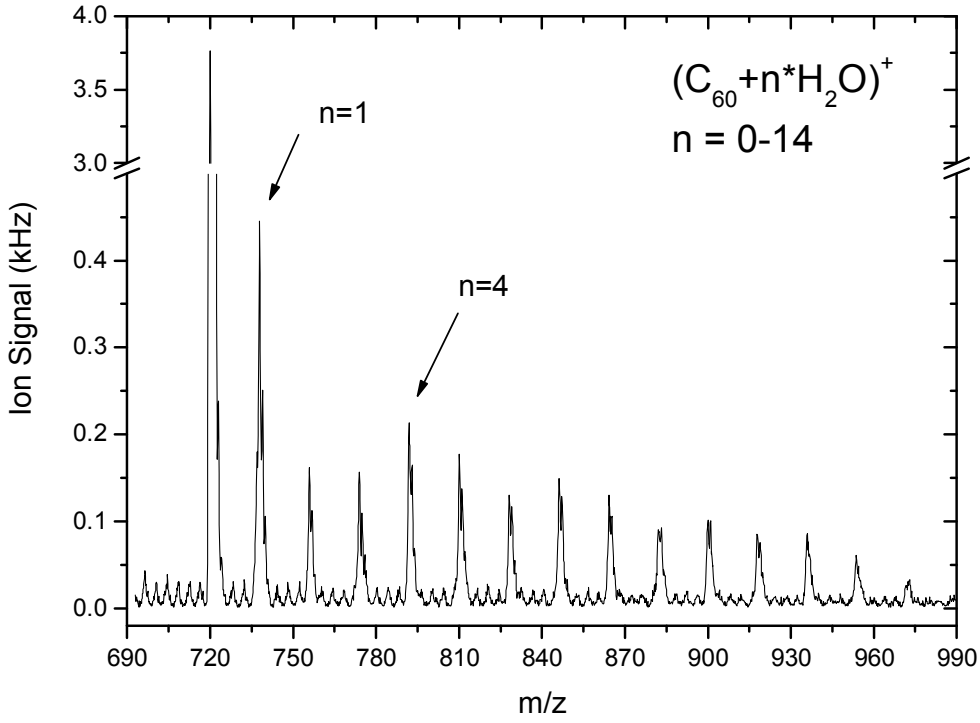

Fig.1 *Electron ionization mass spectrum of $C_{60}(H_2O)_n$ doped helium droplets.*

In case of electron attachment we have measured the ion yields of C_{60}^-, $C_{60}D_2O^-$ and $(C_{60})_2^-$. Electron capture by isolated C_{60} represents the prototype of a non-dissociative electron attachment reaction which yields long-lived parent anion up to electron energies of more than 12 eV. The decline of the anion yield at these energies is explained by thermally activated autodetachment.

The low temperature of C_{60} inside helium droplets leads to efficient cooling of the nascent anions via evaporation of helium atoms from the droplet. The measured spectra are compared with calculated breakdown graphs for autodetachment. The comparison of the breakdown graphs with the yields for $C_{60}D_2O^-$ and $(C_{60})_2^-$ anions leads to the results that for these anions dissociation is in competition with autodetachment.

Acknowledgements

S.D. gratefully acknowledges an APART grant from the Austrian Academy of Sciences. This work has been supported in part by the FWF, Wien, Austria and the European Commission, Brussels, and the Austrian Ministry of Science (infrastructure grant to the LFU scientific computing platform).

References

[1] J. P. Toennies, and A. F. Vilesov, Angew. Chem. Int. Ed. **43**, 2622 (2004) and references cited therein

[2] F. Stienkemeier, and K. K. Lehmann, J. Phys. B: At. Mol. Opt. Phys. **39**, R127 (2006) and references cited therein

[3] W. K. Lewis, C. M. Lindsay, R. J. Bemish, R.E Miller, J. Am. Chem. Soc. **127,** 7235 (2005)

[4] S. Yang, S.M. Brereton, M.D. Wheeler, A. M. Ellis, J. Phys Chem A **110**, 1791 (2006)

[5] A. Boatwright, J. Jeffs, A. J. Stace, J. Phys. Chem. A **111** 7481 (2007)

[6] S. Denifl, F. Zappa, I. Mähr, J. Lecointre, M. Probst, T. D. Märk, P. Scheier, Phys. Rev. Lett. **97,** 043201 (2006)

Cavity enhanced saturation spectroscopy of NH_3 in the near infrared

P. Dietiker, M. Quack, A. Schneider, G. Seyfang, F. Ünlü
ETH Zürich, Laboratorium für physikalische Chemie, peter.dietiker@phys.chem.ethz.ch

Quite often a line by line analysis of measured infrared (IR)-spectra is complicated due to the congestion of overlapping lines and resolution being limited by the Doppler widths. If only a few lines are overlapped, a line shape analysis for overlapping lines can result in reliable line positions. But the method will fail if the lines are too close or if too many lines are overlapped. Then sub-Doppler methods have to be applied in order to reveal the exact line positions. We applied cavity enhanced saturation spectroscopy to determine the line positions of congested parts of the near-IR spectrum of NH_3 around 6600 cm^{-1}. The measured dip positions are compared to line positions obtained from a multiline fit of measured Fourier transform infrared (FTIR) spectra recorded with an instrumental bandwidth significantly smaller than the Doppler width.

Introduction

To simulate infrared or near infrared spectra for astrophysical and atmospherical applications, and also for our work preparing to measure spectroscopically the tiny parity violating energy difference $\Delta_{pv}E$ between the enantiomers of chiral molecules [1], a line by line analysis of the complex absorption spectra of polyatomic molecules is indispensible. Unfortunately, quite often the analysis is hindered due to overlapping lines, even for small molecules like NH_3, CH_4 or C_2H_4. This congestion can often be removed by reducing the number of populated levels and the inhomogeneous linewidth if the spectra are measured at low temperature in a molecular beam. But for the simulation of spectra at higher temperature the results from the analysis of the higher rotational levels and rovibrational excited states have to be included and saturation spectroscopy can be applied to remove the inhomogeneous Doppler-broadening of the absorption lines. Flexible molecules with large amplitude motions are ideal model systems to derive intramolecular energy flow and unimolecular isomerisation dynamics from molecular spectroscopy, combined with theoretical models. Due to the inversion at the nitrogen atom ammonia and its deuterated isotopomers have been prototype molecules for such investigations [2-4]. Already above 6000 cm^{-1}, corresponding to an excitation energy of 75 kJ/mol, the rovibrational infrared spectrum is far from being completely understood [5-8]. For NH_3 four different vibrational bands approximately assigned as $2\nu_1$, $\nu_1+\nu_3$, $2\nu_3$ and $\nu_1+2\nu_3$ are observed in the spectral range around 6600 cm^{-1}, where each one is split into two tunneling components. Therefore the infrared spectrum is quite congested. In addition the analysis is more difficult as the bands are coupled through Darling-

Dennison or Fermi resonances. Rotational constants for a number of these bands have been obtained from microwave optical double resonance experiments and diode laser measurements [5,8]. Based on ground state combination differences obtained from FTIR spectra Lundsberg-Nielsen *et al.* [5] published assignments and line strengths for a number of rovibrational transitions of the $\nu_1+\nu_3$ and $2\nu_3$ band between 6400 and 6800 cm^{-1}. However, large discrepancies are obtained if the positions of their assigned lines are calculated with both sets of published rotational constants from reference 5 and 8.

To resolve these discrepancies and to improve the assignment, more precise data recorded with sub-Doppler resolution are useful. We have compared the results from intracavity enhanced saturation spectroscopy with a line shape analysis based on a multiline fit to FTIR spectra recorded at 300 K and 180 K recorded with an instrumental bandwidth smaller than the Doppler width.

Experimental

We have used a tunable external cavity diode laser with an output power of 5 mW and a line width smaller than 300 kHz for a detection time of 50 ms. Two CaF_2 beam splitters reflect a small fraction of the laser light into a glass cell filled with a reference gas and to a single mode optical fiber for absolute and relative frequency calibration respectively. The single mode fiber has a length of 2 m, resulting in a free spectral range of 50.022 MHz. The fiber was kept in a covered box and its temperature is actively stabilized to better than 0.5 K, resulting in a stability of the free spectral range of the fiber etalon to better than 10 kHz. For a rough frequency estimation a fraction of the laser beam was sent to a wavemeter (Burleigh WA-1500) having a specified accuracy of 0.002 cm^{-1}. An EOM creates side-bands with 30 MHz separation from the center frequency of the laser. Two spherical mirrors with very high reflectivity ($R \sim 0.9999$), radius of curvatures of $r = -1$ m and a separation distance $d = 48$ cm form a stable cavity. It is placed in a vacuum chamber, which allows precise control of the sample pressure inside the resonator from 0.1 Pa to 20 Pa. The length of the cavity is tuned with a piezo-voltage-amplifier in resonance with the laser frequency and using the Pound-Drever-Hall method the laser is locked to a cavity mode. To ensure a stable scanning process and a very efficient coupling of the laser light to the cavity, the laser beam was mode-matched to the cavity modes through a set of lenses. Depending on the sample pressure a laser intensity of 100-250 W/cm^2 is obtained inside the cavity. To tune across a set of absorption lines a slow voltage ramp was applied to the piezo transducer of the cavity and the signal transmitted through cavity was sent to a photodiode. With a ramp-scanning period of 30 s we achieved a tuning range between 0.5 GHz and 3 GHz (0.015 - 0.1 cm^{-1}). Four signals were recorded simultaneously and stored on the oscilloscope (LeCroy 6030): the ramp voltage, the intensity transmitted through the cavity, the reference cell and the single mode fiber.

Results and Discussion

For the pressure range of 0.4-5 Pa used in the experiments applying sub-Doppler-techniques three broadening effects have to be considered: Pressure broadening, power broadening and transit time broadening. The contribution from each of these effects is estimated to be between 0.1 and 1.0 MHz, depending on the exact experimental conditions. The contribution from the natural linewidth is at least two orders of magnitude smaller and can be neglected. The width of the measured dips varied between 1 and 4 MHz. Some of the broadening, especially for the smaller *J*-lines may arise from the hyperfine splittings of the N-atom, which are on the order of several hundred kHz and could not be resolved.

For the FTIR spectra the spectral lineshape is given by a convolution of the instrumental line shape function with a Gaussian Doppler profile. The width of the instrumental line shape was obtained as an average from a fit of the instrumental line shape function to a number of isolated lines. For strongly overlapping lines the position and the intensity of the individual lines were then obtained from a nonlinear fit of the superposition of different lines to the measured spectrum, where the line positions from measured dips were used as starting positions.

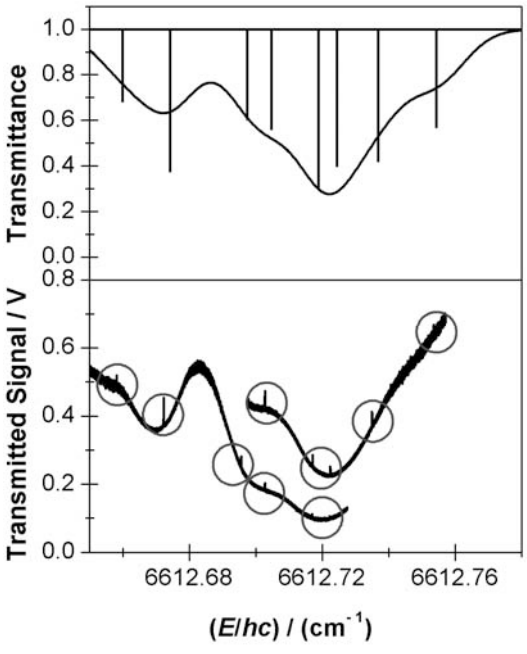

Figure 1: *Comparison of a measured dip spectrum (lower trace) to a multiline fit to the FTIR-spectra measured at 298 K (upper trace). The vertical lines give the positions and intensities of the individual absorption lines. Eight different lines have been identified in the saturation spectra. For a better visibility the measured dips are indicated by a circle. One additional line is included in the fit on the low frequency side of the FTIR spectrum.*

In figure 1 a cluster of eight overlapping lines is shown. The lower trace represents the light intensity transmitted through the cavity and the measured dips are indicated by a circle for better visibility. The upper trace shows the transmittance of the measured FTIR spectrum at

room temperature. The measured line positions obtained from the dip spectrum and from the multiline fit of the FTIR spectrum are summarized in table 1 together with the measured dip widths and the pressure conditions. In general a good agreement is obtained between the dip positions and the results from the FTIR spectra. The accuracy of the measured dip positions is very much dependent on the accuracy of the line positions of the reference gas used.

Trans-ition	$E_{\nu_1+\nu_3\leftarrow\nu_1}/hc$ cm^{-1}		FWHM MHz	p μbar	Ref. Gas
	FTIR	Lamb-Dip			
-	-	6612.6581	2.42	10	CH_4
-	6612.6749	6612.6723	1.37	10	CH_4
(1,1)(1,0)s	-	6612.6956	1.72	10	CH_4
(1,1)(1,0)s	6612.70045	6612.7028	1.56	10	CH_4

Trans-ition	$E_{\nu_1+\nu_3\leftarrow\nu_1}/hc$ cm^{-1}		FWHM MHz	p μbar	Ref. Gas
	FTIR	Lamb-Dip			
(2,1)(2,0)a	6612.7174	6612.7171	1.42	10	CH_4
(2,1)(2,0)a	6612.72373	6612.7224	2.115	10	CH_4
(2,1)(2,0)s	6612.73596	6612.735	2.98	10	CH_4
(3,1)(3,0)a	6612.75426	6612.75248	1.71	10	CH_4

Table 1: *Comparison of the transition frequencies obtained from FTIR and Lamb-Dip spectroscopy of figure 1. Preliminary assignments of the shown lines are taken from [6,7,8] and are given in the column headed "Transition" as (J',K')(J'',K'')$_{inversion\ symmetry}$.*

Acknowledgment

We are indebted to Sieghard Albert for measuring the FTIR spectra and to Andres Laso and Eduard Peyer for technical support. Our work is supported financially by the ETH Zürich and the Schweizerischer Nationalfonds.

[1] M. Quack, J. Stohner, M. Willeke, *Ann. Rev. Phys. Chem.*, 59:741-769, 2008.
[2] R. Marquardt, M. Quack, I. Thanopoulos, D. Luckhaus, *J. Chem. Phys.*, 118(2):643-658,2003.
[3] R. Marquardt, M. Quack, I. Thanopoulos, D. Luckhaus, *J. Chem. Phys.*, 119(20):10724-10732, 2003.
[4] S. N. Yurchenko, J. Zheng, H. Lin, W. Thiel, *J. Chem. Phys.*,123:3236, 2005.
[5] K. K. Lehmann, S.L. Coy, *Spectrochim. Acta A*, 45:47-56, 1985.
[6] L. Lundsberg-Nielsen, F. Hegelund, F. M. Nicolaisen, *J. Mol. Spectr.*, 162:230-245, 1993.
[7] G. Berden, R. Peeters, G. Meijer, *Chem. Phys. Let.*, 207:131-128, 1999.
[8] L. H. Xu, Z. Liu, I. Yakovlev, M. Y. Tretyakov, R. M. Lees, *Infrared Phys. Technol.*,45:31-45, 2004.

The Formation and Dissociation of Small Molecular Ions

Douglas KMD,[1] Price SD[1]

[1] *University College London, Department of Chemistry, 20 Gordon Street, London, WC1H 0AJ, UK*

The ionisation of small molecules is an important fundamental process in many environments, such as in plasmas, which are formed of ionised media, and in planetary atmospheres, where high energy radiation is likely to cause single and multiple ionisation. Any ionised species formed following ionisation can play a significant role in the chemistry of their environments. Therefore, to accurately model such environments accurate and reliable information is required on the formation efficiency of any ions and ion fragments the may be formed. This data is usually presented in the form of total or partial ionisation cross-sections (PICS). Total ionisation cross-sections give a measure of the total number of ions produced following the passage of a number of electrons or photons through a target gas of known uniform number density. To determine PICS requires the additional identification of the products from the ionisation events, rather than just counting the total number of ions formed.

Using a time-of-flight mass spectrometer (TOFMS) coupled with a 2D ion coincidence technique, ionisation cross-sections of methanol (CH_3OH) and hydrogen sulphide (H_2S) have been investigated, together with the dissociation of their single and multiply charged ions. The ionisation of methanol, the simplest alcohol, is a process of particular interest to astrophysicists, as methanol is one of the most abundant molecules detected towards various astrophysical regions such as in comets [1-3], and protostellar regions [4,5], where ionisation events are relatively common. Hydrogen sulphide has also been detected towards various astrophysical regions, including comets [6], giant molecular clouds [7] and star forming regions [8], with both the neutral and ionised products formed following ionisation of H_2S playing significant roles in the chemistry of such regions [9-11].

Our 2D mass spectrometric experiments carried out allow us not only to produce PICS but also precursor specific PICS. These precursor-specific relative PICS represent the relative cross-section for forming a fragment ion X^{m+} by single (n = 1), double (n = 2) and triple (n = 3) ionisation. For example $\sigma_1[H^+]$ represents the formation of H^+ resulting from dissociative single ionisation of the parent molecule, whereas $\sigma_2[H^+]$ and $\sigma_3[H^+]$ represent the formation of H^+ from dissociative double and triple ionisation of the parent molecule respectively. Additionally detailed information on the dynamics of the dissociation of any parent dication or trication formed can also be obtained. This information shows that the contribution from multiple ionisation to the total ion yields of various molecules are more significant than previously thought. In fact many previously measured ionisation cross-sections are

inaccurate, due to the loss of the highly energetic ion fragments formed from the dissociation of multiply charged ions.

From the relative PICS and precursor-specific relative PICS measured following electron ionisation of methanol, it can be seen that contribution from double ionisation to the total ion yield reaches a maximum of 20% between ionising electron energies of 150 and 200 eV. The results also show that although the majority of fragment ions formed following electron ionisation of methanol are primarily from dissociative single ionisation, others are more likely to be formed from dissociative double ionisation. In fact the H_3^+ ion fragment is produced solely from dissociative double ionisation, with no contribution from single ionisation. For many of the ion pairs that do results form dissociative double ionisation, we have also been able to determine the KER upon dissociation of the parent dication, together with the dynamics of the break-up. For example, one such dissociation channel results in the ion pair $CHO^+ + H_2^+$. By examining the peak of this ion pair it has been determined that the methanol dication (CH_3OH^{2+}) initially breaks-up into $CH_3O^+ + H_3^+$, with a kinetic energy release of 2.8 ± 1.0 eV. The H_3^+ fragment then undergoes a secondary brake-up into H_2^+ and H.

From the relative and precursor-specific relative PICS measure following electron ionisation of hydrogen sulphide, it can be seen that contribution to the ion yield from double ionisation reaches a mazimum of 19.5 % at 100 eV ionising electron energy, and that contribution from triple ionisation reaches a maximum of 0.3% at 200 eV ionising electron energy. Good agreement is found between our data and one set of recently published absolute PICS [12], in which the efficient collection of energetic ion fragments is demonstrated. Conversely discrepancies are observed with another set of recently published data [13], in which the majority of calculated relative PICS are smaller than those found here, especially for the lighter fragment ions. These discrepancies are attributed to the loss of some translationally energetic fragment ions in this earlier work. However for one ion (H_2S^{++}) our relative PICS are significantly lower. One possible explanation for this difference is that the significantly higher amounts of H_2S^{++} in this previous data [13] could be due to background OH^+, resulting in a peak at m/z = 17 the same as H_2S^{++}. This OH^+ is the result of background water in the MS-chamber, and is corrected for in our experiments by normalisation to the H_2O^+ peak observed at m/z = 18 in our mass spectra. KER determinations have also been made for several of ion pairs formed following dissociation of the hydrogen sulphide dication (H_2S^{++}). Using these calculated KERs, along with thermochemical data [14] on the products of the break-up reactions, we were also able to estimate precursor state energies of the hydrogen sulphide dication before fragmentation. Several of these precursor state energies can be related to previously determined electronic states of H_2S^{++} [15]. However some of these precursor state energies lie below the double ionisation potential of H_2S, suggesting that the products from some dissociation channels are formed in excited states.

References

[1 M.J. Mumma, N. Dello Russo, M.A. DiSanti, K. Magee-Sauer, R.E. Novak, S. Brittain, T. Rettig, I.S. McLean, D.C. Reuter, L.H. Xu, *Sci.*, **292**, (2001) 1334.
[2] J. Crovisier, D. Bockelee-Morvan, Remote observations of the composition of cometary volatiles, ISSI Workshop on Composition and Origin of Cometary Material, Bern, Switzerland, 1998, p. 19.
[3] D. Bockeleemorvan, J. Crovisier, P. Colom, D. Despois, *Astron. Astrophys.*, **287**, (1994) 647.
[4] K.M. Pontoppidan, E.F. van Dishoeck, E. Dartois, *Astron. Astrophys.*, **426**, (2004) 925.
[5] R.J.A. Grim, F. Baas, T.R. Geballe, J.M. Greenberg, W. Schutte, *Astron. Astrophys.*, **243**, (1991) 473.
[6] J. Crovisier, D. Despois, D. Bockeleemorvan, P. Colom, G. Paubert, *Icarus*, **93**, (1991) 246.
[7] P. Thaddeus, R.W. Wilson, M.L. Kutner, K.B. Jefferts, A.A. Penzias, *Astrophys. J.*, **176**, (1972) L73.
[8] Y.C. Minh, L.M. Ziurys, W.M. Irvine, D. McGonagle, *Astrophys. J.*, **366**, (1991) 192.
[9] R. Lucas, H.S. Liszt, *Astron. Astrophys.*, **384**, (2002) 1054.
[10] T.J. Millar, E. Herbst, *Astron. Astrophys.*, **231**, (1990) 466.
[11] W.W. Duley, T.J. Millar, D.A. Williams, *Mon. Not. R. Astron. Soc.*, **192**, (1980) 945.
[12] B.G. Lindsay, R. Rejoub, R.F. Stebbings, *J. Chem. Phys.*, **118**, (2003) 5894.
[13] M. Rao, S.K. Srivastava, *J. Geophys. Res [Planets]*, **98**, (1993) 13137.
[14] P.J. Linstrom, W.G. Mallard, Eds., *NIST Chemical WebBook; NIST Standard Reference Database Number 69*, National Institute of Standards and Technology, Gaithersburg MD, 20899, (2008)
[15] A. Cesar, H. Agren, A.N. Debrito, S. Svensson, L. Karlsson, M.P. Keane, B. Wannberg, P. Baltzer, P.G. Fournier, J. Fournier, *J. Phys. Chem.*, **93**, (1990) 918.

Low-Energy Electron Damage to Di-Pyrimidines

Achim Edtbauer[1], Christian Mitterdorfer[1], Katherine Russell[2], Linda Feketeova[2], Lukas An der Lan[1], Erna Schuhfried[1], [1]Stephan Denifl[1], Uta Wille[2], Richard O'Hair[2], Tilmann D. Märk[1], Paul Scheier[1]

[1] Institute for Ion Physics and Applied Physics and Centre of Molecular Biosciences Innsbruck, University of Innsbruck, Technikerstr. 25/3, Innsbruck, Austria

[2] School of Chemistry, University of Melbourne, Victoria 3010, Melbourne, Australia

The increase of ultraviolet radiation reaching the earth's surface, caused by the depletion of the stratospheric ozone layer shows the importance of investigating the effects of UV-induced DNA damage. DNA is very sensitive to UV radiation since the absorption maximum of DNA is in the UV region.

UV-radiation is known to induce mutagenic and cytotoxic DNA lesions: e.g. the cyclobutane –pyrimidine dimers [1]. DNA damage is then also induced by secondary processes which occur after irradiation, their nature is either physical or chemical. Among them the action by low energy electrons turned out be highly relevant. This secondary species interact with molecules by DEA (Dissociative Electron Attachment).

Here we study DEA to a 1,2-dimethylcyclobutane pyrimidine dimer methylated at the nitrogen atoms. (See Figure below.)

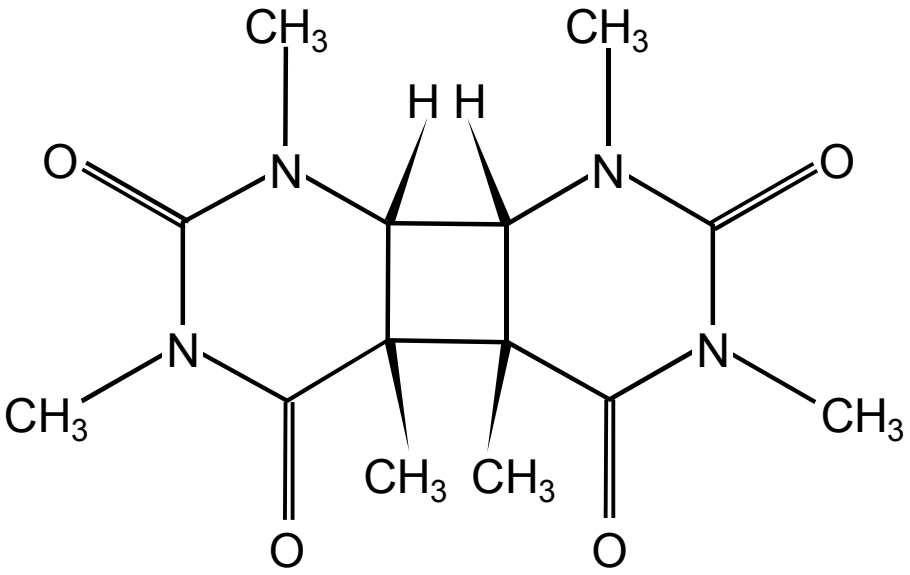

The apparatus used for the presented measurements is a crossed electron/molecule beams-instrument consisting of a neutral molecular beam source, a Nier-type ion source and a double-focusing two sector instrument in reverse BE-geometry with high sensitivity. Through a capillary with the diameter of 1 mm the gaseous molecules effuse directly into the ion block, where the interaction with the electron beam occurs. Negative ions formed are extracted into the mass spectrometer. The mass selected anions are finally detected by a channel electron multiplier.

The electron attachment measurements show a surprising fragmentation pattern at electron energies only slightly above 0eV. The mass spectra reveal that the highest anion fragment is mass 139 which corresponds to a symmetric cleavage minus one methyl group. This fragmentation pattern which reminds of fragmentation patterns of explosives like TNT could perhaps be one reason for the DNA damage caused by these molecules.

Acknowledgements

This work has been supported by the FWF, Wien, Austria and the European Commission, Brussels. S.D. gratefully acknowledges an APART-fellowship from the Austrian Academy of Sciences.

References

[1] Rajeshwar P. Sinha, Donat-P. Häder, *Photochem. Photobiol. Sci.* **1**, 225-236 (2002)
[2] Sylwia Ptasinska, Stephan Denifl, Sascha Gohlke, Paul Scheier, Eugen Illenberger, Tilmann D.Märk, *Angew. Chem. Int. Ed.* **45**, 1893-1896 (2006)
[3] Sylwia Ptasinska, Stephan Denifl, Verena Grill, Tilmann D. Märk, Paul Scheier, Sascha Gohlke, Michael A. Huels, Eugen Illenberger, *Angew. Chem. Int. Ed.* **44,** 1647-1650 (2005)

Imaging UV Photochemistry – from Molecules to Clusters

Juraj Fedor[1], Vikotriya Poterya[1], Andrij Pysanenko[1], Ondřej Votava[1], Michal Fárník[1]
[1] J. Heyrovský Institute of Physical Chemistry of the Czech Academy of Sciences, Dolejškova 3, 18223 Prague
Email: juraj.fedor@jh-inst.cas.cz

We present study of UV photochemical reactions in several systems. Our main goal is to elucidate how the photochemistry changes when moving from isolated molecules to larger complexes – clusters. This approach provides an important bridge between studies of molecules in the gas phase (which is the case in most of experiments performed nowadays) and the processes which are happening in real systems (e.g. biochemical or atmospherical processes).

Experimentally, we measure kinetic energy distributions of photofragments in crossed beam setups. Two apparatuses are utilized in present work: (i) the molecular beam apparatus used for studies of isolated molecules and (ii) the cluster beam apparatus. Both setups use the same laser system. Here we concentrate on photodissociation at 243.1 nm. At this wavelength, the hydrogen atom photofragments are ionized via a (2+1) resonant enhanced multiphoton ionization (REMPI) scheme and are consequently detected. The molecular beam apparatus is equipped with an ion imaging detection system, presently used in the velocity mapping mode [1], which provides information both about the kinetic energy and angular distribution of H-atom photofragments. The much more complex cluster beam apparatus uses a time-of-flight technique for determining the kinetic energy distributions of photofragments [2].

We present results for two classes of compounds: hydrogen halides (HBr, HCl, HI) and small aromatic molecules (benzene C_6H_6, pyridine C_5H_5N). Molecular hydrogen halides fragment into two different channels where the halogen atom is in two different states separated by the spin-orbit splitting. In clusters, additional peak in kinetic energy spectrum appears at very low energies due to caging effect. For the small aromatic molecules, the kinetic energy distributions in molecules and clusters are very similar and have statistical character. This suggests, that already in isolated molecules the phodissociation proceeds via coupling to the ground state and randomization of internal energy among vibrational degrees of freedom.

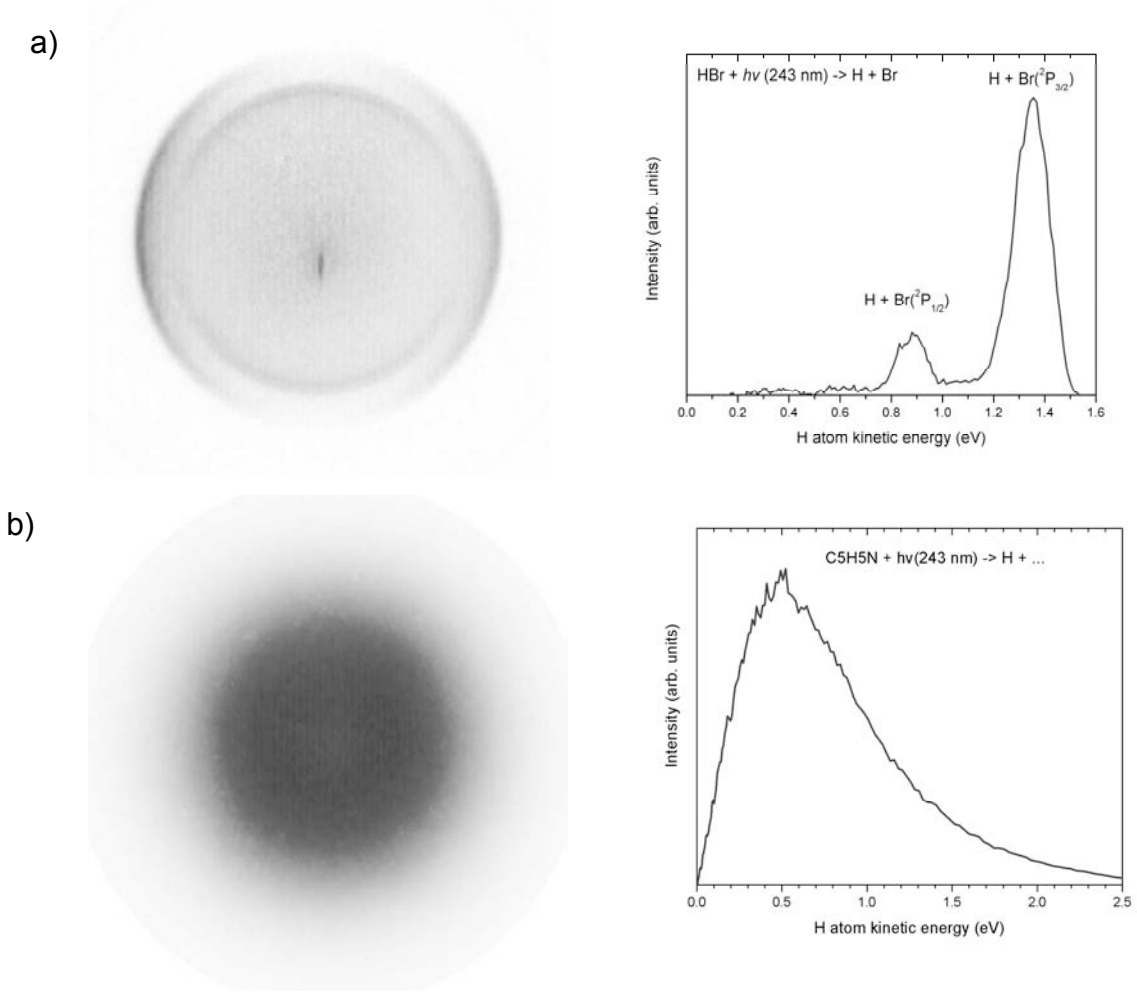

FIG. 1. *Velocity-mapped ion images of ionized H-atom photofragments and the corresponding kinetic energy distributions for a) molecular HBr and b) molecular pyridine C_5H_5N. The laser polarization is parallel to the detector, orientation of the molecular beam is from top to bottom.*

References

[1] A.T.J.B. Eppink, D.H. Parker, Rev. Sci. Instrum 68, 3477 (1997)
[2] U. Buck, J. Phys. Chem. A **106**, 10049 (2002)

The LEEPAR Project: a Combined Physical, Chemical and Biological Study of DNA Radiosensitization by Gold Nanoparticles and Pt Chemotherapeutic Agents

F. Ferreira da Silva [a, b, c], **C. Sicard-Roseli** [a,c], **A. Lafosse** [b,c] **and L. Sanche** [a, b, d]
[a] *Laboratoire de Chimie Physique, Université Paris-Sud, 91405 Orsay France*
[b] *Laboratoire des Collisions Atomiques et Moléculaires, Université Paris-Sud, 91405 Orsay France*
[c] *CNRS, 91405 Orsay France*
[d] *Groupe en Sciences des radiations, Faculté de medicine, Université de Shebrooke, Quebec, Canada J1H 5N4*

It is now well established that low energy electrons (LEE) play a key role in radiation induced processes, particularly in radiobiology and radiotherapy. These LEE are one of the major products of high-energy radiation in biological cells. LEE can efficiently fragment not only small molecules such as H_2O or O_2 but also large biomolecules including oligonucleotides and DNA [1–3]. As shown recently [4,5] increasing the number of LEE near DNA or attaching to DNA chemotherapeutic agents can increase the magnitude of this fragmentation. Such a manipulation of the damage induced by LEE may have considerable consequences to improve chemoradiation therapy.

Gold nanoparticles have been investigated as a potential radiosensitizer in Radiotherapy. Gold nanoparticles have two important features. They increase substantially the absorption of radiation energy, which in turn increases the number of LEE near their location. Furthermore, they accumulate preferentially in tumor cells for diameters near 2nm [6,7].

A particular aim of the LEEPAR (Low-Energy (0-30eV) Electron induced Processes for application to Astrochemistry and Radiotherapy) project is to investigate LEE-reactions in plasmid DNA bonded to radiosensitizers and chemotherapeutic agents. The techniques to be used to understand modifications of LEE-DNA interactions are electron stimulated desorption and HREELS (High Resolution Electron Energy Loss Spectroscopy). The results will be compared to those obtained with: (1) pure plasmid DNA, (2) the indirect effect of radiation in similar studies in solution and (3) cell survival studies.

As preliminary results in our studies, we present in this communication, those obtained from solution of DNA, DNA + a Pt chemotherapeutic agent and DNA + a Pt chemotherapeutic agent + a gold nanoparticles, after bombardment with 18 keV electrons.

References

[1] B. Boudaiffa *et al., Science*, 287, **2000**, 1658
[2] L. Sanche, *Mass. Spec. Rev.*, 21, **2002**, 349
[3] L. Sanche, *Eur. Phys. D – Atom., Mol. Opt. Phys.*, 35, **2005**, 367
[4] Y. Zheng *et al.*, *Radiation Research*, 169, **2008**, 19-27
[5] Y. Zheng *et al.*, *Phys. Rev. Lett.,* 100, **2008**, 198101
[6] A. Anshup *et al. Langmuir*, 21, **2005**, 11562-11567
[7] T. Niidome *et al., Chemm comm.*, **2004**, 1978-1979

Aluminum Hydride Clusters and Their Derivatives: Anion Photoelectron Spectroscopic Studies

Jacob Graham[1], Shawn Li[1], Andrej Grubisic[1], Kit Bowen[1], Puru Jena[2], Gerd Gantefoer[3], and Hansgeorg Schnoeckel[4]

[1] *Dept. of Chemistry, Johns Hopkins University, Baltimore, MD, 21218, USA*

[2] *Dept. of Physics, Virginia Commonwealth University, Richmond, VA*

[3] *Dept. of Physics, Konstanz University, Konstanz, Germany*

[4] *Dept. of Chemistry, Karlsruhe University, Karlsruhe, Germany*

While boron forms many hydrides, aluminum has been thought to form only a few. Using a pulsed arc discharge source, we found that aluminum can form many hydrides. Using anion photoelectron spectroscopy to measure their HOMO-LUMO gaps, we found that some of these species display the hallmarks of significant stability. Calculations and electron counting rules implied specific structures. The bulk synthesis of derivatives of the Al_4H_6 stoichiometry permitted x-ray crystallographic analysis which found the same structure implied by theory. This work follows a path from discovery of previously unknown molecules in the gas phase to the bulk synthesis of their analogs. These studies have implications to hydrogen storage materials and to propulsion. We have enjoyed support and collaborations in this work with G. Gantefoer, P. Jena, and H. Schnoeckel.

Chemical Reactions of PETN Molecules on Cu(110) Driven by STM Techniques

M.Hager[1], C. Urban[2], J. Fernandez[2], F. Iacono[2], R.Otero[2], P. Scheier[1]

[1] *Institut für Ionenphysik und Angewandte Physik, Technikerstraße 25b, 6020 Innsbruck*

[2] *LASUAM, Universidade Autonoma de Madrid, 28049 Madrid*

Motivation:

Pentaerythritol tetranitrate, $C_5H_8N_4O_{12}$ (PETN), belongs to the same chemical family as nitro-glycerine, is highly explosive, chemically stable which can be stored for long periods of time, and has been used as a prime composition in detonator cords, boosters, fuses, hand grenades, bombs, ground mines and artillery ammunition.

Gas phase dissociative electron attachment (DEA) measurements to PETN have been performed in a crossed electron-molecular beam experiment with high-energy resolution. DEA is operative at very low energies close to ~ 0 eV showing unique features corresponding to a variety of several fragment anions being formed. There is no evidence of the parent anion formation. The fragmentation yields are also observed for higher electron energies and are operative via several resonant features in the range of 0 – 20 eV. They involve several remarkable complex reactions associated with multiple bond cleavages and the formation of new bonds [1].

Additionally and complementary to these gas phase experiments we have now investigated chemical reactions of PETN adsorbed on Cu(110) induced by tunneling electrons.

The experimental setup in Madrid

The TIREMISU system is an UHV chamber provided with a Variable Temperature Fast-Scanning STM; a Low-Energy Electron Diffraction (LEED) system to check the crystalline quality of the sample that also enables us to carry out Video-LEED experiments, thereby precisely determining the atomic structure of the sample; Auger-electron spectroscopy to ensure the cleanliness of the surface; a plasma-source for depositing atomic nitrogen; an evaporator specifically designed to work with organic molecules; and several facilities for sample preparation and assessment of the residual gas pressure [2].

Experimental Data

The explosive compound was heated in an external oven and then deposited onto HOPG and Cu(110). In figure 1 an image of PETN on HOPG is shown. It can bee seen that it is not very likely to find PETN on the surface. In contrary in figure 2 areas of self assembled PETN molecules on Cu(110) are visible.

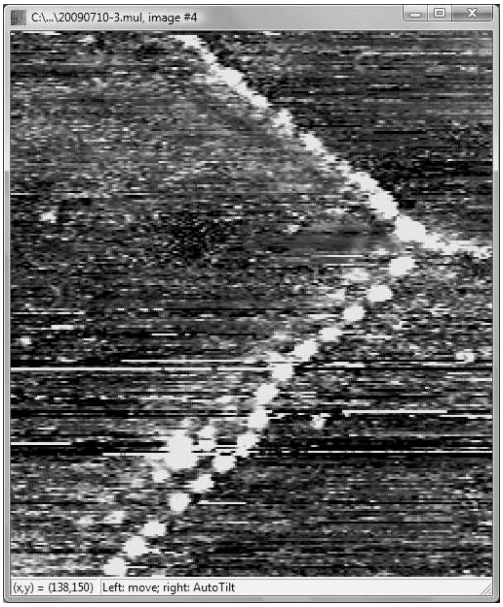

Figure 1: PETN molecules deposited onto HOPG, image size 500Å×500 Å

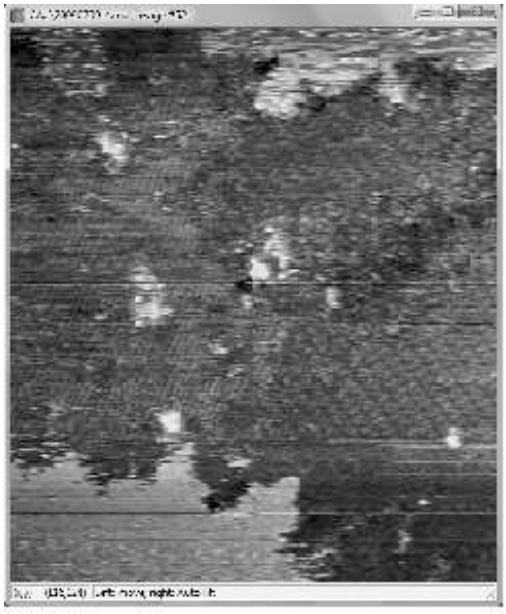

Figure 2: PETN molecules deposited onto Cu(110),image s. 1000 Å×1000 Å

Figure 3:Rectangular ice lands image size 300 Å ×300 Å

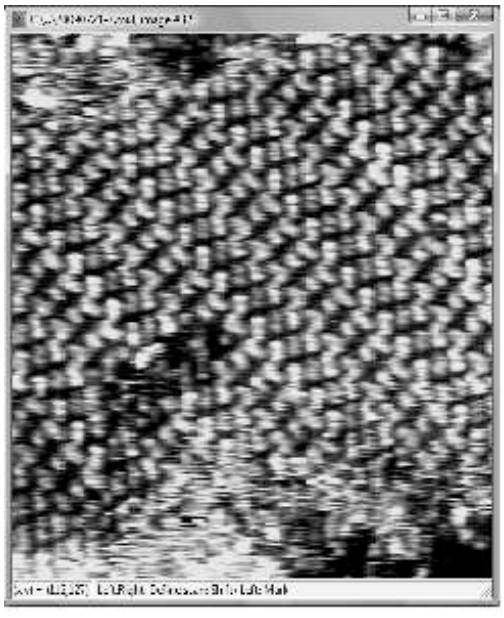

Figure 4: Striped phase image size 150 Å ×150 Å

Based on these first results we chose to concentrate on deposition of PETN onto Cu(110). We started a systematic investigation where we varied different experimental conditions, e.g. deposition temperature, and scanning temperature. We could demonstrate that for deposition and measurements at room temperature molecules tend to form rectangular islands with hexagonal arrangement that are transformed into a so-called striped phase only by measuring a second time over the same area. By deposition onto a cold sample and measuring at cold temperatures (~ -30 °C) it can be seen that the hexagonal phase is the first one to appear which then transforms into the striped phase under certain conditions. If the sample is too cold (below -50 °C) the scanning current and voltage do not suffice to change the rectangular phase into the stripped one. At around -30°C it is still possible to change a rectangular island into a stripped one by applying a voltage ramp to about 3 V. In figure 3 and 4 the two different phases can be seen.

Acknowledgement

Financial support by ECCL, FWF (Austrian Science Fund) and ITS-LEIF

References

[1] A. Edtbauer et al, to be published
[2] http://lasuam.fmc.uam.es/lasuam/tiremisu.php

Temperature Dependent Ion Chemistry of Multiply-Charged DNA Anions Studied in a Penning Trap

Oliver Hampe[1,2], Tatjana Karpuschkin[1], Florian Schinle[1], Marco Neumaier[1], Manfred Kappes[1,2]
[1] *Institut für Nanotechnologie, Karlsruhe Institute of Technology (KIT) - Campus North,*
[2] *Institut für Physikalische Chemie, Karlsruher Institute of Technology (KIT) - Campus South*
email: Oliver.Hampe@kit.edu

An important class of biologically important molecular ions, such as oligonucleotides and peptides, exist in their native environment as multiply charged anions (MCAs). Their properties as isolated entities, however, remained widely uncharted until electrospray ion sources made them accessible to mass-spectrometric investigations. In the gas-phase the interaction between the excess negative charges is less screened compared to the condensed phase (lacking counter-ions and/or a solvation shell) and may lead to an electronic situation which is metastable with respect to decay channels like electron autodetachment and or anion loss.
By now electron autodetachment has been observed and corresponding room-temperature kinetics has been studied for a number of small to medium-sized MCAs with *negative* electron affinities like $PtCl_4^{2-}$ [1], trisulfonated hydroxy-pyrene ($HPTS^{3-}$) [2] and tetrasulfonated metal-phthalocyanines ($CuPc(SO_3)_4^{4-}$) [3]. In this context the oligonucleotide $[dA5\text{-}4H]^{4-}$ was recently shown to be metastable with a *negative* fourth electron affinity EA= –0.3eV [4].
In this contribution we present details of a Penning trap (as part of a Bruker FT-ICR mass spectrometer) capable of operating in a temperature range of T=90-420 K under ultra-high vacuum conditions of $\sim 2 \cdot 10^{-10}$mbar. Using this recently modified instrument we are probing the decay channels and their temperature dependent kinetics for several multiply-charged oligonucletides $[dA5\text{-}4H]^{4-}$ and $[dT7\text{-}6H]^{6-}$ (A=adenine, T= thymine).

Specifically, two reaction channels were observed for $[dA5\text{-}4H]^{4-}$:
(a) loss of a base anion A^- , and
(b) protonation from reactive collisions with (residual) water molecules.

The kinetic data indicate that there might be two (or more) isomers present under our experimental conditions which is currently also studied by ion mobility experiments. For both channels the kinetics were studied in detail as a function of trap temperature and the activation energies were deduced from the observed Arrhenius-type behaviour to be 1.13± 0.05 eV and 0.94±0.05 eV (for the base loss reaction, scheme a) and 0.50±0.05 eV for the protonation reaction (scheme b). [5]

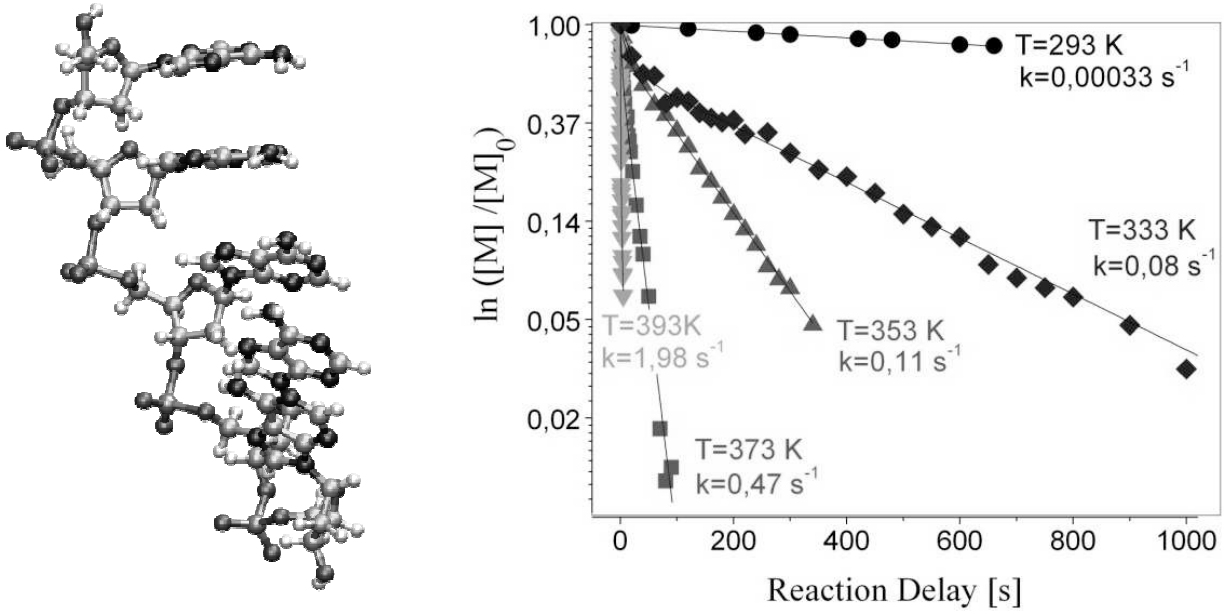

*Fig. 1: Molecular structure of tetra-anionic [dA5-4H]*4*– from a semiemprical PM3 calculation (left panel); kinetics of the parent ion decay channels (shown as logarithmic plot of parent ion intensity vs. time) of [dA5-4H]*4*– for various trap temperatures. Also given are the total rate constants as obtained from the linear fit shown as solid lines (right panel).*

References

[1] M. Blom, O. Hampe, S. Gilb, P. Weis, and M. M. Kappes, Tunneling electron emission from isolated platinum tetrahalide dianions, J. Chem. Phys. **115**, 3690 (2001).

[2] X.-B. Wang, A. P. Sergeeva, X.P. Xing, M. Massaouti, T. Karpuschkin, O. Hampe, A. I. Boldyrev, M. M. Kappes, L.-S. Wang, Probing the electronic stability of multiply charged anions: The sulfonated pyrene tri- and tetra-anions, J. Am. Chem. Soc. **131**, 9836 (2009).

[3] K. Arnold, T. S. Balaban, M. N. Blom, O. T. Ehrler, S. Gilb, O. Hampe, J. E. vanLier, J. M. Weber, and M. M. Kappes, Electron autodetachment from isolated nickel and copper phthalocyaninetetrasulfonate-tetraanions: isomer specific rates, J. Phys. Chem. A **107**, 794-803 (2003).

[4] J. M. Weber, I. N. Ioffe, K. M. Berndt, D. Loeffler, J. Friedrich, O. T. Ehrler, A. S. Danell, J. H. Parks, M. M. Kappes, J. Am. Chem. Soc. **126**, 8585 (2004).

[5] O. Hampe, T. Karpuschkin, M. Massaouti, M. Neumaier, and M. M. Kappes (in prep.).

Correlations between Survival Probabilities and Ionization Energies of Slow Ions Colliding with Carbon, Tungsten and Beryllium Surfaces

Zdenek Herman, Jan Žabka, and Andriy Pysanenko

V. Čermák Laboratory, J. Heyrovský Institute of Physical Chemistry, v.v.i., Academy of Sciences of the Czech Republic, Dolejškova 3, 182 23 Prague 8, Czech Republic

Survival probability of ions colliding with solid surfaces is one of the basic characteristics of ion-surface interactions. The absolute survival probability, S_a(%), is defined as the ratio of the sum of intensities of all product ions scattered from the surface to the intensity of the projectile ions incident on the surface. The values of the absolute survival probabilities were determined for hydrocarbon ions C1, C2, and C3 (either hydrogenated or deuterated) and several non-hydrocarbon ions (Ar^+, N_2^+, CO_2^+) on room-temperature (hydrocarbon-covered) and heated (600°C) surfaces of carbon (HOPG), tungsten, and beryllium. The S_a values were obtained by the ion-surface scattering method using the scattering apparatus EVA for several incident energies from a few eV up to about 50 eV and for the incident angle of 30° (with respect to the surface). The method of extracting the S_a values from the scattering data was described previously [1-5]. Values of S_a published previously [1-4] were complemented by new measured data [5].

A simple correlation between S_a and the ionization energy (IE) of the incident ions was found in the semi-logarithmic plot of S_a vs. IE. The plots of the data at 31 eV (Fig. 1 and Fig. 2) were linear for all studied surfaces and could be fitted by an empirical equation

$$\log S_a = a - b(IE).$$

The values of the parameters a and b were determined for all investigated room-temperature surfaces (carbon, tungsten, beryllium) and for heated surfaces of carbon and tungsten (Table 1).

The data for room-temperature surfaces showed very similar slopes both for carbon, tungsten, and beryllium (Fig. 2, right). This was presumably due to a hydrocarbon layer covering all these surfaces at room temperature. The correlation $S_a = a - b(IE)$. can be used to estimate unknown survival probabilities of ions on these surfaces from their ionization energies.

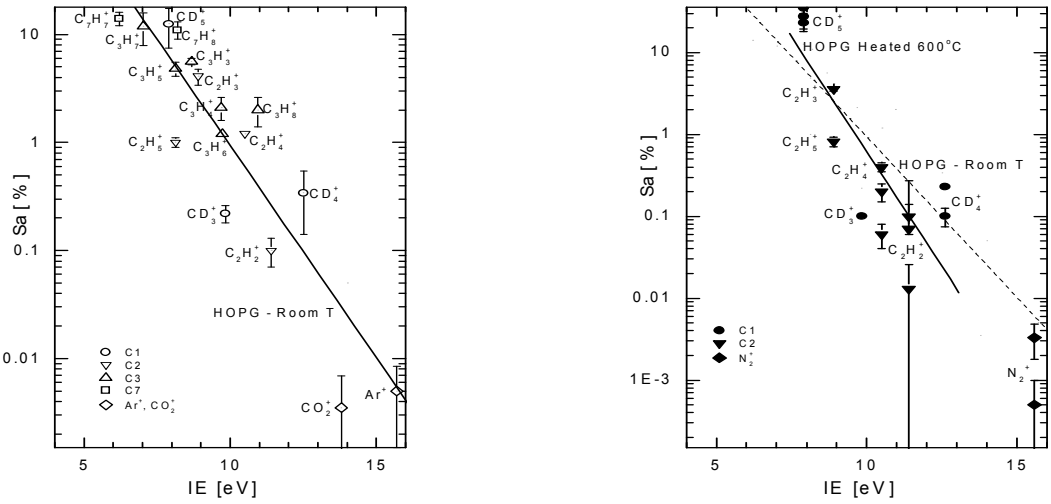

Fig. 1: *Dependence of survival probabilities of ions (S_a) on their ionization energies (IE) for collisions with room-temperature (left) and heated to* 600°C (right) carbon (HOPG) surfaces

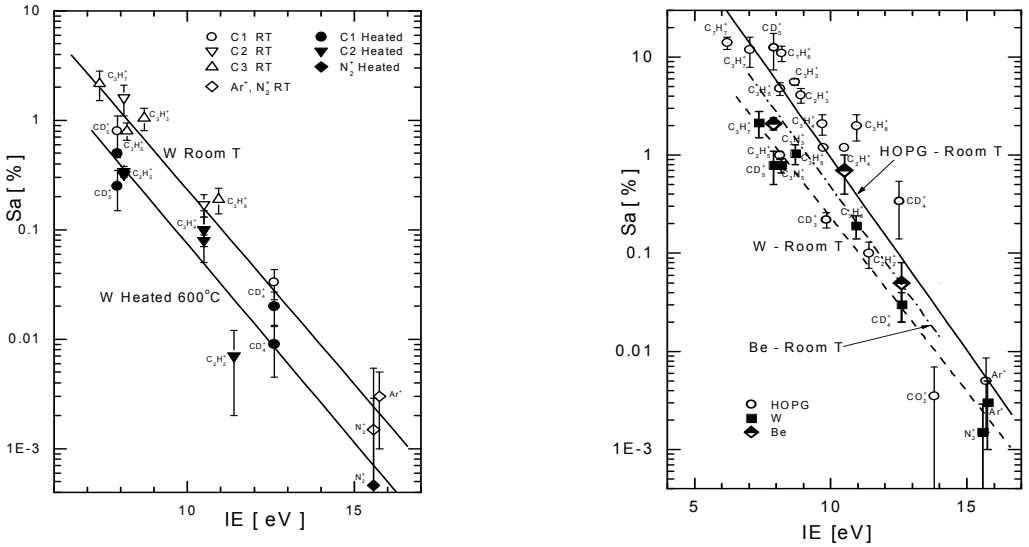

Fig. 2: *Left: Dependence of survival probabilities of ions (S_a) on their ionization energies (IE) for collisions with room-temperature and heated to 600°C surfaces of tungsten. Right: Comparison of the semi-logarithmic plots of the dependence S_a vs. IE for room-temperature surfaces of carbon (HOPG) (open points, see Fig. 3), tungsten (solid points, see Fig. 5), and beryllium (semi-opened diamonds). Incident energy 31 eV, incident angle 30° (with respect to the surface).*

Table 1. Values of parameters *a* and *b* in the plots log $S_a = a - b$(IE) for different surfaces

surface	*a*	*b*
carbon(HOPG),RT	3.9 ± 0.5	0.39 ± 0.04
carbon (HOPG), H	5.4 ±1.1	0.5 ± 0.1
tungsten, RT	2.9 ± 0.2	0.35 ± 0.02
tungsten, H	2.5 ± 0.4	0.35 ± 0.04
beryllium, RT	(3.9)	(0.39)

Note: RT – room-temperature, H- heated to 600° C

References

[1] Roithova, J.; Žabka, J.; Dolejšek, Z.; Herman, Z. *J. Phys. Chem. B*, **2002,** *106*, 8293.
[2] Jašík, J.; Roithová, J.; Žabka, J.; Pysanenko, A.; Feketeová, L.; Ipolyi, I.; Märk, T.D.;
[3] Herman, Z. *Int. J. Mass Spectrom*. **2006,** *249-250,* 162.
[4] Pysanenko, A.; Žabka, J.; Märk, T.D.; Herman, Z. *Int. J. Mass Spectrom* **2008**, *277* 229.
[5] Pysanenko, A.; Žabka, J.; Feketeova, L.; Märk, T.D.; Herman, Z. *Eur. J. Mass Spectrom* **2008,** *14***,** 335.
[6] Herman, Z.; Žabka, J.; Pysanenko, A. *J. Phys. Chem. A* (in press)
[7] Herman, Z. , in "Atomic and Molecular Data for Plasma Modeling", I.A.E.A, Vienna 2009 (in press).

Birch Reduction in the Gas Phase

Robert F. Höckendorf,[1] Christian van der Linde,[1] O. Petru Balaj,[1] Martin K. Beyer[1]

[1] *Institut für Physikalische Chemie, Christian-Albrechts-Universität zu Kiel, Olshausenstraße 40, 24098 Kiel, Germany, beyer@phc.uni-kiel.de*

Benzene and its derivatives are important building blocks in biochemistry and synthetic chemistry. The reduction of an aromatic system is limited by the high barrier of the first electron transfer. While in organic synthesis electrons solvated in liquid ammonia, a very powerful reductant, are utilized to overcome this barrier, in nature enzymes, like the benzoyl-CoA reductase, are catalyzing analogous reactions. We see evidence that chlorobenzene is dearomatized by hydrated electrons $(H_2O)_n^-$ yielding negative charged $OH^-(H_2O)_n$ and the neutral radical $C_6H_6Cl^\bullet$ [1]. Herein we present a detailed systematic reactivity and nanocalorimetry study of fluorine substituted benzene derivatives with hydrated electrons $(H_2O)_n^-$ in the gas phase by FT-ICR mass spectrometry.

Experimental

Hydrated electrons $(H_2O)_n^-$ are produced in an external laser vaporization source and transferred to the trap of an FT-ICR mass spectrometer, where they are reacted with gaseous benzene derivatives. Spectra taken at different reaction delays allow us to follow the reaction. The intensity of each cluster species is summed up and normalized. To produce reliable absolute rate constants a pressure calibration for each reactant was done using adequate ion-molecule reactions combined with collision rates calculated with ADO theory [2].

Results and Discussion

For all difluorobenzene and trifluorobenzene isomers, Birch reduction was observed. For difluorobenzene a strong dependence on the substitution position was seen. Only for the 1,2-isomer, fluorine abstraction was observed. For all trifluorbenzenes the abstraction of the fluorine took place, with a strongly isomer-specific branching ratio. This shows that the chemistry of the benzene derivatives is significant affected by substitution pattern.

For nanocalorimetric analysis, we fit the average number of water molecules as a function of time. The following factors were considered: the gradual loss of water due to black body radiation, which is strongly size dependent in combination with independently derived

reaction kinetics. The fluorine abstraction is in all cases about four times more exothermic than the Birch reduction. The resulting values for the respective reaction enthalpies ΔH are in good agreement with calculated data taken from the bulk in combination with G3 calculations. That indicates that we can derive solution thermochemistry from gas-phase nanocalorimetry [3].

References

[1] Y. Cao, Int. J. Mass Spectrom. 277, 206-209 (2008)
[2] T. Su, M. T. Bowers, Int. J. Mass Spectrom. Ion Phys. 12, 347 (1973)
[3] W. A. Donald, R. D. Leib, J. T. O'Brien, M. F. Bush, E. R. Williams, *J. Am. Chem. Soc.* **130**, 3371 (2008).

Quantum Simulation of Mg^+He_n and Ar^+He_n Clusters

Ji Jiang and Marius Lewerenz

MSME, FRE 3160 CNRS, Bât. Lavoisier, Université Paris-Est (Marne la Vallée), 77454 Marne la Vallée Cedex 2, France, Marius.Lewerenz@univ-paris-est.fr

We present accurate quantum Monte Carlo calculations of the stability and structure of Mg^+He_n and Ar^+He_n clusters using accurate many-body potential surfaces derived from high level ab initio calculations and including spin-orbit effects in the case of Ar^+. The highly quantum nature of the nuclear motion in these systems leads to significant delocalisation such that no sharp shell closure is found for Mg^+ doped helium clusters whereas the interactions are sufficiently strong in Ar^+ doped clusters to allow the appearance of magic numbers.

Introduction

Neutral helium clusters are extreme quantum systems whose cohesive energy pattern is controlled by their immense zero point energy arising from the combination of a small mass with very weak van der Waals interactions [1]. The implantation of one or several atomic and molecular dopants D into these clusters originally developed to understand the structure of the helium cluster itself has developed into an almost routine technique for the spectroscopic observation of stable species and reactive intermediates [2,3] and otherwise hard to prepare molecular or metal cluster systems [4,5]. The final step of most experiments involves ionization of the neutral $D@He_N$ system and leads to the formation of a series of smaller fragment ions of the type $D@He_n$, $n << N$. The relative abundance of individual mixed cluster ions reflects a complicated superposition of the relative stability of product ions and the actual fragmentation dynamics. The assumption of an almost thermodynamical situation often appears justified such that a correlation can be established between theoretical predictions of relative stabilities and observed relative ion count rates. Complementary information on stability patterns comes from ion drift tube experiments where mixed cluster ions are formed in multiple collisions of a dopant ion with helium atoms [6].

Rare gas ions were among the first species to be observed as dopants in helium clusters [7]. Accurate theoretical modeling of $(NeHe_n)^+$ [8] showed distinct, but complicated, binding hierarchies in agreement with experimental observations. Metal ions have attracted increasing interest in experiments aiming at the creation of reactive metal clusters like Mg_m and the search for extreme coordination numbers [9, 10]. The Mg^+ ion has an isotropic interaction of

moderate strength with helium atoms through a $^2\Sigma^+$ state and is thus an ideal candidate for methodological tests and comparison with ionization experiments. Heavier rare gas ions like Ar^+ present additional challenges for theoretical modelling due to the presence of a strongly attractive $^2\Sigma^+$ state and a shallow $^2\Pi$ state and spin-orbit splitting in the ^2P atomic ground state which is comparable with the van der Waals well depths and therefore strongly influences the effective interaction potential.

Computational details

The Mg^+ - He $^2\Sigma^+$ interaction potential of Gardner and Wright [11] which is based on CCSD(T) coupled cluster calculations with extrapolation to the complete basis set limit was fitted to an undamped HFD form with a leading $C_4\ r^{-4}$ term which accounts for the dominant long range charge-induced dipole interaction. For Ar^+-He we carried out CCSD(T) calculations with the MOLPRO suite of programs [12] and the full sequence of cc-pVXZ and aug-cc-pVXZ, X=2-6, basis sets developed by Dunning and coworkers [13]. The ab initio data for both $^2\Sigma^+$ and $^2\Pi$ states were fitted to the same undamped HFD form as above.

The many body surface for Mg^+He_n for the diffusion quantum Monte Carlo (DMC) calculations was constructed as a sum over pairwise contributions with additional terms accounting for the interaction between the induced dipoles carried by the helium atoms and using the experimental polarisability value. For Ar^+He_n a full complex 6x6 spin-orbit matrix was constructed for each particle arrangement with diagonal elements given as sums over pairwise Σ and Π contributions using the appropriate projections with additional induction terms and off-diagonal elements computed from the experimental atomic $^2P_{3/2}/^2P_{1/2}$ splitting of 1431.6 cm^{-1} [14]. The lowest eigenvalue of the matrix was used as potential energy input to propagate the random walkers within the DMC method.

Our DMC calculations were carried out with fixed ensembles of 1000 – 16000 weighted random walkers, imaginary time steps between 10 and 100 E_h^{-1}, and Jastrow/Fermi type trial wave functions as described in our earlier publications [8]. In spite of the use of trial wave functions a significant ensemble size bias on energies was observed such that extrapolations to infinite ensemble size were necessary for $n > 10$.

Results and discussion

Our CCSD(T) calculations for Ar^+He showed several unexpected features. Convergence of the shape and depth of the $^2\Sigma^+$ and $^2\Pi$ wells with respect to basis set size was very slow within the cc-pVXZ series such that even at sextuple zeta, X=6, level no satisfactory convergence

was found. The inclusion of diffuse basis functions in the aug-cc-pVXZ series dramatically improves the convergence but still leaves an uncertainty margin of several cm^{-1} for the well depths of about 435 and 142 cm^{-1} for the Σ and Π states, respectively. The conventional counterpoise correction performs very badly in particular for the ground state. Our final interaction potentials were computed by extrapolation to infinite basis set size using separate exponential and inverse power dependencies for the Hartree-Fock and correlation parts, respectively [15]. The quality of our final potential curves was checked by numerical solution of the radial Schrödinger equation for the X, A_1, and A_2 states arising from the spin-orbit treatment for Ar^+He. We obtained wave numbers of 92.5 and 64.9 cm^{-1} for the v=0→v=1 and v=1→v=2 vibrational transitions in the X state which compare very well with the experimental values of 92.9 and 66.2 cm^{-1} [16]. For the v=0→v=1 transition observed in the A_2 state we find 69.2 cm^{-1} in perfect and probably somewhat fortuitous agreement with experiment [16].

The total energies from our DMC calculations for Ar^+He_n show a marked effect of spin-orbit coupling on the structure of small clusters. Neglect of this effect strongly favors the first two helium atoms which can approach Ar^+ along the deep $^2\Sigma^+$ potential from opposite sides. This preference is significantly reduced due to the mixing of Σ and Π character which reduces the overall anisotropy of the potential. The common magic number of n=12 which is found in the sequence of minimum energy structures for our many body model becomes non magic upon inclusion of zero point energy when spin-orbit coupling is neglected. It reappears as magic in agreement with ion drift tube [6] and large neutral cluster ionization experiments [8] in our full treatment accounting for spin-orbit coupling and zero point energy.

For Mg^+He_n clusters our accurate DMC calculations contradict the pronounced shell structures obtained in the approximate variational Monte Carlo study of Rossi et al. [17]. We find a smooth build up of helium density in a first layer around Mg^+ which reaches saturation at n=18 or 19 at a density of 0.07 $Å^{-3}$, approximately three times the bulk liquid helium density. The energy pattern shows approximately constant binding energy increments near 50 cm^{-1} up to n=10 which thereafter slowly decrease to about 12 cm^{-1}, a value reached at n=18. There is no sharp transition between binding energy regimes which would correspond to shell formation. In fact the radial density build up beyond n=19 shows that the density minimum following the nearest neighbor maximum never drops below values of about 0.01 $Å^{-1}$, a situation which is incompatible with the interpretation as a solid ‘snowball’.

References

[1] J. P. Toennies and A. F. Vilesov, Angew. Chemie Int. Ed.43, 2622 (2004)
[2] F. Stienkemeier and K. K. Lehmann, J. Phys. B 39, R127-R166 (2006)
[3] J. M. Merritt, J. Küpper and R. E. Miller, Phys. Chem. Chem. Phys. 7, 67-78 (2005)
[4] K. Nauta and R. E. Miller, Science 283, 1895 (1999)
[5] T. Döppner, T. Diederich, J. Tiggesbäumker and K.-H. Meiwes-Broer, Eur. Phys. J. D, 16, 13-16 (2001)
[6] T. M. Kojima, N. Kobayashi, and Y. Kaneko, Z. Phys. D 22, 645 (1992)
[7] A. Scheidemann, B. Schilling, J. Northby, and J. P. Toennies, Physica B 165/166, 135 (1990)
[8] C.~A. Brindle, M. R. Prado, K. C. Janda, N. Halberstadt, and M. Lewerenz, J. Chem. Phys. 123, 064312 (2005)
[9] T. Döppner, Th. Diederich, S. Göde, A. Przystawik, J. Tiggesbäumker, and K.-H. Meiwes-Broer, J. Chem. Phys. 126, 244513 (2007)
[10] A. Hermann, M. Lein, and P. Schwerdtfeger, Angew. Chemie Int. Ed. 46, 2444-2447 (2007)
[11] T. G. Wright and A. Gardner, private comm. 2009
[12] MOLPRO is a package of ab initio programs written by H.-J. Werner, P. J. Knowles, R. Lindh, F. R. Manby and others, see http://www.molpro.net (2006)
[13] D. E. Woon and T. H. Dunning, Jr., J. Chem. Phys. 98, 1358 (1993)
[14] A. I. Krylov, R. B. Gerber, and R. D. Coalson, J. Chem. Phys. 105, 4626 (1996)
[15] W. Klopper, J. Chem. Phys. 115, 761-765 (2001)
[16] I. Dabrowski, G. Herzberg, and K. Yoshino, J. Mol. Spectrosc. 89, 491-510 (1981)
[17] M. Rossi, M. Verona, D. E. Galli, and L. Reatto, Phys. Rev. B 69, 212510 (2004)

Ion-Surface Interactions of $C_2D_x^+$ (x=2-6) on Fusion Relevant Carbon Fibre Composite (CFC)

A. Keim,[1*] N. Endstrasser,[1] B. Rasul,[1] F. Zappa,[2] A. Kendl,[1] Z. Herman,[3] P. Scheier,[1] T.D. Märk[1]
[1] *Institut für Ionenphysik und Angewandte Physik, Universität Innsbruck, Assoziation Euratom-ÖAW*
[2] *Instituto de Ciências Exatas, Campus Universitário Juiz de Fora*
[3] *J. Heyrovský Institute of Physical Chemistry, Academy of Sciences of the Czech Republic*
[*] *alan.keim@uibk.ac.at*

Introduction

In the last years the field of ion-surface interactions has developed into a modern and respected branch of science. Research and development of feasible fusion reactors requires reliable fundamental data quantifying plasma-wall interactions. Modelling and computational science for the pioneering project ITER depend on the determination of erosion and deposition coefficients of the involved plasma projectiles on the materials of choice: beryllium, tungsten and carbon, in the form of carbon fibre composite (CFC).
From a chemical point of view additional information on the projectile ion can be obtained by such ion-surface collisions at incident energies up to 100eV. Bond dissociation processes of the impinging ion can be measured, since the converted internal energy lies in the order of typical bond energies [1].

Experimental setup

In the experimental setup of the BESTOF apparatus in Innsbruck deuterated hydrocarbons $C_2D_x^+$ (x=2-6) are produced by electron impact ionization of C_2D_6 (Fig. 1). The ions are then extracted by an acceleration potential of 3kV and mass selected by a reverse geometry double focusing two sector field mass spectrometer. The exit slit of the E-sector is followed by a Faraday cup, which can be moved in and out of the beam line and is used for determination of the ion current. After being focused by an Einzel lens, the ions enter the collision chamber where a set of ion-optical lenses focuses and decelerates the beam to the desired collision energy. The incident angle is 45° with respect to the surface normal, while the scattering angle is 91°. The irradiated surface samples are cut from the non-plasma-exposed back of ASDEX-Upgrade first wall CFC tiles. Secondary ions are accelerated by another set of electrostatic lenses and enter a time-of-flight mass analyzer, terminated by a multi-channel plate detector [2].

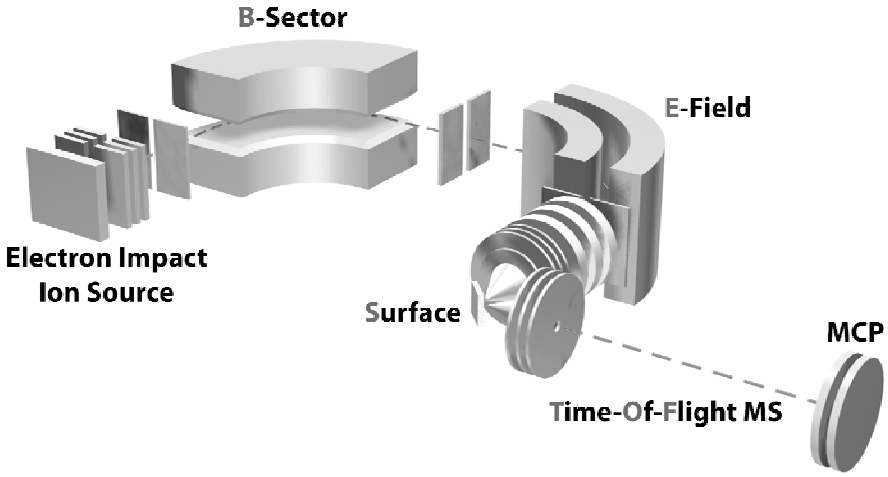

Fig. 1: Experimental setup BESTOF

Product ion mass spectra of $C_2D_x^+$ on CFC

Product ion mass spectra of deuterated hydrocarbons $C_2D_x^+$ on CFC at incident energies ranging from 0-100eV are measured for all fragments produced by electron ionisation of C_2D_6. All measurements were carried out with the surface at room temperature and under these conditions the surface of the sample is covered by a hydrocarbon layer. Significant amounts of sputtered product ions $C_xH_y^+$ (m/z ranges 15-17, 27-29, 39-43) in the mass spectra at incident energies above 50eV confirm the hydrocarbon coverage (Fig. 2). Fragmentation patterns of the different projectile molecules show both D- and D_2-loss and at times even subsequent H-pickup reactions beginning at collision energies as low as 5eV ($C_2D_6^+$ and $C_2D_5^+$) and 10eV ($C_2D_4^+$), respectively. Mass spectra of $C_2D_2^+$ show significant ion yields at m/z = 30, which appear to be the product of surface induced reactions between the projectile ion and embedded deuterated compounds to form $C_2D_3^+$.

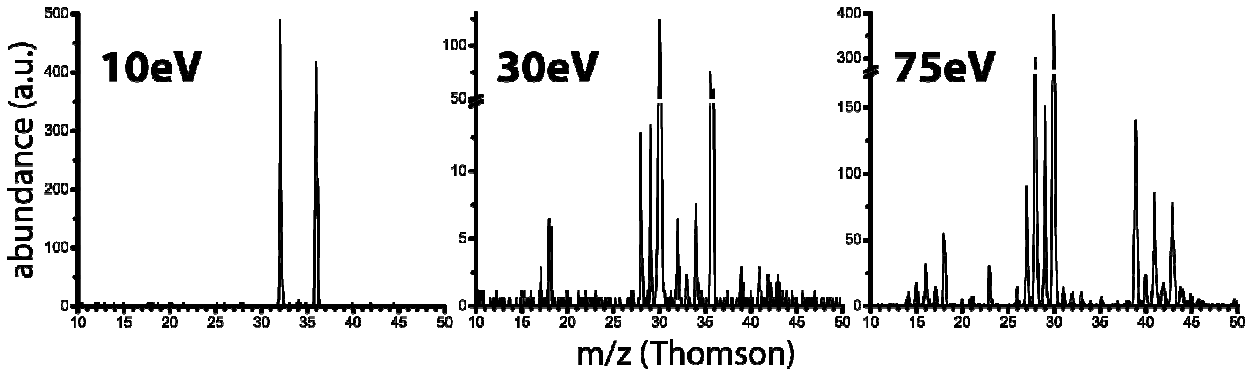

Fig. 2: Product ions of $C_2D_6^+$ on CFC at incident energies of 10eV, 30eV and 75eV

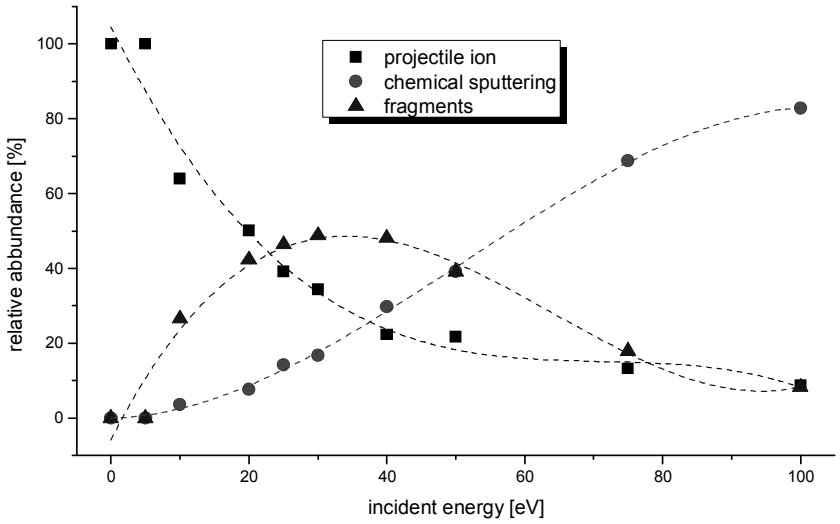

Fig. 3: CERMS of $C_2D_4^+$ on CFC

Collision Energy Resolved Mass Spectra (CERMS) of $C_2D_x^+$ on CFC

More profound aspects of the obtained data are revealed from collision energy resolved mass spectra (CERMS). Relative abundances are determined for each ion I_i in the spectrum by the ratio $100 \cdot I_i/\Sigma I_i$ [3]. In this work all ions are grouped into categories based on the surface induced processes they arise from. CERMS of $C_2D_6^+$ and $C_2D_5^+$ on CFC show a strong tendency towards fragmentation, while the yield of chemically sputtered products is low even for high energies. However CERMS of $C_2D_4^+$ exhibit both a rich fragmentation spectrum in the range of 10-50eV and at elevated incident energies a high yield of product ions, which partly are a result of chemical reactions of carbon chain build-up between $C_2D_4^+$ and hydrocarbons on the surface and to some extent the outcome of chemical sputtering (Fig. 3). Dissociation thresholds are determined for all projectiles and are found to be below 10eV in any case, while appearance energies for chemically sputtered products vary significantly with the type of impinging ion.

Acknowledgement

This work was supported by the FWF, Wien and the Association Euratom ÖAW.

References

[1] L. Feketeova et al., *JASMS.* 20 (2009) 927-938
[2] C. Mair et al., *J. Chem. Phys*. 111 (1999) 2770-2778
[3] J. Jasik et al., *J. Phys. Chem. A* 109 (2005) 10208-10215

Multiphoton Dissociation Dynamics of CH_3Br

Fengyan Wang[1,2], M. Laura Lipciuc [2], Xueming Yang[1] and Theofanis N. Kitsopoulos[2,3*]

[1] State Key Laboratory of Molecular Reaction Dynamics, Dalian Institute of Chemical Physics, Chinese Academy of Sciences, 116023, Dalian, P.R.China

[2] Institute of Electronic Structure and Laser, Foundation for Research and Technology-Hellas, Voutes, 71110, Heraklion, Greece

[3] Department of Chemistry, University of Crete, Voutes, 71003, Heraklion, Greece

* Author to whom correspondence should be addressed: theo@iesl.forth.gr

The state resolved photodissociation dynamics of CH_3Br^+ cation are studied using a combination of slice imaging and velocity mapping. Parent ions are prepared by (2+1) two-photon resonant three-photon ionization of CH_3Br through the 5s Rydberg state in the energy region 29069.8─29976.0 cm^{-1}. Analysis of the photoelectron spectra reveals that CH_3Br^+ ions are produced in the spin-orbit ground electronic states with a wide distribution of vibrational excitation. The photodissociation of CH_3Br^+ produces $CH_3^+(X)$ + $Br(^2P_{1/2})$/ $Br(^2P_{3/2})$ whose product state distribution shows substantial excitation in the umbrella-mode of the CH_3^+ photofragment especially when concurrently producing $Br(^2P_{1/2})$ channel. The shapes of the photofragment angular distributions clearly show the different dissociation mechanisms in the $Br(^2P_{1/2})$ and $Br(^2P_{3/2})$ channel. The dissociation dynamics of the 5s Rydberg state of CH_3Br is also presented and analyzed.

On the Photoionization of Endohedral Atoms

Korol A.V, Solovyov A.V
Frankfurt Institute for Advanced Studies, Ruth-Moufang Str. 1, 60438, Frankfurt am Mai, Germany.
E-Mail-Addresses: korol@fias.uni-frankfurt.de, solovyov@fias.uni-frankfurt.de

Brief introduction

The photoionization process of the atom A encaged in a fullerene C_N in many aspects differs from that of the isolated atom (see, e.g., review paper [6] and references therein). In particular, the photoelectron, when escaping the encapsulated atom, can re-scatter from the the fullerene cage. The interference of the direct and re-scattered waves may result in an oscillatory behaviour of the photoionization cross section $\sigma(\omega)$ as a function of the of the photon energy ω (or of the photoelectron momentum, which is equivalent). As noted in [2] this oscillations have a counterpart in the extended X-ray absorption fine-structure (EXAFS) measurements for solid-state systems, where they appear as a result of the emitted photoelectron scattering from the nearest-neighbour atoms back to the emitter with the subsequent interference of the waves. It is clear that the oscillatory structure of the $\sigma(\omega)$ curve depends on the type of the encapsulated atom, on the fullerene geometry and on the position of the atom inside the cage.

Initially, this effect was theoretically studied in [2] for $Xe@C_{60}$ and $Ba@C_{60}$ within the photon energy range above the atomic 4d ionization thresholds where both of the atoms have a giant dipole resonance in the photoionization spectrum. It was shown that the EXAFS-like effect noticeably affects the cross section curve [1]. In a number of recent publications (see [3-6] and references therein) the modification of the photoionization spectrum due to the interference phenomenon was predicted for different noble gas atoms encapsulated in the center of fullerenes C_{60}, C_{240} and C_{540}. The effect was also discussed for mulstishell spherically-symmetric structures like $Ar@C_{60}@C_{240}$ and even more exotic ones [6].

However, the predicted EXAFS-like resonances (termed also as 'confinement resonances') were not seen experimentally. Müller et al [1] reported the data on the photoionization cross section of a metallofullerene $Ce@C_{82}^{+}$ in the energy range 80—160 eV. In the region $\omega \approx 115$-140 eV the cross section of *an isolated* cerium atom has a giant resonance related to the 4d subshell. No additional confinement resonance structure appears in $\sigma(\omega)$ for the encaged cesium, as one can see from Figure 4 in [1].

---

1 Note that the correct figures for $\sigma(\omega)$ of $Xe@C_{60}$ and $Ba@C_{60}$ are presented in the Erratum in [2]

Brief description of our approach

In out work we present an explanation of between theory and the experiment as well as carry out revision of theoretical predictions on confinement resonances for endohedral noble gas atoms. In contrast to previous theoretical treatments [2-6] we consider, from the very beginning, the non-central position of the atom inside the cage. This implies that the atimic nucleus is displaced by the vector $\vec{a}$ from the center of the cage. As a result, the atomic photoionization cross section acquires the dependence on $\vec{a}$: $\sigma(\omega) \rightarrow \sigma(\omega, \vec{a})$. For the photon energies much higher than the plasmon resonance energy of the fullerene (which is ≈20 eV for C_{60}) one can ignore the ionization of the fullerene. Hence, the cage serves only as a source of additional potential acting on the atomic photoelectron. Following [7,8], one models this potential with a delta-potential well. Then it becomes possible to derive analytically the correction to the electron wavefunction and, at the end, to express the photoionization cross section $\sigma_{en}(\omega, \vec{a})$ of an endohedral atom via the cross section $\sigma(\omega)$ of the isolated atom. We demonstrate that this dependence has the following form:

$$\sigma_{en}(\omega, \vec{a}) = \sigma(\omega)[1 + f(p, \vec{a})]$$

where the $f(p, \vec{a})$ is an oscillatory function with respect to the momentum p of the photoelectron. In the case $\vec{a} = 0$ (central position of the atom) such a procedure has been carried out by Amusia and co-workers (see [3,4] and references therein).

When applying (1.1) to a metallofullerene (e.g., to $Ce@C_{82}^{+}$) one takes into account that due to the hybridization of the outer electrons the atom is displaced by some fixed value of a from the cage center. In the ensemble of the metallofullerenes the spatial orientations of the displacement vector $\vec{a}$ are randomly distributed. Therefore, (1.1) must be averaged over the angles of the displacement vector:

$$\sigma_{en}(\omega, \vec{a}) \rightarrow \overline{\sigma_{en}(\omega, a)} = \sigma(\omega)[1 + F(p, a)]$$

Here $F(p,a)$ stands for the averaged function $f(p, \vec{a})$.

In the case of a noble gas atom A there is no chemical bond between A and the carbon atom. The interaction between the atom and the cage can be considered within the Lennard-Jones model, including thus the attractive van der Waals potential and the repulsive exchange potential. To estimate the probability for an atom to be displaced by a distance a one can introduce the normalized Bolzmann distribution function $W_T(a)$ proportional to $\exp(-U(a)/kT)$, where T is the ensemble temperature and $U(a)$ stands for the atom-cage potential obtained by summing up the pairwise Lennard-Jones potentials for all carbon atoms of the fullerene [10]. Then it is meaningful to average the cross section (1.2) over all allowed values of a:

$$\overline{\sigma_{en}(\omega,a)} \to \overline{\sigma_{en}(\omega)} = \sigma(\omega)[1+\overline{F_T(p)}] \qquad (1.3)$$

where $\overline{F_T(p)} = \int W_T(a)F(p,a)da$.

The case of central position of the atom [2-6] one formally obtains from (1.3) by setting $T=0$.

Below we briefly discuss the results of numerical calculation for the systems $Ce@C_{82}^{+}$, $NG@C_{60}$ and $NG@C_{240}$ with NG=He, Ne, Ar, Kr, Xe. More coherent description of the developed approach as well as more detailed analysis of the numerical results will be presented at the conference and published elsewhere.

Numerical results

The results of calculation of the function *F(p,a)* from (1.2) for $Ce@C_{82}$ are presented in Figure 1. The (average) radius of the fullerene C_{82} was set to 4.15 Å. The range of the photoelectron momentum corresponds to the photon energies 120-180 eV, i.e. the region of the giant resonance in Ce. It is clearly seen that the angular averaging wipes out the resonance structure seen for the central position of the atom.

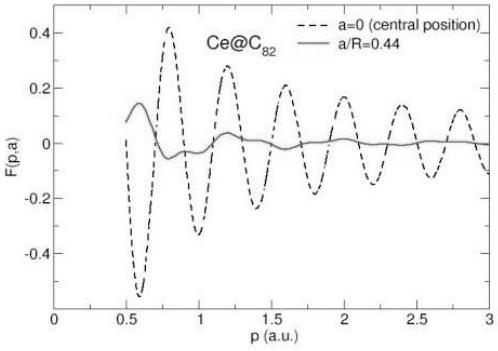

Figure 1. Function *F(p,a)* for *a=0* (central position) and *a/R=0.44,* which corresponds to the position of the cerium atom in C_{82}

Two graphs in Figure 2 represent the dependences of $\overline{F_T(p)}$ (see (1.3)) on *p* calculated for various endohedral nobel gases (as indicated). The averaging was carried out for T=500 using the Lennard-Jones potential in the Bolzmann distribution.

Concluding remarks

- The interference effects in the photoionization process of endohedral atoms are very sensitive to the atom location in the fullerene.
- In metallofullerenes due to the non-central position of the atom the angular averaging smears out the EXAFS-like structure.
- For large fullerenes (e.g. C_{240}) the confinement resonances, predicted for noble gas atoms, do not survive the averaging procedure with the Bolzmann distribution function.

- For smaller fullerenes (C_{20} and C_{60}) a more rigorous consideration of the van der Waals and the exchange potentials between the atom and the cage is needed in order to draw the final conclusion on the feasibility to observe the confinement resonances.
- The impact of non-centrality must be studies for a number of related theoretical predictions made recently by various authors (the Coulomb resonances, the resonances in the angular distributions of photoelectrons, the non-dipole effects, the photoionization of onion-like structures etc).

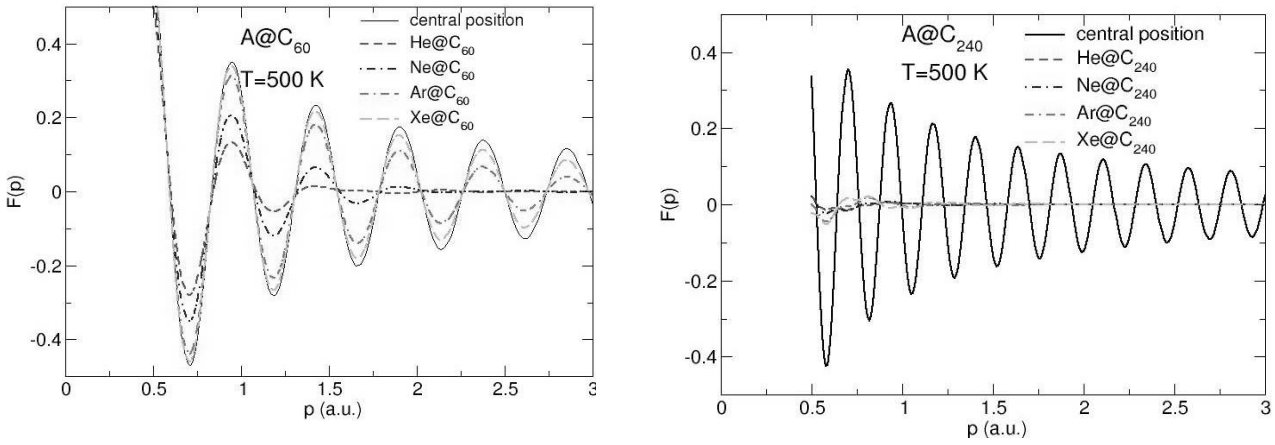

Figure 2. Dependences of $\overline{F_T(p)}$ *calculated for NG@C_{60} (left panel) and for NG@C_{240} (right panel) with NG=He, Ne, Ar, Kr, Xe. In each graph the black solid line stands for the central position of the atom. Brocken and chained curves (the coloured ones) stand for the averaged dependences (1.3).*

References

[1] A. Müller, S. Schippers, R.A. Phaneuf, M., et al, J. Phys.: Conf. Ser. **88** (2007) 012038.
[2] M.J. Puska, R.M. Nieminen, Phys. Rev. A **47** (1993) 1181 (Erratum: ibid. **49** (1994) 629).
[3] M.Ya. Amusia, A.S. Baltenkov, L.V. Chernysheva, Z. Zelfi, A.Z.~Msezane, J. Phys. B: At., Mol., Opt., Phys. **38** (2005) L169.
[4] M.Ya. Amusia, A.S. Baltenkov, L.V. Chernysheva, Phys. Rev. A **75** (2007) 043201; and references therein.
[5] V.K. Dolmatov, S.T. Manson, Phys. Rev. A 73 (2006) 013201; and references therein.
[6] V.K. Dolmatov, Adv. Quantum Chem. vol. 58, Eds J.R. Sabin and E. Brändas (USA, Academic Press, 2009) pp. 13-68; and references therein.
[7] A.S. Baltenkov, J. Phys. B: At. Mol. Opt. Phys. **32** (1992) 100.
[8] L.L. Lohr, S.M. Blinder, Chem. Phys. Lett. **198** (1999) 2745.
[9] S. Lo, A.V. Korol, A.V. Solov'yov, Phys. Rev. A **79** (2009) 063201

Design and Construction of a New TOF-MS Cluster Experiment

C. Leidlmair, H. Schöbel, L. An der Lan, P. Bartl, S. Denifl, T. D. Märk, P. Scheier
Institut für Ionenphysik und Angewandte Physik,
christian.leidlmair@uibk.ac.at

In the past our workgroup has carried out numerous studies on free and deposited cluster complexes with various experimental setups [1,2]. Many of these investigations successfully utilized a He-cluster source along with a sector field mass spectrometer [3]. To go one step further, the gained knowledge has now been used to design and build an entirely new cluster experiment. The setup not only combines proven techniques with state of the art components but also enables new types of experiments.

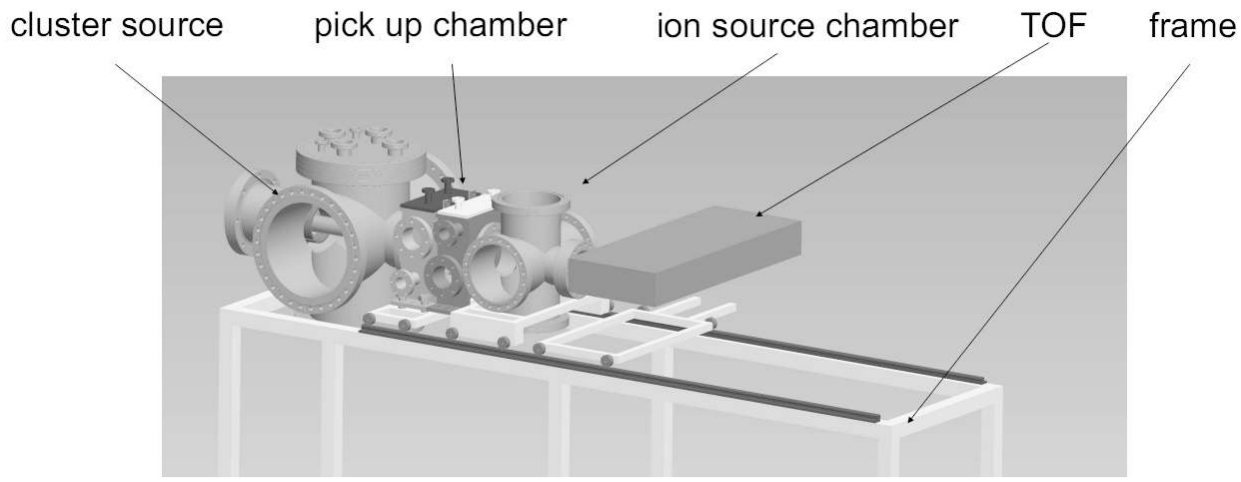

Fig. 1: schematic view of the new TOF-MS cluster experiment

One key element of the apparatus is a new He-cluster source. It produces helium droplets via supersonic expansion of pressurized and pre-cooled helium. Driven by a closed cycle cryostat (Sumitomo F-50, RDK-415D), the accessible range of expansion conditions and thus the average droplet size are dramatically increased by the new source. The nozzle (orifice 5µm) is manufactured by Lenox Laser and allows stagnation pressures of up to 80 bar. Orifices with different diameters can be installed easily due to a VCR compatible screwing mechanism. A copper heat shield, cooled to 50K, is employed to improve the cryostats steady state

temperature with helium load. Downstream from the cluster source, the droplets enter an array of up to four differentially pumped chambers. These separated volumes enable the successive pick-up of four different types of samples while having control over their proportions. Samples may be introduced in gas or liquid phase through a gas inlet, or can be evaporated in an oven in case of low vapor pressures. Currently the ionization is only possible via electron ionization. Electron attachment however, will be available in the final stage of the experiment. Mass spectrometric analysis is carried out by an orthogonal reflectron time-of-flight mass spectrometer, with a resolution of $m/\Delta m = 4500$ (V-mode and 10000 in the W-mode) and a mass per charge range up to 50000 Thomson. Due to the high ion efficiency of the TOF-MS, mass spectra can be acquired very fast reducing measurement time greatly in comparison with sector field mass spectrometers and even quadrupoles. The enhanced mass resolution and accuracy reduce the need for time-consuming post-processing of spectra and also provide better isobaric separation and therefore new insights in cluster compositions.

Acknowledgement:

This work was supported by the FWF (P19073, L633). S.D. gratefully acknowledges an APART grant from the Austrian Academy of Sciences.

References

[1] S. Denifl, F. Zappa, I. Mähr, A. Mauracher, M. Probst, T.D. Märk, P. Scheier, Inelastic Electron Interaction with Chloroform Clusters embedded in Helium Droplets. *J. Am. Chem. Soc.* 15/**130** (2008) 5065-5071

[2] F. Zappa, S. Denifl, I. Mähr, A. Bacher, O. Echt, T.D. Märk, P. Scheier, Ultracold Water Cluster Anions. *J. Am. Chem. Soc.* 16/**130** (2008) 5573-5578

[3] S. Denifl, F. Zappa, I. Mähr, J. Lecointre, M. Probst, T.D. Märk, P. Scheier, Mass Spectrometric Investigation of Anions Formed upon Free Electron Attachment to Nucleobase Molecules and Clusters Embedded in Superfluid Helium Droplets. *Phys. Rev. Lett.* 4/**97** (2006) 043201-4

Shell Structures in $Pb^{2+}He_n$ and $Pb^{+}He_n$ Clusters

Petr Slavíček[1] and Marius Lewerenz[2]

[1] *Department of Physical Chemistry, Prague Institute of Chemical Technology, Technická 6, 166 28 Prague 6, Czech Republic*

[2]*MSME, FRE 3160 CNRS, Bât. Lavoisier, Université Paris-Est (Marne la Vallée), 77454 Marne la Vallée Cedex 2, France, Marius.Lewerenz@univ-paris-est.fr*

We report diffusion quantum Monte Carlo calculations of energies and structures of $Pb^{2+}He_n$ and $Pb^{+}He_n$ clusters based on a non additive potential model whose components are derived from highly correlated ab initio calculations with additional electrostatic terms and which includes spin-orbit effects for Pb^{+}. The spin orbit coupling in $Pb^{+}He_n$ clusters is found to have profound effects on cohesive energies and cluster structures. No clear magic numbers could be identified in $Pb^{+}He_n$. High coordination situations with up to 15 nearest neighbors are found for $Pb^{2+}He_n$ which shows density saturation of the nearest neighbour peak at n=12 but a delayed onset of the build up of second nearest neighbour density.

Introduction

The extreme quantum nature of helium clusters and the usually rather weak interactions with other species lead to remarkable zero point energy effects in these systems. They have been used in recent years as nano-cryostats for a large range of very interesting spectroscopic and dynamic experiments [1,2,3,4,5]. The last step of many experiments involves ionisation of the neutral $D@He_N$ system. Most ionisation processes are believed to proceed via charge transfer from initially formed He^+ to the dopant such that an excess energy of several eV has to be dissipated. This situation gives rise to a long progression of small fragment ions of the type $D@He_n$, $n << N$. The relative ion count rates in mass spectra contain the signature of the relative stability of the ionic product clusters, but distortions due to the dynamics of the fragmentation process cannot be excluded. $Pb^{2+}He_n$ and $Pb^{+}He_n$ fragment ion sequences have been recorded recently [6] and indicate that n=12 is probably a magic size for Pb^{2+} and that n=17 might be a shell closure for Pb^{+}. Additional interest comes from the chemically motivated search for extremely high coordination numbers. A recent ab initio survey of candidate clusters led to the conclusion that $Pb^{2+}He_{15}$ should be a single shell system with essentially equal Pb^{2+}-He distances [7], while n=16 was found to prefer a structure with a single helium atom taking a clearly more distant position. In view of the large zero point energy effects in helium clusters, even after ionization, it remains to be tested if the single shell global electronic minimum structure is robust with respect to zero point energy.

Diffusion quantum Monte Carlo (DMC) calculations can provide this answer, but require a very efficient potential energy evaluation which can be currently provided only by analytical models. We present the construction of such a many-body model for both ionic mixed systems which correctly reproduces all minimum energy structures known from explicit ab initio calculations and the results of accurate DMC calculations using these models.

Computational details

The $^1\Sigma^+$ pair interaction potential between the Pb^{2+} ion and helium atoms has been calculated at the CCSD(T) level with the aug-cc-pV5Z basis set using a super-molecular approach and the standard counterpoise correction of the basis set superposition error. The many-body contribution to the intermolecular potential converges much faster with the basis set size due to its dominantly electrostatic character. The three-body interaction is essentially converged at the CCSD(T)/aug-cc-pVTZ level, which has been used to construct this contribution to the total interaction. The nature of the interaction was analyzed using symmetry-adapted perturbation theory (SAPT) [9] as implemented in MOLPRO [10]. SAPT was specifically used to extract the induction terms from the overall interaction energy. The Pb^+ ^2P ground state gives rise to $^2\Sigma^+$ and $^2\Pi$ states in combination with the ^1S ground state of helium. Pair interaction potentials were calculated using the unrestricted CCSD(T) method with a aug-cc-pV5Z basis set, using an additional set of mid-bond functions.

All pair interactions were fitted to HFD-type analytical models with a leading C_4 coefficient reflecting the dominant long range interaction between a charge and a polarisable atom which was fixed at the value given by the asymptotic electrostatic expression. Interactions between the induced dipoles carried by the helium atoms were included and also the induced dipole carried by Pb^{2+} in the field of the other dipoles. This model gave very satisfactory agreement with explicit ab initio scans of cuts of the $Pb^{2+}He_2$ surface. For Pb^+He_n a full complex 6x6 spin-orbit matrix [12] was constructed for each particle arrangement with diagonal elements given as sums over pairwise Σ and Π contributions using the appropriate projections with additional induction terms and off-diagonal elements computed from the experimental atomic $^2P_{3/2}/^2P_{1/2}$ splitting. The lowest eigenvalue of the matrix was used as potential energy input for the DMC method. Structural predictions for larger clusters based on both models were checked by direct electronic structure calculations at the DFT level using the PBE0 functional [11]. The purpose of the DFT calculations is only to check if our many body models exhibit any major deficiencies. Our DMC calculations were carried out with fixed ensembles of 1000 – 16000 weighted random walkers, imaginary time steps between 10 and 100 E_h^{-1}, and Jastrow/Fermi type trial wave functions as described in our earlier publications [8]. In spite of the use of trial wave functions a significant ensemble size bias on energies was observed such that extrapolations to infinite ensemble size were necessary to achieve best accuracy.

Results and discussion

Total energies and incremental energies are shown for both systems in Fig. 1 ($Pb^{2+}He_n$) and Fig. 2 ($Pb^{+}He_n$) and show the clear appearance of a magic number at n=12 for Pb^{2+} but also that a new energetic binding motive is reached only starting at n=15. For $Pb^{+}He_n$ the full model with spin-orbit coupling predicts a rather smooth transition between initial strong binding and a weak binding large cluster limit. Neglect of the strong mixing due to spin-orbit coupling leads to qualitatively wrong energetic and structural predictions. DMC radial density profiles for $Pb^{2+}He_n$ show that the peak helium density increases almost linearly with n and slowly shifts outward up to n=12 where a value of about 0.26 $Å^{-3}$ is reached, 12 times the bulk liquid helium density. By comparison with the density of solid helium (0.032 $Å^{-3}$) this shell might be called solid already for very small n. This interpretation is, however, improper because for most n this shell is structurally disordered. From n=12 to n=15 a single shell structure is observed which now exhibits a noticeable increase of its width indicative of the progressive disordering of the symmetric packing reached at n=12. The formation of a second density maximum clearly sets in only at n=16. The peak density of this second maximum again exceeds the bulk helium density and in an exploratory calculation for n=125 we actually observed a well developed third maximum. While n=15 marks the end of a structural motive it probably cannot be regarded as a simple coordination system since it is involved into active particle exchange with its surroundings via the pronounced helium density between nearest and second nearest neighbor density maxima.

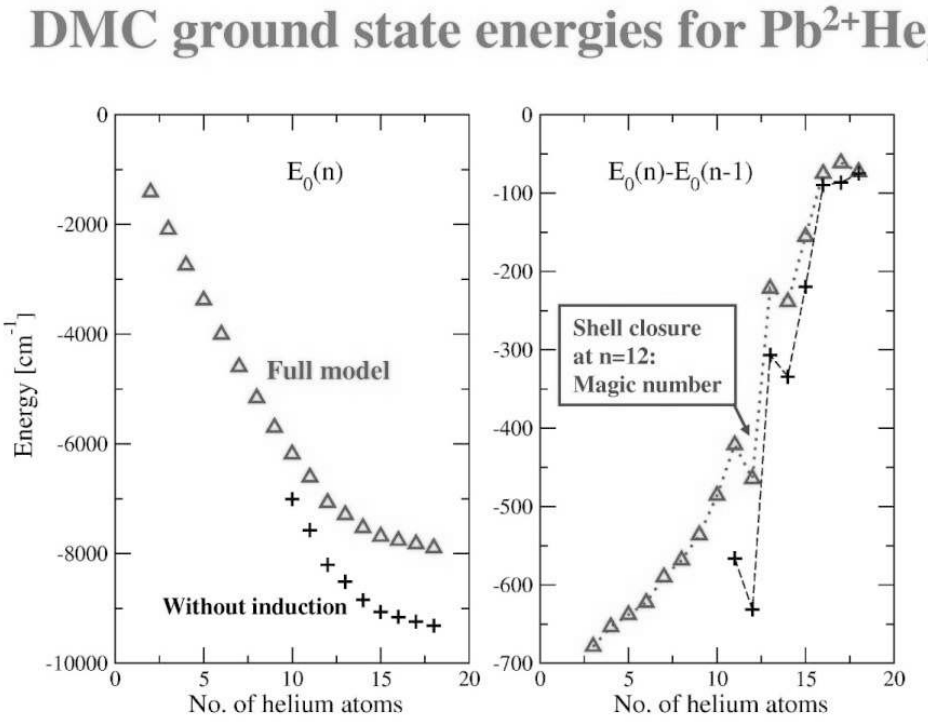

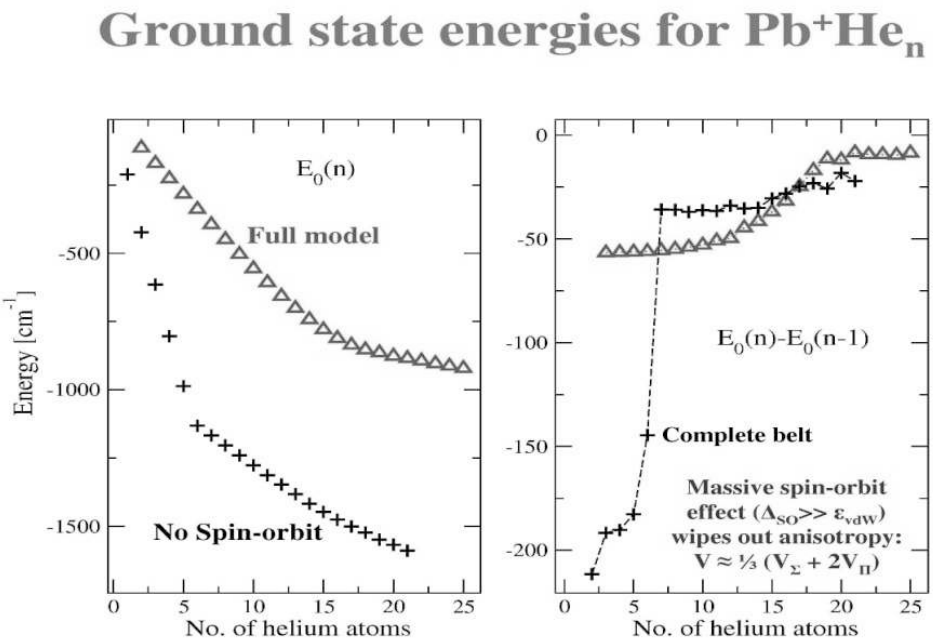

References

[1] J. P. Toennies and A. F. Vilesov, Angew. Chemie Int. Ed.43, 2622 (2004)
[2] F. Stienkemeier and K. K. Lehmann, J. Phys. B 39, R127-R166 (2006)
[3] J. M. Merritt, J. Küpper and R. E. Miller, Phys. Chem. Chem. Phys. 7, 67-78 (2005)
[4] K. Nauta and R. E. Miller, Science 283, 1895 (1999)
[5] T. Döppner, T. Diederich, J. Tiggesbäumker, and K.-H. Meiwes-Broer, Eur. Phys. J. D, 16, 13-16 (2001)
[6] T. Döppner, T. Diederich, A. Przystawik, N. X. Truong, Th. Fennel, J. Tiggesbäumker, and K.-H. Meiwes-Broer, Phys. Chem. Chem. Phys. 9, 4639-4652 (2007)
[7] A. Hermann, M. Lein, and P. Schwerdtfeger, Angew. Chemie Int. Ed. 46, 2444-2447 (2007)
[8] C.~A. Brindle, M. R. Prado, K. C. Janda, N. Halberstadt, and M. Lewerenz, J. Chem. Phys. 123, 064312 (2005)
[9] B. Jeziorski, R. Moszynski, and K. Szalewicz, Chem. Rev. 94, 1887 (1994)
[10] MOLPRO is a package of ab initio programs written by H.-J. Werner, P. J. Knowles, R. Lindh, F. R. Manby and others, see http://www.molpro.net (2006)
[11] C. Adamo and V. Barone, J. Chem. Phys. 110, 6158 (1999)
[12] A. I. Krylov, R. B. Gerber, and R. D. Coalson, J. Chem. Phys. 105, 4626 (1996)

The Dynamics and Energetics of Dication-Neutral Reactions Studied Using a Position-Sensitive Coincidence Technique

Lockyear JF, Parkes MA, Price SD

University College London, Department of Chemistry, 20 Gordon Street, London, WC1H 0AJ, UK

Our group employs a position-sensitive coincidence (PSCO) methodology in conjunction with time-of-flight (TOF) mass spectrometer to study the reactions of doubly-charged atoms or molecules with neutral atoms or molecules. These dication-neutral reactions have been proposed to be significant in the chemistry of ionised media and planetary ionospheres such as those of Mars [1], Titan [2] and Venus [3]. One might expect electron-transfer to be the only reactive process which would occur between a molecular dication and a neutral species, specifically, at large interspecies separations. However, despite charge transfer reactions accounting for a large part of the chemistry between dications and neutrals, a significant proportion of collision-systems exhibit bond-forming processes that occur by complexation between the two reactants. Some of these complexes exist in very deep potential wells, as low as 10 eV, as has been shown in several of our computational calculations of the potential energy surfaces. In some reactive encounters these complexes appear to be fairly long-lived and significant bond-rearrangement has been observed, for example, in the reaction between O_2^{2+} and CH_4 we have observed CO_2^+ as a bond-forming product. Bond-forming reactions proceeding *via* stripping of atoms or even groups of atoms from one of the reactants have also been observed [4, 5]. Our PSCO methodology allows us to unambiguously determine which of these processes, stripping or complex formation, occurs in each reaction channel between the molecular dications and neutrals. Hence, our reaction dynamics data, of un-precedented angular resolution, provides valuable insight into how dications react with neutrals. In addition, we are able to construct kinetic energy release spectra for each reaction channel sometime meaning we can identify the vibronic states of the reactants or products.

We have used the PSCO mass spectrometer to study the electron transfer reaction between Ar^{2+} with He [6] and the very complex chemistry occurring between O_2^{2+} with CH_4. The reaction between Ar^{2+} and He demonstrates both the good angular and energy resolution which we obtain that allows us to distinguish the reactions of the ground ^3P and first excited ^1D electronic states of Ar^{2+}, as seen in the energy release distribution in Figure 1. We have studied the Ar^{2+} - He electron transfer at five different collision energies which led to the observation of some dramatic changes in the scattering angles of the product ions with changing collision energy. Such changes in the product angular distributions had not previously been observed for Ar^{2+} (^1D) at these low energies and at this angular resolution.

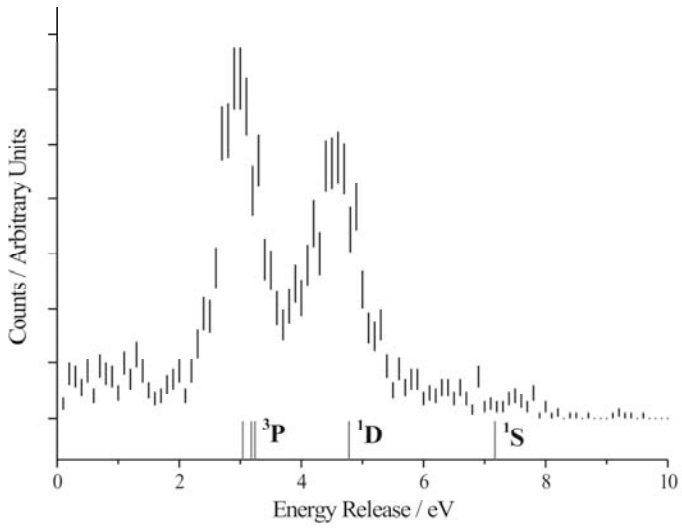

Figure 1. The energy release spectrum for the electron-transfer reaction between Ar^{2+} and He at E_{CM} = 1.18 eV.

Classical trajectory simulations have proved very ineffective at reproducing the major features of the angular distributions observed for Ar^{2+} (^{1}D), seeming to imply that quantum effects are dominant for this particular state.

The reaction of O_2^{2+} with CH_4 has been studied at collision energy of 4.7 eV in the centre-of-mass frame and bond-forming reactions have been observed which demonstrate significant re-arrangement of the reactant atoms. Three different bond-forming products have been observed, which are HO_2^+, HCO^+ and CO_2^+. Dominating the chemistry between O_2^{2+} and CH_4, however, are the single electron-transfer reactions. Comparing the kinetic energy release spectra for the non-dissociative electron transfer reaction to a simulation of the energy release with the appropriate Franck-Condon factors has led us to the conclusion that in the non-dissociative single electron transfer, the O_2^+ cannot be formed in the ground $X^2\Pi_g$ state and must be formed in the $A^2\Pi_u$ state. In addition, we have used similar calculations to show that in the majority of the dissociative single electron-transfer channels, the O_2^+ must exclusively be formed in the ground $X^2\Pi_g$ state, thus demonstrating the strength of the PSCO technique.

References

[1] O Witasse, O Dutuit, J Lilensten, R Thissen, J Zabka, C Alcaraz, P L Blelly, S W Bougher, S Engel, L H Andersen and K Seiersen 2002 *Geophys Res Lett* **29** 1263
[2] J Lilensten, O Witasse, C Simon, H Solidi-Lose, O Dutuit, R Thissen and C Alcaraz 2005 *Geophys Res Lett* **32** L03203
[3] G Gronoff, J Lilensten, C Simon, O Witasse, R Thissen, O Dutuit and C Alcaraz 2007 *Astron Astrophys* **465** 641
[4] M A Parkes, J F Lockyear and S D Price 2009 *Int J Mass Spec* **280** 85 10.1016/j.ijms.2008.07.027
[5] D Ascenzi, P Tosi, J Roithova, C L Ricketts, D Schroeder, J F Lockyear, M A Parkes and S D Price 2008 *Phys Chem Chem Phys* **10** 7121
[6] J F Lockyear, M A Parkes and S D Price 2009 *J Phys B* **42** 9

Effect of the Temperature on Dissociative Electron Attachment to Bromochlorotoluene Isomers

M. Mahmoodi Darian, A. Aleem, B. Rittenschober, T. D. Märk and P. Scheier
Institut für Ionenphysik und Angewandte Physik, Universität Innsbruck, Technikerstraße 25, A-6020, Innsbruck,Austria
e-mail: masoomeh.mahmoodi@uibk.ac.at

An enhancement of the relative dissociative electron attachment cross section close to the threshold for 2-bromo-5-chlorotoluene, 5-bromo-2-chlorotoluene as a function of temperature has been measured. The temperature has been varied from 393 to 520 K within the limits of the apparatus and anion efficiency curves have been measured in the electron energy range from 0-2eV. A trochoidal electron monochromator with an energy spread of ΔE~70meV was utilized in combination with a quadrupole mass spectrometer and a temperature controlled effusive molecular beam source. The evolution and relative increase of the low-energy resonance in the anion efficiency curve reveals the activation energy required for a particular dissociation channel, i.e., in the present case the formation of halogen anions. In both isomers the low-energy peak of Br^- and Cl^- increases dramatically when the gas temperature is raised. Activation energies for dissociative electron attachment of 73.84 ± 20 meV, 122 ± 20 meV for the formation of Br^- and Cl^- from 2-bromo-5-chlorotoluene and 64.61± 20 meV, 184.98± 20 meV for Br^- and Cl^- from 5-bromo-2-chlorotoluene have been determined respectively.

Introduction

Dissociative electron attachment (DEA) to molecules is often a very effective reaction and responsible for negative ion formation in plasmas [1]. The reactive species produced, a halogen anion X^- and a hydrocarbon radical M, play an important role in dry etching plasmas Moreover, such species are possibly also involved in the processes leading to ozone depletion in the atmosphere. Furthermore, there exists a similarity between DEA to halohydrocarbons and the process of reductive dehalogenation promoted by bacteria in anaerobic sediments, sewage sludge and aquifer materials [2]. In this contribution we study systematically the influence of the temperature on electron attachment processes for two halohydrocarbon molecules. The experiment involves a crossed electron / molecular beam arrangement with a mass spectrometric detection for the anions formed. If a free electron interacts with a neutral molecule XM, a temporary negative ion can be formed by resonant electron capture [1, 3, 4]

$$e^- + XM \rightarrow XM^{-(*)} \quad (1)$$

Such an attachment process usually occurs within a restricted energy range since it represents a transition from a continuum state to a discrete electronic state. A negative ion state thereby formed is embedded in its autodetachment continuum and is hence principally unstable towards autodetachment (AD). In this contribution we are restricted to gas phase molecules under collision-free conditions. Under such conditions a TNI usually relaxes via autodetachment (the reverse of Eq. (1), AD) or via unimolecular decomposition into thermodynamically stable fragments M + X^- (DEA). It has been known for as long as three decades that the temperature may have a strong effect on DEA. Thus, the occupation of the vibrational states of the neutral molecule can have strong effects on their fragmentation. How this influence manifests itself in the ion yield curves of the individual fragments is complex and depends largely on the relative disposition of the involved neutral and anionic potential energy surfaces [1,4]. Heating of the molecule and thus increasing the population of vibrationally excited states extends the Franck-Condon region, thus allowing transitions to the repulsive ionic potential energy curve at lower electron energies and hence resulting in higher dissociation probability. In addition, the temperature dependence reflects the thermodynamics of the particular dissociative attachment reaction and also gives some insight into the underlying mechanisms and dynamics. The dependence of the ion signal on the temperature T at very low electron energies is described by the Arrhenius equation:

$$I(T) = I_0 . \exp(E_A / K_B T)$$

Where I (T) is the ion current close to 0 eV and k_B is the Boltzmann constant. For reactions without an activation energy, the cross-section for DEA reactions at low electron energies does not depend on T.

Experiment

The present study has been carried out using a high-resolution electron-molecular beam apparatus. A schematic of the apparatus is shown in the Figure 1. The electron beam formed by a trochoidal electron monochromator (TEM) and accelerated to the selected electron energy is crossed by a molecular beam formed by an effusive molecular beam source (EMBS). The negative ions produced in the collision chamber (CC) are extracted by a weak electric field from the interaction region and focused into the entrance of the quadrupole mass spectrometer (QMS). The mass selected negative ions are detected as a function of the electron energy in a single-ion counting mode using a secondary electron multiplier (SEM), an ion counting electronics and a PC acquisition system. The entire system is situated in a high vacuum chamber.

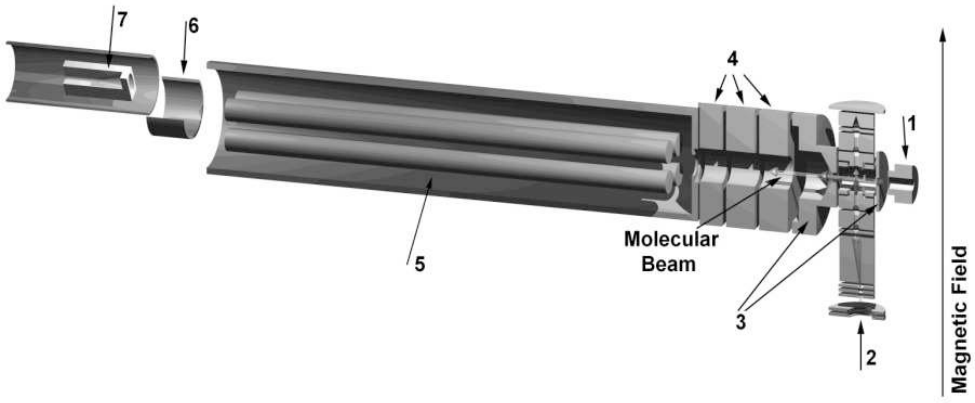

Fig.1 Schematic view of the Experimental Setup, 1. Molecular beam source, 2. monochromator, 3. ion extraction field, 4. ion optics, 5. quadrupole, 6. ion deflector, 7. channeltron

Results

Figure 2a displays the electron energy dependence of the relative cross-sections for the fragment ion Cl^- and Br^- observed from 2-bromo-5-chlorotoluene recorded at different temperatures. An Arrhenius plot for the zero energy peak of this molecule is presented in Figure2b. From the slope of the Arrhenius plot, activation energy for Br^- of 73.84± 20 meV and of 122± 20 meV for Cl^- has been deduced.

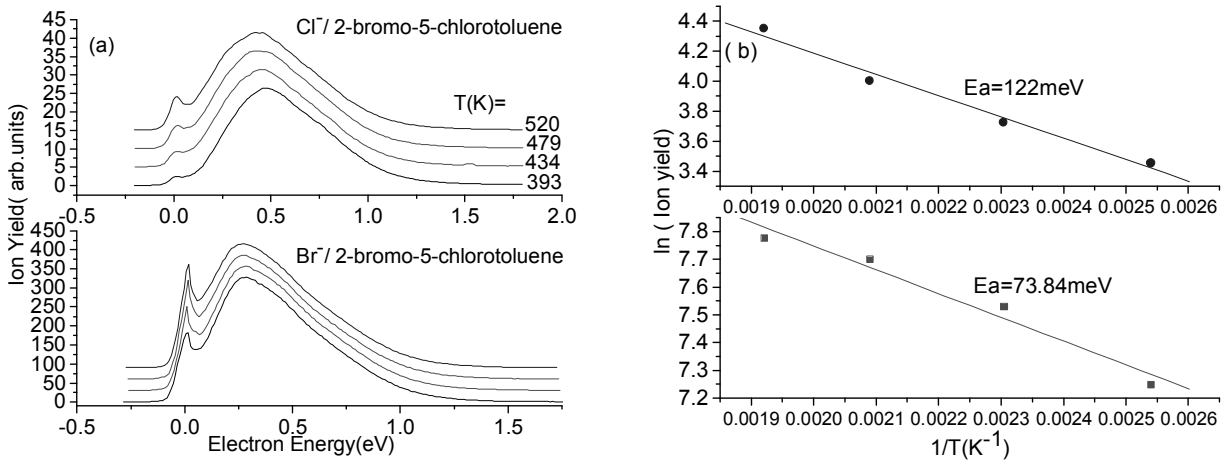

Fig.2 *(a) Dependence of Cl^- and Br^- yield due to DEA to 2-bromo-5-chlorotoluene on the gas temperature. The respective anion yields were normalized to the same value at the higher energy peak and are shifted by adding a constant value to each subsequent spectrum for clarity. (b) Arrhenius plot of the threshold intensity. The slope of the straight line corresponds to activation energy for Cl^- formation of 122 meV and for Br^- of 73.84meV.*

Figure 3a shows the ion yields for the negative ions Cl^- and Br^- recorded at gas temperatures within the range of 391 – 514 K. An Arrhenius-type plot of the maximum intensity of the peak at zero energy yields an activation energy of 64.6± 20 meV for Br^- and 185 ± 20 meV for Cl^-.

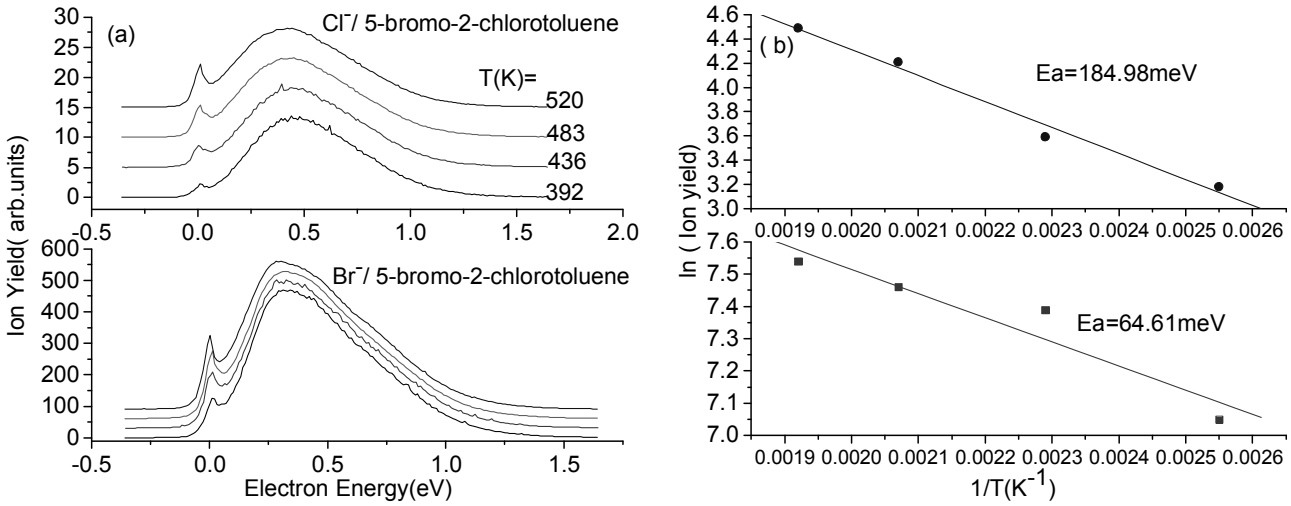

Fig.3 *(a)Dependence of Cl^- and Br^- yield due to DEA to 5-bromo-2-chlorotoluene on the gas temperature over the range T = 393 – 520 K. The respective anion yields were normalized to the same value at the higher energy peak and are shifted by adding a constant value to each subsequent spectrum for clarity. (b) Arrhenius plot of the threshold intensity. The slope of the straight line corresponds to activation energy for Cl^- formation of 184.98 meV and for Br^- of 64.61meV.*

Acknowledgement: This work was supported by the FWF, Wien.

References

[1] L.G. Christophorou (ed.), Electron-Molecule Interactions and Their Applications, Academic Press, Orlando, FL, 1984.
[2] R.A. Larson, E.J. Weber, CRC Press: Boca Raton, Fl, (1994); p 171.
[3] H.S.W. Massey, Negative Ions, Cambridge University Press, Cambridge, 1976.
[4] E. Illenberger, J. Momigny, Gaseous Molecular Ions: An Introduction to Elementary Processes Induced by Ionization, Steinkopff/Springer, Darmstadt/New York, 1992.

Electron Induced Fluorescence Study of the Second Positive System of N_2

Kočíšek J[1], Kubala D[1], Matejčík Š[1]

[1] *Department of Experimental Physics, Comenius University Bratislava, Slovakia, matejcik@fmph.uniba.sk*

The electron impact excitation of the second positive system of N_2 (2nd PS N_2) have been studied in a new crossed electron/molecular beams apparatus. The excited statets $C\ ^3\Pi_u(v')$ (v'=0..3) were excited using high resolution electron beam. The electron induced optical spectra in UV/VIS range (290 – 440 nm), the excitation thresholds of particular vibrational states $C\ ^3\Pi_u(v')$, the emission cross sections of the 2nd PS and the excitation cross sections of the $C\ ^3\Pi_u(v')$ states were measured with high resolution and sensitivity.

Introduction

Electron excitation of the nitrogen molecule plays an important role in atmospheric phenomena and laser physics. The second positive system $C\ ^3\Pi_u(v') \rightarrow B^3\Pi_g(v'')$ belongs to the most intensive bands in the emission spectrum of the nitrogen. Thus the electron impact excitation of the $C\ ^3\Pi_u(v')$ draws much attention due its importance for atnospheric processes and the electric discharges in nitrogen. The electron-impact cross sections for the various vibrational bands of the second positive systems have been already measured by researchers in several laboratories [1-4] still exist considerable discrepancies in the published data. Therefore an accurate knowledge of the excitation cross sections of the $C\ ^3\Pi_u(v')$ state is of primaly interest for the understanding of several important phenomena in nitrogen. In the present work the total cross sections for excitation of the v'=0,1, 2 and 3 vibrational levels of the $C\ ^3\Pi_u(v')$ state have been measured by the detection of the photonsfrom the second positive system in the 290-440 nm spectral range. Excitation functions of several optical lines have been measured and normalized to obtain absolute values of the cross sections. The present measurements have been carried out with higher electron energy resolution and more accurate incident energy calibration than the previous studies of the emission cross sections. This has allowed the energy dependence of the cross sections to be established with higher accuracy and the excitation cross sections to be determined in the near-threshold region.

Experimental setup

The new apparatus for electron impact excitation, used to study the optical excitation of N_2 is shown schematically in the Figure 1. It consists of an electron monochromator to produce a collimated beam of electrons, a collision chamber filled with a target gas and a system to detect spectrally analysed photons. The incident beam with an energy spread of

approximately 100 meV and a typical electron current of 20 nA is produced by a trochoidal electron monochromator (TEM). Photons emitted from the collision region are collected by a lens and transmitted via vacuum window outside of the vacuum chamber and refocused by second lens onto the entrance slit of an 0.25 m optical monochromator equipped with a cooled Hamamatsu H8259 photomultiplier at its exit slit. The magnetic field (5×10^{-3} T) is produced by a pair of coils which allow for accurate alignment of the direction of the field with respect to the electron spectrometer symmetry axis. The measurements were carried out for a pressure range

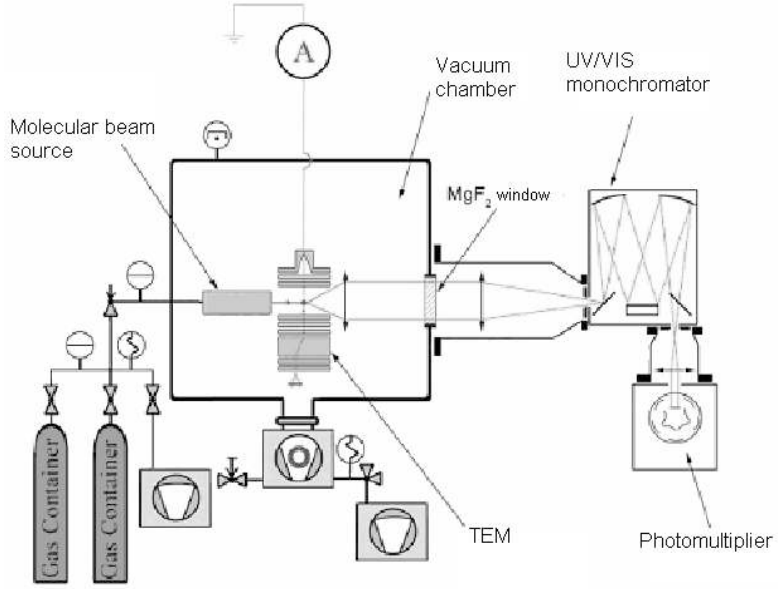

Figure 1. Schematic view of the experimental setup

in the collision region which gave linear dependence between detected photons intensity and target pressure. It was also ensured that the detected photon intensity increased linearly with the electron beam current.

Results and discussion

The fluorescence spectrum of the 2nd PS N_2 induced by the electrons with kinetic energy of 14.2 eV is shown shown in the Figure 2. The (ν′,ν″) transitions of the second positive system have been identified and are idicated in the spectrum. The intensities of the observed transitions enable to estimate the relative emission cross sections.

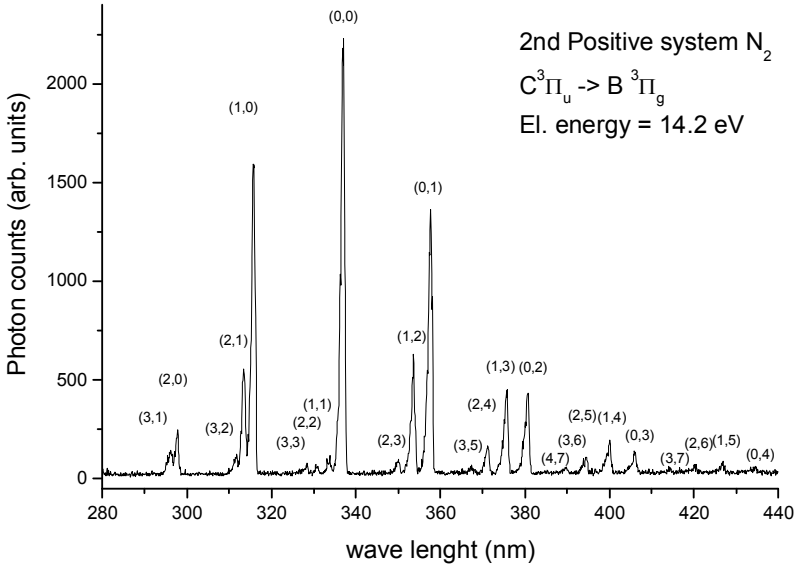

Figure 2 Emission spectrum of the 2nd PS in N2 induced by the electrons with kinetic energy of 14.2 eV.

The excitation cross section of the strongest emission band of the 2nd PS $C\ ^3\Pi_u(v'=0)$ to $B\ ^3\Pi_g(v''=0)$ (337 nm) is presented in the Figure 3. The excitation cross section has been measured in the energy region from threshold to 80 eV and it has been norinelized to the absolute emission cross section at its maximum at 14.1 eV. The electron energy range and the absolute value of the cross section has been calibrated to cross section measured by Zubek[1]. Excitation cross sections of additional transition lines of the 2nd PS of the N_2 have been measured. The excitation cross sections σ_v of the particular vibrational states of the $C\ ^3\Pi_u$ can be obtained from the measured emission cross sections σ_v^{em} using following relation:

$$\sigma_{v'} = \sigma_{v''}^{em} A_{v',v''} \tau_{v'} \qquad (1)$$

where $A_{v',v''}$ is the transition probability and $\tau_{v'}$ is the mean lifetime of level v'.

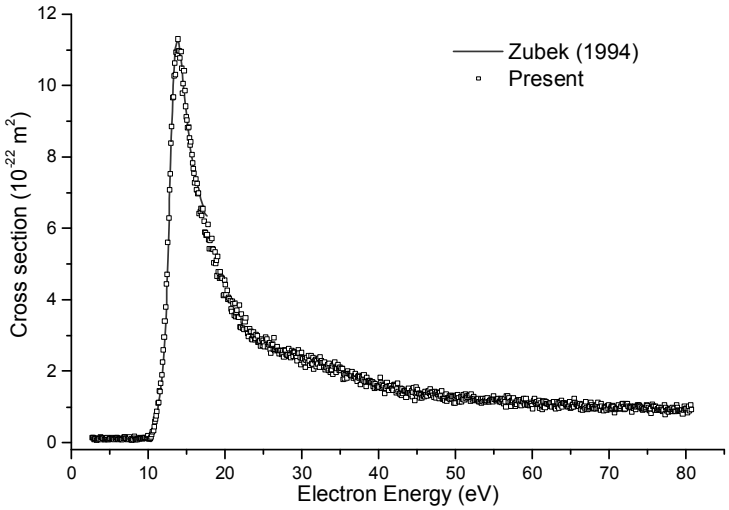

Figure 3: Emission cross section of the C $^3\Pi_u$(v'=0) to B $^3\Pi_g$(v''=0) (337 nm) transition of 2nd Positive system in N_2.

The high energy resolution of the electron beam has been used to estimate with high precision the thresholds of the excitation functions for particular vibrational states v' of the $C\ ^3\Pi_u$ electronic state of N_2.

.

Acknowledgment

This work was supported by Slovak Science and Technology Assistance Agency under the contracts No. APVV-07-0365 and LPP-0143-06.

References

[1] M. Shaw and J. Campos, J. Quont. Speetrosc. Radiat. Transfer 30 (1983) 73
[2] M. Zubek, J. Phys. B: At, Mol. Opt. Phys., 27 (1994) 573
[3] J.T. Fons, Phys. Rev. A, 53 (1996) 2239
[4] D.E. Shemansky, J.M. Ajello, I. Kanik, Astrophys. J., 452(1995) 472

Advanced modeling in He droplets

Andreas Mauracher, Daniel Spångberg, Kersti Hermansson
Department of Chemistry, Uppsala University, Box 538, S-751 21, Uppsala, Sweden

Since the discovery of condensation in a helium nozzle expansion in 1961 [1], helium clusters have been a focus of cluster research as they are known to possess various fascinating properties at low temperatures.
One major impetus has been the extreme quantum nature of these clusters, paralleled by only one other system, namely hydrogen clusters [2]. The behavior of these van der Waals aggregates of light atomic and molecular species is dominated by quantum delocalization and exchange effects. The occurrence of superfluidity in ^4He_n clusters containing as few as n = 60 atoms has been established by theory and experiment at the end of last century. On the one hand path-integral Monte Carlo calculations have been used to study manifestations of superfluid behavior of ^4He clusters at low temperatures [3]. On the other hand infrared spectroscopy of small molecules inside pure ^4He droplets could demonstrate the existence of free rotations and therefore superfluidity by spectacularily narrowed rotational lines [4].
Another reason that has made helium droplets a "hot topic" is their use as nano-reactors to study ion-molecule reactions, such as efficient charge transfer via electron-impact generated He^+ to molecules embedded within the droplet [5]. Also for spectroscopy at subkelvin temperatures helium nano droplets have been stated to be an ultimate matrix, which surpasses any solid matrix as it combines the benefits of both the gas phase and the classical matrix-isolation techniques [6].
Yet another reason for the unabated interest is the formation of bubbles around electrons and electronically excited helium atoms within or at the surface of helium clusters [7,8].
The ingenuity of technical approaches taken in the study of helium clusters is breathtaking. Even though helium clusters are much more difficult to generate than other weakly bound elemental clusters, helium is the only system for which the size distribution of neutral clusters has been measured over a wide range by diffraction of nano-structured grids [9].

The main goal of this project will be the development of force fields to describe the interaction of Helium atoms with molecules. From an experimental point of view there are many questions which cannot be answered within the experiment in Innsbruck. For example, after the ionization process the ionic products are expelled from the droplet and a few Helium atoms might stay attached to the ionized molecule. Whereas the composition of such a complex can be easily determined from its mass, the arrangement of the Helium atoms around the charged atom or molecule remains unknown. Also the arrangement of two different molecules within a superfluid Helium droplet cannot be answered with the experiments. This

would be of major interest in the case where, for example, different DNA bases form mixed and pure dimers. The structure of such complexes could, for example, give detailed insight in the possible formation of complexes on interstellar dust in outer space. Cold temperatures and the presence of slow electrons generated via the photoelectric effect on dust particles are in many ways analogous to the scenario in the Helium droplets we want to model.

The theoretical work in Sweden is divided in four steps and altogether these steps will allow us to model molecules and ions solvated by Helium atoms. In the first part of the project, the interaction of Helium atoms with small neutral, cationic and anionic atomic and molecular systems (e.g. Chloride ion, chloroform and water) will be studied using quantum mechanical (QM) electronic structure (ab initio) calculations. These calculations are performed using different levels of theory and basis sets of different accuracy to determine the level required for a reliable description of small gas phase clusters containing these molecules and ions, as well as one to several Helium atoms. The interaction of the Helium atoms with the molecules is very weak and therefore it is essential to use a method that can reliably compute these weak bonds. For instance, the performance of extrapolation methods will be explored for these systems. In extrapolation methods several energy calculations are performed for each geometry and the resulting energy values are combined to form the final energy. As an example the energy of very accurate but very expensive Coupled Cluster (CC) calculations obtained with a smaller basis set may be combined with MP2 calculations using very large basis sets, since it is often the case that the finite basis set errors are similar for the CC and MP2 methods, i.e. accurate energies may be obtained by the extrapolation E(MP2/aug-cc-pV5Z)+E(CCSD(T)/aug-cc-pVTZ)-E(MP2/aug-cc-pVTZ).

The project altogether as well as the first results of the step mentioned above are presented to the scientific community at the SASP 2010 conference in Obergurgl.

Acknowledgement:

This work is supported by the Swedish Research Council. A.M. gratefully acknowledges an ‘Erwin-Schrödinger-abroad’ stipend from the FWF, Vienna (Austria).

References

[1] E.W. Becker, R. Klingerhofer, P. Lohse, Increase of separation of isotopes in separation nozzles by addition of light gases. Z. Naturforschg. 16a (1961), 1259.

[2] K.B. Whaley, Structure and dynamics of quantum clusters. *Int. Rev. Phys. Chem*. **13** (1994), 41-84.

[3] P. Sindzingre, D.M. Ceperley, M.L. Klein, Path-Integral Monte Carlo Studay of Low-Temperature ^{4}He Clusters. *Phys. Rev. Lett.* **63** (1989), 1601.

[4] S. Grebenev, J.P. Toennies, A.F. Vilesov, Superfluidity within a small helium-4 cluster: the microscopic Andronikashvili experiment. *Science* **279** (1998) 2083-2086.

[5] M. Farnik, J. Toennies, Ion-molecule reactions in 4He droplets: flying nano-cryo-reactors. *J. Chem. Phys.* **122** (2005), 014307.

[6] J. P. Toennies, A. F. Vilesov, Matrix techniques: Superfluid helium droplets: a uniquely cold nanomatrix for molecules and molecular complexes. *Angew. Chem. Int. Ed.* **43** (2004), 2622-2648.

[7] U. Henne, J.P. Toennies, Electron capture by large helium droplets. *J. Chem. Phys.* **108** (1998) 9327-9338.

[8] K. von Haeften, T. Laarmann, H. Wabnitz, T. Möller, Bubble Formation and Decay in ^{3}He and ^{4}He Clusters. *Phys. Rev. Lett.* **88** (2002), 233401.

[9] W. Schöllkopf, J.P. Toennies, Nondestructive mass selection of small van der Waals clusters. *Science* **266** (1994), 1345-8.

Supersonic Jet Isotope Selective Infrared Spectroscopy of the Second Overtone Polyad of the NH-Stretching Vibration in $C_6H_5NH_2$, $C_6D_5NH_2$ and C_6H_5NDH

E. Miloglyadov, A. Kulik, M. Quack, G. Seyfang[1]

[1] *Physical Chemistry, ETH Zürich, CH-8093 Zürich, Switzerland, miloglyadov@ir.phys.chem.ethz.ch*

We report the spectra of the second NH-stretching overtone (polyad with N=3) of rotationally cold $C_6H_5NH_2$, $C_6D_5NH_2$ and C_5H_5NHD isotopomers of aniline measured by mass and isotope selective overtone spectroscopy (ISOS) in a molecular beam. Comparison of the assignments for $C_6D_5NH_2$ and normal aniline $C_6H_5NH_2$ confirmed the applicability of the normal mode model to the NH_2-infrared-chromophore in aniline. To extract the tunnelling splitting the second NH-stretching overtone spectrum in the C_5H_5NHD has been measured at different rovibrational temperatures. The further decrease of the tunneling splitting in C_6H_5NHD with higher NH-stretching excitation demonstrates the inhibiting nature of the NH-stretching mode.

Introduction

The investigation of the vibrational structure and dynamics in aniline has a long history. The inversion motion of the NH_2 group over the plane of the phenyl ring can be described by a double well potential with a saddle point of the potential hypersurface at the planar geometry. An early determination [1] led to a barrier of about 450 cm^{-1}. The tunneling process through the barrier splits the ground state and also many vibrationally excited states into two tunneling components. The dependence of the effective inversion tunneling potential upon the excitation of some vibrational modes was approximately treated using the quasi-adiabatic channel reaction path Hamiltonian (RPH) [2,3,4]. Supersonic jet ISOS spectroscopy has been used in our group to measure the tunneling splitting in the first NH-stretching overtone region of $C_6H_5NH_2$ and C_5H_5NHD, showing the NH-stretching to be an inhibiting mode [5,6]. Some measurements in the gas phase at room temperature of the N=3, 4, 5 overtone polyads using intra cavity acoustic spectroscopy have been reported more recently [7] including a vibrational analysis [8]. The main goal of the present experiments is the measurement of the vibrationally state resolved spectra of the second NH-stretching overtone (polyad with N=3) of rotationally cold $C_6H_5NH_2$, $C_6D_5NH_2$ and C_5H_5NHD anilines by the ISOS method in a molecular beam [3,4,9,10]. Comparison of the assignment for $C_6D_5NH_2$ and normal aniline $C_6H_5NH_2$ confirmed the applicability of the normal mode model to the NH_2-chromophore in aniline in the preliminary analysis of the spectra reported here. The vibrational analysis on the basis of overtone data, including Fermi coupling between NH-stretching and symmetric NH_2-

bending overtone, will be presented as well as our most recent results of the -NHD isotopomer, which shows isotopic short time chirality [3-5,11]. As this isotopomer occurs only in a mixture with $C_6H_5NH_2$ and $C_6H_5ND_2$ ISOS is essential for measuring its spectra accurately.

Experimental setup

To measure the near infrared (NIR) spectra we used infrared excitation combined with detection of the excited molecules by the REMPI method with the advantage of isotope selectivity provided by a time-of-flight mass spectrometer (TOF, Kaesdorf, Munich). The mass resolution of the ion spectra allowed us to separate isotope substituted ions from the main ion species. The description of the experimental setup and an explanation of the ISOS method can be found in refs. [5] and [6]. The rotational temperature of the aniline molecules in the molecular beam was estimated from the rotational contour to be about 20 K. The infrared absorption of the molecules during the scanning of the NIR (IR) wavelength is monitored by the change of the ion yield of the REMPI process. The NIR (IR) spectra were calibrated by ammonia, acetylene and water absorption lines, measured in a photo-acoustic cell in parallel.

Results and discussion

Assignment of the measured second overtone action spectra of the anilines $C_6H_5NH_2$ and $C_6D_5NH_2$ are presented in the Table 1.

Table 1 *Assignment of the vibrational states in the range of the second NH stretching overtone spectra of the anilines $C_6H_5NH_2$ and $C_6D_5NH_2$ measured in a molecular beam.*

		$C_6D_5NH_2$		**$C_6H_5NH_2$**	
approximate assignment	Transition symmetry	$\tilde{\nu}$ /cm^{-1}	relative intensity	$\tilde{\nu}$ /cm^{-1}	relative intensity
$3\nu_s(+)$	A_1	9862.9(5)	0.534	9864.5(5)	0.52575
$2\nu_s+\nu_{as}$ (+)	B_2	9878.9(5)	0.222	9881.8(5)	0.14485
$2\nu_s+2\beta_s(+)$	A_1	9923.6(10)	0.0504	9930.6(10)	0.05365
$\nu_s+\nu_{as}+2\beta_s(+)$	B_2	9947.3(10)	0.06855	9953.7(10)	0.11803
Anharm. res.		9959.7(10)	0.05847		
$2\nu_{as}+2\beta_s(+)$	A_1	10059.7(5)	0.00874	10063.5(5)	0.02682
Anharm. Res.				10127.2(5)	0.00966
$2\nu_{as}+\nu_s$ (+)	A_1	10157.0(5)	0.0457	10159.6(5)	0.09174
$3\nu_{as}(+)$	B_2	10280.6(5)	0.01075	10282.7(5)	0.02951

Table 2 *Preliminary parameters of the effective Hamiltonian for $C_6H_5NH_2$ obtained from the fits.*

Parameter	7 param. fit value	11 param. fit value
ν'_s/cm^{-1}	3446.61	3447.06
β'_s/cm^{-1}	1594.86	1624.41
ν'_{as}/cm^{-1}	3517.09	3543.07
x'_{ss}/cm^{-1}	-35.89	-38.68
x'_{bb}/cm^{-1}	12.66	-4.39
$x'_{as,as}/cm^{-1}$	-35.89	-45.46
$x'_{s,as}/cm^{-1}$	-143.55	-149.01
x'_{sb}/cm^{-1}	-18.96	-9.18
$x'_{as,b}/cm^{-1}$	-18.96	-22.62
k_{sbb}/cm^{-1}	59.58	58.68
$\gamma_{ss,asas}/cm^{-1}$	143.55	140.67
RMS/cm^{-1}	8.44	1.77

Both spectra have been measured at expansion conditions where only one component of the tunneling doublets was observed. The analysis of the vibrational spectra of the NH_2 group was done in the framework of a normal mode model for quasi-triatomic molecules of the C_{2v} (M_{S4}) molecular symmetry group treating the phenyl-group fragment as a quasiatom. The modes considered are: symmetric stretching vibration ν_s, bending mode β_s and asymmetric stretching vibration ν_{as}. For an intermediate analysis of the effective Hamiltonian that in our case appears to be a function of 11 parameters we have used approximations [12] for a triatomic molecule, which reduced the number of parameters to 7. For the vibrational analysis of the NH stretching overtone spectra we have used the assignment of the data in the polyads N=1/2, 1, 3/2 and 2 from ref. [2], [5], [13] which together with our data in the polyad N=3 gave a set of 17 band centers used for the fit. The fitted model parameters are summarized in table 2. These vibrational parameters are obtained from vibrational band positions derived as averages from the tunneling doublets.

We have also extended the overtone measurements for the isotopomer C_6H_5NHD to the second overtone range.

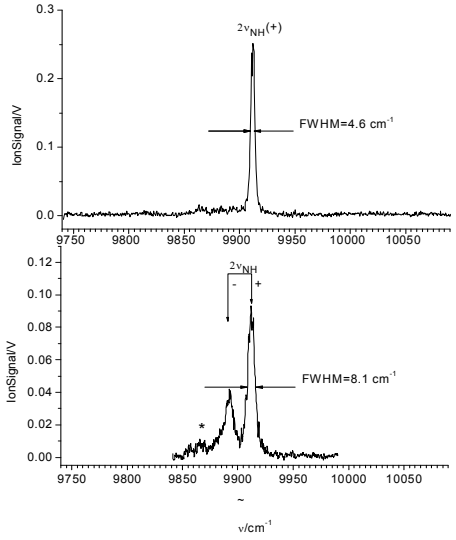

Figure 1 *Second overtone ISOS spectra of aniline $^{12}C_6H_5NHD$ and $^{13}C^{12}C_5H_5NH_2$(*) measured in the molecular beam with an instrumental resolution 0.15 cm^{-1}, as an ion signal mass-gated at m/z=94. The upper trace is the spectrum obtained in a jet expansion with 0.8 bar of Ar; the lower trace is the spectrum obtained in a jet expansion with 0.35 bar of Ar. The appearance of the bands corresponding to the lower tunneling doublet component in the lower trace indicates a higher vibrational temperature estimated to be about 40K.*

The measurements were accomplished at different temperatures by changing the seeding conditions in the supersonic jet expansion. The spectrum obtained in the expansion of a

mixture of 7 mbar aniline with 800 mbar of Ar buffer gas showed only one band at 9911.9(2) cm^{-1} corresponding to a transition between the lowest components of the tunneling splitting. The spectrum recorded at these expansion conditions is presented in the upper trace of figure 1. Reduction of the pressure of the Ar buffer gas to 350 mbar led to an increase of the internal temperature and consequently to a rise of the second band of the tunneling doublet at 9891.6(5) cm^{-1} (see lower trace of figure 1). The assignment of NH-stretching fundamental and overtone bands of C_6H_5NHD aniline from ref. [13] and [5] and the present paper are summarized in table 3.

Assignment	Transition $\tilde{\nu}$ /cm^{-1}	$\Delta\tilde{\nu}$ /cm^{-1}
Ground state		23.8 (23.7)
ν_{NH} (u, u)	3450.1 [2,13]	12.5(12.0)
ν_{NH}(l, l)	3461.4 [2]	
$2\nu_{NH}$(u, u)	6747 [5]	6.6
$2\nu_{NH}$(l, l)	6764.2 [5]	
$3\nu_{NH}$ (u, u)	9891.6(5) this work	3.5
$3\nu_{NH}$(l, l)	9911.9(2) this work	

Table 3. *Assignment of NH-stretching fundamental and overtone bands of C_6H_5NHD aniline. The transition wave number $\tilde{\nu}$ connects upper, upper (u, u) and lower, lower (l, l) inversion sublevels. $\Delta\tilde{\nu}$ is the inversion splitting of the vibrational state, theory [2] in parentheses*

Acknowledgements. Our work was financially supported by the Schweizerischer Nationalfonds. We thank Michael Hippler and Andreas Schneider for help and discussions and Reto Ulrich for the synthesis of the $C_6H_5ND_2$.

[1] M. Quack, M. Stockburger, J. Mol. Spectrosc., 43, 87 (1972)
[2] B. Fehrensen, D. Luckhaus, M. Quack, Z. Phys. Chem., 209, 1 (1999)
[3] B. Fehrensen, D. Luckhaus, M. Quack, Chem. Phys. Lett., 300, 312 (1999)
[4] B. Fehrensen, D. Luckhaus, M. Quack, Chem. Phys., 338, 90 (2007)
[5] B. Fehrensen, M. Hippler, M. Quack, Chem. Phys. Lett., 298, 320 (1998)
[6] M. Hippler, M. Quack, Isotope Selective Infrared Spectroscopy Intramolecular Dynamics, in "Isotope Effects in Chemistry and Biology", by A. Kohen and H. Limbach(eds.), Taylor & Francis, 2006, pp.305-359
[7] D. Howard, T. Robinson, A. Fraser, H. Kjaergaard, Phys. Chem. Chem. Phys., 6, 719 (2004)
[8] V. Hanninen, L. Halonen, J. Chem. Phys., 126, 064309 (2007)
[9] M. Hippler, M. Quack, Chem. Phys. Lett., 231, 75 (1994)
[10] M. Hippler, M. Quack, J. Chem. Phys., 104, 7426 (1996)
[11] M. Quack, Angew. Chem. Intl. Ed. (Engl.), 28, 571 (1989)
[12] I. M. Mills, A. G. Robiette, Molec. Phys., 56, 743-765 (1985)
[13] B. Fehrensen, Infrarotspektroskopie und Quantendynamik der Stereomutation von Anilin und H_2O_2 und ihren Isotopomeren, PhD thesis, ETH Zurich, no. 13253, 1999

CH Stretching Overtone Spectra of $^{12}CH_3I$ and $^{12}CHD_2I$ Measured by NIR-Pump UV-Probe Experiments

E. Miloglyadov, V. Krylov, A. Kushnarenko, M. Quack, G. Seyfang
Physical Chemistry, ETH Zürich, CH-8093 Zürich, Switzerland, miloglyadov@ir.phys.chem.ethz.ch

We report the vibrational spectra of the first CH-stretching overtone of rotationally cold $^{12}CH_3I$ and CHD_2I, measured by isotope selective overtone spectroscopy (ISOS) in a molecular beam. The action spectra of $^{12}CH_3I$ measured at a rotational temperature of 5 K differ significantly from the room temperature FTIR spectrum, which may be indicative of incomplete redistribution of vibrational energy (IVR) at a delay time of about 100 ns. The observed vibrational structure is attributed to the combination bands of sets of the CI-stretching vibrations with levels strongly coupled to the overtone of the CH-stretching vibration.

Introduction

The fundamental process of intramolecular vibrational energy redistribution (IVR) involves the transfer of energy from a well-defined time-dependent initial state to other nearly isoenergetic states in the absence of collisions or any other interaction of the isolated molecule with its surrounding. IVR is important for a large number of chemical processes in general and for our understanding of unimolecular reactions in particular [1, 2]. The present work was motivated by previous studies on the ultra fast evolution of UV-absorption changes induced by IVR in CH_3I excited to the first overtone of the CH-stretching vibration [3-5]. To explain the relaxation behaviour in the NIR-pump-UV-probe experiments [5] the measurement and vibrational analysis of state resolved spectra of rotationally cold CH_3I is required.

Experimental setup

To measure the NIR spectra we used an infrared excitation combined with detection of the absorbed photons by the REMPI method with the advantage of isotope selectivity provided by a time-of-flight mass spectrometer. The mass resolution of the ion spectra allowed us to separate isotope substituted ions from the main ion species. The description of the experimental setup and an explanation of the ISOS method can be found in refs. [6-8]. The NIR (IR) spectra were calibrated by methane absorption lines, measured in a photoacoustic cell in parallel. Action spectra of methyl iodides were obtained as ion yield changes of the REMPI signal of excited iodine ($^2P_{1/2}$) resulting from the UV+NIR excitation of the molecules to dissociative S_1 state through the $5s^25p^46p^2$ $D^o_{3/2}$ state of the iodine at 65208 cm^{-1}.

Results and discussion

Five different vibrational bands have been assigned by Duncan et al. [9] in the spectral region of the first overtone of the CH-stretching vibration. Between the two bands with A_1-symmetry $2\nu_1$ and $2\nu_4^0$ at 5891.03 cm^{-1} and 6052.23 cm^{-1}, a strong Darling-Dennison resonance with a coupling matrix element of W_{1144} = 57.1 cm^{-1} has been found. The two bands with E-symmetry, $\nu_4^{\pm1} + 2\nu_5^0$ and $\nu_1+\nu_4^{\pm1}$ at 5874.0 cm^{-1} and 5941.05 cm^{-1} are coupled in the normal mode description through a Fermi resonance with a coupling matrix element of W_{155}=33.00 cm^{-1} [9,10]. The higher lying E-type band $2\nu_4^{\pm2}$ at 6102.15 cm^{-1} is coupled to the $\nu_1+\nu_4^{\pm1}$ vibrational state with W_{1444} = 57.2 cm^{-1}. For CHD_2I the CH-stretching vibration ν_1 is coupled to overtones of the two bending modes ν_3 and ν_8 by a strong Fermi resonance. From the analysis of a 3-dimensional subspace coupling constants of k_{133} = 85 and k_{188} = 45 cm^{-1} have been obtained [11]. Experimental overtone action spectra for CH_3I and CD_2HI are presented in figure 1. The intensity distribution across the action spectrum does not reproduce the intensity distribution expected for the absorption spectrum according to the assigned five main bands. Around 6052 cm^{-1} where the $2\nu_4^0$ vibrational band has been assigned one observes only rotationally unresolved band of much smaller relative intensity and rotationally unresolved dense structure that can not be related to the methyl iodide itself but perhaps to methyl iodide clusters. No rotational structure around the assigned band center of the $2\nu_4^0$ band with A_1 symmetry was observed. The typical structure of the $2\nu_4^{\pm2}$ perpendicular band at 6102.15 cm^{-1} was also not observed, but only one Q branch coinciding with assigned position of the $^PQ_1$ branch at 6097.1 cm^{-1}. In the lower frequency part of the spectrum below 6000 cm^{-1} the $^RQ_0$, $^RQ_1$ and $^PQ_1$ branches of the $\nu_1+\nu_4^{\pm1}$ band with a small intensity can be identified. Most of the bands carrying intensity in the action spectrum are concentrated around 5885 cm^{-1}. One parallel band at 5891.45 cm^{-1} assigned to $2\nu_1$ and four perpendicular bands centered according to a band simulation at 5863.7, 5864.75, 5886.5 and 5894.4 cm^{-1}. Also a second parallel band (A_1) at 5980.5 cm^{-1} was found in the action spectrum. Only the $2\nu_1$ and $\nu_1+\nu_4^{\pm1}$ bands have been assigned in the room temperature near-IR spectrum. No detailed rovibrational analysis in the overtone region is available yet. The analysis would be important for the understanding of the fast relaxation kinetics found in femtosecond pump-probe experiments with sensitive UV-probing. Stimulated Raman probing of dissociating CH_3I (after UV-excitation) [12] and theoretical calculations of the UV-absorption spectrum [13] show that the shift of the UV-spectrum, which is detected in the UV-probing, is related to the excitation of the CI-stretching vibration ν_3. Therefore vibrations including ν_3 will be preferentially detected in the action spectrum and it should be possible to identify at least some of the directly coupled states which are important for the fast relaxation process in the femtosecond experiments from the rovibrationally resolved molecular beam spectra. For the region of the fundamental CH-stretching vibration two major Fermi resonances were

identified for the vibrations with A_1-symmetry: The coupling of the ν_1 to the first overtone of the CH-bending mode ν_5 and to the combination band $\nu_5^{\pm1}+\nu_3+\nu_6^{-/+1}$. In a later high resolution study [14] one more resonance between $\nu_5^{\pm1}+\nu_3+\nu_6^{-/+1}$ and $2\nu_3+2\nu_6^{0}$ has been included in the coupling scheme, confirming the Fermi constant k_{356}=29.7 cm^{-1} which has been well determined in previous studies [15,16].

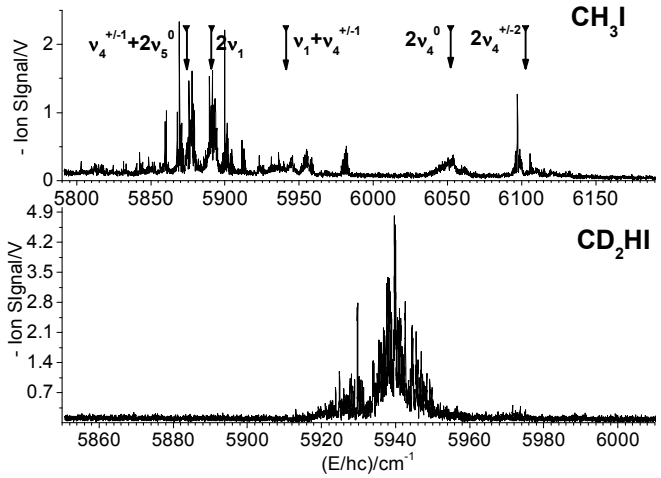

Fig. 1: Action spectra of CH_3I (upper trace) and CD_2HI (lower trace) in the spectral region of the first overtone of the CH-stretching vibration measured by the ISOS method in a molecular beam at a rotational temperature of about 5 K. The centers of the five vibrational bands in CH_3I, identified in the absorption spectrum by Duncan et al. [9], are indicated.

It has been fixed in the C-H stretching overtone analysis [9,10]. Taking into account only the anharmonic couplings and neglecting the contributions from Fermi and Darling-Dennison resonances the energies of the two different vibrational levels $\nu_3+\nu_4^{\pm1}+\nu_5^{-/+1}+\nu_6^{\pm1}$ and $\nu_3+\nu_4^{\pm1}+\nu_5^{\pm1}+\nu_6^{-/+1}$ are calculated to 5888.6 cm^{-1} and 5879.5 cm^{-1}, where the splitting arises from the two possible combinations of the angular momenta l_i. These two levels are coupled to the same the level $2\nu_3+\nu_4^{\pm1}+2\nu_6^{0}$ calculated at a vibrational energy of 5848.1 cm^{-1}. The corresponding coupling matrix element between $\nu_4^{\pm1}+2\nu_5^{0}$ and $\nu_3+\nu_4^{\pm1}+\nu_5^{-/+1}+\nu_6^{\pm1}$ / $\nu_3+\nu_4^{\pm1}+\nu_5^{\pm1}+\nu_6^{-/+1}$ is W_{345}=10.5 cm^{-1} and between $\nu_3+\nu_4^{\pm1}+\nu_5^{-/+1}+\nu_6^{\pm1}$ / $\nu_3+\nu_4^{\pm1}+\nu_5^{\pm1}+\nu_6^{-/+1}$ and $2\nu_3+\nu_4^{\pm1}+2\nu_6^{0}$ is W'_{345}=14.85 cm^{-1} [9,10]. These four coupled levels together with $\nu_1+\nu_4^{\pm1}$ are forming a pentad of states. In the action spectrum of CH_3I at the assigned position of $\nu_1+\nu_4^{-/+1}$ a band at 5941 cm^{-1} was observed, but it has a very small intensity. Three of four strong E-bands in the action spectrum at 5864.75, 5886.5 and 5894.4 cm^{-1} can be assigned according to the coupling scheme to $\nu_4^{\pm1}+2\nu_5^{0}$, $\nu_3+\nu_4^{\pm1}+\nu_5^{\pm1}+\nu_6^{-/+1}$ and $\nu_3+\nu_4^{\pm1}+\nu_5^{-/+1}+\nu_6^{\pm1}$. The weak band at 5837.8 cm^{-1} is the most probable candidate for $2\nu_3+\nu_4^{\pm1}+2\nu_6^{0}$. Considering the vibrational states with A_1-symmetry a medium strong Fermi resonance between the ν_1- and the $2\nu_2+\nu_3$-state have been found with a coupling matrix element of W_{1223}=4.5 cm^{-1} [17]. In the anharmonic approximation a vibrational energy of 5978.9 cm^{-1} is obtained for the unperturbed $\nu_1+2\nu_2+\nu_3$-state. One parallel band that belongs to transitions to the states with A_1-symmetry was observed at 5980.5 cm^{-1} in the action spectrum and it is assigned to the

$\nu_1+2\nu_2+\nu_3$ transition. For the two $2\nu_4$ vibrational states with A_1- and E-symmetry only the $(\nu_2+\nu_4+2\nu_6)$-states with calculated energies of 6069.3 cm^{-1} $(\nu_2+\nu_4^{\pm1}+2\nu_6^{0})$, 6071.8 cm^{-1} $(\nu_2+\nu_4^{\pm1}+2\nu_6^{-/+2})$, and 6080.6 cm^{-1} $(\nu_2+\nu_4^{\pm1}+2\nu_6^{\pm2})$ have to be considered. A quite weak resonance with a coupling matrix element W_{4266}=0.7 cm^{-1} has been determined between the vibrational states $\nu_4^{\pm1}$ and $\nu_2+2\nu_6^{\pm2}$ [18]. Around the $2\nu_4^{\pm2}$ transition only a part of a band with a single Q branch at 6097.1 cm^{-1} has been observed, and is most probably related to a transition which is Coriolis coupled to $2\nu_4^{\pm2}$.

Coming to the analysis of the overtone action spectra of CHD_2I it should be mentioned that only one state can be clearly assigned. According to the simulations a hybrid band centered at 5936.8 cm^{-1} fits to the position of $2\nu_1$ reported at 5936 cm^{-1} by [11] in the room temperature spectra. The other observed two bands, centered at 5926.8 cm^{-1} and 5939.7 cm^{-1} cannot yet be assigned definitely. While the present analysis of the spectra is very preliminary, our results provide a first access to obtain rates of IVR including lower frequency modes, beyond the analysis of the very fast femtosecond IVR of CH stretching and bending modes [11].

Acknowledgements. Our work was financially supported by the Schweizerischer Nationalfonds. We thank Michael Hippler and Jürgen Stohner, and Martin Willeke and Andreas Schneider for help and discussions.

[1] M. Quack, Molecular femtosecond quantum dynamics between less than yoctoseconds and more than days: Experiment and theory, Chapter 27 in "Femtosecond Chemistry", J. Manz and L. Woeste (eds.), Verlag Chemie, 1995, pp. 781 – 818
[2] R. Marquardt and M. Quack, Energy Redistribution in Reacting Systems, in "Encyclopedia of Chemical Physics and Physical Chemistry", J. Moore and N. Spencer (eds.) , Vol. 1 (Fundamentals), Chapter A.3.13, IOP Publ., Bristol, 2001, 897 – 936
[3] V. Krylov, M. Nikitchenko, M. Quack, and G. Seyfang, Proc. of SPIE.5337, 178 (2004).
[4] C.G. Elles, M.J. Cox, and F.F. Crim, J. Chem. Phys. 120, 6973 (2004)
[5] V. Krylov, E. Miloglyadov, M. Quack, and G. Seyfang, SASP 2006 Contributions, V. Grill, T. D. Märk (eds.), Innsbruck University Press, ISBN: 3-901249-82-6, 238 (2006)
[6] B. Fehrensen, M. Hippler, M. Quack, Chem. Phys. Lett., 298, 320 (1998)
[7] M. Hippler and M. Quack, Chem. Phys. Lett. 231, 75 (1994).
[8] M. Hippler and M. Quack, Isotope Selective Infrared Spectroscopy and Intramolecular Dynamics, Chapter 11 in "Isotope Effects in Chemistry and Biology", A. Kohen and H.-H. Limbach (eds.), Taylor&Francis, 2006
[9] J.L. Duncan, A.M. Ferguson, and S. Mathews, J. Chem. Phys. 91, 783 (1989).
[10] M.M. Law, *J. Chem. Phys.* 111, 10021 (1999).
[11] V. Horká, M. Quack, and M. Willeke, Mol. Phys., 106, 1303 (2008)
[12] D. Imre, J. L. Kinsey, A. Sinha, and J. Krenos, J. Phys. Chem. 88, 3956 (1984).
[13] A.B. Alekseyev, H.P. Liebermann, R.J. Buenker, J. Chem. Phys. 126, 234103 (2007).
[14] F. Lattanzi, J. Chem. Phys. 92, 4380 (1990).
[15] H. Matsuura and J. Overend, J. Chem. Phys. 56, 5725 (1972).
[16] Y. Morino, J. Nakamura, and S. Yamamoto, J. Mol. Spectr. 22, 34 (1967).
[17] R. Paso, R. Antilla, and G. Guelachvili, J. Mol. Spectrosc. 140, 46 (1990).
[18] R. Antilla, R. Paso, and G. Guelachvili, J. Mol. Spectrosc. 119, 190 (1986).

The GAMBIT Project Shall Utilize the XMCD Effect to Determine the Spin- and Orbit Contributions to the Magnetic Moments of Isolated Transition Metal Clusters

H. Kampschulte[1], S. Peredcov[3], S. Peters[3], M. Neeb[3], W. Wurth[2], W. Eberhardt[3], G. Niedner-Schatteburg[1]

[1] *Fachbereich Chemie and Forschungszentrum OPTIMAS, Technische Universität Kaiserslautern, Erwin-Schrödinger-Straße 52, 67663 Kaiserslautern, Germany*

[2] *Universität Hamburg, Insitut für Experimentalphysik, Luruper Chaussee 149, 22761 Hamburg, Germany*

[3] *Helmholtz-Zentrum Berlin für Materialien und Energie, Wilhelm-Conrad-Röntgen-Campus Adlershof, Elektronenspeicherring BESSY II, Albert-Einstein-Straße 15, 12489 Berlin, Germany*

X-ray induced Magnetic Circular Dichroism (XMCD) is an established technique to determine the spin and orbit contributions to the total magnetic moments within bulk samples, thin metal films or supported macro molecules. Only recently such experiments have succeeded on size selected transition metal clusters which were deposited on an appropriate support [1,2]. It showed that strong electronic coupling of the clusters to the support takes place rendering the determination of intrinsic cluster properties difficult.

Our own current and previous research has focussed on the IR spectroscopy and on the reactivity of molecular clusters and of transition metal clusters when isolated under single collision conditions [3-5]. We felt it worthwhile to complement our findings with research on the electronic structure of such clusters. This brought about the concept of the new GAMBIT project. For this purpose we have setup a new Fourier-Transform-Ion Cyclotron Resonance (FT-ICR) mass spectrometer with an external cluster ion source. The instrument is connected to the X-ray undulator beam line UE-52-PGM at the BESSY synchrotron light source in Berlin. [6]

The XMCD-effect emerges upon inner shell ionization of samples with oriented magnetic moments. The required high degree of orientation arises from application of sufficiently strong homogeneous magnetic field (up to 7 Tesla) to cluster ions of kinetic energies as low as 20 Kelvin. The magnetic field comes with the FT-ICR instrument while the cluster cooling needs additional efforts. We have designed and built a dedictated ultra high vacuum module that incorporates a novel cryogenically cooled FT-ICR-cell. It was tested to work at cell temperatures as low as 16 Kelvin while shielding stored ions against black body radiation.

This cryo-ICR-module is scheduled to migrate to, and to integrate into the GAMBIT setup by December 2009.

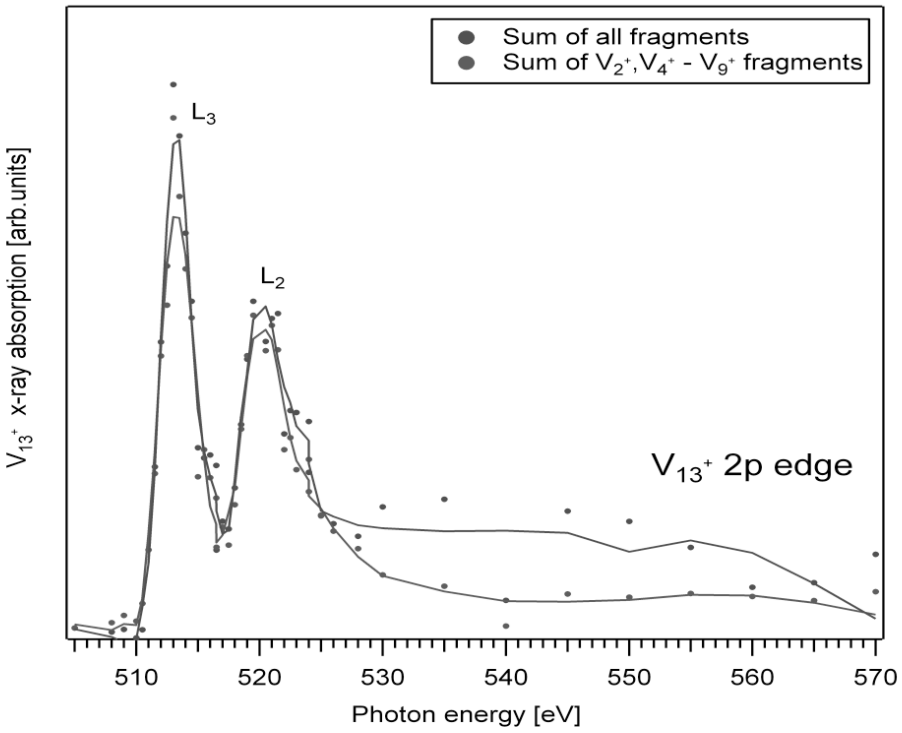

Our contribution aims to provide the latest update on our current achievements. We aim to record the X-ray polarization de-pendent variation of the relative intensities of the fine structure components at the L-edge of 3d transition metals. By virtue of subsequent "sum rule analysis", we will yield the spin and orbit contribution to the total magnetic moments as a function of cluster size. Subsequent variation of the magnetic field, of the cluster temperature, and of the cluster net charge (anionic/cationic) will provide for unique data on the electronic structure which would otherwise not be available. Please note, that prior Stern-Gerlach experiments did record total magnetic moments without resolving them for their spin and orbit contributions.

References

[1] J. T. Lau, A. Föhlisch, M. Martins, R. Nietubyc, M. Reif and W. Wurth,
New J. Phys. 4 (2002) **98**,1 - 98.12
[2] J. T. Lau, A. Föhlisch, R. Nietubyc, M. Reif and W. Wurth,
Phys Rev. Lett. (2002) **89** 057201
[3] T. Pankewitz, A. Lagutschenkov, G. Niedner-Schatteburg, S.S. Xantheas, and Y.T. Lee, J. Chem. Phys. **126**, 074307 (2007)
[4] G. Niedner-Schatteburg, Angew. Chem. Intern. Ed. **47**, 1008 (2008)
[5] B. Pfeffer, S. Jaberg, and G.Niedner-Schatteburg, J.Chem.Phys (2009), in print
[6] We gratefully acknowledged funding by the „Deutsche Forschungsgemeinschaft", DFG grant Nie325/10-1

Effect of Aluminum Clusters Size on Barriers to Hydrogen Adsorption

Ilaria Pino, Marc C. van Hemert and Geert-Jan Kroes
University of Leiden, Gorlaeus Laboratories, Einsteinweg 55, 2333CC Leiden, The Netherlands

Safe and efficient hydrogen storage is one of the main challenges that needs to be addressed to put the hydrogen economy in place. Several new solid materials have been identified which could act as hydrogen absorbers and releasers depending on working pressure and temperature. However, none of these is efficient enough in terms of operating times (kinetics) and temperature, volumetric and gravimetric density, reversibility, and stability under cycling, in order to be used in some high-performance practical applications such as motoring [1,2,3]. For these reasons, further research is required for tuning and optimizing the already known materials or for finding more efficient new ones. To this aim, it is important to understand the principal mechanisms which govern the macroscopic behavior of these systems, by means of synergistic theoretical and experimental studies. It has been found that alanates (complex hydrides containing $AlH_n^{-(n-3)}$ anions) exhibit improved kinetics and low-temperature efficiency in hydrogen absorption/release by decreasing particle size at the nanometric scale level [4], or if they are doped with some metals, such as Ti [5,6], or ball milled with carbon [7,8], or adsorbed on carbon supports [9,10]. Sodium alanate in particular ($NaAlH_4$) is very promising for its large theoretical reversible storage capacity on condition that improved kinetics would make it efficient at lower operating pressure and temperature. It has been commonly accepted that the elementary reactions governing hydrogen release and uptake are the following [11]:

$$NaAlH_4 \rightarrow \tfrac{1}{3}\, Na_3AlH_6 + \tfrac{2}{3}\, Al + H_2$$

$$\tfrac{1}{3}\, Na_3AlH_6 \rightarrow NaH + \tfrac{1}{3}\, Al + \tfrac{1}{2}\, H_2$$

$$NaH \rightarrow Na + \tfrac{1}{2}\, H_2$$

As in the first two steps aluminum atoms are released or adsorbed together with hydrogen molecules, several attempts have been made to understand the role played by aluminum in the overall process. Hydrogen adsorption on bare aluminum surfaces can only occur via dissociation of the hydrogen molecule (dissociative chemisorption) and it shows quite high barriers, the smallest one being of about 0.5 eV on Al(110) [12], whereas a Ti-doped Al(100) surface was found to have barrierless minimum energy paths for the same reaction for particular Ti atom arrangements [13].

H_2Al_n	DFT/B3LYP/6-311+G*			
n	**2S+1**	**E_a / eV**	**ΔE / eV**	**E_a(ICS) / eV**
2	**3**	0.687		0.687
	1	0.013	0.371	0.384
3	**2**	0.624		0.624
	4	0.984	0.152	1.100
4	**3**	0.942		0.942
	1	0.185	0.241	0.426
5	**2**	0.782		0.782
	4	0.737	0.400	1.137
6	**3**	0.939		0.939
	1	0.074	0.006	**0.080**

Table 1. *Calculated reaction barriers for a hydrogen molecule dissociation on different size aluminum clusters, and for different spin multiplicities (E_a). ΔE is the relative stability with respect to the most stable reactant (cluster + molecule) with the same spin. E_a(ICS) is the minimum barrier associated to a hypothetical intercrossing-system between different spin reaction paths.*

In this work we investigate the effect of size of small aluminum clusters on hydrogen adsorption barriers, since, in absence of Ti doping, hydrogen adsorption could be catalyzed by the presence of very small aluminum clusters with special properties with respect to surfaces. These could be highly correlated to the operative temperature and times, and to the reversibility yield of the process, because it was recognized earlier that the main elementary reactions involve the formation of chemical bonds between pure aluminum and hydrogen molecules [11].

An experimental work, based on pulsed cluster beam flow reactor technique, studied the reactivity of small aluminum clusters Al_n (n = 2-80) with deuterium molecules, and found the rate constant to be maximum and sharply peaked at Al_6 [14].

Transition states and reaction paths for a hydrogen molecule dissociating on small aluminum clusters have been calculated by means of density functional theory. The two lowest spin states have been taken into account for all the considered clusters Al_n with n = 2-6. The aluminum dimer, which shows a $^3\Pi_u$ electronic ground state, has been also studied at the coupled cluster and configuration interaction level, for comparison, and to check the accuracy of single determinant calculations in this special case, where two degenerate configurations should be taken into account. The calculated reaction barriers give an explanation of the experimentally observed reactivity of hydrogen on Al clusters of different size and reproduce the high reached reactivity of the Al_6 cluster. The electronic structure problem was also systematically investigated in order to determine the role played by interactions of specific molecular orbitals for different nuclear arrangements.

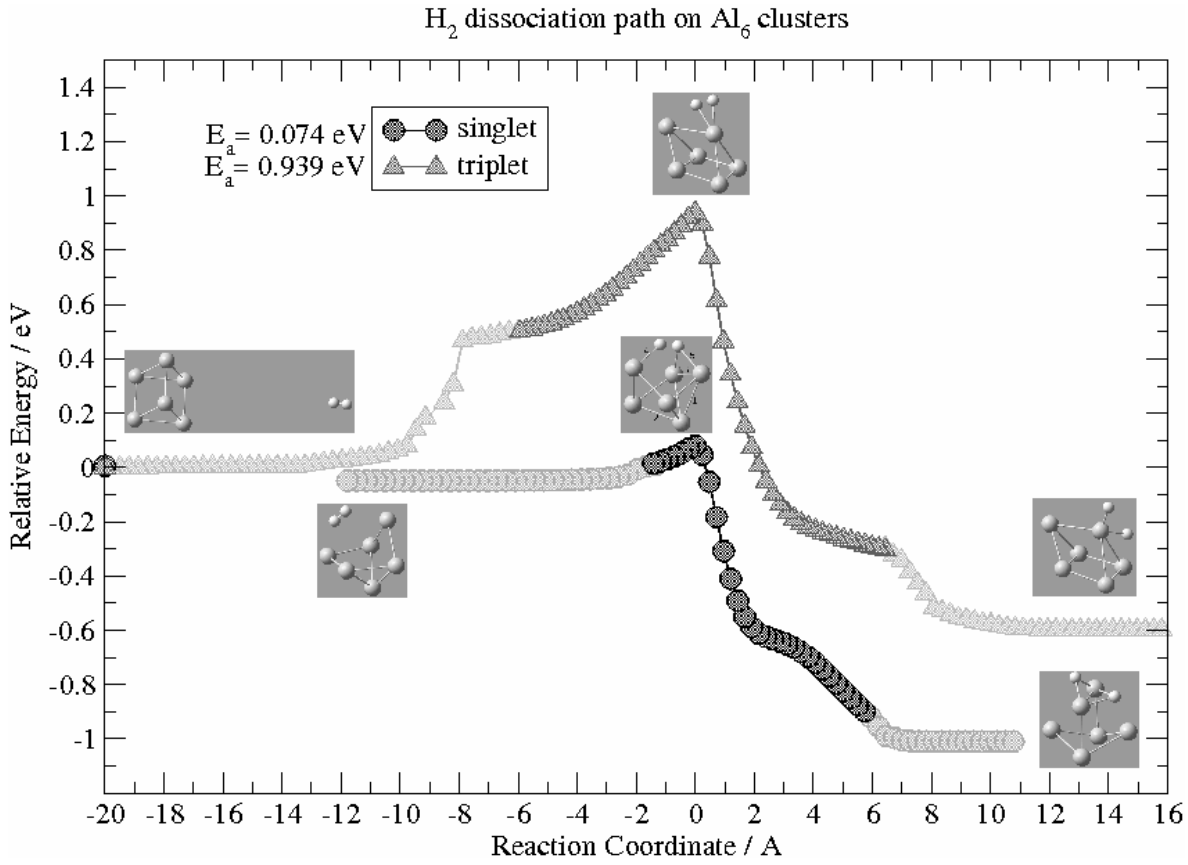

Figure 2. *Minimum reaction paths for the dissociation of a H_2 molecule on singlet and triplet aluminum hexamers.*

References

[1] S.-I. Orimo, Y. Nakamori, J. R. Eliseo, A. Züttel, and C. M. Jensen, *Chem. Rev.* **107**, 4111 (2007).

[2] M. Felderhoff, C. Weidenthaler, R. von Helmolt, and U. Eberle, *Phys. Chem. Chem. Phys.* **9**, 2643 (2007).

[3] R. Zidan et al., *Chem. Comm.* 10.1039/b901878f, 3717 (2009).

[4] C. P. Baldé, B. P. C. Hereijgers, J. H. Bitter, and K. P. de Jong, *J. Am. Chem. Soc.* **130**, 6771 (2008).

[5] B. Bogdanović and M. Schwickardi, *J. Alloys Compd.* **253**, 1 (1997).

[6] S. S. Srinivasan, H. W. Brinks, B. C. Hauback, D. Sun, and C. M. Jensen, *J. Atmos. Chem.* **377**, 283 (2004).

[7] C. Cento et al., *J. Alloys Compd.* **437**, 360 (2007)

[8] P. A. Berseth et al., *Nano Lett.* **9**, 1501 (2009).

[9] C. P. Baldé, B. P. C. Herijgers, J. H. Bitter, and K. P. de Jong, *Angew. Chem. Ind. Ed.* **45**, 3501 (2006).

[10] P. Adelhelm, K. P. de Jong, andP. E. de Jongh, *Chem. Comm.* 6261 (2009), DOI: 10.1039/b910461e.

[11] E. C. Ashby and P. Kobetz, *Inorg. Chem.* **5**, 1615 (1966).

[12] K. Gundersen, K. W. Jacobsen, J. K. Nørskov, and B. Hammer, *Surf. Sci.* **304**, 131 (1994).

[13] J.-C. Chen, J. C. Juanes-Marcos, A. Al-Halabi, R. A. Olsen, and G. -J. Kroes, *J. Phys. and Colloid Chem.* (2009) 10.1021/jp80963j CCC.

[14] J. A. Howard, R. Sutcliffe, J. S. Tse, H. Dahmane, and B. Mile, *J. Phys. Chem.* **89**, 3595 (1985).

[15] D. M. Cox, D. J. Trevor, R. L. Whetten, E. A. Rohlfing, and A.Kaldor, *J. Chem. Phys.* **84**, 4651 (1986).

Cations of Even-Numbered Hydrogen Clusters

Andreas Mauracher[1], Michael Probst[1], Olof Echt[2], Diethart Bohme[3], Paul Scheier[1], Stephan Denifl[1], Tilmann Märk

[1] *Institute of Ion Physics and Applied Physics, University of Innsbruck, Technikerstrasse 25, 6020 Innsbruck, Austria*

[2] *Department of Physics, University of New Hampshire, Durham, New Hampshire 03824, USA*

[3] *Department of Chemistry, York University, Toronto, Ontario M3J 1P3, Canada*

Recent experimental studies on molecular hydrogen inserted into droplets of liquid Helium and subsequently ionized have exhibited an interesting stability of some even-numbered H_n^+ clusters [1]. H_6^+ is found to be especially abundant. H_n^+ clusters have been the subject of many quantum-chemical studies but previous experiments have found odd-numbered clusters to be dominant and therefore even-numbered ones have received less attention. Previous theoretical works indicate that there exist two low-lying isomers of this prototypical cluster cation - the most stable one with three H_2 units perpendicular to each other and the other one a with H_3^+ at the center. We searched the potential energy surface of this multidimensional system and checked the stability of a series of geometries generated by a Monte-Carlo procedure. We did not discover isomers that were more stable than the ones already known but found some other interesting local minima.

Details of our calculations

Besides generating the possible geometries with some point group symmetry, a sample of about 50 asymmetric configurations was randomly generated and optimized at the QCISD /aug-cc-pVTZ level. They converged to a small set of isomers described below.

H_6^+

Early *ab initio* studies [2] suggested that H_6^+ consists of an equilateral H_3^+ triangle surrounded by neutral H and H_2 at two of its apices. Such a *Cs* - symmetric structure is weakly bound with respect to loss of H. Montgomery and Michels [3] identified a more stable isomer with *D*2*d* symmetry consisting of a central H_2^+ weakly bound to two H_2 molecules. More recently, Kurosaki and Takayanagi [4] optimized the geometries of H_6^+ at the MP2/cc-pVTZ level of theory and calculated their energies on the 4^{th} order Møller-Plesset perturbation theory level including single to quadruple excitations. They found that the *D*2*d* structure lies 0.17 eV below *Cs*; the latter being separated from the ground state configuration by a small (0.02 eV) barrier. The *D*2*d* structure has also been confirmed in an electron spin resonance study of hydrogen ion radicals produced by radiolysis of solid parahydrogen. There and in a path integral molecular dynamics study [5] the two outer H_2 molecules were found to rotate almost freely.

We have searched the H_6^+ potential energy surface for other possible isomers. Since also H_{30}^+ clusters are found experimentally, it would be interesting to know if there is a connection between H_6^+ units and this larger cluster, for example if H_6^+ serves as a core to accumulation of a shell of H_2 molecules.

We started this search by generating both structures with a symmetry higher than C_1 and random structures with C_1 symmetry. The sample of about 30 configurations was optimized at the QCISD/aug-cc-pVTZ level of theory. Our geometries converged to the six minima on the potential energy surface shown in the figure below.

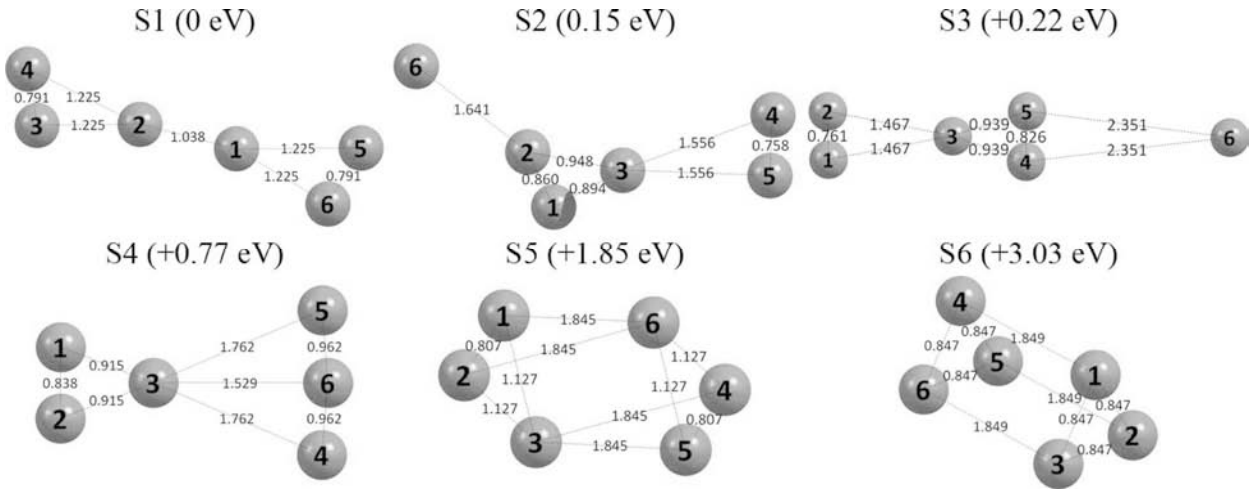

The *Cs* isomer S2 lies 0.15 eV above S1 (*D*2*d*) which is the lowest-energy structure, nearly reproducing the value of 0.17 eV calculated by Kurosaki and Takayanagi[4]. Structure S3 is only slightly higher in energy than S2. It may be best characterized as $H_5^+ + H$. It is not quite a symmetric variation of S2 because the single H is further away from the central H3 unit. A structure consisting of one linear and one triangular H_3 unit (S4) as well as the trigonal antiprismatic (S5) and prismatic (S6) structures are all significantly higher in energy than S3. Whereas S1–S4 are true locally stable isomers, S5 and S6 are stable only when confined to their symmetries *C*2*h* and *D*3*h*, respectively.

Mulliken (MULL) and natural population analysis (NPA) of the hydrogen partial charges listed in the table below show, for example, that the positive charge in S1 is indeed quite delocalized, in agreement with a molecular dynamical study [6].

H	S1		S2		S3		S4		S5		S6
	MULL	NPA	MULL	NPA	MULL	NPA	MULL	NPA	MULL	NPA	MULL
1	0.32	0.20	0.39	0.24	0.07	0.06	0.44	0.28	0.18	0.15	0.29
2	0.32	0.20	0.13	0.25	0.07	0.06	0.45	0.28	0.18	0.15	0.11
3	0.09	0.15	0.31	0.32	0.18	0.33	0.00	0.34	0.15	0.19	0.11
4	0.09	0.15	0.05	0.05	0.34	0.26	-0.04	0.13	0.18	0.15	0.29
5	0.09	0.15	0.05	0.05	0.34	0.26	-0.04	0.13	0.18	0.15	0.11
6	0.09	0.15	0.08	0.10	0.01	0.01	0.18	-0.17	0.15	0.19	0.11

In S2 the positive charge is mostly concentrated on the H_3^+ core which is only weakly bound to the outer H_2 and H. In the picture below the spatial spin distribution is shown. The neutral H atoms in S2 and S3 and the cationic H_3 units in S2 and S4 can easily be identified.

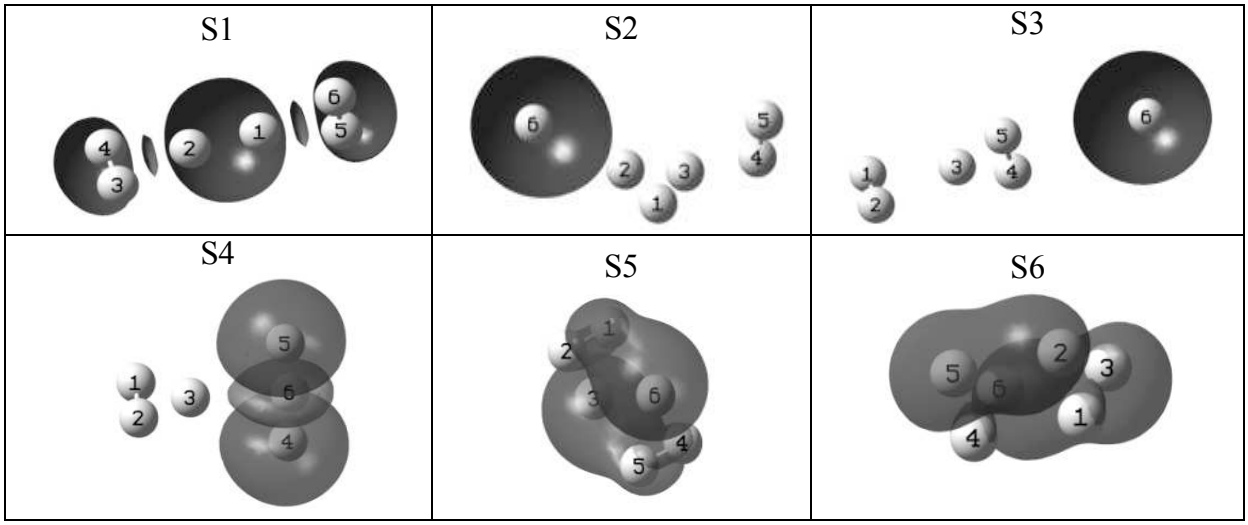

Our calculations were performed without taking into account quantum effects due to low mass of H and shallow potential surfaces. Therefore one must distinguish minima on the energy surface (which we describe) from actual cluster geometries that only coincide with topological minima if delocalization is neglected.

References

[1] S. Jaksch, A. Mauracher, A. Bacher, S. Denifl, F. Ferreira da Silva, H. Schöbel, O. Echt, T. D. Märk, M. Probst, D. K. Bohme, and P. Scheier, J. Chem. Phys 129, 224306 (2008)
[2] L. R. Wright and R. F. Borkman, J. Chem. Phys. 77, 1938 (1982)
[3] J. A. Montgomery and H. H. Michels, J. Chem. Phys. 87, 771 (1987)
[4] Y. Kurosaki and T. Takayanagi, Chem. Phys. Lett. 293, 59 (1998)
[5] A. Kakizaki, T. Takayanagi, and M. Shiga, Chem. Phys. Lett. 449, 28 (2007)
[6] Y. Kurosaki and T. Takayanagi, J. Chem. Phys. 109, 4327 (1998)

Conformational Heterogeneity in Gas-Phase Peptides

A. Svendsen, M. Guidi, U. Lorenz, N. Nagornova, G. Papadopoulos, C. Seaiby, O. V. Boyarkin and T. R. Rizzo
Laboratoire de Chimie Physique Moléculaire
EPFL-SB-ISIC-LCPM, Station-6, Lausanne, CH-1015, Switzerland

The function of biological molecules is not only related to their structure but also to their ability to change their conformation. For this reason, understanding the potential energy landscape of flexile biological molecules – both the stable conformations and the barriers that separate them – is important for unraveling their function.

We perform spectroscopic studies of cold, isolated peptide ions generated in the gas phase by electrospray and cooled to ~10 K in a cooled, RF ion trap [1-3]. The application of UV-IR double resonance spectroscopic techniques allows us to measure their conformer-specific infrared spectra, which, in combination of theory, provides information on their structure. Once having spectroscopically characterized the stable conformations, we then use the spectra to monitor laser-induced isomerization between them.

This poster will present our most recent results in pushing these techniques to peptides of ten or more amino acids. Special emphasis will be given to the techniques we are implementing to deal with the greater degree of conformational heterogeneity of larger systems.

References

[1] O. V. Boyarkin, S. R. Mercier, A. Kamariotis, and T. R. Rizzo, J. Am. Chem. Soc. **128**, 2816 (2006).

[2] J. A. Stearns, C. Seaiby, O. V. Boyarkin, and T. R. Rizzo, Phys. Chem. Chem. Phys. **11**, 125 (2009).

[3] T. R. Rizzo, J. A. Stearns, and O. V. Boyarkin, Int. Rev. Phys. Chem. **28**, 481 (2009).

Positive Atomic Ion Reactions with Acetone, Trifluroacetone and Hexafluoroactone: An Investigation of the Effects of Molecular Structure on the Dynamics and Kinetics of Ion-Molecule Reactions

L Rycroft[1], P Watts[1], and C A Mayhew[1]

[1] *School of Physics and Astronomy, University of Birmingham, Birmingham, B15 2TT, UK, pab437@bham.ac.uk*

Abstract

A selected ion flow tube study of the reactions of a series of gas-phase atomic cations (S^+, Xe^+, O^+, Kr^+, N^+, Ar^+, and Ne^+) spanning a large range of recombination energies (10.4 – 21.6 eV), with acetone, 1,1,1-trifluoroacetone, hexafluoroacetoneare reported. Experimental reaction rate coefficients and product branching ratios measured at 295K are reported.

Introduction

Acetone, $(CH_3)_2CO$, is an important molecule, found in many environments. For example, it is present in the interstellar medium, being formed through a series of ion-molecule reactions. Acetone is used as a molecular dopant in the latest generation of Ion Mobility Spectrometers (IMS), used to detect airborne threats such as chemical warfare agents. Within the IMS, protonated acetone cluster species are formed which will react with any threat agents present leading to their detection.

Despite its importance, surprisingly, there have been no detailed investigations of the ion chemistry involving acetone as the neutral species. Here we partly address this disparity by presenting investigations of the reactions of atomic cations with acetone.

The effects of the changes of molecular structure and their influence on the kinetics and the dynamics of ion-molecule reactions is fundamentally interesting. Thus, in addition to the atomic cation-acetone reactions, we present here an investigation of the ion chemistry of 1,1,1-trifluoroacetone, CH_3COCF_3, and hexafluoroacetone, $(CF_3)_2CO$, compared to that of acetone.

The adiabatic ionization potentials of the neutral reagents are 9.7 eV for acetone, 11.0 eV for 1,1,1-trifluotoacetone and 11.6 eV for hexafluoroacetone. Thus, with the exception of S^+ with the fluorinated species, charge transfer is exothermic for all other reactions. Charge transfer (involving the transfer of an electron from the neutral reactant species to the reagent cation can be nondissociative. However, more complex reactions involving the transfer of atoms can also occur in competition with or instead of charge transfer. These types of ion-molecule reaction processes have been investigated in this study.

Experimental Details

Rate coefficients and products for the ion-molecule reactions have been measured using a SIFT apparatus. Details of its operation are given in several reviews [1,2], and only a brief description is given here. Reagent ions were generated from a suitable precursor gas in a high-pressure electron ionization source. By transmitting the generated ions through a quadrupole mass filter, the required reactant ion was selected and admitted into the flow tube. The tube was filled with ca. 0.5 Torr of helium buffer gas moving with a high linear velocity, ca. 100 m s^{-1}. The neutral reagent was injected downstream into the flow tube via one of two different inlets. At the end of the flow tube cations were focused through a 1 mm orifice in a Faraday plate into a second quadrupole mass filter and detected by an off-axis channeltron. The amount of injected neutral was varied from zero to a value which depleted the reactant ion signal by ca. 90%. The loss of reagent ion and the increase in product ions were recorded as a function of neutral reagent concentration under pseudo-first-order conditions. The error in the rate coefficient determined from data analysis is estimated to be 20%, and the apparatus is limited to measuring reactions with rate coefficients greater than ca. 10^{-13} cm^3 $molecule^{-1}$ s^{-1}. Branching ratios were derived from plots of ion signal versus neutral concentration, and extrapolation to zero flow of the neutral molecule allowed for the effects of any secondary reactions. We quote an error of 15% in product branching ratios; this error increasing for ratios below 10%.

The halogenated compounds were purchased from Sigma-Aldrich with stated purities of greater than 97%. Acetone was purchased from Fisher with a stated purity of greater than 99%. Acetone and 1,1,1-trifluoroacetone were purified by several freeze-pump-thaw cycles.

Results

To illustrate the type of results obtained table 1 presents details of the reactions of S^+, Xe^+, O^+, Kr^+, N^+, Ar^+ and Ne^+ with acetone. The reagent ions are listed (top to bottom) in order of increasing recombination energy (RE). The measured rate coefficients, k_{exp}, the product cations and their branching percentages for the reactions are provided. To assess the efficiency of the reactions, the experimentally determined rate coefficients are compared in the table with the predictions of capture theory, k_{coll}, calculated using parametrized fits to results from trajectory calculations [4].

Table 1

Product branching ratios and rate coefficients for the reactions of acetone with molecular ions studied (S^+, Xe^+, O^+, Kr^+, N^+, Ar^+ and Ne^+).

Acetone, (IP = 9.7 eV) CH_3COCH_3

Reagent (RE/eV)	Product Ions (BR %)	k_{coll} (10^{-9} cm^3 s^{-1})	k_{exp} (10^{-9} cm^3 s^{-1})
S^+ (10.36)	$C_3H_5^+$ (40) CH_3CO^+ (22) $CH_3COCH_3^+$ (38)	2.8	0.9
Xe^+ (12.13)	CH_3CO^+ (95) $CH_3COCH_3^+$ (5)	2.0	2.7
O^+ (13.62)	CH_3CO^+ (84) $CH_3COCH_3^+$ (16)	3.5	2.4
Kr^+ (14.0/14.7)	CH_3^+ (2) CH_3CO^+ (98)	2.1	3.1
N^+ (14.53)	CH_3CO^+ (88) $CH_3COCH_3^+$ (12)	3.7	3.5
Ar^+ (15.76)	CH_3^+ (15) CH_3CO^+ (85)	2.6	3.5
Ne^+ (21.56)	CH_3^+ (45) CH_3CO^+ (55)	3.2	3.2

k_{coll} calculated using MADO and viscosity relative to air = 0.47. Molecular formula not necessarily representative of structure of molecule. Neutral products not listed as not well defined.

References

[1] Smith, D.; Adams, N. A. *Adv. At. Mol. Phys.* **1988**, *24*, 1
[2] Graul, S. T.; Squires, R. R. *Mass Spectrom. Rev.* **1988**, *7*, 263
[3] Bohme, D. K. *Int. J. Mass Spectrom.* **2000**, *200*, 97
[4] Su, T.; Chesnavich, W. J. J. Chem. Phys., **1982**, *76*, 5183

Thermodynamics of the Carbon Gas-Fullerene Transition

Adilah Hussien[1], Alexander V. Yakubovich[1,2], Andrey V. Solov'yov[1,2] and Walter Greiner[1]

[1] *Frankfurt Institute for Advanced Studies, Ruth-Moufang-Str. 1, Frankfurt am Main, Germany 60438, e-mail: yakubovich@fias.uni-frankfurt.de*

[2] *On leave from A.F. Ioffe Institute, St. Petersburg, Russia*

Introduction

In this contribution, we present a novel theoretical approach for the description of the fragmentation and formation of fullerenes. The prominent feature of our approach is that we study fragmentation and formation not as separate processes but as one general process of *phase transition* in fullerenes. We focus on the phase transitions of C_{60} and C_{240} using molecular dynamics simulations combined with a statistical mechanics model [1]. The advantage of this model is that the phase transition temperature can be predicted at any arbitrary pressure, e.g. at the pressure conditions found in arc-discharge experiments. Furthermore, the model indicates an upper temperature/pressure limit at which the C_{60} fragments into a carbon gas. Together with this model, we have developed a topologically-constrained forcefield which allows one to gain computational time by considering only the necessary fullerene formation channel. The topologically-constrained forcefield has been benchmarked to the tight-binding[2] and Tersoff potentials [3], and shows a good correspondence for the C_{60} and C_2 structures. Using this forcefield, we then conducted half a microsecond long constant temperature molecular dynamics simulations of the C_{60}, as well as the C_{240}.

Forcefield and molecular dynamics simulations.

In order to investigate the phase transition of our two-state model $C_{60} \leftrightarrow 30\ C_2$ using molecular dynamics, we have constructed a topologically-constrained forcefield to restrict the system to this particular channel.
The forcefield is given by:

$$\mathbb{V}(\mathbf{r}_i) = \sum_{j \neq k,l,m}^{N} V_{vdW}(r_{ij}) + \sum_{j=k,l,m} V_{cov}(r_{ij})$$

where it differentiates between two types of interactions: the long-range *van der Waals* (vdW) and the short-range *covalent* (cov) bonding.

The interatomic distance r_{ij} between atoms *i* and *j* is defined as $r_{ij} = |\mathbf{r_i} - \mathbf{r_j}|$. The sum in the covalent term is over the three nearest-neighbours of atom *i*: atoms *k*, *l* and *m*; while the sum in the van der Waals term is over the other (N-4) non-neighbours of atom *i*. Hence, each atom is allocated 3 covalent nearest neighbours, determined by their positions relative to atom *i*, and (N-4) van der Waals non-neighbours. In this way, the atom is *topologically-constrained* to interact with a certain type of bonding with other atoms in the system. Both short and long-range interactions in the system are modelled with the Lennard-Jones potential. The parameters of the interaction are fitted to reproduce well the geometry and the energy of the fullerene cage obtained from quantum mechanical calculations.

We then performed constant-temperature molecular dynamics simulations for C_{60} and C_{240} with a timestep of 1fs and a total of 10^8 steps to give a total simulation time of 500ns. The simulation was performed using periodic boundary conditions with a unit cell of length 20Å per side. Temperature control was achieved by means of the Langevin thermostat with a damping constant of $100ps^{-1}$. The simulations were conducted for temperatures between 3000K and 8500K.

Results and discussion.

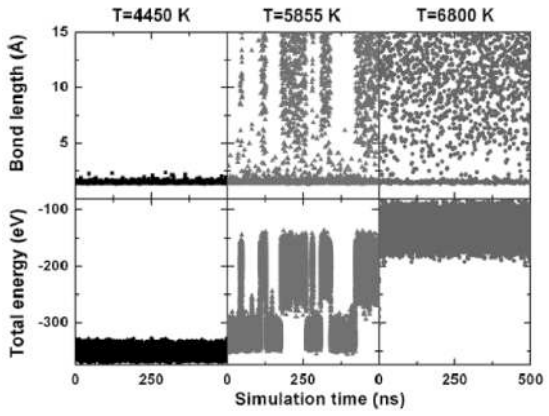

Fig. 1: Total energy and bond-length fluctuations within a single a trajectory at different temperatures

To analyse the behaviour of the system during phase transition, we have plotted in Fig. 1, the total energy and the bond length of a single C-C bond of the C_{60} as a function of the simulation time. The three parts of Fig. 1 show when the C_{60} is in its cage phase (in black), the phase transition (in red) and in the gaseous phase (in blue). The phase transition region (in red) displays a mixture of both cage and gaseous phases. Here, one can observe that the system fluctuates between states of higher and lower total energies, signalling that the system is continuously jumping between the cage and gaseous phases. This on-and-off distribution is characteristic of a two-phase coexistence regime that has been observed as well for finite-size clusters. At the phase transition temperature, the C_{60} oscillates between the fullerene cage and the carbon gas states, signifying that the difference between the free energies of the two phases is on the order of *kT*. To the best of our knowledge, our

work is the first where the processes of fragmentation and formation of a fullerene are observed several times in the course of the simulation.

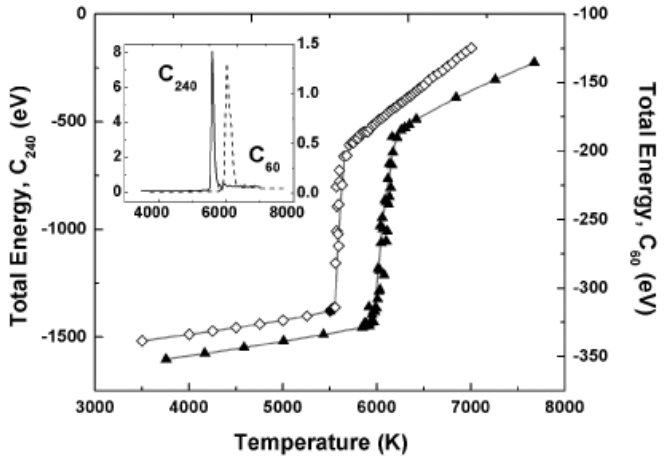

Fig. 2: Caloric curves and heat capacity plots (inset) for C_{60} (black triangles) and C_{240} (open diamonds)

In the Fig. 2, we present the caloric curves for C_{60} and C_{240} and their associated heat capacity curves.

The heat capacities shown in the inset of Fig. 2 were obtained from the caloric curves by C_v=dE/dT. The maximum of each peak in the heat capacity denotes the phase transition temperature, T_c = 5855K for C_{60} and T_c = 5500K for C_{240}

To predict the phase transition temperature at experimentally accessible conditions, one has to develop a statistical mechanics model of this process. Here, we outline the basic physical effects that our model accounts for (see Ref. 1 for full details of the model).

Firstly, one has to introduce the corrections associated with the topological constraint of the forcefield. Indeed, there are $2^{30}30!$ ways to assemble a carbon cage from 30 dimers, but in our molecular dynamics simulations we account for only one of them. Accounting for multiple possibilities of the carbon cage assembly will lead to a certain correction to the entropy of the cage state. Another issue is regarding the pressure in the system. At experimental conditions[4,5], the usual range of pressures is 10-100 kPa. However, in our simulations it is about 0.4 GPa due to the small size of the box. Another correction to the entropy of the gaseous state is regarding the finite size of the atoms. To correctly describe the gaseous state of the system, one has to account for the excluded volume associated with repulsion between atoms. In our work, we have estimated the radius of the atom as being such that the repelling forces between a pair of atoms equals *kT*. Combining all the discussed corrections, we arrive to the following dependence of the phase transition temperature on pressure (see Fig. 3).

Conclusions

In this communication, we present and discuss the statistical mechanics model to describe the formation/fragmentation of fullerenes as phase transitions. The advantage of this model is that it allows one to predict the phase transition temperature at any arbitrary pressure, thus

enabling us to predict the phase transition temperature in the pressure conditions found in arc-discharge experiments.

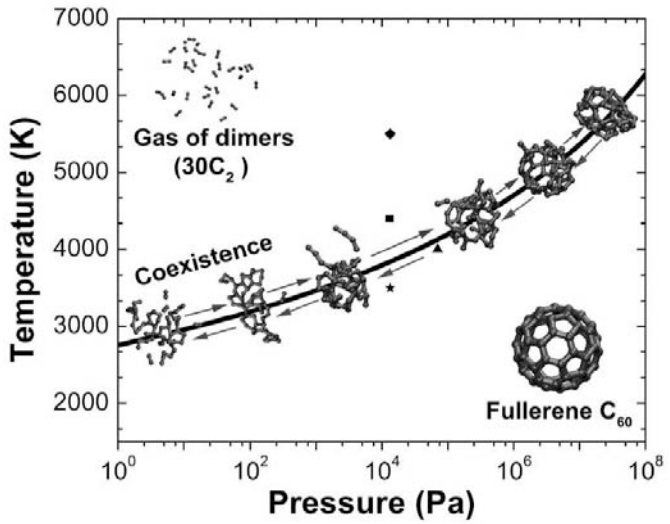

Fig. 3: Phase diagram of C_{60} showing the upper limit of the fullerene phase before fragmentation to a gas of dimers. The data points in the figure refer to experimental results (see Ref. 1 for further details).

Together with this model, we have developed a topologically-constrained forcefield with which we have conducted constant temperature molecular dynamics simulations of up to 500 ns, two orders of magnitude longer than previous works. Results of the simulations show that our model C_{60} and C_{240} demonstrate a phase transition at temperatures of 5855K and 5500K respectively. We have also demonstrated that the process of fullerene fragmentation and reassembly is a first-order-like phase transition between gaseous and cage states in the finite system by means of heat-capacity plots. Furthermore, we have extended our statistical mechanics model to take into account entropic corrections in the form of permutational and pressure corrections. These corrections have lowered the phase transition temperature obtained from the MD simulations and have allowed us to take into account the effect of pressure on the phase transition. This pressure factor is critical in correlating our statistical mechanics model to real experimental conditions in arc-discharge experiments.

Taking account all these factors, we have obtained for the C_{60} a phase transition temperature of 3800-4200K corresponding to a pressure of 10-100 kPa in good agreement with experimental results. The novelty of the present work is in the fact that it treats the fullerene formation process as a carbon gas - fullerene cage phase transition.

[1] A. Hussien, A. Yakubovich, A. Solov'yov and W. Greiner, submitted to Eur. Phys. J. D; arXiv:0807.4435v1 [physics.atm-clus]
[2] L. Horváth, T. A. Beu, Phys. Rev. B 77, 075102 (2008)
[3] J. Tersoff, Phys. Rev. Lett. 61, 2879 (1988)
[4] K. Säidane, M. Razafinimanana, H. Lange, A. Huczko, M. Baltas, A. Gleizes, J.L. Meunier, J. Phys. D: Appl. Phys. 37, 232 (2004)
[5] H. Lange, Fullerenes, Nanotubes and Carbon Nanostruct. 5, 1177 (1997)

Understanding the Formation Process of Exceptionally Long Fullerene-Based Nanowires

Ilia A. Solov'yov[1], Junfeng Geng[2], Andrey V. Solov'yov[1] and Brian F. G. Johnson[2]

[1]*Frankfurt Institute for Advanced Studies, Goethe University, Ruth-Moufang-Str. 1, 60438 Frankfurt am Main, Germany*

[2]*Department of Chemistry, University of Cambridge, Cambridge, United Kingdom*

ilia@fias.uni-frankfurt.de

Introduction

The growth of one-dimensional (1D) nanocrystals represents an important research topic in crystal engineering for nanotechnology [1]. The growth of 1D fullerene (C_{60}) nanocrystals (or nanowires) has proven to be of considerable scientific and technological interest because of the properties associated with the low-dimensionality, quantum confinement effect, and potential electronic, magnetic and photonic applications [2]. To this end, there have been a number of reports on the growth, structural characterisation, and application-related investigations of C_{60} nanowires [3-5]. In particular, a recent publication by Miyazawa and co-authors [6] indicates that a pristine C_{60} nanowire, prepared by the liquid-liquid interfacial precipitation method using a pyridine solution of C_{60} and isopropyl alcohol [7], exhibits electrical conducting behaviour, and the outer C_{60} oxide covering may be potentially used as the dielectric layer for single C_{60} nanowire-based field-effect transistors for nanoelectronics.

In a recent study, we demonstrated that exceptionally long fullerene nanowires, with a length-to-width aspect ratio as large as ~3000, can be grown from 1,2,4-trimethylbenzene (TMB) solution of C_{60} [8]. These nanowires, denoted as C_{60}·TMB, have been observed to possess a highly unusual shape that retains unchanged even after removing the solvent at elevated temperatures. This excellent property has offered a new approach to the formation of a fullerene-based carbon 1D nanostructure, but importantly, without the involvement of any metal species as the growth catalyst. Consequently, the normally employed post-growth purification process for the removal of metal is no longer necessary, in a marked contrast to the chemical vapour deposition (CVD) technique for growing carbon nanotubes [9].

The understanding of the exact nature of the C_{60}-solvent interaction should provide useful insights into the mechanism of the crystal growth and offer a potential method for the control of the crystal shape and structure. Here we report on our investigations of this important topic from both experimental observations and theoretical calculations. Our approach includes the detailed observation of the crystal morphology and structure using high-resolution electron microscopic techniques, in conjunction with the search of the C_{60}-solvent interaction modes in the crystal unit cell, followed by the calculations of the kinetic energies required for the crystal growth along the principal growth axes.

Theoretical Methods

The interactions between the C_{60} and the TMB molecules in the crystalline lattice were investigated by accounting for the van der Waals and Coulomb interactions between them. The partial charge of each atom in the TMB molecule was calculated within the framework of the *ab initio* density functional theory employing the B3LYP density functional [10].

In the calculations we consider C_{60} and TMB molecules as rigid objects. This assumption is reasonable because the energies involved in the inner dynamics of the molecules are significantly larger than the interaction energies between the molecules [11,12]. Therefore at the temperature of the nanowire growth (~300 K), the constituent molecules remain stable. Freezing the internal degrees of freedom of the molecules significantly reduces the dimensionality of the problem, hence allowing us to study nanowires of larger size. The idea behind the theoretical analysis performed in the present work is to understand to what extent the intermolecular interactions can explain the large anisotropy of the nanowires.

The energetics of the system was calculated by considering the intermolecular potentials described by several parameters such as the depth of the potential well (ε_0), the bonding length of an atomic pair (σ), and the atomic charges (q), derived from the *ab initio* DFT calculations. Optimization of the structure of the crystalline unit cell was performed using conjugate gradient method implemented within the MBN Explorer program [13]. The adhesion energies were defined for the system and calculated, in order to determine the energy needed for a unit cell to extend along a specific growth direction. Finally the theoretical results were compared with the experimental observations.

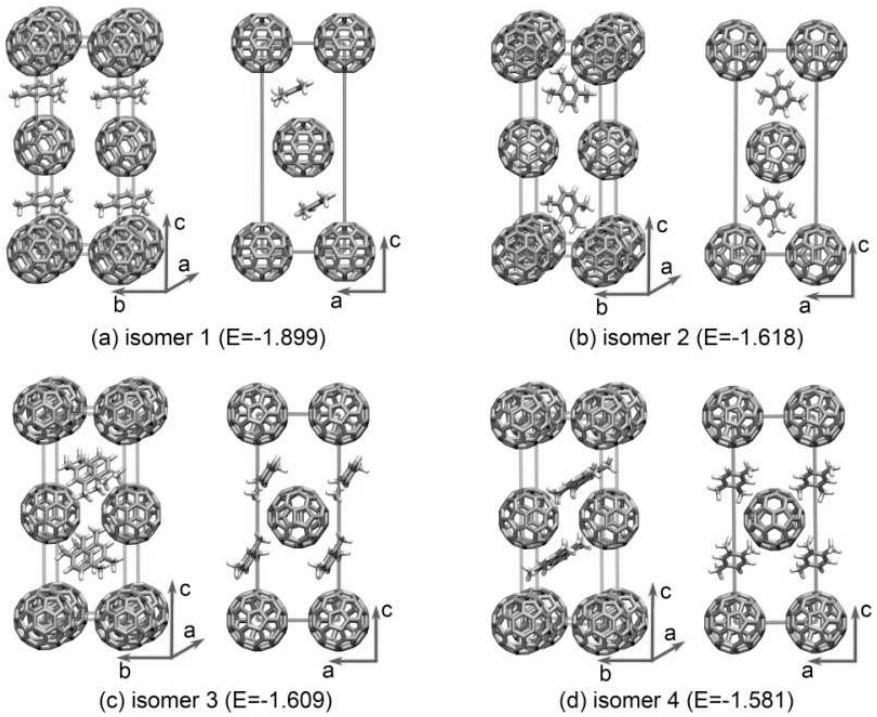

Figure 1: Optimized isomeric states in the C_{60}·TMB nanowire unit cell as derived from the calculations.

The number in the brackets below each image shows the energy of the structure (in eV).

Results

We have performed a thorough theoretical analysis, aiming at gaining an in-depth understanding of to explain the exceptionally large aspect ratio of C_{60}-based nanowires. By accounting for different interactions in the system we have calculated the structures of the unit cell and determined the role of the fullerene and of the solvent molecules in the crystallization process of the nanowires [14]. The structures of four energetically favorable isomers of the unit cell are shown in the Fig. 1. We have also calculated the adhesion energy of C_{60} molecules to the nanowire surface, and on the basis of this explained the growth anisotropy of the crystal.

As a second step towards understanding of nanowires growth anisotropy we demonstrate theoretically that at room temperature the effect of electron polarization is negligibly small and, therefore, cannot become the driving force for nanowire growth along one preferential direction [15]. Experimental measurements are in agreement with the theoretical analysis: the nanowires have been observed to emerge from the polar 1,2,4-trimethylbenzene and non-polar 1,3,5-trimethylbenzene solution of C_{60}, while no nanowires from polar toluene, 1,2,3-trimethylbenzene and non-polar benzene solutions could be recorded (see Fig. 2).

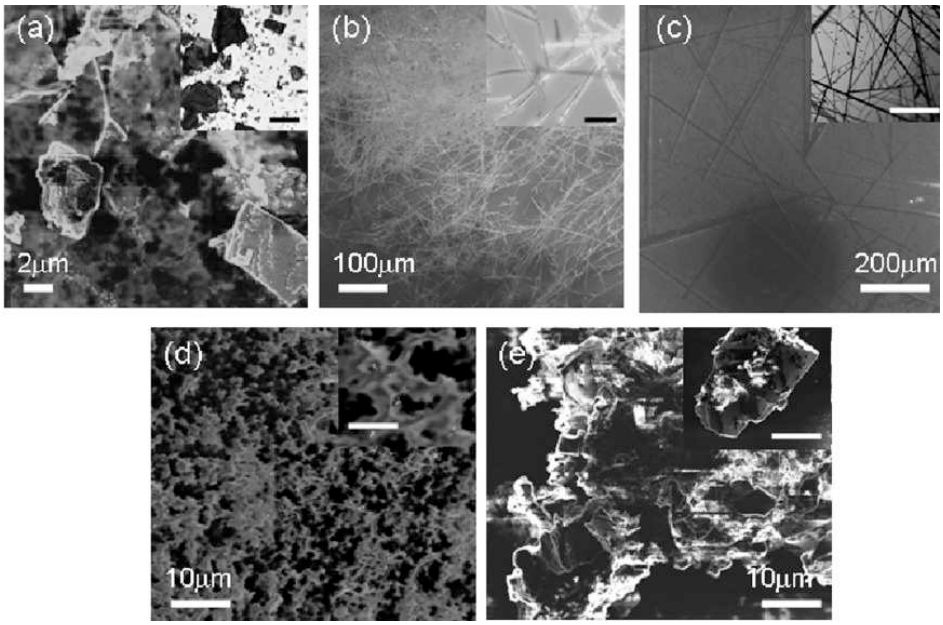

Figure 2: *Scanning electron microscopic images of the fullerene (C_{60}) crystals (either in the form of wires or particles) grown by using the solvents of 1,2,3-trimethylbenzene (a), 1,2,4-trimethylbenzene (b), 1,3,5-trimethylbenzene (c), benzene (d), and toluene (e). The insets of (a), (b) and (c) are the corresponding optical microscopic images, with the scale bars being 2 μm, 10 μm and 200 μm, respectively. The insets of (c) and (d) are SEM images of higher magnifications to show the individual crystalline particles, with the corresponding scale bars being 5 μm and 10 μm, respectively.*

To get a more profound understanding of the nanowire growth mechanism we have also studied the possible polymerization reactions occured between the C_{60} and the solvent molecules [16].

References

[1] C.M. Lieber, Z.L. Wang, MRS Bull. **32**, 99 (2007).
[2] M.S. Dresselhaus, G. Dresselhaus, P.C. Eklund, Science of Fullerenes and Carbon Nanotubes; Academic Press: San Diego, CA, (1996).
[3] K. Miyazawa, J. Minato, T. Yoshii, M. Fujino, T. Suga, J. Mater. Res. **20**, 688 (2005).
[4] H. Liu, Y. Li, L. Jiang, H. Luo, S. Xiao, H. Fang, H. Li, D. Zhu, D. Yu, J. Xu, B. Xiang, JACS **124**, 13370 (2002).
[5] K. Ogawa, T. Kato, A. Ikegami, H. Tsuji, N. Aoki, Y. Ochiai, J.B. Bird, Appl. Phys. Lett. **88**, 112109, (2006).
[6] M. Xu, Y. Pathak, D. Fujita, C. Ringor, K. Miyazawa, Nanotechnology **19**, 075712 (2008).
[7] J. Minato, K. Miyazawa, Diamond Relat. Mater. **15**, 1151 (2006).
[8] J. Geng, W. Zhou, P. Skelton, W. Yue, I. Kinloch, A.H. Windle, B.F.G Johnson, JACS **130**, 2527 (2008).
[9] J. Kong, N. Franklin, C. Chou, S. Pan, K.J. Cho, H. Dai, Science **287**, 622 (2000).
[10] M.J. Frisch, *et al.* Gaussian 03, revision C.02; Gaussian, Inc.: Wallingford, CT, (2004).
[11] I.A. Solov'yov, A.V. Yakubovich, A.V. Solov'yov, W. Greiner, Phys. Rev. E **75**, 051912 (2007).
[12] I.A. Solov'yov, A.V. Yakubovich, A. V. Solov'yov, W. Greiner, J. Exp. Theor. Phys. **103**, 463 (2006).
[13] I.A. Solov'yov, O. Obolensky, A.V. Yakubovich, A. Lyalin, A.V. Solov'yov, MBN Explorer 1.0.0; Frankfurt Institute for Advanced Studies: Frankfurt am Main, Germany, (2008).
[14] J. Geng, I. Solov'yov, W. Zhou, A.V. Solov'yov, and B.F.G Johnson, *J. Phys. Chem. C* **113**, 6390 (2009).
[15] I.A. Solov'yov, J. Geng, A.V. Solov'yov, and B.F.G Johnson, *Chem. Phys. Lett,* **472**, 166 (2009).
[16] J. Geng, I.A. Solov'yov, D.G. Reid, A.E.H. Wheatley, A.V. Solov'yov and B.F.G. Johnson, arXiv.org: arXiv:0906.2216v1 physics.chem-ph (2009).

Theoretical Study of Nanofractal Stability on the Surface

Veronika V. Dick, Ilia A. Solov'yov, Andrey V. Solov'yov
Frankfurt Institute for Advanced Studies, Goethe University, Ruth-Moufang-Str. 1, 60438 Frankfurt am Main, Germany
semenikhina@figss.uni-frankfurt.de

We present a detailed systematical theoretical analysis of the post-growth processes occurring in a nanofractal on surface. For this study we developed a method which describes the internal dynamics of particles in a fractal and accounts for their diffusion and detachment. We demonstrate that these kinetic processes are responsible for the formation of the final shape of the islands on surface after post-growth relaxation.

Introduction

An important goal of nanotechnology is the development of controllable, reproducible and industrially transposable, nanostructured materials [1]. In this context, controlling of the final architecture of such materials by tuneable parameters is a fundamental problem.

The investigation of the dendritic structures (fractals) has attracted considerable attention of many scientists [2]. The formation of such systems provides a natural framework for studying disordered structures on surface, because fractals are generally observed in far from equilibrium growth regime. During the last years fractal shape have been recordered for a variety of systems. Fractals consisting of Ag clusters [3] and C_{60} molecules [4] have been fabricated on graphite surface with the use of the cluster deposition technique.

The post-growth transformation of silver cluster fractals to compact droplets on graphitic surface was experimentally studied [5]. It was demonstrated that depending on the experimental conditions the shape and the size of the stable silver droplets changes significantly [6].

The self-organization dynamics of particles on a surface was also studied theoretically. An efficient theoretical tool for describing particle dynamics on a surface is the diffusion limited aggregation (DLA) method [7]. Within the framework of this method each particle on a surface moves freely in a random direction until it collides with another particle, in which case both particles stick together and become immobile. The DLA model was used for a qualitative description of the process of fractal formation on the surface.

Contrary to the process of fractal formation, the process of the post-growth relaxation and the question of stability of deposited structures is still not well understood. The understanding of the post-growth relaxation processes would allow one to controllably influence the self-organization processes of particles on the surface and therefore to obtain patterns with predictable properties.

Here we present a detailed systematical theoretical analysis of the post-growth processes occurring in a nanofractal on surface. For this study we developed a modified DLA method which describes the internal dynamics of particles in a fractal and accounts for their diffusion and detachment. We demonstrate that these kinetic processes control the final shape of the islands on surface after the post-growth relaxation.

Theoretical methods

In our model we consider fragmentation of a fractal consisting of non-elastic particles of equal radii. In this case, the relaxation of a fractal on a surface is controlled by diffusion of particles along the fractal periphery and particle detachment from the fractal. The diffusion and detachment rate depend on the activation energy and particle-particle interaction. The diffusion rates of a particle along the periphery of a fractal can be written as:

$$\Gamma_d(m,n) = \nu \exp\left[-\frac{mE_b}{kT} - \frac{n\Delta\varepsilon}{kT} - \frac{E_a}{kT}\right], \quad (1)$$

where m is the number of bonds that are broken in the course of particle motion, E_b is the bonding energy between two particles, n is the number of unbroken neighbouring bonds between two particles and $\Delta\varepsilon$ is the energy barrier of a particle diffusion. E_a is the activation energy of a particle on the surface and ν is the characteristic frequency of particle vibration in the vicinity of the minimum of the potential well. The evaporation (detachment) rate of a particle from the fractal is given by

$$\Gamma_e(l) = \nu \exp\left[-\frac{lE_b}{kT} - \frac{\Delta\mu}{kT} - \frac{E_a}{kT}\right], \quad (2)$$

where l is the number of bonds, broken after particle detachment from the fractal, $\Delta\mu$ is the chemical potential of particle detachment.

From Eqs. (1)-(2) follows that the probability of the different kinetic processes in the system depends on the values of E_a, E_b, $\Delta\varepsilon$, $\Delta\mu$. In the present work we perform a systematic study of fractal stability by varying these kinetic parameters [8].

Results

Using the DLA method we obtained several fractal structures which mimic silver cluster fractals on graphite surface studied in [6]. We use the fractal structure shown in Fig. 1a for the study of the post-growth relaxation processes. The experimentally grown silver cluster fractal is shown in Fig.1d.

We present several scenarios of a fractal relaxation on a surface. The rate of fractal decay depends on the binding energy between particles, while the barrier energy for particle diffusion defines the morphology of the fragments during the relaxation of a fractal [8].

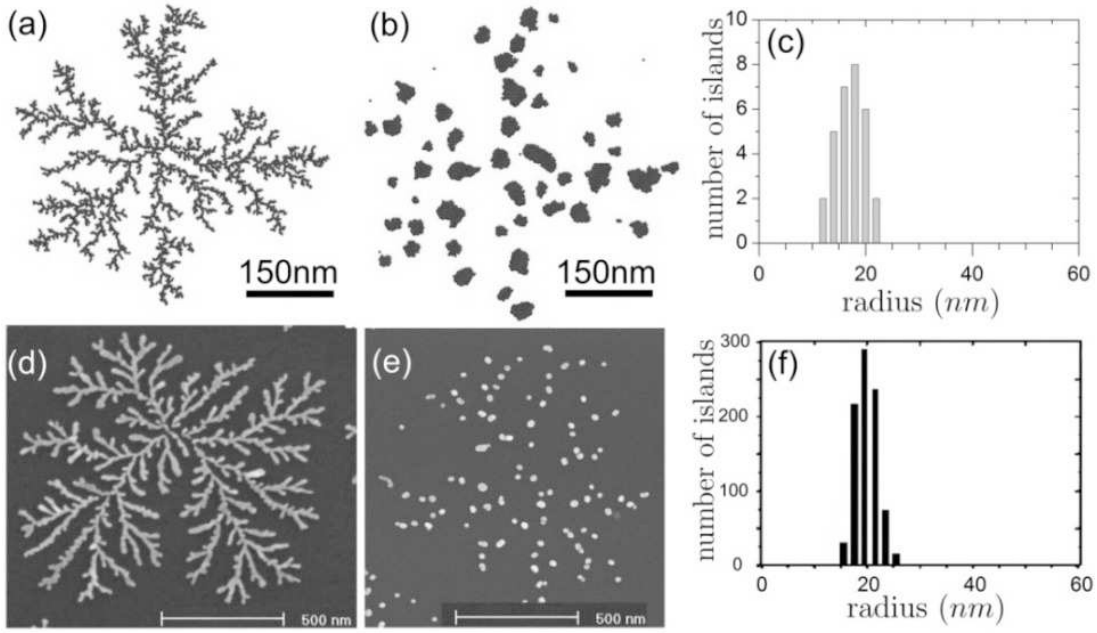

Fig. 1: Evolution of the fractal structure, calculated with the DLA model with accounting for the internal dynamics of the particles in the fractal (a)-(c) and comparison with the experimental observation of the silver fractal perturbation by adding of oxygen impurities to the silver clusters (d)-(f). (a) fractal structure grown by the DDA method; (b) snapshots of the fractal structure after fragmetation, calculated with the DLA model; (c) size distribution of the islands after fractal fragmentation; (d) structure of the silver cluster fractal grown by cluster deposition technique on the graphite surface from Ref. [6]; (e) results of experimental observation of perturbed silver fractal by adding additional oxygen atoms to the silver clusters [6]; (f) size distribution of the silver island on the graphite substrate after pertubation [6]

Figure 1b shows the results of fractal structure evolution calculated with the DLA model with accounting for the internal dynamics of the particles in the fractal. Kinetic parameters E_a, E_b, $\Delta\varepsilon$, $\Delta\mu$ in this example are equal to *0.5 kT, 3kT, 0.6 kT* and *10 kT,* respectively. The temperature is assumed to be equal *300 K*. The results of the numerical calculation are compared with the experimental observation of the silver fractal perturbed by the thermal annealing or by adding impurities to the system [6]. Figure 1e shows the results of experimental observation of perturbed silver fractal by adding of oxide impurity to the silver clusters.

The distribution of the island sizes which emerge after fractal fragmentation is a useful characteristic in experimental analysis, used to describe the topology of the system. In our work we analyse this distribution after fractal fragmentation. The results of the calculation are shown in the Fig. 1c. The distribution of the island sizes in the perturbed silver fractal after adding of oxyde impurity to the system is shown in Fig. 1f. The most probable radius of a silver cluster islands is equal to *18 nm*. The same value follows from theoretical calculation. The number of islands is different, because in the calculation we consider only a single fractal, while the results of the experiment are shown for several silver cluster fractals fragmenting on the graphite surface. Thus, for N_{fr} fractals on surface the number of islands formed after fragmentation can be approximated as $N_{tot} = N_{fr} <N_{isl}>$, where $<N_{isl}>$ is the average number of islands formed after fragmentation of a single fractal.

We demonstrate that stability of the fractal structure depends strongly on several factors, such as the concentration of impurities and temperature [9]. Therefore the suggested model can be used to predict evolution of the system topology during the fractal fragmentation process.

References

[1] C. Bréchignac, P. Houdy, M. Lahmani editors, "Nanomaterials and Nanochemistry", Cambridge University Press, Springer, (2007)
[2] P. Jensen, Rev.Mod.Phys. **71**(5), 1695, (1999)
[3] C. Bréchignac, Ph. Cahuzac, F. Carlier, M. De Frutos, N. Kébaïli, J. Le Roux, A. Masson, B. Yoon, EPJ D **24**, 265, (2003)
[4] H. Liu and P. Reinke, Surf.Science **601**, 3149, (2007)
[5] A. Lando, N. Kébaïli, Ph. Cahuzac, C. Colliex, M. Couillard, A. Masson, M. Schmidt, C. Bréchignac, Eur. Phys. J. D **43**, 151, (2007).
[6] A. Lando, N. Kébaïli, Ph. Cahuzac, A. Masson, C. Bréchignac, PRL **97**, 133402, (2006)
[7] T.A. Witten and L.M. Sander, PRL **47**(19), 1400, (1981)
[8] V.V. Dick, I.A. Solov'yov, A.V. Solov'yov, Book of abstracts, The 4th International Symposium Atomic Cluster Collisions: structure and dynamics from the nuclear to the biological scale, ISACC 2009, Ann Arbor, USA, July 14-18, (2009), p. 34
[9] V.V. Dick, I.A. Solov'yov, A.V. Solov'yov, Proceedings of 4th International Symposium "Atomic Cluster Collisions: structure and dynamics from the nuclear to the biological scale", ISACC 2009, Ann Arbor, USA, July 14-18, (2009), in print

Rotational Line Shifts due to Parity Violation in Chiral Molecules

Jürgen Stohner[1,2] and Martin Quack[2]

[1] *Institute for Chemistry and Biological Chemistry (ICBC), Zürich University for Applied Sciences (ZHAW), CH-8820 Wädenswil, sthj@zhaw.ch*

[2] *Physical Chemistry, ETH-Zürich (Hönggerberg), CH-8093 Zürich, martin@quack.ch*

We extend our earlier studies on spectroscopic signatures of molecular parity violation by investigating the influence on rotational spectra. Therefore, we determine vibrationally averaged moment of inertia tensors with anharmonic vibrational wavefunctions including effects from parity violating potentials. This approach goes beyond the calculation of the influence on rotational constants via changes in the geometry and therefore also in the moment of inertia tensor (see Quack, Stohner, Phys. Rev. Lett. **84**, 3807 (2000)). It turns out that the rotational constants are very strongly influenced by parity violation when including excitation in bending modes. These investigations help our understanding of fundamental symmetry violation in nature.

Introduction

The Standard Model of Particle Physics [1,2] summarizes our current knowledge of fundamental laws in physics in general including chemistry in particular. The last and most fundamental revision of our knowledge and understanding of fundamental laws governing nature stems from 1959 when parity violation was predicted and shortly thereafter confirmed experimentally in particle physics [3,4]. Molecular spectroscopy can probe interactions under well defined conditions when intermolecular interactions are absent. This is important if one wants to study very small effects which tend to be masked by interaction with the environment. Due to a violation of space-inversion symmetry or parity, left- and right-handed molecules (enantiomers) are not exactly equivalent energetically. In the limit of a high barrier for interconversion, the tunneling splitting between enantiomers is much smaller than the parity violating energy difference $\Delta_{\mathrm{pv}}E$, which thus becomes a measurable quantity [2,5-8].

Early quantitative estimates [9,10] were incorrect by one to two orders of magnitude typically. We have more recently corrected for this deficiency by much improved theoretical calculations [2,11-13]. The Hamiltonian for parity violating potentials in chiral molecules [9-14] is given (in SI units) by

$$\widehat{H}_{\mathrm{pv}} \approx \frac{G_{\mathrm{F}}}{2\hbar\sqrt{2}m_{\mathrm{e}}c}\sum_a Q_a \sum_i \left[\vec{p}(i)\cdot\vec{s}(i), \delta^3(\vec{r}(i)-\vec{R}(a))\right]_+ \qquad (1)$$

In this expression, contributions to parity violation due to nuclear spin effects have been neglected. It is summed over nuclei *a* and electrons *i*; m_e is the mass of the electron, *c* is the velocity of light, *h* is Planck's constant, G_F is the Fermi-coupling constant, $\vec{p}(i)$ is the electron momentum, and $\vec{s}(i)$ is the spin of the electron. $\delta^3\left(\vec{r}(i)-\vec{R}(a)\right)$ is the Dirac delta distribution which confines the interaction to the positions of the nuclei, whereas $[...]_+$ denotes the anti-commutator. The weak charge Q_a is approximately given by N_a - (1 - 4 $\sin^2$ θ_W)Z_a where N_a denotes the neutron number of nucleus *a* and Z_a the electric nuclear charge. θ_W is the Weinberg angle [15]. The parity violating Hamiltonian given above introduces a tiny energy difference between left- and right-handed molecules (S- and R-enantiomers), $\Delta_{pv}E$ with a corresponding heat of reaction for stereomutation of S = R with $\Delta_r H_0^0 \approx N_A\,\Delta_{pv}E$ and $\left|\Delta_{pv}E\right| = 2\left\langle E_{pv}\right\rangle$. $\left\langle E_{pv}\right\rangle$ is the expectation value of the parity violating potential $V_{pv}(\vec{q})$ calculated with dependence upon all internal coordinates $\vec{q}$ by means of $\hat{H}_{pv}$ and using a spin-orbit perturbed electronic ground state wavefunction [11,12,16]. $\Delta_{pv}E$ might be a directly observable quantity if the experiment is performed in the time domain following earlier proposals [5-7]. Another experiment to determine the influence of parity violation on molecular properties is to try to observe a shift of the vibrational frequencies between enantiomers [17,18]. We have shown [16,19-21] that the current experimental accuracy still lacks some orders of magnitude for the measurement of the relative vibrational frequency shift between both enantiomers of CH(D)BrClF in the range of the CF-stretching fundamental at about 1078 cm^{-1}; an even higher accuracy would be needed to measure it in camphor which was the second example were early attempts have been undertaken to measure parity violation in molecules [22]. Among the molecular systems for which (relative) vibrational frequency shifts caused by parity violation have been calculated based on our theoretical approach described briefly below (more details can be found in [2,13] and references cited therein) are as follows: CHBrClF [16,19-21,23,24]; CFXYZ (X,Y,Z=H,Br,Cl,I) [25]; F-oxirane (C_2H_3FO) [26]; BiHFBr, BiHFI [27]; $PH_3AuCHFCl$, ClHgCHFCl [28]; Camphor ($C_{10}H_{16}O$) [29,30]; $CBrClF^+$, $CBrClF^-$ [31]; PHBrF, AsHBrF [32]; polyhalomethanes [33]; SeOXY (X,Y=H,F,Cl,Br,I) [34,35]. We have also considered rotational frequency shifts [18-21] which are the topic of the present paper.

Theory

In our investigations, the parity violating potential V_{pv} has been determined using the RPA and MC-LR CASSCF ab initio method [13] along the reduced dimensionless normal coordinates $\vec{q}$ for all relevant vibrational degrees of freedom. In our early calculations [20,21] we assumed $V_{pv}(\vec{q})$ diagonal in q_i. $V_{pv}(\vec{q})$ was then fitted to a polynomial expansion in q_i and the relative frequency shift has been determined on various levels of approximation:

One-dimensional in the separable harmonic or anharmonic adiabatic approximation (SHAA or SAAA), or fully coupled by solving the multi-dimensional vibrational Schrödinger equation

$$\widehat{H}_{\mathrm{mol}}(\vec{p},\vec{q}) = \widehat{H}^{0}_{\mathrm{mol}}(\vec{p},\vec{q}) + V_{\mathrm{pv}}(\vec{q}) \qquad \text{with} \qquad E_n \approx E^0_n + \langle \Psi^0_n | V_{\mathrm{pv}}(\vec{q}) | \Psi^0_n \rangle \tag{2a}$$

$$\Delta_{\mathrm{pv}} E_n = \left(E^{(\mathrm{R})}_n - E^{(\mathrm{R}\,0)}_n\right) - \left(E^{(\mathrm{S})}_n - E^{(\mathrm{S}\,0)}_n\right) \approx 2\,\langle \Psi^0_n | V_{\mathrm{pv}}(\vec{q}) | \Psi^0_n \rangle \tag{2b}$$

$V_{\mathrm{pv}}(\vec{q})$ is expanded in a polynomial, $\left\langle \Psi^0_n \,|V_{\mathrm{pv}}(\vec{q})\,|\,\Psi^0_n \right\rangle$ is evaluated numerically.

$$\frac{\Delta_{\mathrm{pv}}\ \nu^{\mathrm{ul}}}{\nu^{\mathrm{ul}}} \approx \frac{2\,[\langle \Psi^0_{\mathrm{u}} | \tilde{V}_{\mathrm{pv}}(\vec{q}) | \Psi^0_{\mathrm{u}} \rangle - \langle \Psi^0_{\mathrm{l}} | \tilde{V}_{\mathrm{pv}}(\vec{q}) | \Psi^0_{\mathrm{l}} \rangle]}{(\tilde{E}^0_{\mathrm{u},j} - \tilde{E}^0_{\mathrm{l},j})} \tag{3}$$

In our previous work on vibrational frequency shifts we also considered both the anharmonic parity conserving Born-Oppenheimer potential for vibrational motion and the parity violating potentials $V_{\mathrm{pv}}(\vec{q})$ coupled between several normal modes [16,36]. $|\,\Psi^0_n\rangle$ is then the anharmonic eigenfunction to the eigenvalue $\tilde{E}^0_n$ of the complete (parity-conserving) vibrational molecular Hamiltonian ($\hat{H}^0_{\mathrm{mol}}$) for the upper (u) or lower (l) molecular state, and the denominator gives the corresponding energy difference. The factor of 2 in eq. (3) arises from considering the difference between both enantiomers, which is twice the individual shift (see [16,20,21] for more details). Rotational shifts have first been investigated for CHBrClF by calculating the change in geometry caused by an additional parity violating potential energy, which leads to a change in bond length and therefore also in the moment of inertia tensor. This can be used to estimate the change in rotational constants [20,21]. A better approximation is to vibrationally average the moment of inertia tensor. From eq. (2) and the perturbation expansion of the wavefunction

$$\Psi_n \approx \Psi^0_n + \Psi'_n + \Psi''_n + \cdots \tag{4}$$

we obtain the vibrationally averaged moment of inertia tensor (in the SAAA)

$$\langle \Psi_0 | I^0 | \Psi_0 \rangle \approx \underbrace{\langle \Psi^0_0 | I^0 | \Psi^0_0 \rangle}_{X_0} \underbrace{-2 \sum_k \frac{(V_{\mathrm{pv}})^{(\nu_i)}_{k0}}{E^0_k - E^0_0}\ \langle \Psi^0_k | I^0 | \Psi^0_0 \rangle}_{+\,\Delta X^{(\nu_i)}} \tag{5}$$

Results and Conclusions

The reduced normal coordinate dependence of the parity violating potential energy has been used to determine anharmonic wavefunctions in CDBrClF. The contributions to the vibrationally averaged rotational constants are shown in the Table for each mode ν_i [30]. The total effect from all modes is compared to the estimation from the equilibrium geometry in the last two lines of the Table. In contrast to the vibrational domain it seems that bending

modes show larger contributions to rotational constants (rows ν_7 to ν_9 of the Table), as expected. However, further investigations are needed by, for example, considering multi-dimensional couplings although they are known to have less influence on bending modes [16,30].

	A/hc	*B/hc*	*C/hc*	
(in cm^{-1})	0.21101	0.06632	0.05279	*ab initio* (X_e)
	0.21089	0.06631	0.05279	vib. averaged (X_0)
$\Delta\tilde{X}^{(\nu_i)}/(10^{-18}\ \mathrm{cm}^{-1})$	0.0127	0.0012	-0.0001	ν_1 CD str
	1.4042	0.0318	0.0716	ν_2 CF str
	0.3459	0.0143	0.0106	ν_3 CD be (a)
	1.0808	0.0849	0.0639	ν_4 CD be (b)
	-2.0260	-0.1641	-0.1559	ν_5 CCl str
	0.8554	0.1728	0.0940	ν_6 CBr str
	13.391	0.8002	1.5674	ν_7 ClCF be
	-4.5302	-2.3783	-1.8981	ν_8 BrCF be
	-4.8046	1.8422	0.8848	ν_9 BrCCl be
Total $\Delta\tilde{X}/(10^{-18}\ \mathrm{cm}^{-1})$	5.7292	0.4050	0.6553	
from change in geometry	5.79	0.83	1.09	after [16,20,21]

Acknowledgement:
Our work is supported financially by the Schweizerischer Nationalfonds and ETH Zürich.

References

[1] M. Gaillard, P. Grannis, F. Sciulli, Rev. Mod. Phys., **71**, S96 (1999).
[2] M. Quack, J. Stohner, Chimia, **59**, 530 (2005).
[3] T. D. Lee, C. N. Yang, Phys. Rev., **104**, 254 (1956).
[4] C. S. Wu, E. Ambler, R. W. Hayward, D. D. Hoppes, R. P. Hudson, Phys. Rev., **105**, 1413 (1957).
[5] M. Quack, Chem. Phys. Lett., **132**, 147 (1986).
[6] M. Quack, Angew. Chem. Int. Ed. Engl., **28**, 571 (1989).
[7] M. Quack, Chem. Phys. Lett., **231**, 421 (1994).
[8] M. Quack, J. Stohner, M. Willeke, Annu. Rev. Phys. Chem., **59**, 741 (2008).
[9] D. W. Rein, R. A. Hegstrom, P. G. H. Sandars, Phys. Lett., **A71**, 499 (1979).
[10] R. A. Hegstrom, D. W. Rein, P. G. H. Sandars, J. Chem. Phys., **73**, 2329 (1980).

[11] A. Bakasov, T. K. Ha, M. Quack. In J. Chela-Flores and F. Rolin, editors, Proc. of the 4th Trieste Conference (1995), *Chemical Evolution: Physics of the Origin and Evolution of Life*, pages 287-296, Dordrecht, (1996). Kluwer Academic Publishers.
[12] A. Bakasov, T. K. Ha, M. Quack, J. Chem. Phys., **109**, 7263 (1998).
[13] R. Berger, M. Quack, J. Chem. Phys., **112**, 3148 (2000).
[14] A. Barra, J. Robert, L. Wiesenfeld, Phys. Lett. A, **115**, 443 (1986).
[15] T. Cvitas, J. Frey, B. Holmström, K. Kuchitsu, R. Marquardt, I. Mills, F. Pavese, M. Quack, J. Stohner, H. L. Strauss, M. Takami, and A. J. Thor. *Quantities, Units and Symbols in Physical Chemistry*. IUPAC & The Royal Society of Chemistry, Cambridge, 3rd Edition, 2nd Printing, (2008).
[16] M. Quack, J. Stohner, J. Chem. Phys., **119**, 11228 (2003).
[17] C. Daussy, T. Marrel, A. Amy-Klein, C. Nguyen, C. Bordé, C. Chardonnet, Phys. Rev. Lett., **83**, 1554 (1999).
[18] A. Bauder, A. Beil, D. Luckhaus, F. Müller, M. Quack, J. Chem. Phys., **106**, 7558 (1997).
[19] J. Stohner, A. Beil, H. Hollenstein, O. Monti, M. Quack. In 37th IUPAC Congress and 27th GDCh Meeting, Berlin, Germany, August 14-19, 1999, Frontiers in Chemistry: Molecular Basis of the Life Sciences, page 525. ISBN 3-924763-82-8.
[20] M. Quack, J. Stohner, Phys. Rev. Lett., **84,** 3807 (2000).
[21] M. Quack, J. Stohner, Z. Physik. Chemie, **214**, 675 (2000).
[22] E. Arimondo, P. Glorieux, T. Oka, Opt. Commun., **23**, 369 (1977).
[23] J. K. Laerdahl, P. Schwerdtfeger, H. M. Quiney, Phys. Rev. Lett., **84**, 3811 (2000).
[24] R. Viglione, R. Zanasi, P. Lazzeretti, A. Ligabue, Phys. Rev. A, **62**, 052516 (2000).
[25] P. Schwerdtfeger, J. Laerdahl, C. Chardonnet, Phys. Rev. A, **65**, 042508 (2002).
[26] R. Berger, M. Quack, J. Stohner, Angew. Chem. Intl. Ed. (Engl.), **40**, 1667 (2001).
[27] F. Faglioni, P. Lazzeretti, Phys. Rev., **A67**, 032101 (2003).
[28] R. Bast, P. Schwerdtfeger, Phys. Rev. Lett., **91**, 023001 (2003).
[29] P. Schwerdtfeger, A. Kuhn, R. Bast, J. Laerdahl, F. Faglione, P. Lazzeretti, Chem. Phys. Lett., **383**, 496 (2004).
[30] M. Quack, J. Stohner, 13th SASP Symposium, Going, Austria (2002), and to be published.
[31] J. Stohner, Int. J. Mass Spectrometry, **233**, 385 (2004).
[32] R. Viglione, J. Chem. Phys., 121, 9959 (2004).
[33] R. Berger, J. L. Studer, Mol. Phys., **105**, 41 (2007).
[34] D. Figgen, P. Schwerdtfeger, Phys. Rev. A, **78**, 012511 (2008).
[35] D. Figgen, P. Schwerdtfeger, J. Chem. Phys., **130**, 054306 (2009).
[36] A. Beil, H. Hollenstein, O. Monti, M. Quack, J. Stohner, J. Chem. Phys., **113**, 2701 (2000).

Cavity Ring-Down (CRD) Spectrum of the $\nu_2+2\nu_3$ Subband of CH_4 in a Supersonic Expansion Below 40 K

Martin Suter, Carine Manca Tanner, and Martin Quack
Laboratorium für Physikalische Chemie, ETH Zürich, Switzerland

The $N=v_1+v_3+0.5(v_2+v_4)=2.5$ polyad of $^{12}CH_4$ is composed of 20 overtone and combination bands. The $\nu_2+2\nu_3$ band has been first assigned in 1933 at low resolution [1]. Further assignments have been done later still at low resolution (0.3 cm^{-1}) at room temperature and 77 K [2]; The CRD measurements performed in our group some years ago [3] were the first using supersonic expansions; they provided first high resolution analyses and an accurate location of the vibrational level $\nu_2+2\nu_3$ at 7510.3378 cm^{-1}. Since these measurements, we have devoted a large effort to improve the supersonic expansion itself. We reinvestigate this spectral region at lower temperatures. In a first approach, we use the assignment of the $\nu_2+2\nu_3$ band already known in our group to better estimate the rotational temperature of the expansion. As we obtain spectra at very low temperatures, these measurements can also be considered as a further investigation of nuclear spin symmetry conservation in CH_4 in a supersonic expansion at temperatures below 40 K.

Experiment

A tunable external cavity cw-InGaAsP laser diode emitting a beam of a few mW at 1.3 μm (7465-8025 cm^{-1}) in single-frequency mode is coupled to the TEM_{00} mode of a cavity composed of two mirrors of high reflectivity separated by 33 cm. The weak transmitted light leaking out the cavity is detected by a fast InGaAs photodiode (125 MHz). The typical ring-down time of the cavity is larger than 5 μs. Under these conditions, the cavity finesse is of F=30000 and the minimum detectable absorption per pass of 10^{-5}. The cavity is pumped by a pumping system composed of an oil diffusion, a roots and a mechanical pump, which allows a residual vacuum not larger than 10^{-6} mbar. A 33 mm x100 μm slit of a pulsed solenoid valve is mounted in the direction of the pumps and aligned along the spatial cavity axis. The home-built valve produces gas pulses of less than 1 ms duration with a backing pressure of 0.6 bar and a repetition rate of 4 to 8 Hz. The remaining dynamical pressure in the cavity during an expansion does not exceed $2x10^{-4}$ mbar. More details on the experimental setup are given in references [3-7].

The samples were composed of 2 to 13% of CH_4 (Pangas, 99.995%) used without further purification and mixed with either Ar (Pangas, 99.9990%) or He (Pangas, 99.9990%). Due to the dilution of CH_4 in the gas mixture, the absorption is expected to be much weaker than that

of an expansion of pure methane used in previous work in our group [3]. On the other hand, the temperature of the gas mixture is expected to be lower and therefore low *J* value states more populated.

Results

Figure 1 shows the CRD spectrum of the Q branch of $\nu_2+2\nu_3$ of CH_4 in Ar and He supersonic expansions (1:7 and 1:40, respectively). We get a good agreement in the line position with the previous measurements performed with this setup in our group [3] at higher temperatures, see Table 1: for most of the lines, the deviation of the line position does not exceed 10^{-3} cm^{-1}. Each line was fitted with a Gaussian profile; the width is ~0.008 cm^{-1} in the case of the CH_4:Ar expansion (Figure 1a), which corresponds to a formal Doppler temperature of roughly 40 K. Moreover, from the three F_1 components (*J*=1, 3, and 4), a Boltzmann distribution leads to a temperature of 37(1) K. The spectrum is at least 10 K colder than the previous measurements of pure methane in our group [3]. The spectrum of the He expansion (Figure 1b) exhibits even lower relative intensities for the large *J* values and the temperature has been estimated to be 26(1) K (See below). Interestingly, we have managed to get similar signal to noise ratio than the previous measurements with the setup at 50 K, which proves that lower temperatures can still be measured with this experimental setup.

Transition	$\Gamma(T_d)$	$\Gamma(T_d)\uparrow S_4$*	(E/hc) / cm^{-1}	
			Ref. [3]	This work
$R^{(-)}(3)$	A_2	$A_2^+ + A_1^-$	7552.7361	7552.7365
	F_2	$F_2^+ + F_1^-$	7552.8059	7552.8044
	F_1	$F_1^+ + F_2^-$	7552.8779	7552.8789
$Q^{(0)}(1)$	F_1	$F_1^+ + F_2^-$	7510.2873	7510.2877
$Q^{(0)}(2)$	E, F_2	$E^+ + E^-$, $F_2^+ + F_1^-$	7510.1531	7510.1515
$Q^{(0)}(3)$	A_2	$A_2^+ + A_1^-$	7510.1902	7510.1915
	F_2	$F_2^+ + F_1^-$	7510.0533	7510.0541
	F_1	$F_1^+ + F_2^-$	7509.9636	7509.963
$Q^{(0)}(4)$	F_2	$F_2^+ + F_1^-$	7510.0309	7510.0299
	E	$E^+ + E^-$	7509.8820	7509.8829
	F_1	$F_1^+ + F_2^-$	7509.7682	7509.768
	A_1	$A_1^+ + A_2^-$	7509.5727	7509.5726

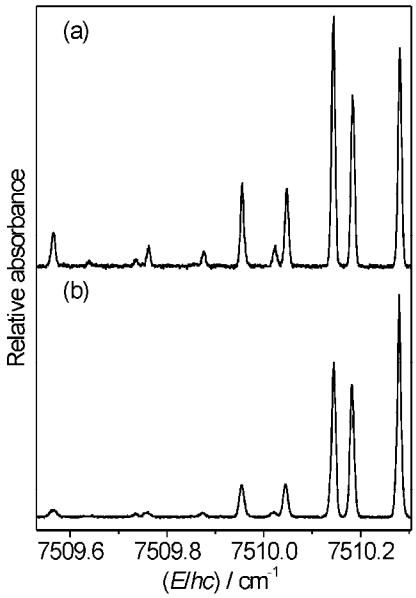

Table 1 *(left): Observed transitions of $\nu_2+2\nu_3$ band of CH_4 according to the assignment of reference [3].* ***Figure 1*** *(right): CRD spectra of the Q branch of $\nu_2+2\nu_3$ band of CH_4. (a) Ar expansion (1:7), (b) He expansion (1:40). The absorbance of the Q(1) line has been normalized to compare the two spectra on equal footing.*

CH_4 is composed of three nuclear spin isomers, i. e. meta (nuclear spin I=2) with the representation Γ=A, ortho (I=1) with the representation Γ=F, and para (I=0) with the representation Γ=E. In case of nuclear spin symmetry conservation [8], the three nuclear spin states keep their relative population set at room temperature before the expansion and one observes a Boltzmann distribution within the rovibrational levels of each nuclear spin isomer. Conversely in case of nuclear spin symmetry relaxation, the nuclear spin states are allowed to change during the collisional process of the expansion and the relative populations should represent the global thermal equilibrium among all the states at cold temperatures. Parity is conserved intramolecularly on short time scales << 1 ms [9], but may change in collisions [8,10].

According to the work of Amrein *et al.* [10], the integrated absorption strength of a given transition is proportional to the relative population of the corresponding ground state of the representation. Figure 2(a) shows the modifications of the population probabilities of the three nuclear spin isomers as function of the equilibrium temperature for the two models, those in the case of nuclear spin symmetry conservation being of course constant. Depending on the sensitivity of the experiment, one might determine whether nuclear spin relaxation occurs at temperatures below 40 K since the population ratios of the nuclear spin isomers become strongly T-dependent at low temperatures.

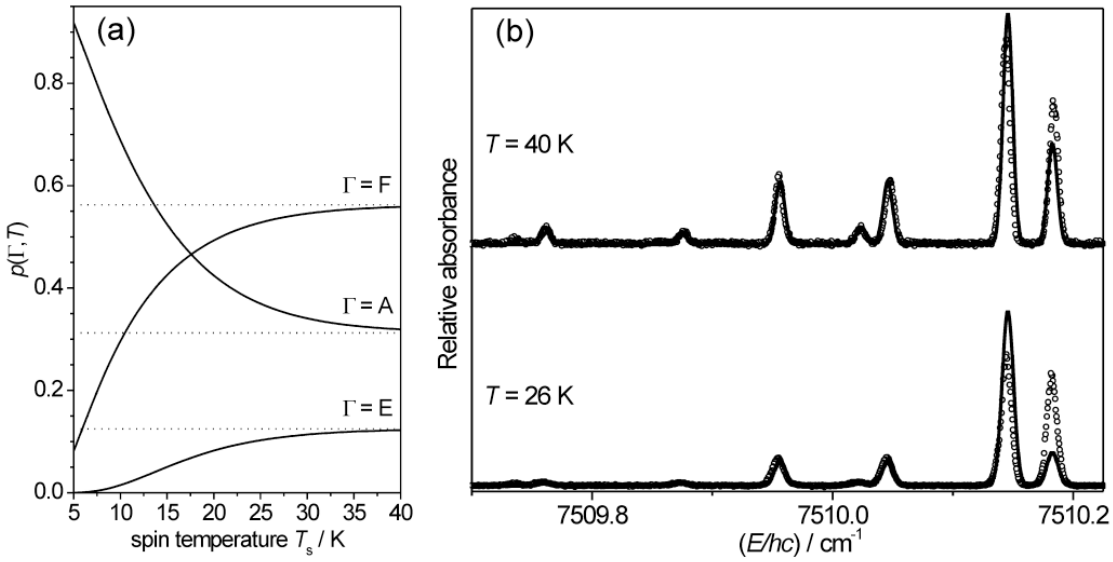

Fig. 2: *(a) Population probabilities of the three nuclear spin isomers as function of the equilibrium temperature assuming spin symmetry relaxation (full line) or conservation (dotted line). (b) Experimental (symbols) and simulated (line) spectrum of the Q branch of the $\nu_2+2\nu_3$ band of CH_4:Ar at 40 K (top) and CH_4:He at 26 K (bottom). The absorbance of the Q(1) line (not shown here) has been normalized to compare the two spectra on equal footing.*

In our case, as we can not rigorously estimate the population of the three different components from the intensities of a molecular beam spectrum, we base our analysis on intensity ratios and relative concentrations instead of absolute concentrations. Figure 2 shows the simulation of the spectrum at 40 K and 26 K for the expansion in Ar and He, respectively, under the assumption of full nuclear spin symmetry conservation. The simulation mainly reproduces quite well the spectrum at 40 K; we nevertheless observed some discrepancies in relative intensity at lower temperatures for the line assigned as the $Q(3)A_2$ component. Analogous discrepancies have been observed also using direct absorption spectroscopy in a cryogenic cell [11] and in a previous work in our group at 11 K around 3000 cm^{-1} [10]. Further analyses of the P branch of the $\nu_2+2\nu_3$ band at low temperatures combined with the work from our group in a low temperature cell reported at a previous meeting [12] indicate that the discrepancies can be resolved by a reassignment.

References

[1] W. NORRIS and H. UNGER, *Phys. Rev.* **43**, 467 (1933).
[2] K. CHAN, H. ITO, and H. INABA, *Appl. Opt.* **22**, 3802 (1983).
[3] M. HIPPLER and M. QUACK, *J. Chem. Phys.* **116**, 6045 (2002).
[4] Y. HE, M. HIPPLER, and M. QUACK, *Chem. Phys. Lett.* **289**, 527 (1998).
[5] M. HIPPLER and M. QUACK, *Chem. Phys. Lett.* **314**, 273 (1999).
[6] M. HIPPLER, M. OELTJEN, and M. QUACK, *J. Phys. Chem. A* **111**, 12659 (2007).
[7] C. MANCA and M. QUACK, Dynamics in the hydrogen bonded systems $(HF)_2$ and HF/DF studied by means of cw-CRD spectroscopy, in *Contributions, 16th Symposium on Atomic and Surface Physics and Related Topics, Les Diablerets, Switzerland, 20. - 25.1.2008*, edited by R. D. BECK, M. DRABBELS, and T. R. RIZZO, pp. 170 – 173, Innsbruck University Press, ISBN 978-902571-31-1, Innsbruck, 2008.
[8] M. QUACK, *Mol. Phys.* **34**, 477 (1977).
[9] M. QUACK, J. STOHNER, and M. WILLEKE, *Ann. Rev. Phys. Chem.* **59**, 741 (2008).
[10] A. AMREIN, M. QUACK, and U. SCHMITT, *J. Phys. Chem.* **92**, 5455 (1988).
[11] E. SCIAMMA-O'BRIEN, S. KASSI, B. GAO, and A. CAMPARGUE, *J. Quant. Spectr. Rad. Transf.* **110**, 951 (2009).
[12] H. M. NIEDERER, S. ALBERT, S. BAUERECKER, M. QUACK, and G. SEYFANG, Contribution L1 p. 261, The 21st Colloquium High Resolution Molecular Spectroscopy. Castellammare di Stabia, September 2009, and *to be published*.

Photostability of Small Heterocyclic Molecules in Hydrogen Bonded Clusters: Evidence from Photodissociation and Mass Spectrometric Experiments

O. Tkáč[1], V. Poterya[1], A. Pysanenko[1], P. Slavíček[2], U. Buck[3] and M. Fárník[1]

[1]*J.Heyrovský Institute of Physical Chemistry AS CR, Dolejškova 3, 18223 Prague 8, Czech Republic, michal.farnik@jh-inst.cas.cz*

[2]*Department of Physical Chemistry, Institute of Chemical Technology, Technická 5, Prague 6, Czech Republic*

[3]*Max-Planck-Institut für Dynamik und Selbstorganisation, Bunsenstr. 10, Göttingen, Germany*

The heterocyclic nitrogen containing molecules, e.g. pyrrole and imidazole, represent important building blocks in many biomolecules fulfilling important functions in living organisms. Radiation damage of these molecules (by UV photons or electrons) can threaten functioning of these biomolecules. In order to understand the photostability of these rather complex species at a detailed molecular level, we have to investigate the photochemistry of their simpler constituents, namely of the UV chromophores such as the heterocyclic compounds studied here. However, the studies of the isolated molecules in the gas phase do not necessarily provide the complete picture about the photochemistry of the more complex biological systems. Therefore, the further step towards unraveling the photochemistry of biomolecules is to study the photochemistry of the smaller constituent species solvated in finite size molecular clusters. This way the effects of the solvent on the photochemistry can be revealed.

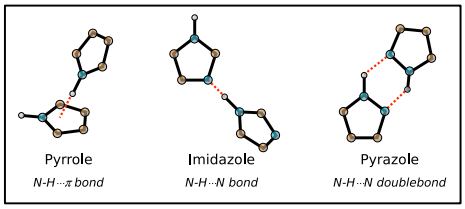

Fig. 1: *Different hydrogen bonding motifs of pyrolle, imidazole and pyrazole dimers.*

Here we present the study of UV photodissociation and photoionization of pyrrole, imidazole and pyrazole molecules in clusters. All three molecules, although structurally very similar, generate clusters with quite different bonding motifs, as illustrated in Fig. 1 for dimers: In the pyrolle dimer N-H···π bond is present, while imidazole dimer is bound by the N-H···N hydrogen bond and in the pyrazole dimer a double bond is present similar to the DNA base pairs bonding motif. One of the questions addressed here is, how these different bonding motifs influence the photochemistry of these species.

The UV-absorption and photochemistry of the above molecules in the gas phase has been studied in great detail previously (see e.g. [1] and references cited therein) and following general picture arise: It has been postulated by Sobolewski and Domcke [2] that the photostability of these molecules is determined by an excited $\pi\sigma^*$ state of a dissociative Rydberg character. The corresponding potential energy surface (PES) for this state exhibits conical intersections (CI) with the optically active $\pi\pi^*$ state, to which the molecules are excited by photon absorption, and with the ground S_0 state. These CIs are located along the N-H dissociation coordinate. Thus upon UV excitation the molecule can quickly transfer via the $\pi\sigma^*$ PES to the S_0 state, where the energy can be dissipated preventing a fluorescence photon to be irradiated from these molecules or the damaging excited state chemistry to happen. As the experimental spectroscopic fingerprint of this dynamics, the kinetic energy distribution spectra (KED) of the H-fragment after photodissociation of these molecules in the gas phase were measured by several groups ([1] and references therein). These KED generally exhibit bimodal character with a Gaussian shaped peak of faster fragments (with energies around 1 eV) and an underlying slow-fragment distribution peaking near 0.1-0.3 eV originating from the statistical decay from the hot ground state. The character of these spectra can be seen in Fig. 2 below, where similar spectra measured in our experiment for clusters are presented. To investigate the influence of solvation on photochemistry of these molecules we have studied UV-photolysis and ionization of the above molecules in various cluster environments [3,4,5].

Photodissociation in clusters

In the photodissociation experiments, the clusters are photolyzed by an UV laser pulse (243 nm or 193 nm) and the H-fragments are (2+1) REMPI photoionized at 243 nm and their KED is measured by a time-of-flight (TOF) spectrometer in the low field mode (~1V.cm^{-1}).

Figure 2 shows the H-fragment KED after the photodissociation of the pyrrole and imidazole clusters. All the spectra exhibit the bimodal character observed previously in the photodissociation of molecules discussed above. However, the fast fragment contribution, which is the major channel for the molecule, decreases in the intensity relative to the slow component with the increasing cluster size. The observed trends in the KEDs can be qualitatively explained in terms of PES. For pyrrole the theoretical calculations show that the $\pi\sigma^*$ state moves higher in energy, when a solvent molecule is added to the system, so that the CI with the ground state along the N-H coordinate disappears and the direct dissociation channel producing the fast H-fragments is closed.

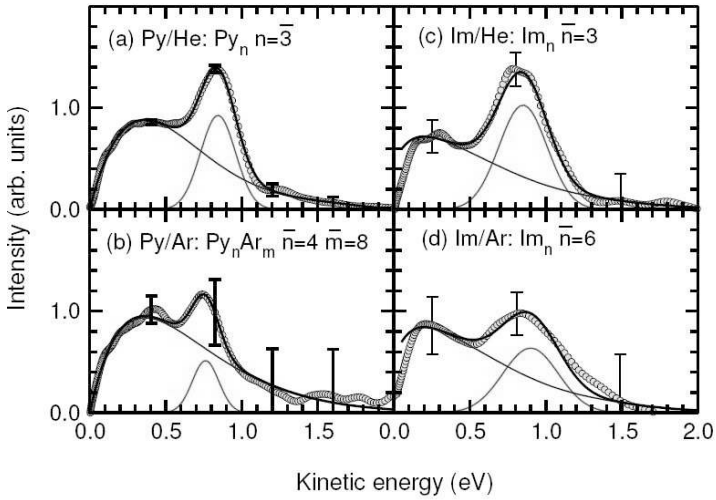

Fig. 2: *H-fragment kinetic energy distributions after 243 nm photolysis of pyrrole and imidazole clusters.*

In imidazole the experiment shows analogical behaviour, however, the calculations show that a different reaction mechanism is operational. Due to the N-H···N bonding, the hydrogen transfer (HT) between the imidazole units can play a role in the excited imidazole cluster. Upon the excitation the system evolves to the region on PES where the two hydrogens are bound to nitrogens of the same molecule and where a CI with the ground state occurs. The system can evolve through this CI to S_0 thus dissipating the energy between the imidazole units. Thus the HT process in the cluster has a stabilizing effect on the imidazole molecule.

Mass spectrometry of clusters

Finally, the mass spectrometry of various clusters of pyrrole, imidazole and pyrazole molecules was investigated. In these experiments the clusters were ionized by successive multiphoton ionization absorbing two or more 193 nm (6.4 eV) photons (UVMPI). Alternatively, the clusters were ionized by a 70 eV electron impact (EI) and subsequently mass analyzed with a quadrupole mass spectrometer.

Several conclusions could be made from these mass spectrometric studies. First, the successive UVMPI leads to a significantly higher degree of fragmentation than the EI ionization. Second, the pyrrole clusters are ionized to molecular Py_k^+ fragments, while the imidazole and pyrazole clusters fragment to protonated Im_kH^+ and Pz_kH^+ ions, respectively, for both EI and UVMPI methods. This observation is in agreement with the HT or proton transfer channel in the photochemistry of imidazole and pyrazole clusters. Finally, the mass spectra also confirm the conclusion from the photodissociation studies, that the HT process stabilizes the molecule in the cluster.

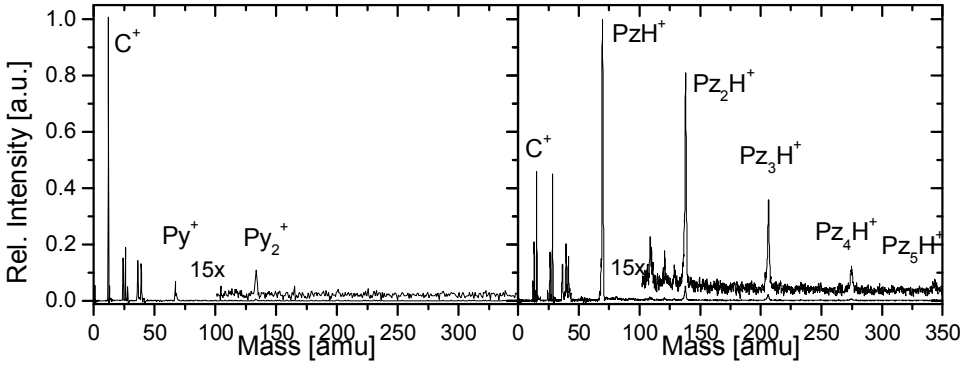

Fig. 3: *TOF mass spectra of the large pyrrole and pyrazole.*

This is illustrated in Fig. 3, where the comparison of the UVMPI spectra from the large pyrrole and pyrazole clusters is shown. The pyrazole spectrum is dominated by the strong protonated monomer peak and protonated cluster peaks are also present. On the other hand, the pyrrole clusters, where the HT process cannot occur, fragment completely, generating very little parent Py^+ ion and Py_2^+, but mainly fragments smaller than the molecule occur. The imidazole spectrum closely resembles the pyrazole one. Thus in the hydrogen bonded clusters the molecules are, indeed, stabilized by the hydrogen or proton transfer process upon UV excitation.

Acknowledgements:

Vakuum Praha 100002/3597, Czech Academy of Sciences KAN400400461, and Grant Agency of the Czech Republic KJB400400902 are acknowledged.

References

[1] M.N.R. Ashfold, B. Cronin, A.L. Devin, R.N. Dixon, M.G.D. Nix, Science **312**, 1637 (2006).
[2] A. L. Sobolewski, W. Domcke, C. Dedonder-Lardeux, C. Jouvet, Phys. Chem. Chem. Phys. **4**, 1093 (2002).
[3] V. Poterya, V. Profant, M. Fárník, P. Slavíček, U. Buck, J. Chem. Phys. **127**, 064307 (2007).
[4] V. Profant, V. Poterya, M. Fárník, P. Slavíček, U. Buck, J. Phys. Chem. A **111**, 0751561 (2007).
[5] V. Poterya, V. Profant, M. Fárník, L.·Šištík, P. Slavíček, P.; Buck, U. J. Phys. Chem. A (2009).

Multi-Mass Imaging Using a Fast Frame-Transfer CCD Camera

Claire Vallance, Edward Wilman, Alexander Johnsen, Weihao Yuen, and Mark Brouard,
Department of Chemistry, University of Oxford, Oxford, UK

Andrei Nomerotski,
Department of Physics, University of Oxford, Oxford, UK

Renato Turchetta, Jamie Crooks and Andrew Clark
Rutherford Appleton Laboratory, Harwell Science and Innovation Campus, Oxfordshire, UK

Velocity-map imaging has been used with great success in the field of small-molecule reaction dynamics to study both molecular photofragmentation and a range of photoinitiated bimolecular events. A velocity-map imaging apparatus consists of a time-of-flight mass spectrometer fitted with a position sensitive detector and employing a velocity-mapping electrostatic lens in place of the more usual Wiley-McLaren ion optics. By adjusting the electrode potentials, the lens may be tuned such that either the positions or the velocities of the ions at their point of formation are projected in two dimensions onto the detector

The position sensitive detector usually consists of a pair of chevron microchannel plates (MCPs) coupled to a phosphor screen. An ion striking the front face of the channel plates initiates an electron cascade within one of the channels, and the burst of electrons emitted from the back face of the channel plates elicits a flash of light on the phosphor screen. In this way, the spatial distribution of ions striking the front face of the MCPs is transformed into an image on the phosphor, which may be captured using a CCD camera. Typically, a single photofragment or reaction product is selected for imaging by time-gating either the microchannel plates or an image intensifier located in front of the camera, such that a signal is only detected when the chosen mass arrives at the detector. For small molecule studies, characterisation of a single fragment is often sufficient to obtain a fairly complete picture of the dynamics of a photoinitiated process. However, larger molecules often have much more complex dissociation dynamics and may separate into numerous fragments. In these cases, characterisation of a single product is often insufficient, and the ability to record images of several fragments simultaneously becomes highly desirable. Previously, there have been two techniques developed to perform 'multimass imaging', both of which rely on spatial separation of the images at the detector through the application of static or pulsed electric or magnetic fields. The technique developed by Suits et al [1] employs a pulsed deflection field to achieve spatial separation of ions of different masses transverse to the time-of-flight axis,

and has been used to study the dissociation dynamics of the ethylene cation, $C_2H_4^+$ [2,3]. While this is a promising approach, it does have the disadvantage that the mass resolution and mass range, as well as the spatial resolution of individual images, are limited significantly by the combination of the detector size and the maximum speed of the nascent fragment ions, which determines the individual image sizes. A second technique, developed in the group of Y. T. Lee [4] and based on a radial cylindrical energy analyser, yields the speed distributions for ions of different masses, but no angular information. This latter technique has, however, been used with great success in studying the dissociation dynamics of a wide range of organic species [5].

We propose a new method of multimass imaging in which the multimass modality is achieved by temporally resolving the images for different masses by replacing the standard CCD detector with an ultrafast framing CCD or CMOS sensor. We have carried out proof-of-concept work using a programmable ultrafast frame-transfer CCD camera, clocked to the arrival times of the various masses, in the detection step. Using our method, images for different masses are separated in time rather than in space, allowing the use of a completely standard velocity-map imaging setup with no additional fields required. In principle, the method has the potential to offer essentially unlimited mass channels, mass range and spatial resolution. Our prototype camera is capable of recording up to 16 images per event at user-defined times with a time resolution of 10 ns and a spatial resolution of 64x64 pixels. After each trigger cycle, the stored images are transferred from the chip to a PC at standard data rates for processing and permanent storage. We are also developing a CMOS-based event-counting sensor, which will have several advantages over the framing CCD approach, and expect the first prototype for testing in mid 2010.

After briefly describing the working principles of our sensors, we will present some of our proof of concept work on the technique and outline some of the potential applications for the new technology in the areas of both velocity-map imaging of gas phase samples and spatial map imaging of surfaces.

References

[1] M.H. Kim, B.D. Leskiw, L. Shen, and A.G. Suits, Int. J. Mass Spectrom., **252**, 73 (2006).
[2] M.H. Kim, B.D. Leskiw, and A.G. Suits, J. Phys. Chem., **109(35)**, 7839 (2005).
[3] M.H. Kim, B.D. Leskiw, L. Shen, and A.G. Suits, J. Phys. Chem. A, **111(31)**, 7473 (2007).
[4] S.T. Tsai, C K. Lin, Y.T. Lee, and C.K. Ni, Rev. Sci. Instrum., **72**, 1963 (2001).
[5] See for example: C. K. Ni and Y. T. Lee, Int. Rev. Phys. Chem., **23(2)**, 187 (2004), and references therein.

Reactions of Nitrogen Oxides with Hydrated Radical Anions of Atmospheric Interest

Christian van der Linde[1], Robert F. Höckendorf[1], O.-Petru Balaj[1], Martin K. Beyer[1]

[1] *Institut für Physikalische Chemie, Christian-Albrechts-Universität zu Kiel, Olshausenstraße 40, 24098 Kiel, Germany, beyer@phc.uni-kiel.de*

In the chemistry of the troposphere, nitrogen oxides play an important role [1]. Their reactivity with various volatile organic compounds is well understood, but radical anion reaction pathways may also take place in aqueous environment. Free electrons are generated in the atmosphere by ionizing radiation or lightning. These electrons are able to combine with molecular oxygen or carbon dioxide and form hydrated cluster species in the aqueous environment of the atmosphere. In our investigation we studied the reactions of $X^-(H_2O)_{30\text{-}70}$ with X = e^-, O_2^-, CO_2^- and with N_2O, NO and NO_2 in order to get information about the kinetics and thermochemistry of the reactions.

Experimental

The experiments were performed on a modified Bruker CMS47X Fourier transform ion cyclotron resonance (FT-ICR) mass spectrometer equipped with an infinity cell. The clusters were produced in an external laser vaporization source, transferred by an electrostatic lens system, and stored in the ICR cell. The reactants were introduced at a constant pressure into the ultra high vacuum region of the FT-ICR by a needle valve. Spectra at different reaction delays were taken to monitor the reactions and follow the kinetic behavior.

Results and Discussion

Hydrated electron clusters $(H_2O)_n^-$ showed reactivity towards all used nitrogen oxides while $O_2^-(H_2O)_n$ and $CO_2^-(H_2O)_n$ were reactive only towards the radical species NO and NO_2.

Hydrated electron clusters $(H_2O)_n^-$ react with nitrogen oxide taking up to three NO molecules into the cluster. The uptake of the first molecule is a fast process while the uptake of a second and a third NO is less efficient. We determined the rate constants of the first two reaction steps: $k_1 = 3.5\text{x}10^{-10}$ cm^3 s^{-1} and $k_2 = 3.8\text{x}10^{-11}$ cm^3 s^{-1}. From the difference in the average number of water molecules between reactant and product the reaction enthalpy is determined using a new nanocalorimetry model for fitting the resulting curves.

For example the uptake of the first NO molecule e.g. evaporates 5.4 water molecules. Since the evaporation of one water molecule needs 43.3±3.1 kJ mol^{-1} it results in a reaction enthalpy ΔH of -233.9±20 kJ/mol [2].

Using data from literature it is possible to determine further thermochemical data like hydration enthalpies of the product ions by using Hess law. The calculation for the NO^- ion is shown in the Table.

Table 1: Calculation of the hydration enthalpy of NO^-.

	reaction	***ΔH / kJ mol^{-1}***	
(a)	$NO(g) + e^-(aq) \rightarrow NO^-(aq)$	-233.8 ± 20	
(b)	$NO^-(g) \rightarrow NO(g) + e^-(g)$	+2.5 ± 0.5	[3]
(c)	$e^-(g) \rightarrow e^-(aq)$	-171.9 ± 3.8	[4]
	$NO^-(g) \rightarrow NO^-(aq)$	-403.2 ± 24.3	

References

[1] P. J. Crutzen, *Annual Review of Earth and Planetary Sciences* 1979, *7*, 443-472.
[2] C. Hock, M. Schmidt, R. Kuhnen, C. Bartels, L. Ma, H. Haberland, B. v. Issendorf, *Phys. Rev. Lett.* 2009, *103*.
[3] M. J. Travers, D. C. Cowles, G. B. Ellison, *Chem. Phys. Lett.* 1989, *164*, 449-455.
[4] H. Shiraishi, G. R. Sunaryo, K. Ishigure, *J. Phys. Chem.* 1994, *98*, 5164.

Dissociative Electron Attachment to CO_2 and N_2O Clusters

V.Vizcaino, S.Denifl, T.D.Märk and P.Scheier
Institut für Ionenphysik und Angewandte Physik, Leopold-Franzens-Universität Innsbruck, Technikerstr. 25, A-6020 Innsbruck, Austria., violaine.vizcaino@uibk.ac.at

This contribution presents electron attachment to $(CO_2)_n$ and $(N_2O)_n$ clusters in the size range up to n=10 and an electron energy range from threshold up to 5eV. Measurements are performed on a crossed electron / cluster beam apparatus. For both clusters, the energy dependence of the cluster anions yield exhibits vibrational Feschbach resonances below 1eV and a rather broad resonance around 2eV (for N_2O) and 3eV (for CO_2). As the cluster size increases the position of both resonances is gradually shifting toward lower energy.

1- Introduction

Collision processes between low-energy electrons and atoms, molecules or clusters are of great interest from a fundamental viewpoint and for a wide range of technological applications. Dissociative electron attachment is among the most important processes in this low energy range. For molecular clusters, due to the molecular surrounding, the process of electron attachment can be quite different than for single molecules. Among these differences one can mention solvation effects (e.g., resonances appear shifted toward lower energy), stabilisation of transient negative ion (evaporative attachment), new resonance ("cluster resonance") where the electron is not trapped into the orbital of a single molecule of the cluster but collectively bound to the cluster.
Electron attachment to both N_2O and CO_2 clusters have been the object of few studies [2-7] in the past years. Early studies only show the presence of the higher resonance around 2eV (for N_2O) [2-4] and 3eV (for CO_2) [2-3], due to poor energy resolution. More recently, Hotop and co-workers [5-7] using a high-resolution (1meV) laser photoelectron attachment method show that, at very low energy (0-200meV) the formation of $(N_2O)_n^-$, $(N_2O)_nO^-$or $(CO_2)_n^-$ occurs via narrow vibrational Feschbach resonances, the attachment spectra revealing very sharp structures at energies just below the vibrational excitation (bending and symmetric stretching modes) of the neutral clusters .
To our knowledge, the present data are the first to propose complete spectra from threshold to 5eV which reveal both resonances.

2- Experimental Setup

The experimental setup has been described extensively in previous papers [1,4]; only a brief statement is given here. Clusters are produced in the first of the two differentially pumped chambers by expanding the gas through a nozzle (Ø = 10μm) at a stagnation pressure of about 3-4 bar and at a controlled temperature. In the present series of measurements, different nozzle temperatures have been tested ranging from 220K to 300K. The cluster beam passes then a 0.8mm diameter skimmer before entering the interaction chamber. The electron beam, obtained from a hemispherical electron monochromator with a typical energy resolution of 80meV, is crossed at right angles with the cluster beam. Negative ions formed in the collision chamber upon electron attachment are extracted by a weak electric field towards the entrance of a quadrupole mass spectrometer, the mass selected ions are detected by a channeltron detector. Energy calibration is made against the well-known zero energy Cl^-/CCl_4 peak.

3- N_2O Cluster

Electron attachment to $(N_2O)_n$ clusters leads to the production of $(N_2O)_n^-$, $(N_2O)_nNO^-$ and $(N_2O)_nO^-$ anions, the last being the predominant fragment. Some of the measured electron attachment spectra are reported below in Figure 1 as an example.

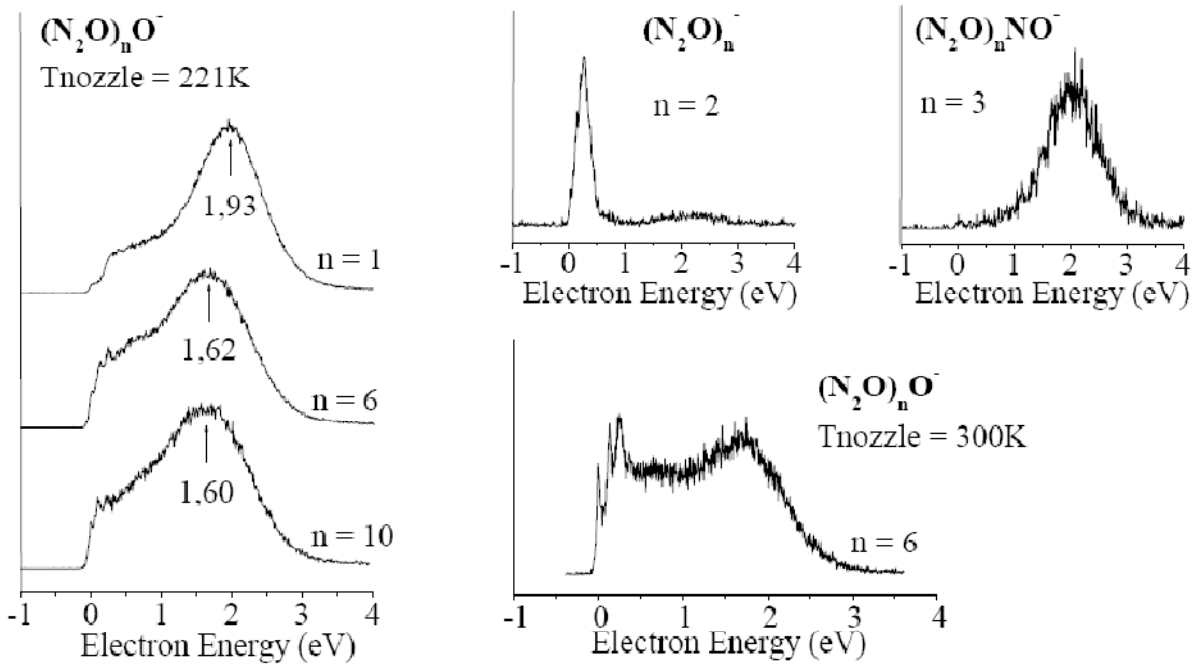

Figure 1: Energy dependence of $(N_2O)_n^-$, $(N_2O)_nNO^-$ and $(N_2O)_nO^-$ yield.

At low energy (below 1eV) vibrational Feshbach resonances (VFR) are observed for both $(N_2O)_n^-$ and $(N_2O)_nO^-$. While for small clusters (typically n<5) the narrow peaks attributed to vibrational excitation are hardly visible they become much more distinguishable for larger clusters. Also measurements performed with the nozzle at room temperature exhibit sharp structures as shown for $(N_2O)_6O^-$ in Figure 1.
A second resonance is observed at around 2 eV for $(N_2O)_nNO^-$ and $(N_2O)_nO^-$ fragments and very weakly for $(N_2O)_n^-$. The position of the peak is gradually redshifting with increasing cluster size due to solvation effects from 2.4eV for O^- to only 1.6eV for $(N_2O)_{10}O^-$.
In this energy range the formation of $(N_2O)_nNO^-$ ions by dissociative electron attachment is not thermodynamically possible, the observed fragments $(N_2O)_nNO^-$ are likely to be originating from $(N_2O)_{n+1}O^-$ (via a subsequent internal ion-molecule reaction).

4- CO_2 Cluster

The electron attachment spectra for $(CO_2)_n$ clusters are quite similar to those of $(N_2O)_n$. The yield of $(CO_2)_n^-$ shows vibrational Feshbach resonances below 1eV and a broad resonance at around 3eV which is attributed to the $^2\Pi_u$ shape resonance. The asymmetric profile of the shape resonance seems to indicate the presence of another resonance at around 2eV, the contribution of this new feature depends quite significantly on the nozzle temperature as shown for $(CO_2)_4^-$ in Figure 2. As for $(N_2O)_n$ clusters, a red shift in the position of the resonances is observed with increasing cluster size.

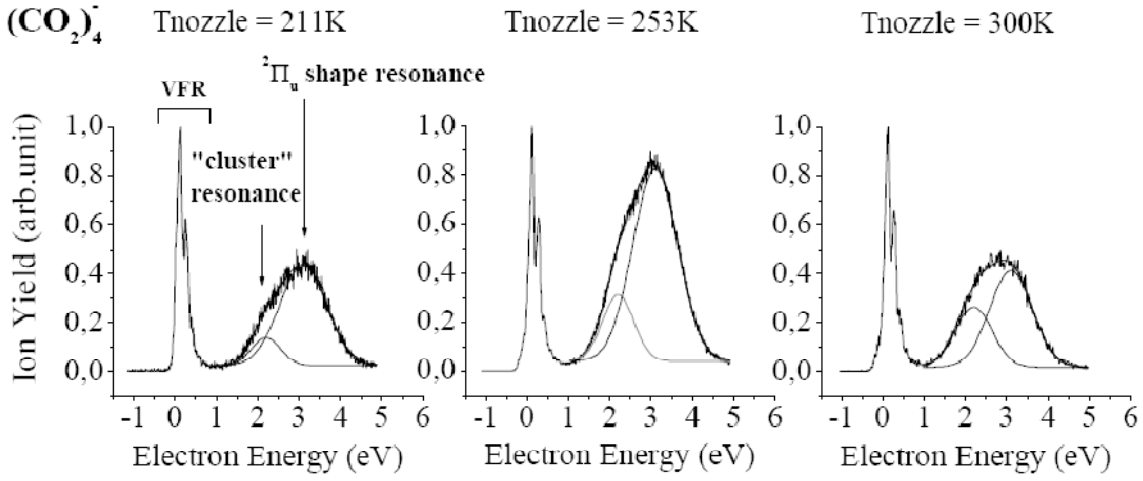

Figure 2: Energy dependence of $(CO_2)_4^-$ yield for different nozzle temperature.

Measurements on electron attachment to CO_2 clusters embedded in He droplets, where the clusters are cooled to their vibrational ground state due to the ultra cold environment, have also been performed and will be compared to the present data.

References

[1] D. Muigg, G. Denifl, A. Stamatovic, O. Echt and T.D. Märk. *Chem. Phys.* **239** (1998), p409.
[2] C.E. Klots and R.N. Compton*, J. Chem. Phys*. **69** (1978), p1636
[3] M. Knapp, O. Echt, D. Kreisle, T.D. Märk and E. Recknagel, *Chem. Phys. Lett.* **126** (1986), p225.
[4] G. Hanel, T. Fiegele, A. Stamatovic, T.D. Märk, *International J. Mass. Spect.* **205** (2001), p65.
[5] J.M. Weber, E. Leber, M.W. Ruf and H. Hotop,. *Phys. Rev. Lett*. **82** (1999), p516.
[6] E. Leber, S. Barsotti, J. Bömmels, J.M. Weber, I.I. Fabrikant, M.W. Ruf and H. Hotop, *Chem. Phys. Lett.* **325** (2000), p343.
[7] S. Barsotti, E. Leber, M.W. Ruf and H. Hotop, *International J. Mass. Spect.* **220** (2005), p. 313.

Observation of an Anomalous Cage Effect in Multiphoton Photodissociation of Acetylene Clusters

Votava, O[1]. Fárník M.[1], Poterya V.[1], Ončák M.[1,2], Slavíček P.[1,2], Buck U.[3]

[1] *J.Heyrovský Institute of Physical Chemistry AS CR, Dolejškova 3,18223 Prague 8, Czech Republic, votava@jh-inst.cas.cz*

[2] *Institute of Chemical Technology, Technická 5, Prague 6, Czech Republic*

[3] *Max-Planck-Institut für Dynamik und Selbstorganisation, Bunsenstr. 10, Göttingen, Germany*

The profound effect of the solvent on the photochemistry has been known for a long time. In 1936, Franck and Rabinowitch introduced the concept of the cage effect to explain the lowering of the iodine photodissociation yield upon solvation [1]. More generally, the slowing down the molecular fragments and preventing the molecules from the dissociation by the solvent cage are manifestations of solvent induced photostability.

Various experiments can manifest such cage effects: (i) photofragment concentration measurements - the photofragment yield decreases upon caging, (ii) time domain measurements - the caging slows down the fragmentation process, and (iii) energy domain measurements – the kinetic energy of a photofragment changes by the interaction with the cage atoms/molecules. In the latter case slowing down of the photofragment to near zero kinetic energies is a typical evidence for a pronounced caging.

In this work, we investigate the solvent effects on the acetylene photodissociation dynamics. The photochemistry of acetylene is dominated by hydrogen dissociation $C_2H_2 \rightarrow C_2H + H$, with quantum yield close to 1 at 193 nm and 121.6 nm wavelengths [2]. The dissociation can proceed via singlet and triplet channels [3] The singlet channel is open approximately above 6.3 eV while the triplet channel seems to be operational during the near-threshold acetylene photoabsorption [4].

In the current experiments the solvent is represented either by other acetylene molecules in $(C_2H_2)_n$ clusters and/or by rare gas atoms in $(C_2H_2)_n \cdot Ar_m$ clusters in molecular beams. The clusters were prepared in supersonic expansions under various conditions and the corresponding mean cluster sizes were determined, for which the photodissociation at 193 nm was studied. The kinetic-energy distributions (KEDs) of the H-fragment following the acetylene photodissociation were measured using the time-of-flight technique [5,6].

The measured KEDs of the H-fragments from the acetylene clusters display some common features with the KED spectrum of the isolated molecules, in particular the KED maximum is located at approximately 0.2 eV both for isolated and solvated acetylene. In contrast to the isolated molecule however, two major differences are observed: First, a fraction of zero energy hydrogen fragments is observed and second, the long energy tail extending up to 2 eV is observed for the solvated acetylene. While fragments with zero energies are a typical feature of the solvent cage effect, the photofragment acceleration upon solvation is a rather unusual phenomenon.

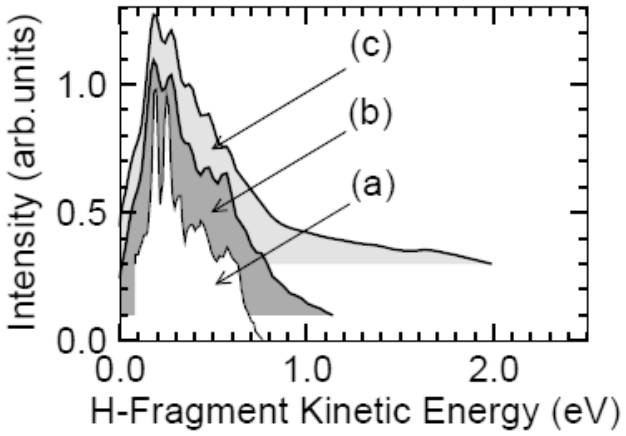

Figure 1*: H-fragment KED from photodissociation of acetylene at 193 nm: (a) the spectrum of C_2H_2 molecule from the literature [7] for comparison (b) spectrum measured with C_2H_2 isolated molecules in our experiment, and (c) the spectrum obtained in the molecular beam containing small $(C_2H_2)_n$ clusters with the mean cluster size $n \approx 10$.*

The analysis based on ab initio calculations suggests the following mechanism that explains the observed photofragment acceleration: (i) At 193 nm, photodissociation of acetylene occurs mostly in the singlet manifold. (ii) The solvent stabilizes the acetylene molecule, preventing it from hydrogen dissociation and funneling the population into a vibrationally hot ground state. (iii) The excited C_2H_2 absorbs the next photon and eventually dissociates, yielding the H fragment with a higher kinetic energy corresponding to the first C_2H_2 excitation. Thus the H-fragment KED extending to higher energies is a fingerprint of the cage effect and the multi-photon nature of the observed processes. We argue that even though our experiment operates in the energy domain, by changing the photon flux it can provide some information also in the time domain. In particular, the photon flux dependence of the KEDs reflects the rate of the vibrational flow from the hot ground state of acetylene to the neighboring solvent molecules, as schematically indicated in figure 2.

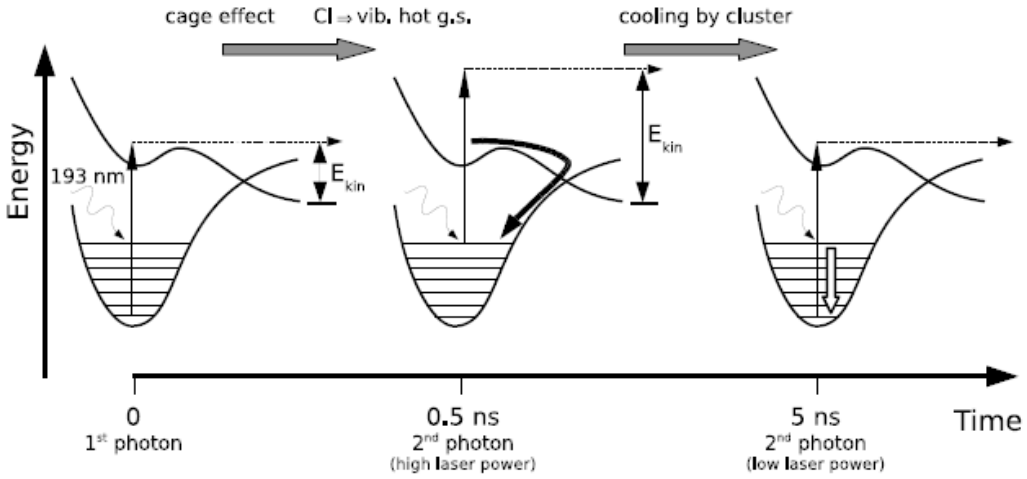

Figure 2: *Schematic picture of the multi-photon dissociation providing time-domain information about the cage effect by the energy-domain measurement. In time zero the molecule is excited, subsequently the cage effect quenches the molecule into the vibrationally hot ground state, and the second photon dissociates the molecule from this state resulting in fragment with a higher kinetic energy. If the second photon time delay is longer, the molecule is further cooled by the cluster into the lower vibrational state from which the slower fragments originate upon the photodissociation.*

Acknowledgement: The present work has been supported by the program "Nanotechnology for society" of the Czech Academy of Sciences KAN400400461, and by the grants Nr. KJB400400902 and 203/09/0422 of the Grant Agency of the Czech Republic.

[1] Franck, J.; Rabinovitsch, E. Trans. Far. Soc. **1934**, 30, 120
[2] Lauter, A.; Lee, K.; Jung, K.; Vatsa, R.; Mittal, J.; Volpp, H. Chem. Phys. Lett. **2002**, 358, 314.
[3] Cui, Q.; Morokuma, K.; Stanton, Chem. Phys. Lett. **1996**, 263, 46.
[4] Mordaunt, D. H.; Ashfold, M. N. R.; Dixon, R. N.; Loffler, P.; Schnieder, L.; Welge, K. H. J. Chem. Phys. **1998**, 108, 519.
[5] Fárnk M., Poterya V., Votava O., Ončák M., Slavíček P., Dauster I., Buck U., J. Phys. Chem. A **2009**, 113, 7322
[6] Poterya, V.; Votava, O.; Fárník, M.; Ončák, M.; Slavíček, P.; Buck, U.; Friedrich, B. J. Chem. Phys. **2008**, 128, 104313
[7] Balko, B. A.; Zhang, J.; Lee, Y. T. J. Chem. Phys. **1991**, 94, 7958.

Modelling Molecular Physisorption and Chemisorption on Metal Oxides

Kersti Hermansson, Carsten Müller and David Raymand
Materials Chemistry, Uppsala University, Box 530, S-75121 Uppsala, Sweden

Metal oxides are used as active components in a very large number of practical and industrial applications where molecular surface processes are vital for the material's functionality. Heterogeneous catalysis is a particularly important example since the majority of all products of the chemical industries is produced with the help of heterogeneous catalysts, while at the same time, catalysis is maybe the most important mechanism by which many technical processes can be made friendly to the environment. Unfortunately, for large classes of heterogeneous catalysts, the development of better catalysts is still largely a matter of trial and error, and the main reason for this is the lack of fundamental knowledge about the intrinsic nature of the catalyst's active sites. Generally only a few percent of the surface is believed to actually participate in the catalysis.

It is a tremendous scientific challenge to try to identify and describe the active sites in complicated metal oxides systems, especially for realistic reaction conditions of, sometimes, several hundred degrees centigrades. To derive valuable molecular-level information about such surface systems, experiments need to be complemented by theoretical investigations that manage to address as many of these effects as possible, as well as the different types of molecule-surface interaction at play, ranging from weak physisorption (at low temperatures only) to strong chemisorption.

ZnO and CeO_2 (ceria) are in focus in this report. Both are active components in a range of catalytic applications. The water-gas shift reaction, by which CO and H_2O is converted to H_2 and CO_2, is one important example.

Details of our calculations: hierachical models and multiscale modelling

In the solid state as well as in surface studies, the "standard" type of quantum-mechanical (QM) electronic structure calculations are periodic DFT calculations. However, periodic calculations introduce a periodic repetition which might be highly unwanted in large-scale interface systems where neither the structure nor any defects are periodic in nature. The remedy here would be very large supercells, but then the QM system easily becomes too large for present-day computers. We propose an alternative approach namely *a hierachical embedded-cluster model* to be able to describe active sites and molecular adsorption without the problems of periodic repetitions. Moreover, it will enable the use of advanced QM methods beyond DFT. A serious limitation with regular DFT calculations is namely that many electronically complicated situations are not properly described. One example is metal oxides with partially filled *d*- or *f*- shells. In ceria systems with oxygen vacancies, for

example, the DFT calculations fail because the electron localization for the *f* orbitals of Ce ions is not correctly treated using standard DFT methods. Various "fixes" have been tried in the literature, but these are tricky and largely empirical in nature, with limited predictive power. The embedded-cluster approach will allow high-level QM calculations, treating exchange and correlation.

In Ref. 1 we put forward a robust and high-quality embedded-cluster QM scheme, which manages to describe both ordered and highly distorted ionic surfaces. The embedding scheme is illustrated in **Fig. 1a**. The QM cluster is centered around the surface site to be examined.

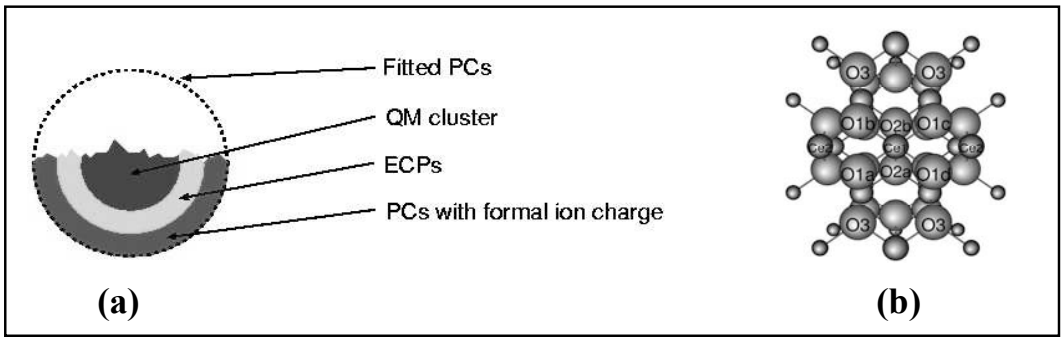

Fig.1 *Schematic picture of our embedding scheme, as applied to a ceria surface. (a) The hierarchical embedding model. (b) An example of a QM cluster.*

We have recently applied the embedded-cluster model to the study of the $CeO_2(111)$ and $CeO_2(110)$ surfaces with defects (oxygen vacancy) or adsorbed molecules (CO and N_2O). The QM part of one of the ceria (110) embedded clusters is seen from above in **Fig. 1b**. CO can both physi- and chemisorb on ceria surfaces, but as mentioned, the physisorption phenomenon is particularly challenging to describe. Again, here the embedded cluster model allows the use of higher-level QM calculations, more suitable than DFT to describe e.g. dispersion interactions. Results from these studies using MP2 and coupled-cluster (CC) calculations are presented below.

There are other matters of great concern in condensed-matter calculations, namely the issue of the attainable length and time scales. Thus, one of the greatest obstacles to further progress towards realistic simulations is the lack of accurate models to describe the interatomic interactions for large-scale systems, i.e. systems with many atoms that can be studied for a long time. The problem is that, on the one hand, QM calculations (periodic of embedded-cluster) cannot be used for large systems or long simulation times, and on the other hand, models purely based on analytical potential functions are often too inaccurate (or do not exist). In so-called *reactive force fields*, the binding between atoms is taken into account in the sense that bonds can be broken or formed "on the fly".

The ReaxFF force-fields, developed by van Duin et al. [2], constitute such a family of advanced many-body potentials. They are derived from QM calculations and provide a fast, transferable method for simulating chemical and physical interactions in materials.

We have applied the ReaxFF method to perform MD simulations of ZnO–water surface systems. Based on a large number of B3LYP calculations for Zn_mO_n clusters, crystal polymorphs and surfaces, we constructed a force-field which manages to well reproduce the QM data (energies, geometries and charges) for the same systems. Combined with potentials for the water-ZnO, we have studied the molecular dynamics of water (from one molecule *to* one monolayer *to* very much water) on the wurtzite ZnO(1 0 -1 0) surface at a range of temperatures, as a first step in the description of the water-gas shift reaction.

Results

Below we present some results for ceria and ZnO surfaces, as a flavour of the information that modern surface calculations manage to provide.

Ceria

Electron correlation (dispersion/electrostatic interactions) plays a key role in the ceria-CO interaction, i.e. the descriptions of the permanent and (especially) the induced dipole moments of CO are important. **Table 1** illustrates that the permanent dipole moment is very sensitive to the computational method used. It is seen that it is necessary to describe the electron correlation at a high level to achieve agreement with experiment. **Table 2** shows the resulting CO physisorption energies on ceria calculated using different methods. More details are found in Refs. 3 and 4. Neither the Hartree-Fock nor the B3LYP method give satisfactory results, while MP4 and CCSD(T) appear to do so. The latter two methods would normally be prohibitively expensive for this kind of system but were here made possible thanks to the use of an embedded-cluster model and a *local* electron correlation method (see Ref. 3).

Table 1. Dipole Moment of CO using the aug-cc-pVTZ basis set (in Debye)

Exp.	***+0.112***
HF	–0.1487
LDA	+0.2221
PW91	+0.1866
B3LYP	+0.0946
MP2	+0.1731
CCSD	+0.0678
CCSD(T)	+0.1016

Table 2. CO physisorption energy on top of a Ce atom on the ceria (110) surface

HF	15 kJ/mol = 0.15 eV
B3LYP	10 kJ/mol = 0.10 eV
MP2, full	24 kJ/mol = 0.24 eV
MP2, incremental	24 kJ/mol = 0.24 eV
MP4, incremental	21 kJ/mol = 0.21 eV
CCSD(T), incremental	21 kJ/mol = 0.21 eV

ZnO

We find that for *one water molecule* adsorbed on the wurtzite ZnO(1 0 -1 0) surface, the water molecules prefers to stay intact and not dissociate. However, for *a monolayer of water* adsorbed at 300 K, a zig-zag pattern forms, in agreement with predictions from experiment and the 0 K structure optimized from electronic-structure calculations in the literature. When a *liquid water film* is adsorbed on the surface, a *new and dynamic* water structure emerges, where more of the water molecules have dissociated, as a consequence of the cooperative interactions zinc cation - - - water (first layer) - - - water (second layer) interactions which dissociate about 3/4 of the water molecules and creates a characteristic and persistent hydroxide- - -water - - - hydroxide pattern next to the ZnO surface (**Fig. 2**). More details are found in Refs. 5 and 6.

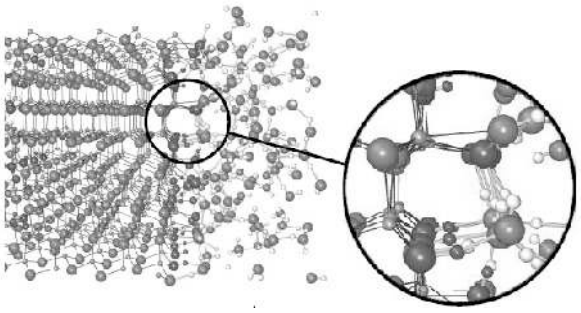

Fig. 2 *Snapshot from an equilibrated MD simulation of a ZnO slab at 300 K calculated with a ReaxFF force field. The system contains 12 ZnO layers and 256 water molecules in the MD box.*

Summary

In summary, it is now becoming feasible to use computational chemistry/physics calculations with hierachical models and multi- or interscale approaches to obtain accurate and valuable molecular-level information for rather large-scale models of functional materials at realistic temperatures.

[1] B. Herschend, M. Baudin, K. Hermansson, J. Chem. Phys. 120, 4939 (2004).
[2] A. C. T. van Duin, S. Dasgupta, F. Lorant, and W.A. Goddard III, J. Phys. Chem. A 105, 9396 (2001).
[3] C. Müller, B. Herschend, K. Hermansson, and B. Paulus, J. Chem. Phys. 128, 214701 (2008).
[4] C. Müller, B. Paulus, and K. Hermansson, and B. Paulus,Surface Science 603, 2619 (2009).
[5] D. Raymand, A. C.T. van Duin, M. Baudin, and K. Hermansson, Surface Science 602, 1020 (2008).
[6] D. Raymand, T. Edvinsson, D. Spångberg, A. van Duin, and K. Hermansson, Proc. SPIE, Vol. **7044**, 70440E (13 pp) (2008).

Astrochemistry - The Opportunity and the Challenge

Nigel J Mason and Bhala Sivaraman
Department of Physics and Astronomy, The Open University, Milton Keynes, MK7 6AA, United Kingdom

An understanding of the chemical evolution of the universe necessarily requires that we gain a detailed knowledge of the complex chemistry occurring in both the present and past history of the universe. Such 'astrochemistry' is distinct from that occurring in the terrestrial and industrial environments within which traditional chemical studies have been conducted for several reasons:
(i) Due to the low densities encountered in many astronomical regions the time scale of chemical evolution of astronomical objects may be tens of thousands (or even millions) of years.
(ii) The chemistry often takes place at much lower temperatures than those commonly encountered on Earth, emphasizing so-called 'barrierless' chemical reactions.
(iii) Chemical species not commonly found on Earth play a key role in astrochemistry e.g. the molecular ions H_3^+ and HeH^+ both of which are believed to take part in the first chemical reactions to have ever occurred in the history of the universe.
(iv) Much of the chemistry in 'heterogeneous' chemistry takes place on the surface of micron sized grains. The physical and chemical properties of these grains are more akin to aerosols/particulates that are fundamental to nanotechnology than traditional bulk surface chemistry.

Obtaining information on the different chemical environments within our universe relies critically upon the continuing technological advances in observational astronomy and computer modelling combined with a growing experimental programme that seeks to recreate such conditions in the laboratory. Recent space borne (e.g. Spitzer and, from 2010, Herschel) and ground based radio to far-infrared telescopes (including the commissioning of ALMA) are revolutionizing our 'Chemical' picture of the universe providing, for the first time, detailed chemical maps of the Universe with tantalising hints as to the chemical evolution of the cosmos. However, it has only been in the last two to three decades that our knowledge of the major chemical processes underpinning the chemical evolution in the Universe has developed sufficiently that we may now, with some confidence, propose reasonable hypotheses to describe some of the observational data and explore how such chemistry affects star/planet formation. Furthermore the discovery of, and increasing observational studies of 'exoplanets', is leading to fundamental questions as to the role of astrochemistry in the formation of molecules essential to the emergence of life - the latter being a core part of the

new scientific discipline of ‘Astrobiology’ upon which much of the ESA and NASA space programmes will be focused in the 21st Century.

Astrochemistry is therefore a research field that provides, in the next decade, unparalled opportunities but equally a field where there are significant challenges (scientific, technological and even philosophical) to be overcome requiring a truly interdisciplinary approach. This review talk will therefore both complement talks by other speakers (Bredehöft, Dutuit and Kaiser) at the Symposium but will crucially seek to identify key questions that need to be answered if we are to understand the mechanisms by which complex molecular species are formed in the Interstellar Medium (ISM) and during star and planet formation.

Soft Photo Ionisation Mass Spectrometry for Analysis of Organic Compounds Evolved in Thermal Analysis

Zimmermann R*, Saraji-Bozorgzad M, Geißler R, Streibel, T
Joint Mass Spectrometry Centre of Helmholtz Zentrum München and University Rostock, Helmholtz Zentrum München, D-85764 Oberschleißheim, Germany,
**ralf.zimmermann@uni-rostock.de*

Abstract:
A thermoanalytical instrument (i.e. Thermogravimetry device, TG) was coupled to a single photon ionisation mass spectrometer (SPI-MS) for evolved gas analysis (EGA). Single photon ionisation (SPI) was performed with a new type of VUV-light source, the so called electron beam pumped rare gas excimer lamp (EBEL). SPI does in most cases not fragment molecules upon the ionisation process. Thus a direct recording of the molecular fingerprint in the evolved gases from thermal composition of carbonaceous material is possible. In this work the thermoanalytical (TA) data and the SPI-MS information on the released organics for bio mass, fossil as well as for polymer samples) is presented The potential of hyphenating thermal analysis instruments and soft photo ionisation mass spectrometry (EBEL-SPI-MS) for fundamental and applied research and material analysis is discussed.

Introduction and Experimental:
Thermogravimetry – mass spectrometry (TG-MS) is a powerful hyphenated technology for analysis of thermal products from organic materials such as polymers, crude oils or coals. In the thermogravimetric analysis a sample of typically some mg is treated by a temperature program (often a linear temperature ramp of ~ 10-20 K/min starting at ambient temperature ending at about 1200 K) while the sample weight loss (vaporization/pyrolytic decomposition) is recorded by a sensitive balance. The evolved gases subsequently are analyzed in real-time by the on-line coupled mass spectrometer. However, if electron ionization (EI) is applied, TG-MS mainly gives information on small molecules such as CO_2 or CH_4. More complex organic molecules usually are not detectable due to the fragmentation associated with EI. TG-MS using soft single photon ionisation (SPI) recently was successfully applied for analysis of the evolved pattern of intact organic molecules [1]. In the simplest setup the gas inlet of the mass analyzer was coupled via a heated transfer line to the TG system (Typ STA 409, Netzsch Gerätebau, Selb, Germany). A special heated adapter was developed for the TG-system to avoid memory effects of the released higher boiling organic compounds. Note that the MS could be operated in both, electron impact ionisation or single photo ionisation (SPI) mode. A sketch of the setup of the device is shown in Figure 1A

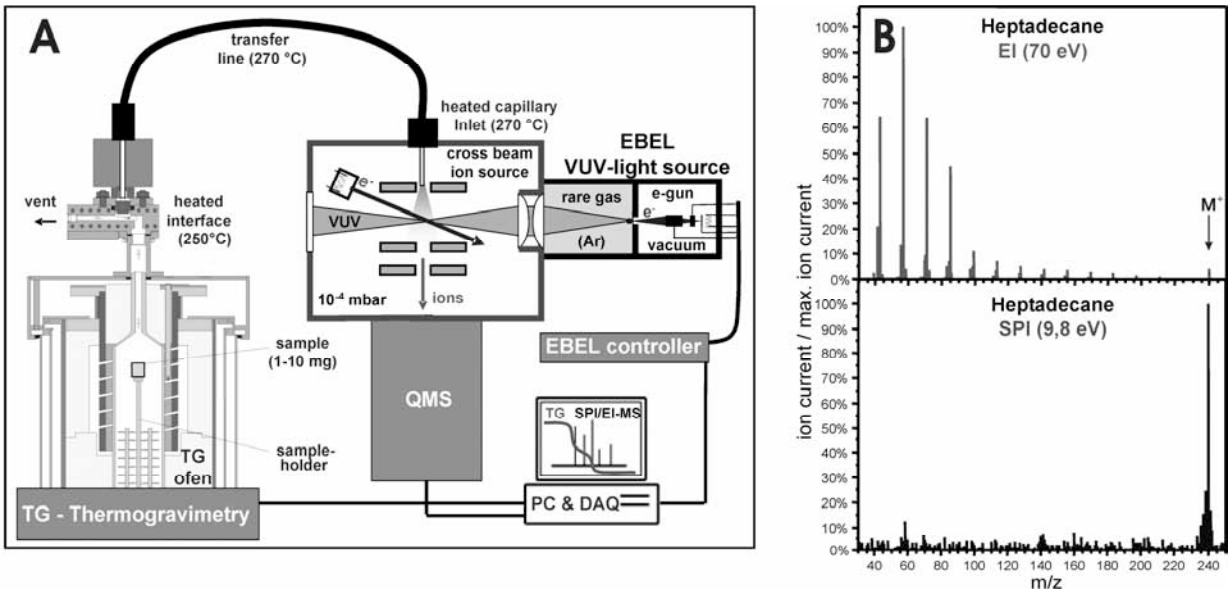

Figure 1: A) Schematic representation of the TG-EBEL-SPI-QMS prototype. B) TG- quadrupole mass spectra of heptadecane recorded with the developed TG-QMS instruments using the conventional electron impact ionisation (EI, 70 eV; hard ionisation top) single photon ionisation (Ar-EBEL, 9.8 EV: soft ionisation, bottom)

SPI allows soft ionisation, even of rather unstable molecules such as alkanes. In figure 1B two mass spectra of heptadecane are presented, recorded by EI (top) and SPI (bottom), for comparison. An innovative electron beam pumped rare gas excimer VUV-lamp (EBEL) technique is used for the soft photo ionisation process. In the EBEL-VUV light source a 0.7 × 0.7 mm^2 ceramic silicon nitride (SiN_x) foil of only about 300 nm thickness separates the rare gas volume (i.e. the luminescence medium, pressure > 1 bar) from a vacuum chamber which is containing an electron gun (EG). A 13-keV electron beam is generated by the EG and directed onto the foil. Electrons penetrate through the SiN_x foil into the rare gas volume with low-energy loss. The electrons excite and the rare gas atoms and in successive processes excited, meta-stable diatomic rare gas molecules (excimers) are formed and subsequently are dissociate again within a few microseconds. Upon the dissociation of the rare gas excimers, VUV-radiation is emitted. The excimer formation occurs solely in a small volume in the close proximity of the electron entrance foil. The rare gas volume can be filled with different rare gases or gas mixtures, in this experiments Ar was used (emission maximum: 126 nm, 9.8 eV centre photon energy) [1,2].

Results and Discussion:

Figure 2 shows the TG/DTG curves of polyethylene (PE, upper panel) recorded in inert atmosphere (nitrogen) at 20°C/min. heating rate. Furthermore two mass spectra obtained from the evolved gases at 480-510 °C, are shown, using either conventional EI ionisation (middle panel) or the EBEL-SPI photo ionisation (lower panel).

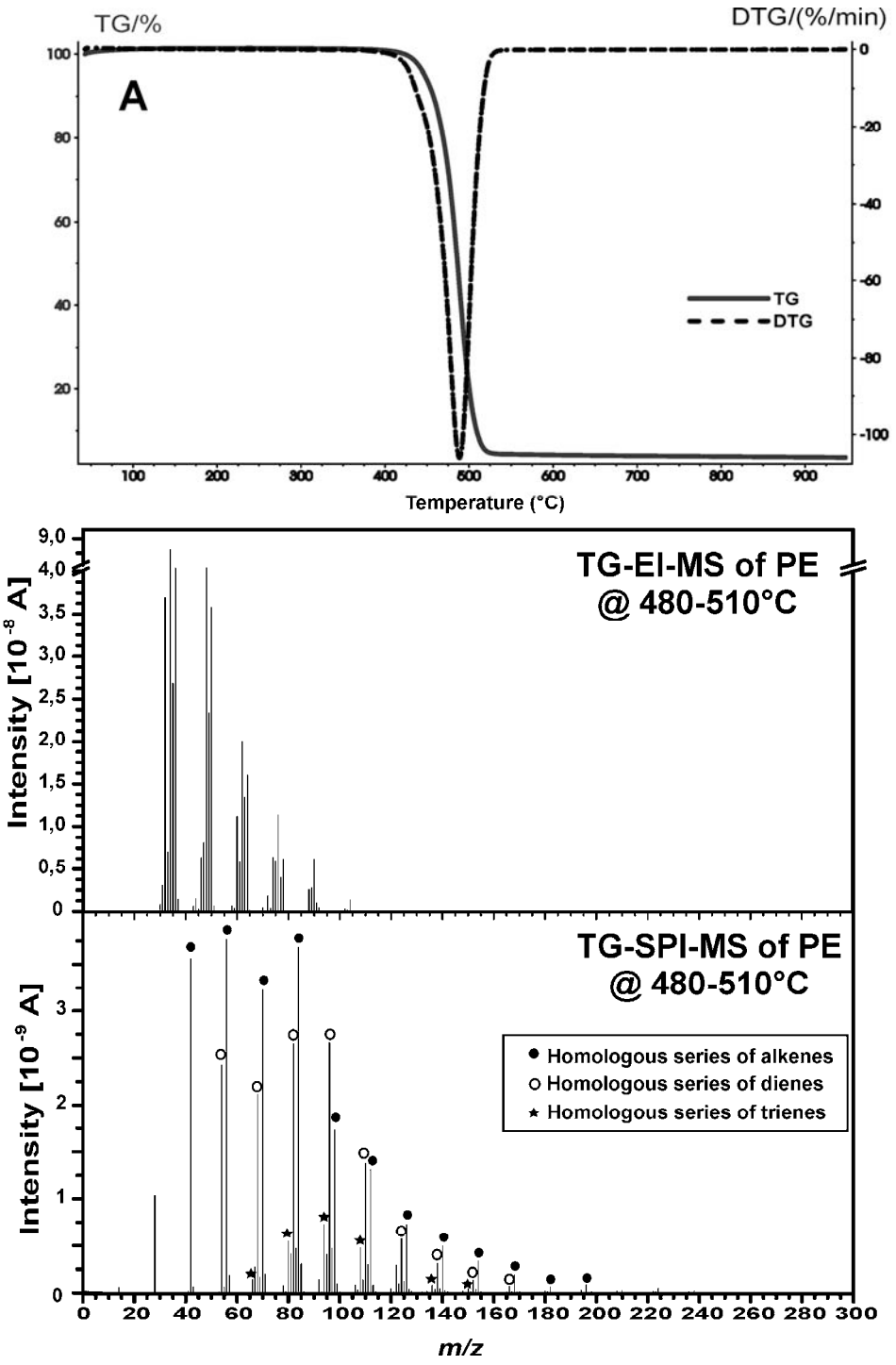

Figure 2: Thermogravimetry-single photo ionisation quadrupole mass spectrometry (TG-SPI-QMS with EBEL) results of polyethylene (PE): top) TG and DTG curves; middle) Electron impact mass spectrum (EI, 70 eV); bottom) SPI mass spectrum recorded during the maximal decomposition rate.

The TG curve depicts that PE decomposes in a one-step process at about 500 °C with a minimal residue. The weight loss slowly starts at 400 °C and reaches a maximum at about 490°C (easily seen from the DTG curve which is the 1st derivative of the TG curve). The EI mass spectrum is dominated by fragments. From the EI mass spectrum thus it can only be stated that the content of aromatic pyrolysis products is rather low in comparison to the aliphatic pyrolysis products. No further information of the evolved chemical profile can be drawn. In contrast, the soft EBEL-SPI mass spectrum reveals clearly the homologous series of alkenes, dienes as well as trienes up to C_{14}. Here the oligomer-distribution of the PE pyrolysis products can be analyzed. The observed on-line TG-SPI-MS data on the PE pyrolysis is in well accordance with results obtained by sophisticated off-line chemical analytical methods [3]. In the meantime several other polymers such as polyvinyl chloride (PVC) or polystyrene (PS) as well a natural products (mineral oil, wood) have been investigated. In Figure 3 an example of the chemical profile of the pyrolysis of the ABS-polymer is given as it was on-line recorded by TG-SPI-MS. With increasing complexity of the polymeric composition also the complexity of the chemical fingerprint increases. Currently improved couplings between TA und mass spectrometry have been developed. On the one hand a skimmed supersonic expansion coupling of TA to a EBEL photo ionisation Time-of-Flight Mass Spectrometer was developed (TG-Skimmer-SPI-TOFMS). This device makes it in principle possible to investigate lower volatile compounds. For examples the allotropy of sulphur as well as the thermal decomposition of several polymers was investigated with the new TG-Skimmer-SPI-TOFMS System. On the other hand improved concepts for implementing a fast gas chromatographic separation step in evolved gas analysis have been realized. The current results demonstrate the potential of evolved gas analysis (EGA) of organic compounds by soft ionisation mass spectrometry for thermal analysis (TA).

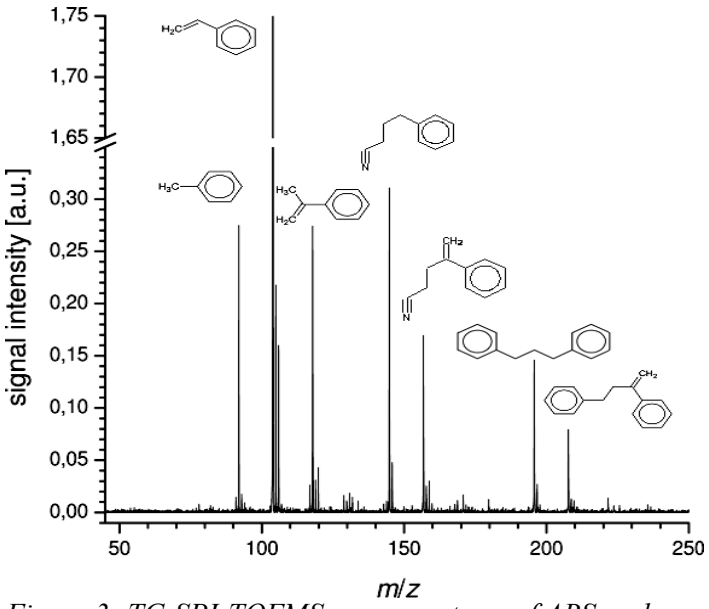

Figure 3: TG-SPI-TOFMS mass spectrum of ABS- polymer showing the evolved molecular pyrolysis products at 400 °C.

References:

[1] M. Saraji, R. Geissler, T. Streibel, F. Mühlberger, M. Sklorz, E. Kaisersberger, T. Denner R. Zimmermann, Anal. Chem. 80 (2008) 3393-3403

[2] Wieser, J.; Murnick, D. E.; Ulrich, A.; Huggins, H. A.; Liddle, A.; Brown, W. L. Review of Scientific Instruments 1997, 68, 1360-1364.

[3] Anthony, G. M. Polymer Degradation and Stability 1999, 64, 353-357.

Author Index